

5-2012

Structure and Rheology of the Sandhill Corner Shear Zone, Norumbega Fault System, Maine: a Study of a Fault from the Base of the Seismogenic Zone

Nancy Ann Price

Follow this and additional works at: <http://digitalcommons.library.umaine.edu/etd>



Part of the [Geology Commons](#), and the [Geophysics and Seismology Commons](#)

Recommended Citation

Price, Nancy Ann, "Structure and Rheology of the Sandhill Corner Shear Zone, Norumbega Fault System, Maine: a Study of a Fault from the Base of the Seismogenic Zone" (2012). *Electronic Theses and Dissertations*. 1874.
<http://digitalcommons.library.umaine.edu/etd/1874>

This Open-Access Dissertation is brought to you for free and open access by DigitalCommons@UMaine. It has been accepted for inclusion in Electronic Theses and Dissertations by an authorized administrator of DigitalCommons@UMaine.

**STRUCTURE AND RHEOLOGY OF THE SANDHILL CORNER SHEAR ZONE,
NORUMBEGA FAULT SYSTEM, MAINE: A STUDY OF A FAULT FROM
THE BASE OF THE SEISMOGENIC ZONE**

By

Nancy Ann Price

B.S. The Richard Stockton College of New Jersey, Pomona, 2005

M.S. University of Massachusetts, Amherst, 2007

A THESIS

Submitted in Partial Fulfillment of the

Requirements for the Degree of

Doctor of Philosophy

(in Earth Sciences)

The Graduate School

The University of Maine

May, 2012

Advisory Committee:

Scott E. Johnson, Professor of Earth Sciences, Advisor

Christopher C. Gerbi, Assistant Professor of Earth Sciences

Peter O. Koons, Professor of Earth Sciences

Martin G. Yates, Instructor of Earth Sciences

David P. West Jr., Professor of Geology, Middlebury College

Rachel J. Beane, Professor of Earth and Oceanographic Science, Bowdoin College

LIBRARY RIGHTS STATEMENT

In presenting this thesis in partial fulfillment of the requirements for an advanced degree at The University of Maine, I agree that the Library shall make it freely available for inspection. I further agree that permission for "fair use" copying of this thesis for scholarly purposes may be granted by the Librarian. It is understood that any copying or publication of this thesis for financial gain shall not be allowed without my written permission.

Signature:

Date:

**STRUCTURE AND RHEOLOGY OF THE SANDHILL CORNER SHEAR ZONE,
NORUMBEGA FAULT SYSTEM, MAINE: A STUDY OF A FAULT FROM
THE BASE OF THE SEISMOGENIC ZONE**

By Nancy Ann Price

Thesis Advisor: Dr. Scott E. Johnson

An Abstract of the Dissertation Presented
in Partial Fulfillment of the Requirements for the
Degree of Doctor of Philosophy
(in Earth Sciences)
May, 2012

Determining the structure and rheology of a seismogenic fault at frictional-to-viscous transition (FVT) depths is vital for understanding its strength and behavior. Few studies describe a fault from within this depth level, so the architecture of a shear zone at these depths as well as the effect of transient coseismic and postseismic deformation on the rheology of the shear zone is poorly-understood. The Sandhill Corner strand of the Paleozoic Norumbega fault system of Maine is the one of the few known examples of a subvertical, strike-slip fault exhumed from FVT depths. Using a suite of samples collected from the Sandhill Corner shear zone, this study (a) identifies coseismic and postseismic structures; (b) investigates the history of deformation from quartz data; (c) characterizes the across-strike structure; and (d) considers the strength and rheology of a shear zone within the FVT.

The shear zone initially localized along the contact between two rheologically-contrasting units. Quartz microstructural data from monomineralic quartz ribbons suggest a history of initial

localization at relatively higher temperatures influenced by a strong pre-existing crystallographic preferred orientation (CPO) followed by a lower temperature overprint. Based on maps showing the spatial distribution of rock type, pseudotachylyte, quartz microstructure, and quartz grain sizes, this study proposes across-strike divisions of an outer shear zone, an inner shear zone, and a shear zone core. In the outer shear zone, the lower temperature quartz overprint is variable with grain sizes of 10-80 μm . In the inner shear zone, the quartz grains are completely overprinted with grain sizes of 10-20 μm , indicating flow stresses of 60-100MPa. Contrasting quartz misorientation and CPO data also distinguish the inner shear zone from the outer shear zone.

The shear zone core is a zone of ultramylonite/phyllonite contained within the inner shear zone that is coincident with the lithologic contact. The ultra fine-grained, micaceous ultramylonite/phyllonite of the shear zone core derived largely from deformed pseudotachylyte would have promoted grain size sensitive, diffusion-mediated creep in the matrix surrounding quartz ribbons, leading to the formation of the weakened fault core that flowed at stresses lower than those estimated from the quartz grain sizes.

THESIS
ACCEPTANCE STATEMENT

On behalf of the Graduate Committee for Nancy Ann Price, I affirm that this manuscript is the final accepted thesis. Signatures of all committee members are on file with the Graduate School at the University of Maine, 42 Stodder Hall, Orono Maine.

Dr. Scott E. Johnson, Professor of Earth Sciences

ACKNOWLEDGEMENTS

Financial support for this research was provided by the National Science Foundation through grants EAR-0810039, EAR-0911150, EAR-0207717, and MRI-0820946. Additional support was provided by University of Maine through an MEIF Summer Research Fellowship, a Chase Fellowship, and a Doctoral Research Fellowship. Field and laboratory costs were covered through a Geological Society of America (GSA) Graduate Student Research Grant and two University of Maine Graduate Student Research Grants. Travel costs to present at conferences were largely covered through several University of Maine Graduate Student Travel Grants, NE-GSA travel grants, and the National Science Foundation support through GSA for student travel to the August 2011 Penrose Conference in Spain.

First, I would like to thank Scott Johnson for all the time and effort he devoted to the success of my Ph.D. A lot of important living and learning has happened over the past five years, and I am grateful for those experiences. I am glad to have had the opportunity to learn from you....and, perhaps, you have learned something from me. In the very least, I have learned that having your advisor's pet cat pass away on your watch while you are house/pet sitting is not grounds for immediate failure (RIP Sancho).

Many thanks also to Chris Gerbi for all your time, advice, and support. Your guidance and patience has also played a vital role in the success of my Ph.D. I hope you realize that you have become such an important part of our research group, and that we are stronger for your perspective and your example.

Thank you also to the other members of my thesis committee. I am grateful for the pressure from Peter Koons to keep my research relevant to the larger questions in geology/geodynamics. I hope to achieve greater success than simply being a door-to-door vacuum salesman. Thank you to Marty for his advice and expertise over the years that have helped to keep me and my ideas grounded in the realistic and practical. I enjoyed working with

Dave West on the NEIGC field trip and guidebook. Thank you for enthusiastically introducing me to all the good Sandhill Corner outcrops. Many thanks to Rachel Beane for the time and efforts spent working with me early in my EBSD work as well as for all the warm support and encouragement for my professional growth. Although not on my committee, special thanks to Ed Grew for the discussions, the research advice, and all the unwavering support over the years.

I am very appreciative to all those other people that have helped me and supported my research in both big and small ways. Very big thanks to Caleb Churchill for access to his property, for the gift of the rock samples, and for making me feel at home on his property. Thank you to Alice Kelley for all your help, feedback, support, and encouragement with 101 teaching. I am grateful to Sheila Seaman for the opportunity to learn FTIR. Thank you, thank you, thank you to Dianne Perro! What would I have done without you? I am grateful for the help of Dan Phillips, Patrick Ryan, and April in the field and in the lab. Thank you to Brad for yelling at me to go home before I got in trouble (...”come on get happy”). Many thanks to the graduate students past and present, including but not limited to: Ben Hooks, Eva Wadoski, Meredith Petrie, Charles Rodda, Holly Theriault, Katie Pingree (Shippee), Sam Roy, Wonjoon Song, JohnRyan MacGregor, Eileen Spinney, and Margo Mansfield. A special thanks to the hard rock group these last two years, particularly Deb Shulman and Ben Frieman. We had some good times together, and I am happy to have had the opportunity to end my time at UMaine with such loving, supportive, and accepting people.

Finally, I am eternally grateful for those people that have kept me sane through this intellectual marathon. To my love, Khamkeo Vongpaseuth, grateful is an understatement. Even at such a distance, you hold me up, cheer me up, and keep me waking up every morning with a smile. To Félice Naus-Thijssen, I would not have been able to survive this experience without you. You and Harm were my family while you were here, and you helped me to forget how far away Kham really was. Thank you for being a part of my life. Of course, a big thank you to all my family and friends, particularly my mom and dad (Marie and Joseph Price), my sister and her

husband (Missy and Joe Raab), my Aunt Marie and Uncle Tony, and my best girlfriends from Jersey, Kristen Witucki and Meg Iannacone. I do not take for granted the fact that you have been there to listen to me and support me, no matter what happens. Thank you to Gail Tunstead and Dave Flewelling. It was a blessing that I found 104 Main St. and the both of you to visit and chat with! I am grateful to David Snoeyenbos for the conversations and for being an example from which I can learn. Thank you also to Manasa Gudherti, the ladies (and Paul) at the Orono Public Library, and Kathy and the group at Firesign. And last but not least, I am grateful for my interaction with all my fuzzy friends: hamsters Hamilton, Linus, and Felix, and dogs BeeBee, Baxster, Gunner, Moxie, Princess, and Indy.

TABLE OF CONTENTS

ACKNOWLEDGEMENTS	iii
LIST OF FIGURES	xi
LIST OF TABLES	xvi

Chapter

1.	INTRODUCTION	1
1.1	Purpose of Study.....	1
1.2	The Frictional-to-Viscous Transition Within a Seismogenic Fault	4
1.3	Geologic Setting	7
1.3.1	Regional Geology	7
1.3.2	Exposure of the Norumbega Fault System in Maine.....	12
1.3.2.1	Eastern Maine	15
1.3.2.2	South-Central Maine.....	16
1.3.2.3	Casco Bay Restraining Bend and Coastal Brittle Zones	17
1.3.3	Geologic Setting of the Study Area: The Sandhill Corner Shear Zone	19
2.	IDENTIFYING DEFORMED PSEUDOTACHYLYTE AND ITS INFLUENCE ON THE STRENGTH AND EVOLUTION OF A CRUSTAL SHEAR ZONE AT THE BASE OF THE SEISMOGENIC ZONE.....	22
2.1	Chapter Abstract	22
2.2	Introduction.....	23
2.3	Pseudotachylyte-derived Ultramylonite Layers.....	25
2.4	Field Observations	29
2.5	Analytical Methods.....	31

2.6	Microscale Observations.....	34
2.6.1	Undeformed Pseudotachylyte	34
2.6.1.1	Quartzofeldspathic Unit.....	34
2.6.1.2	Schist Unit	36
2.6.1.3	Calc-silicate Granofels Unit.	37
2.6.2	Recrystallized and Deformed Pseudotachylyte	39
2.6.2.1	Quartzofeldspathic Unit.....	45
2.6.2.2	Schist Unit	46
2.6.2.3	Calc-silicate Granofels Unit.	47
2.7	Discussion.....	48
2.7.1	The Transformation From Pseudotachylyte Veins to Ultramylonite/Phyllonite Layers	48
2.7.2	Criteria for the Identification of Deformed Pseudotachylyte	51
2.7.3	Implications for the Global Abundance of Deformed Pseudotachylyte	57
2.7.4	Deformation Mechanisms and Rheology of a Deformed Pseudotachylyte Vein.....	59
2.7.5	The Influence of Pseudotachylyte on the Strength and Evolution of the Sandhill Corner Shear Zone.....	63
2.8	Summary and Conclusions	64
3.	COMPLEX QUARTZ RECRYSTALLIZATION FABRICS FROM SHEARED QUARTZ RIBBONS WITH A STRONG PRE-EXISTING CRYSTALLOGRAPHIC PREFERRED ORIENTATION	66
3.1	Chapter Abstract	66
3.2	Introduction.....	67

3.3	Interpreting Non-Coaxial Quartz Deformation Fabrics	70
3.3.1	Optical Microstructures	70
3.3.2	CPO Patterns and Fabric Evolution	72
3.3.3	Crystallographic Misorientation Analysis	75
3.4	Field Observations	78
3.5	Analytical Methods.....	78
3.6	Quartz Microstructures	81
3.6.1	Grain Type 1- Amoeboid, Low Aspect Ratio Grains	81
3.6.2	Grain Type 2- Elongate, High Aspect Ratio Grains	84
3.6.3	Grain Type 3- Small, Equant Grains	84
3.6.4	Combinations of Grain Types.....	85
3.6.5	Atypical Quartz Microstructures	87
3.7	Quartz CPO Patterns	89
3.7.1	Host Rock CPO.....	89
3.7.2	Shear Fabric CPO Patterns	89
3.7.3	CPO Patterns and Quartz Microstructures.....	93
3.8	Misorientation Analysis.....	93
3.9	Discussion	100
3.9.1	Interpretation of Quartz Microstructures	100
3.9.2	The Pre-existing CPO in Recrystallized Quartz CPO Patterns	103
3.9.3	Quartz CPO Data and IPF Plots of Misorientation Rotation Axes.....	105
3.9.4	Misorientation Rotation Angles.....	107

3.9.5	Factors Affecting Quartz Fabric Development.....	109
3.9.5.1	Deformation Conditions	109
3.9.5.2	The Inherited Fabric	111
3.9.5.3	Twinning and Deformation Mechanisms.	113
3.9.6	Quartz Fabric Evolution in the Sandhill Corner Shear Zone.....	115
3.10	Implications for the Deformation History of the Sandhill Corner Shear Zone	117
3.11	Conclusions.....	119
4.	THE ALONG- AND ACROSS-STRIKE STRUCTURE OF A SHEAR ZONE AT THE BASE OF THE SEISMOGENIC ZONE, NORUMBEGA FAULT SYSTEM, MAINE.....	120
4.1	Chapter Abstract	120
4.2	Introduction.....	121
4.3	Analytical Methods.....	122
4.4	Spatial Distribution of Data Within the Sandhill Corner Shear Zone	125
4.4.1	Rock Types	125
4.4.2	Pseudotachylite and Deformed Pseudotachylite	136
4.4.3	Quartz Microstructural and Orientation Data	137
4.4.4	Quartz Grain Size Data.....	139
4.5	Discussion.....	140
4.5.1	The Structure of the Sandhill Corner Shear Zone	140
4.5.2	Interpreting the Deformation History of the Sandhill Corner Shear Zone	143
4.5.3	Shear Zone Rheology and Fault Strength.....	145
4.5.4	Correlation With Other Crustal Levels.....	147
4.6	Summary and Conclusions	148

REFERENCES	150
APPENDIX. SAMPLE LOCATIONS WITHIN THE SANDHILL CORNER	
SHEAR ZONE.....	163
BIOGRAPHY OF THE AUTHOR	172

LIST OF FIGURES

Figure 1.1.	A representative strength-depth diagram for the crust.....	1
Figure 1.2.	A schematic diagram showing the changes in rock type, rock strength, and seismic behavior with depth in a seismogenic fault.....	3
Figure 1.3.	A series of schematic displacement-depth diagrams showing the displacement of a fault at different depth levels during the three stages of the seismic cycle.....	6
Figure 1.4.	Geologic map of the coast of Maine showing the location of the peak metamorphic zones	9
Figure 1.5.	Geologic map of the coast of Maine showing the location of the known strands of the Norumbega fault system.....	10
Figure 1.6.	Geologic map of the coast of Maine showing the known locations of transient, coseismic structures	11
Figure 1.7.	Geologic map of the central and southern coast of Maine showing the location of samples analyzed for $^{40}\text{Ar}/^{39}\text{Ar}$ hornblende and muscovite mineral cooling ages	13
Figure 1.8.	Geologic map of the central and southern coast of Maine showing the location of samples analyzed for apatite fission track ages and the temperature ranges estimated from quartz microstructures	14
Figure 1.9.	Geologic map of the study area within the Norumbega fault system	19
Figure 2.1.	Field observations from rocks of the Sandhill Corner shear zone	30
Figure 2.2.	Photomicrographs, SEM-BSE images, and element distribution maps of primary pseudotachylyte features from the quartzofeldspathic, schist, and calc-silicate granofels units	35

Figure 2.3.	Representative powder x-ray diffraction spectra of pseudotachylyte matrix material from the Sandhill Corner shear zone.....	40
Figure 2.4.	A change in the mineral assemblage and texture occurs during the formation, recrystallization, and deformation of pseudotachylyte in each rock type.	41
Figure 2.5.	Examples of the stages of transformation of a pseudotachylyte vein to an ultramylonite/phyllonite layer within the three rock types of the Sandhill Corner shear zone.	42
Figure 2.6.	Examples of the features seen in deformed pseudotachylyte veins.....	43
Figure 2.7.	Average percent mica content of the recrystallized matrix of deformed pseudotachylyte in the mylonites of the quartzofeldspathic unit as compared to the host rock.....	45
Figure 2.8.	SEM-EBSD derived quartz c-axis pole figures from a sample of the quartzofeldspathic mylonites.	46
Figure 2.9.	A clast size-frequency diagram of clasts within a deformed pseudotachylyte in the calc-silicate granofels unit displays a modified power-law relationship.	48
Figure 2.10.	Examples of deformed pseudotachylyte distribution at the thin section scale in rocks from the Sandhill Corner shear zone.....	57
Figure 2.11.	A conceptual model for weakening during the formation and recrystallization of a single pseudotachylyte vein and during the lifetime of the shear zone.....	62
Figure 3.1.	Field images of quartz ribbons within the schist host rock and sheared schist of the Sandhill Corner shear zone.....	79

Figure 3.2.	A chart showing the across strike variation in rock type and quartz microstructures from the Sandhill Corner shear zone within the southern part of the study area.....	82
Figure 3.3.	Quartz microstructures comprise one or a combination of three primary quartz grain types within deformed quartz ribbons of the Sandhill Corner shear zone	83
Figure 3.4.	The replacement of large, amoeboid quartz grains by smaller, more equant grains in quartz ribbons in the protomylonite is more prevalent where shear fractures and rare pseudotachylyte occur	86
Figure 3.5.	Atypical quartz microstructures observed within deformed quartz ribbons of the Sandhill Corner shear zone.....	88
Figure 3.6.	The pre-existing host rock quartz fabric	90
Figure 3.7.	A suite of c-axis and a-axis pole figures showing CPO patterns typical of quartz veins found within the quartzofeldspathic mylonite, protomylonite, and sheared schist of the Sandhill Corner shear zone	91
Figure 3.8.	Quartz CPO patterns for different grain size fractions of a deformed quartz ribbon. Orientation maps and pole figures show all sizes, >80mm, and <30mm.....	94
Figure 3.9.	Fine-grained samples with layered grain orientation domains show different CPO patterns and misorientation rotation angle histogram profiles for each of the grain domains	95
Figure 3.10.	Misorientation rotation angle histogram plots, misorientation angle boundary maps, mineral orientation maps, and c-axis pole figure of selected samples from the Sandhill Corner shear zone.....	96
Figure 3.11.	Misorientation data for four selected samples from the Sandhill Corner shear zone.	99

Figure 3.12.	A schematic diagram showing how the passive rotation of folded quartz ribbons of the host rock would change the location of the inherited CPO in the rocks of the Sandhill Corner shear zone	100
Figure 4.1.	Geologic map of the study area within the Norumbega fault system showing the location of Sites A, B and C	123
Figure 4.2.	Maps of Site A showing the spatial distribution of rock type, the relative amounts of pseudotachylyte and deformed pseudotachylyte, quartz microstructures, and quartz grain sizes.....	126
Figure 4.3.	Maps of Site B showing the spatial distribution of rock type, the relative amounts of pseudotachylyte and deformed pseudotachylyte, quartz microstructures, and quartz grain sizes.....	127
Figure 4.4.	Maps of Site C showing the spatial distribution of rock type, the relative amounts of pseudotachylyte and deformed pseudotachylyte, quartz microstructures, and quartz grain sizes.....	128
Figure 4.5.	Quartz crystallographic preferred orientation, grain size, and microstructural data for a representative selection of six samples from Site A.....	129
Figure 4.6.	Quartz crystallographic preferred orientation, grain size, and microstructural data for a representative selection of six samples from Site B.....	131
Figure 4.7.	Quartz crystallographic preferred orientation, grain size, and microstructural data for a representative selection of six samples from Site C.....	133
Figure 4.8.	Schematic diagram showing the across-strike structure of the Sandhill Corner shear zone	141

Figure A1.	A map of the blueberry field area showing the location of numbered samples.....	169
Figure A2.	A map of the Crummett Mountain area showing the location of numbered samples.	170
Figure A3.	A map of the Quarry area showing the location of numbered samples.....	171

LIST OF TABLES

Table 2.1.	EMPA mineral compositions from within the matrix of pseudotachylyte veins in comparison with the composition of minerals from the surrounding host rock.	38
Table A1.	Location data for samples from the Sandhill Corner shear zone used within this study	163

Chapter 1

INTRODUCTION

1.1. Purpose of Study

The structure and rheology of km-scale, vertical strike-slip faults vary with depth as fracture and frictional sliding within the upper crust transitions to thermally-dependent viscous creep in the mid-to-lower crust (Scholz, 1998). The nature of the change in deformation behavior is transitional over a variable depth interval that is referred to as the frictional-to-viscous transition (Schmid and Handy, 1991). The frictional-to-viscous transition coincides with the strength maximum between the rocks of the upper crust where deformation occurs on discrete surfaces in accordance with Byerlee's Law and the mid-to-lower crust where strain is accommodated in broader zones of viscous flow as is approximated by laboratory-derived flow laws (Fig.1.1; Brace and Kohlstedt, 1980; Handy, 2007). The depth range of the frictional-to-

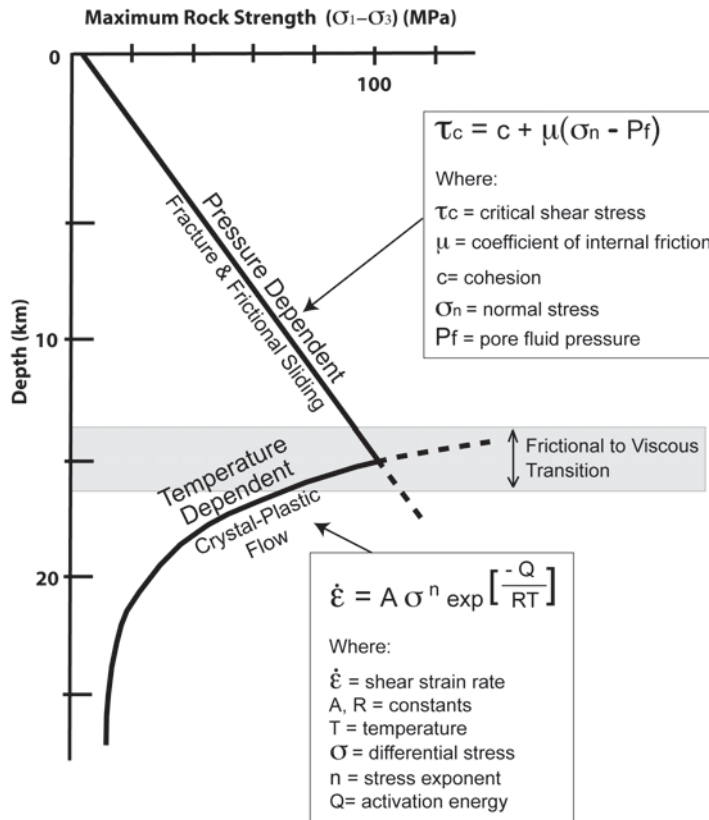


Figure 1.1. A representative strength-depth diagram for the crust. The upper crust deforms through pressure-dependent fracture and frictional-sliding following Byerlee's Law (shown above), while the mid-to-lower crust deforms by temperature-dependent crystal plastic deformation, typically dislocation creep following a power law relationship (shown below). The frictional-to-viscous transition is the depth interval over which the two lines intersect.

viscous transition coincides with the maximum earthquake rupture depth (Fig. 1.2; Handy et al., 2007; Scholz, 1998; Sibson, 1986), and mylonites from the frictional-to-viscous transition exhibit quartz microstructures that indicate higher differential stresses than mylonites from deeper in the crust where increasing temperatures lead to a decrease in the differential stress required for viscous flow (Stipp et al., 2002b; Behr and Platt, 2011). The frictional-to-viscous transition, therefore, exerts first-order control over the state of stress throughout the entire crust and coupling of deformation between the upper and mid-to-lower crust. Because of this, understanding the structure, rheology, and evolution of a shear zone within the frictional-to-viscous transition of a crustal-scale seismogenic fault is an essential step in understanding how stresses and strains are transferred across the frictional-to-viscous transition.

Study of a fault from frictional-to-viscous transition depths (~10-15km) depends on observations from excellent examples of exhumed fossil faults. A fossil frictional-to-viscous transition is best identified by the presence of mutually-overprinting frictional and viscous structures (Handy et al., 2007). Few studies describe the structure and rheology of a fault from within or across this depth level (e.g. Alpine Fault- Toy et al., 2008, 2011; Woodruffe Thrust, Lin et al., 2005; Outer Hebrides Thrust- Sibson, 1980; White, 1996), and most of these structures have a thrust or normal component. Among the documented examples of shear zones with coeval frictional and viscous structures, the Norumbega fault system of Maine is the only (or one of the few) known example with an exhumed fossil frictional-to-viscous transition from a large-displacement, subvertical, strike-slip fault zone (Sibson and Toy, 2006). The Sandhill Corner shear zone of the Norumbega fault system contains mutually-overprinting mylonite and pseudotachylite, and was exhumed with little to no post-deformational thermal or structural overprint, making it the ideal place to investigate the role the frictional-to-viscous transition plays in transferring stresses and strains through coupling between the upper crust and the mid-to-lower crust.

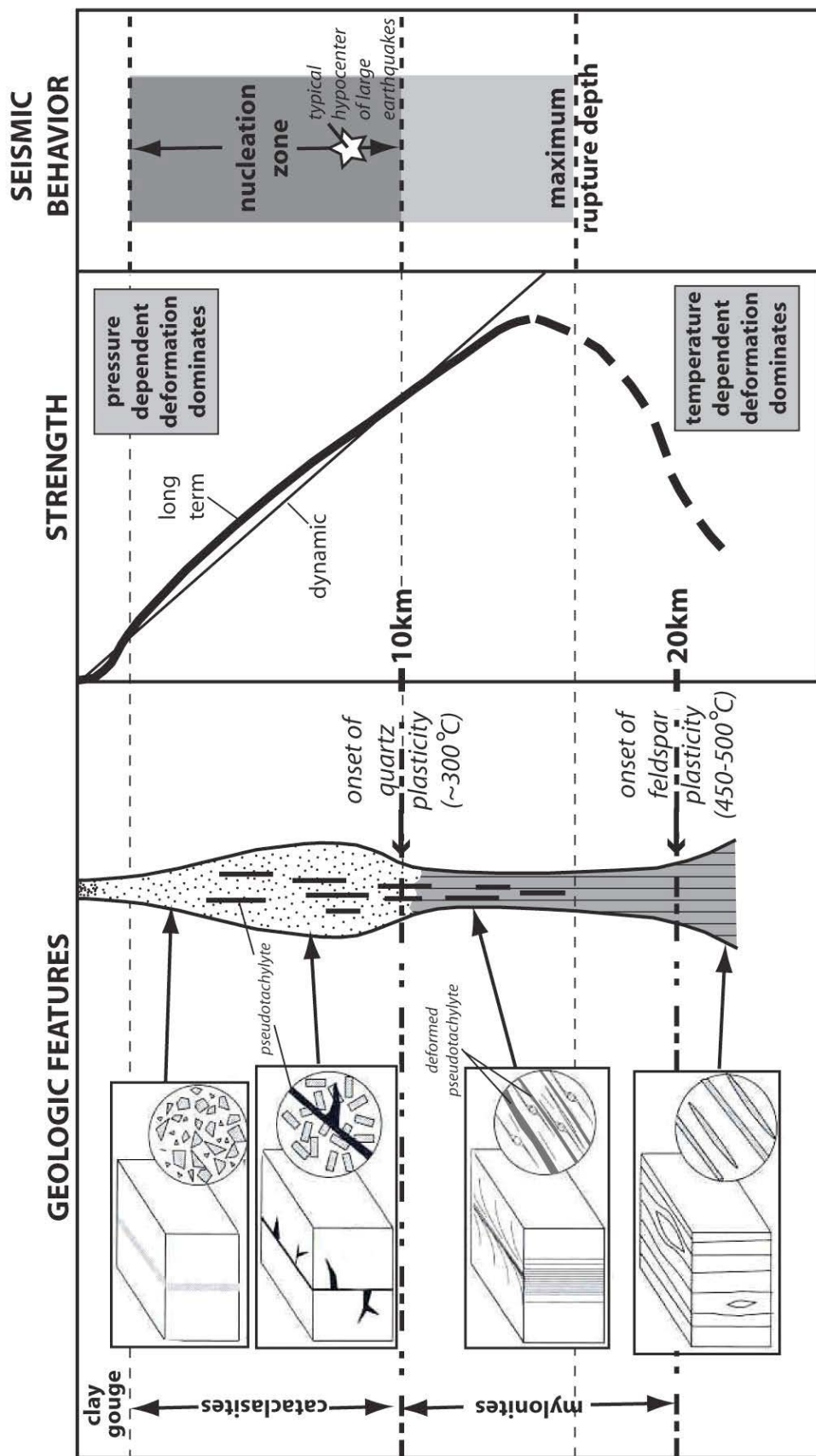


Figure 1.2. A schematic diagram showing the changes in rock type, rock strength, and seismic behavior with depth in a seismogenic fault. Adapted from Scholz, 2002; Passchier and Trouw, 2005.

A suite of samples was collected in several across-strike transects along a section of the Sandhill Corner shear zone in south-central Maine in an effort to describe the across- and along-strike structure and rheology of a shear zone within the frictional-to-viscous transition of a seismogenic fault. Structures indicating coseismic slip (frictional melt veins called pseudotachylyte) were characterized (Chapter 2) and a list of criteria for identifying deformed pseudotachylyte was compiled. These criteria were used to estimate the percent of the rock that comprise deformed pseudotachylyte veins and to consider the effect the formation, recrystallization, and deformation of multiple generations of pseudotachylyte may have had on the rheology and evolution of the shear zone. Quartz fabrics were also described (Chapter 3) from deformed quartz ribbons in these samples in an effort to better understand the development of the shear fabrics over time given a strong pre-existing crystallographic preferred orientation and to determine what information monomineralic quartz ribbons may provide for the interpretation of the deformation history of the shear zone. Finally, the spatial distribution of pseudotachylyte, quartz microstructures, and quartz grain size data were used to determine the across- and along-strike structure of the Sandhill Corner shear zone (Chapter 4). A discussion of the rheology and strength of a seismogenic fault within frictional-to-viscous transition depths follows in Chapter 4.

This chapter contains a short introduction to the frictional-to-viscous transition within seismogenic faults, briefly describes the regional geology of Maine, presents the current understanding of the geologic history of the Norumbega fault system, and describes the geological setting of the study area. More detailed background information relevant to the specific parts of the study described above can be found in the corresponding chapters.

1.2. The Frictional-to-Viscous Transition Within a Seismogenic Fault

In the most basic sense, the frictional-to-viscous transition, or the brittle-ductile transition (Schmid and Handy, 1991), is where the line defining the stress at failure by fracture and

frictional-sliding described by Byerlee's Law intersects the power law curve of the temperature-dependent viscous flow on a differential stress-depth diagram (Fig. 1.1; Brace and Kohlstedt, 1980; Handy et al., 2007; Kohlstedt et al., 1995; Scholz, 1998, 2002; Sibson, 1986). The depth level of this intersection and the maximum stress at failure (i.e. the crustal strength maximum) is dependent on a number of factors, including the mechanisms accommodating the viscous flow, the geothermal gradient, the strain rate, and the rock type. Typically, the viscous flow line plots the dislocation creep flow law for wet quartz at constant, near "steady-state" strain rates (10^{-12} to 10^{-14} s $^{-1}$), placing the start of the frictional-to-viscous transition at ~10km coincident with the onset of quartz plasticity at ~300°C and ending between ~15-20km before the onset of feldspar plasticity at ~450-500°C (Fig. 1.2; Scholz, 2002; Stipp et al., 2002a,b). A mineral weaker in flow or a higher geothermal gradient can shift the frictional-to-viscous transition to shallower depths and lower differential stress values (e.g. Imber et al., 2001), whereas a stronger mineral type and/or a lower geothermal gradient can put the frictional-to-viscous transition at greater depths and higher values of stress at failure. Because of these factors and others, the frictional-to-viscous transition is considered a depth interval where either frictional or viscous deformation mechanisms may dominate.

Within a seismogenic fault, strain rates vary with the seismic cycle affecting the style of deformation within the frictional-to-viscous transition (e.g. Handy et al., 2007; Rolandone et al., 2004; Scholz, 1998). The seismic cycle consists of a long-term (10^3 - 10^5 yr) period of interseismic deformation where the mylonites and gneisses in the mid-to-lower crust (Fig. 1.2) are flowing viscously while the upper crust is frictionally locked (Fig. 1.3). Transient coseismic slip occurs over seconds to minutes when the frictional resistance of the fault in the upper crust is overcome and the fault slips seismically causing an earthquake. Depending on where the earthquake nucleates and the magnitude of the earthquake, the rupture could either propagate into the frictional-to-viscous transition causing fractures, frictional-sliding (i.e. breccias and

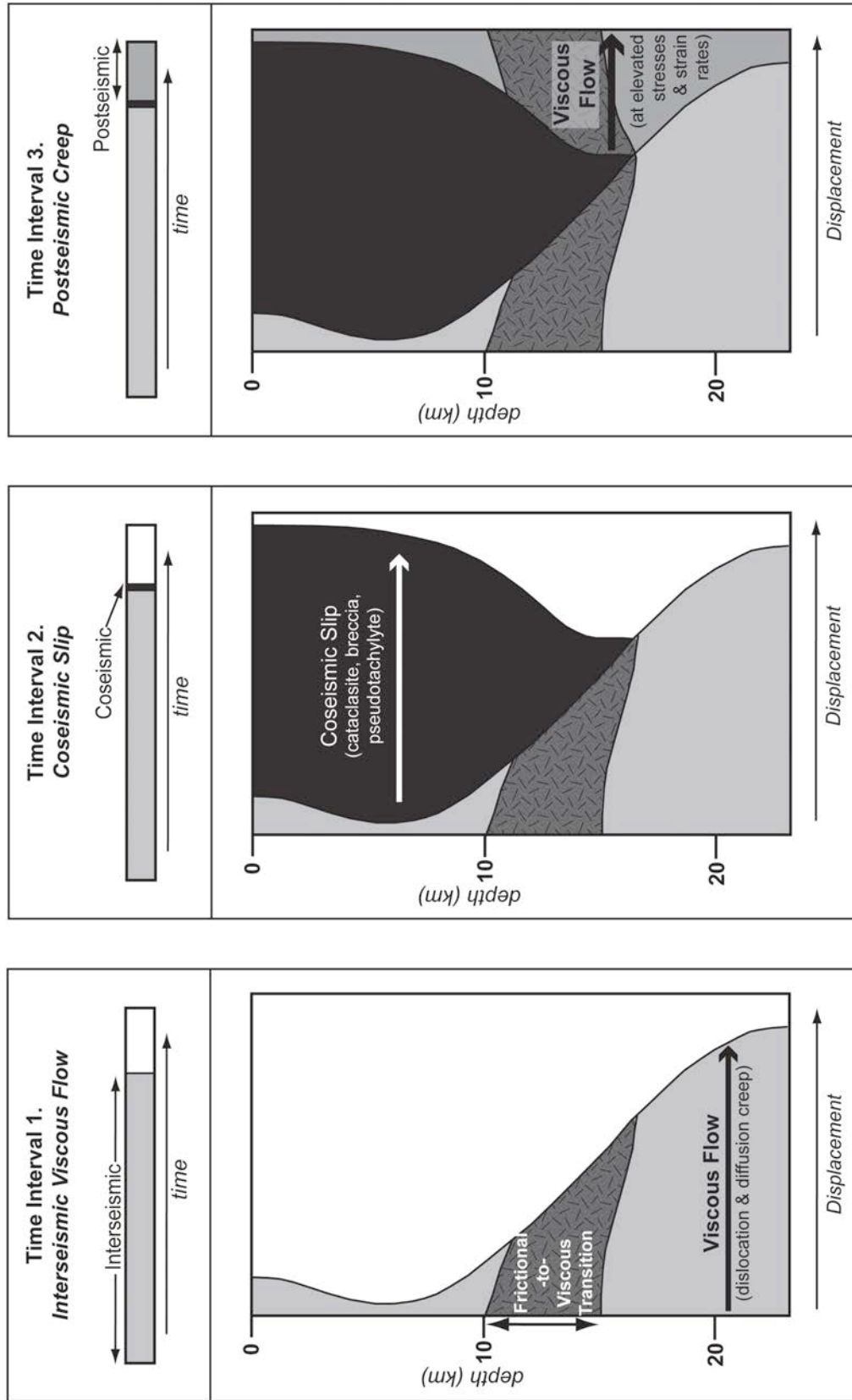


Figure 1.3. A series of schematic displacement-depth diagrams showing the displacement of a fault at different depth levels during the three stages of the seismic cycle. The relative length of each stage of the seismic cycle is shown in the timeline above the diagrams. Adapted from Handy et al., 2007.

cataclasite), and frictional melting (i.e. pseudotachylyte) at transiently elevated strain rates, or slip in the upper crust would cause the frictional-to-viscous to be loaded with higher stresses immediately below the rupture. The postseismic period that follows coseismic slip is associated with the dissipation of the higher stresses through elevated but rapidly decaying strain rates (e.g. Ellis et al., 2006; Ellis and Stöckert, 2004a,b; Montési, 2004; Rolandone et al., 2004) leading to heterogeneous microstructures (Küster and Stöckert, 1999; Trepmann and Stöckert, 2003). A return to interseismic elastic loading on a frictionally-locked fault in the upper crust reestablishes interseismic “steady-state” strain rates in the middle crust during which time frictional structures are viscously deformed and post-seismic structures are overprinted within the frictional-to-viscous transition (Handy et al., 2007). Coseismic slip within the next seismic cycle forms new frictional structures that overprint the pre-existing viscous and deformed frictional structures, creating the mutually-overprinting relationship characteristic of the frictional-to-viscous transition (Handy et al, 2007; Passchier, 1982; Sibson, 1980).

1.3. Geologic Setting

1.3.1. Regional Geology

The eastern margin of the Appalachian orogen in Maine is characterized by a series of northeast-striking lithotectonic belts that record a complex history of Silurian-Devonian subduction-related orogenesis, metamorphism, and plutonism (Guidotti, 1989; Hibbard, 1994; Hussey, 1988; Tucker et al., 2001; van Staal, 2007; West and Hubbard, 1997). Silurian to early Devonian shortening led to early thrusts and recumbent folds (F1) followed by the northeast-trending upright, tight isoclinal folds (F2) that dominate the regional map pattern (Tucker et al., 2001). Crustal thickening and the emplacement of a wide variety of granitoids during orogenesis caused Siluro-Devonian high-temperature, low-pressure regional metamorphism and local contact metamorphism (Gerbi and West, 2007; Guidotti, 1989). Local plutonism also continued throughout the Devonian and into the Carboniferous, including the emplacement of the Sebago

Pluton (U-Pb monazite age of $\sim 293 \pm 2$ Ma; Tomascak et al., 1996) and associated contact metamorphism (Fig. 1.4; Guidotti, 1989). Late small-scale, north-trending asymmetric folds (F3) overprint the upright folds in many areas, including within the study area and are thought to reflect a change in the Middle to Late Devonian to west-directed, dextral transpressive shortening (West, 1999). The onset of dextral shear deformation in south-central Maine was syn- to post-metamorphic, but prior to regional cooling below muscovite mineral closure temperatures (West and Lux, 1993).

Dextral shear deformation associated with the development of the Norumbega fault system involved early, distributed, viscous shearing followed by localized slip on focused faults and shear zones (Fig. 1.5; e.g. Ludman and Gibbons, 1999; Swanson, 1999a; West and Hubbard, 1997). Early regional deformation was accommodated by heterogeneously distributed, non-coaxial, viscous, dextral deformation (i.e. asymmetric boudinage, asymmetric folding, and localized pervasive shear bands) in a zone that ranges in width from 5 to 40 km along strike, with rock type playing a large role (Ludman, 1998; Short and Johnson, 2006; Swanson, 1992, 1999a; Wang and Ludman, 2004; West and Hubbard, 1997). A mean kinematic vorticity number (a dimensionless number expressing the ratio of the pure to simple shear components of deformation, where pure shear is zero and simple shear is one) of 0.67 was calculated from measurements of deformed and rotated calcite veins on the outer edges of the fault system, indicating a moderate non-coaxial component to the transpressional deformation in that area (Short and Johnson, 2006), likely at the time of distributed viscous deformation. Dextral shear deformation was subsequently focused into narrow (≤ 2 km) strands of highly localized deformation forming near-vertical zones of mylonites, ultramylonites, phyllonites, cataclasites, and/or breccia (Fig. 1.6; Ludman and Gibbons, 1999; Swanson, 1988, 2006a,b; Wang and Ludman, 2004; West and Hubbard, 1997). Johnson et al. (2009a,b) calculated a higher mean kinematic vorticity number of 0.97 ± 0.03 for one of these strands (i.e. the Sandhill Corner shear zone of this study).

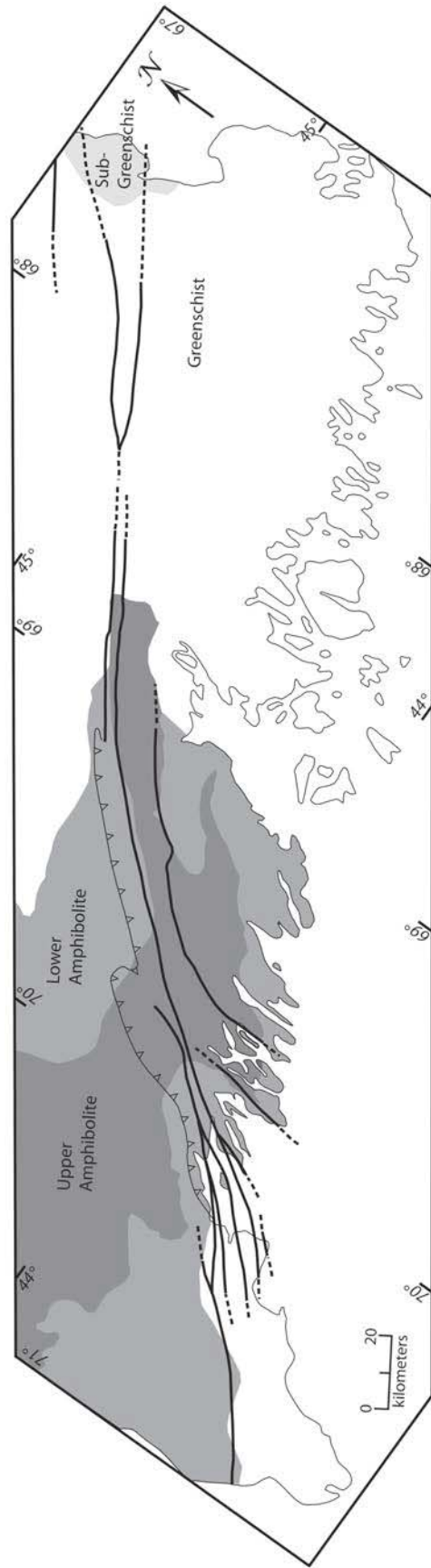


Figure 1.4. Geologic map of the coast of Maine showing the location of the peak metamorphic zones. Based on Guidotti, 1989; Osberg et al., 1985.

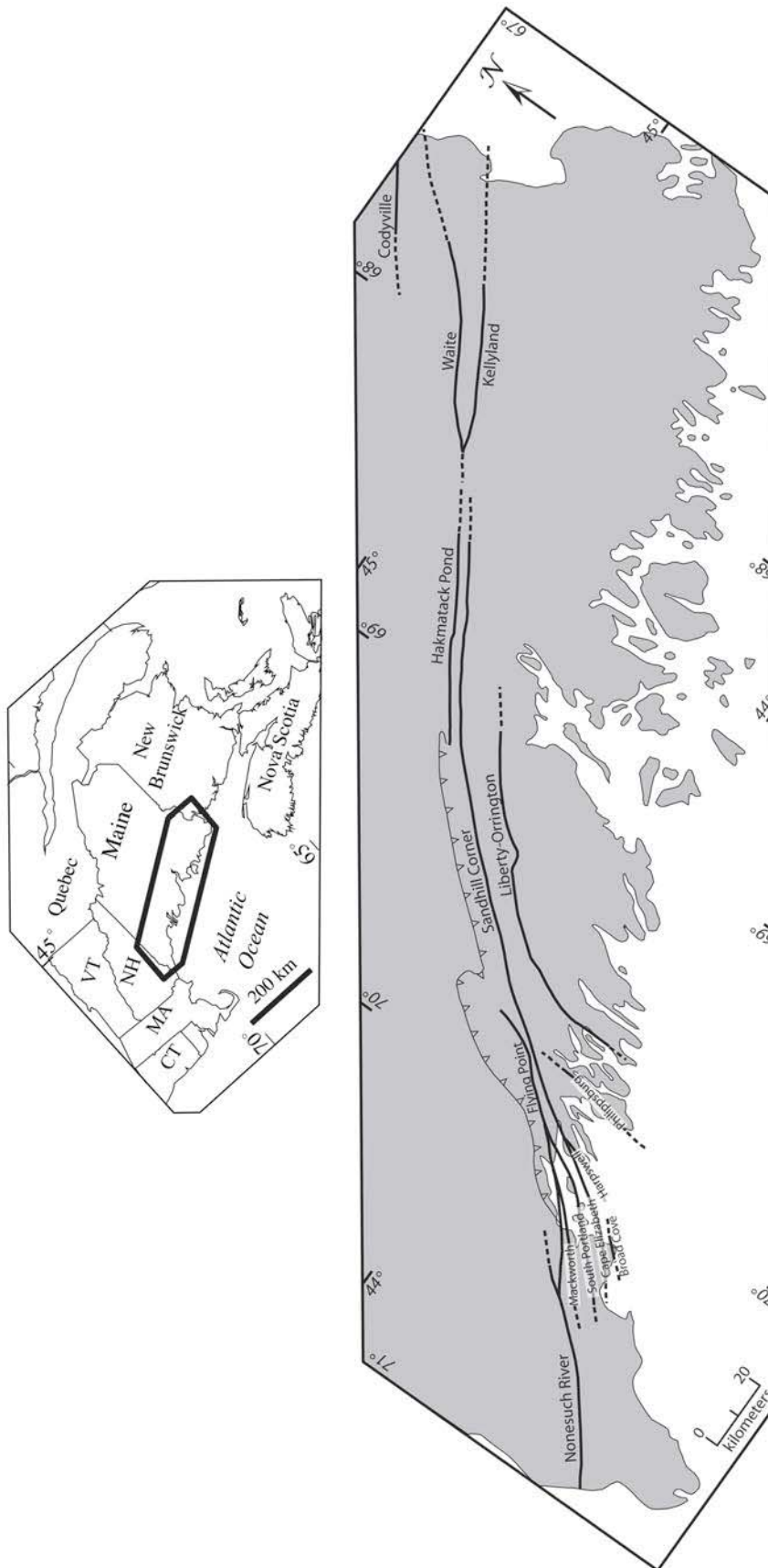


Figure 1.5. Geologic map of the coast of Maine showing the location of the known strands of the Norumbega fault system. Map and fault strand locations are based on Gerbi and West, 2007; Hubbard and Wang 1999; Ludman, 1998; Ludman and Gibbons, 1999; Osberg et al., 1985; Swanson, 1992, 1999 a,b, 2006a,b, 2005; Swanson and Bampton, 2009; Wang and Ludman, 2004; West, 1999; West et al., 1993; West and Lux, 1993; West and Rodin-Tice, 2003.

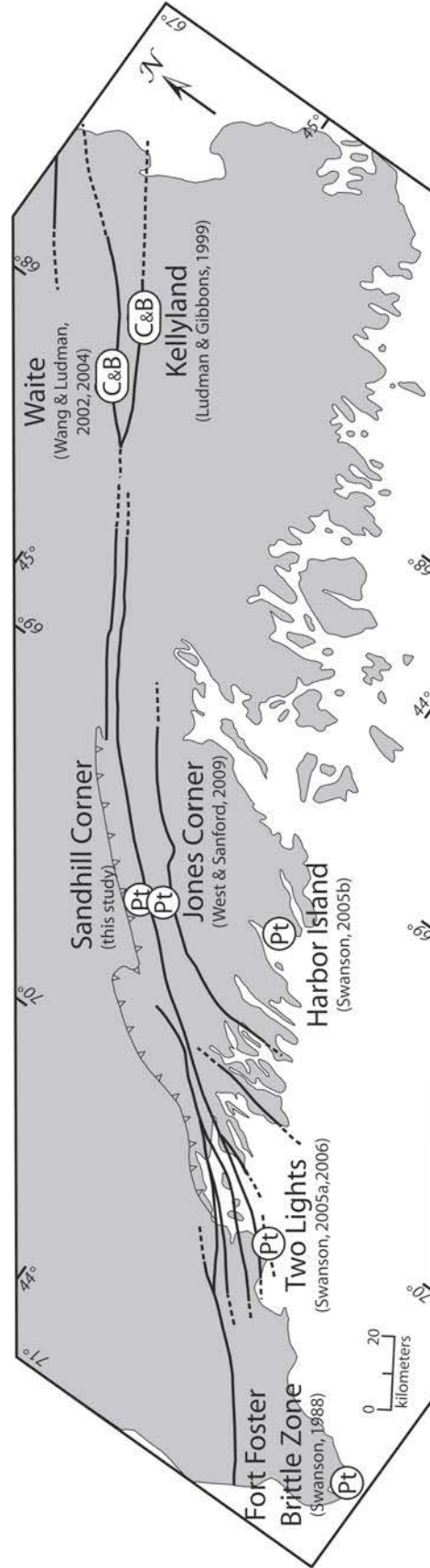


Figure 1.6. Geologic map of the coast of Maine showing the known locations of transient, coseismic structures. C-cataclasite; B-breccia; Pt-pseudotachylyte (frictional melt veins). Based on Ludman and Gibbons, 1999; Swanson, 1988, 2005a,b, 2006a,b; Wang & Ludman, 2002, 2004; West and Sanford, 2009.

$^{40}\text{Ar}/^{39}\text{Ar}$ and U-Pb zircon and monazite ages, and timing constraints from sheared plutons bracket the time of dextral shearing and faulting to between Middle Devonian and Early Permian time (Gerbi and West, 2007; Ludman et al., 1999; West and Hubbard, 1997). It is not entirely clear whether dextral deformation was continuous for this ~80-100 my span of time or if, alternatively, the relatively narrow zones of intense dextral shear deformation represent localized episodic reactivation between periods of relatively little displacement (West, 1999). Estimates of total right-lateral displacement along the Norumbega fault system based on piercing points and estimated shear strain values range from ~25-300km (e.g. Hubbard, 1999; Swanson, 1992; Wang and Ludman, 2004).

Thermochronological discontinuities ($^{40}\text{Ar}/^{39}\text{Ar}$ mineral cooling age- Fig. 1.7; apatite fission track ages- Fig. 1.8) suggest post-Paleozoic, east-side-down vertical movement along parts of the Norumbega fault system associated with normal faulting during the Mesozoic opening of the Atlantic Ocean (Ludman et al., 1999; West, 1999; West and Roden-Tice, 2003; West et al., 1993, 2008). Crustal scale reactivation of the Norumbega structures offsets the Moho, suggesting that thinning associated with rifting may have played a part in the exhumation and exposure of the deeper crustal levels of the Norumbega fault system (Stewart, 1989; Doll et al., 1996). There is little evidence via either the quartz microstructures, a change in the mineral assemblages (including a lack of pervasive chlorite retrogression), or thermobarometric discontinuities to indicate that the Sandhill Corner shear zone experienced later, low temperature reactivation or overprint in the study area (West and Hubbard, 1997).

1.3.2. Exposure of the Norumbega Fault System in Maine

Peak metamorphic grade decreases across the state from upper amphibolite in the southwest to greenschist and sub-greenschist in the northeast (Fig. 1.4). Differential exhumation of the crustal section along strike during regional cooling (up to a 4 degree tilt) is thought to account for these differences (Fig. 1.5; Guidotti, 1989; Hubbard et al., 1995; Ludman and

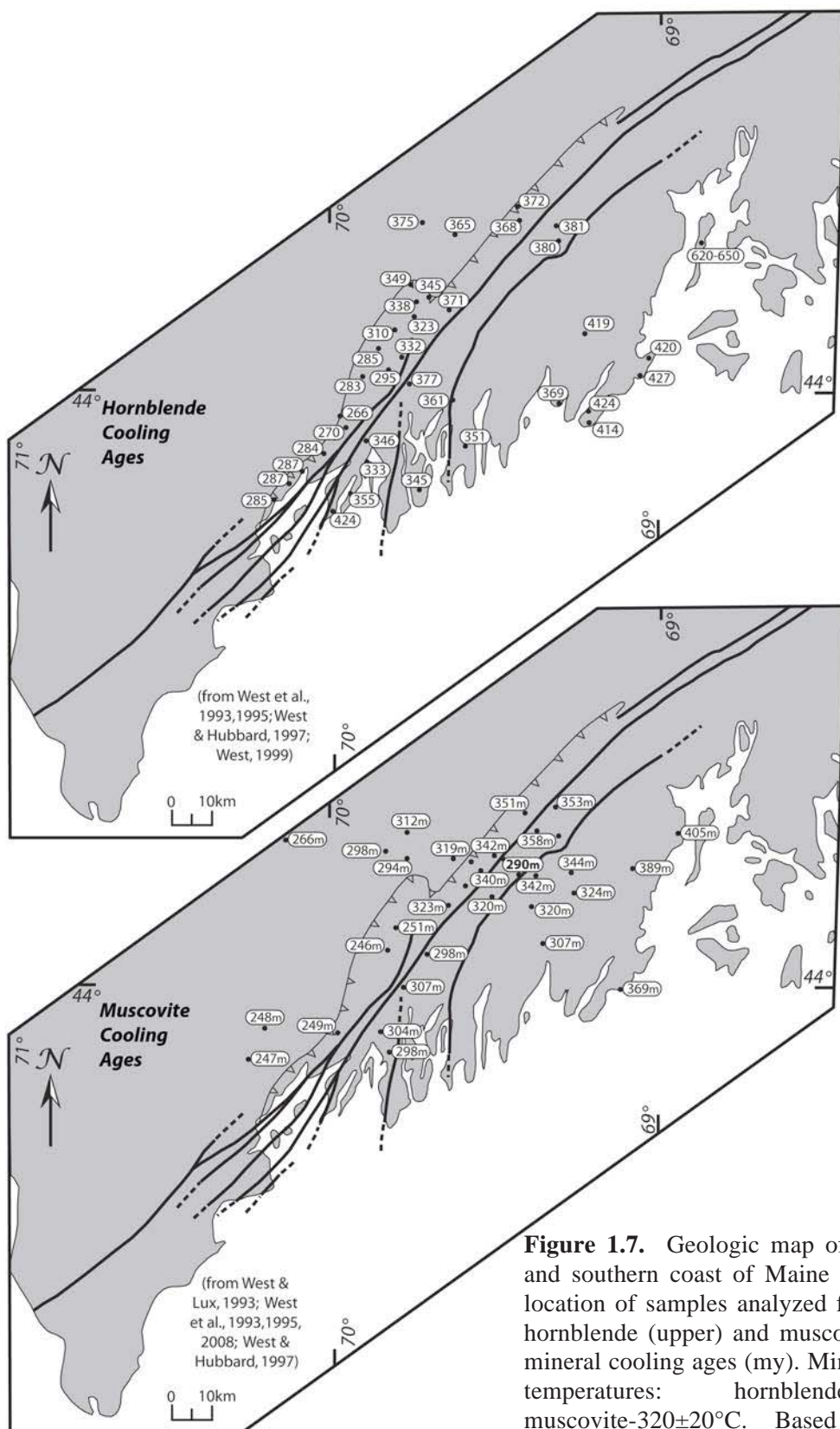


Figure 1.7. Geologic map of the central and southern coast of Maine showing the location of samples analyzed for $^{40}\text{Ar}/^{39}\text{Ar}$ hornblende (upper) and muscovite (lower) mineral cooling ages (my). Mineral closure temperatures: hornblende- $480\pm 20^\circ\text{C}$; muscovite- $320\pm 20^\circ\text{C}$. Based on West 1999; West and Hubbard, 1997; West and Lux, 1993; West et al., 1993, 1995, 2008.

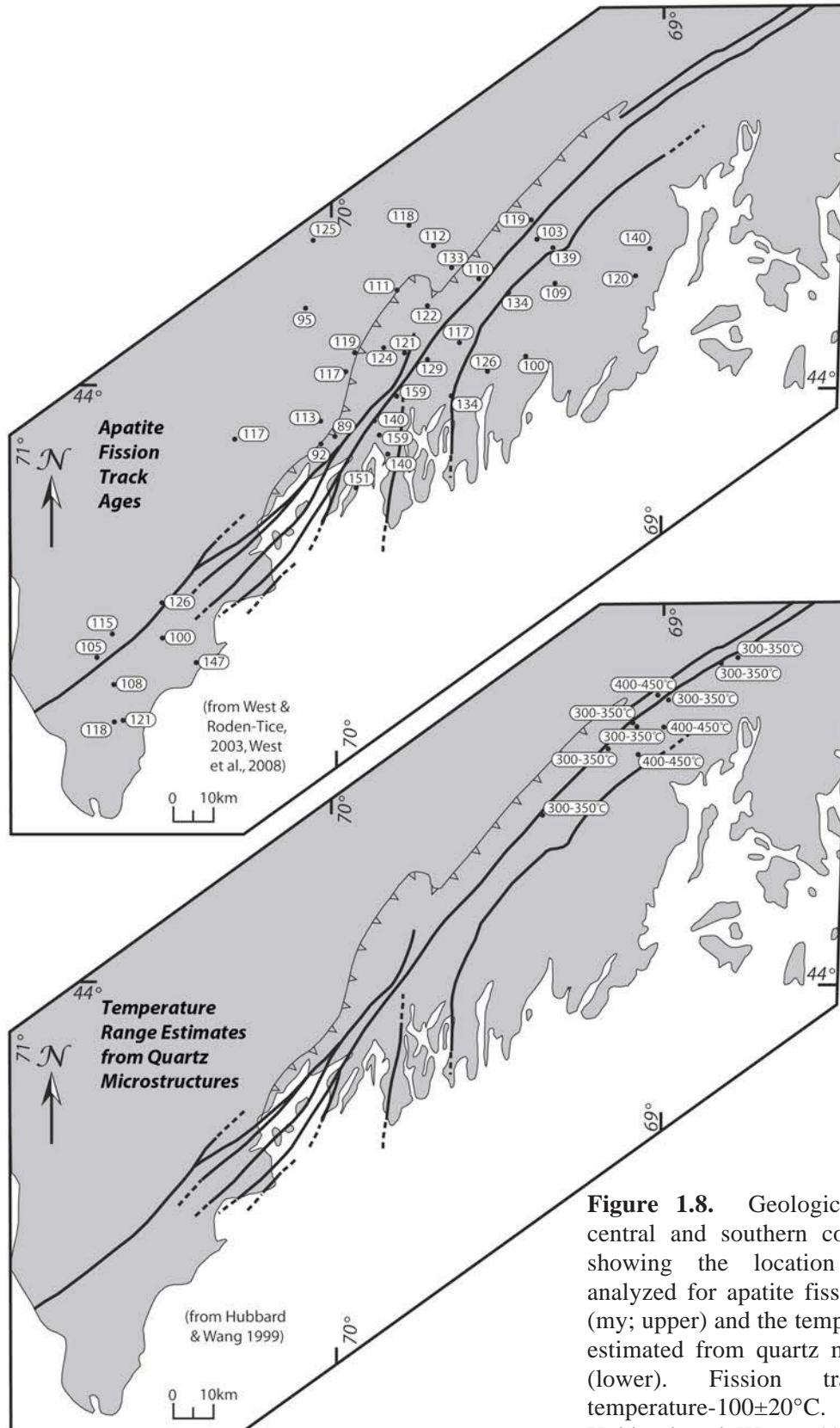


Figure 1.8. Geologic map of the central and southern coast of Maine showing the location of samples analyzed for apatite fission track ages (my; upper) and the temperature ranges estimated from quartz microstructures (lower). Fission track closure temperature- $100\pm 20^{\circ}\text{C}$. Based on Hubbard and Wang, 1999; West and Roden-Tice, 2003; West et al., 2008.

Gibbons, 1999; Swanson 1999a,b; West and Hubbard, 1997; Wang and Ludman, 2004; West et al., 1993, 2008). Deformation character also varies along strike within the Norumbega fault system, with the coastal and south-central sections of the fault representing the “deep” exposure and the eastern section representing the “shallow” exposure (Hubbard et al., 1995).

1.3.2.1. Eastern Maine. The eastern section of the Norumbega fault system includes the Kellyland, Waite, and Codyville strands and represents the “shallow” section of the system. Chlorite is pervasive in this section with only a localized occurrence of biotite (Ludman, 1998; Ludman and Gibbons, 1999). Rocks that deformed during the early stages of dextral deformation exhibit quartz microstructures indicative of subgrain rotation recrystallization with minor grain boundary migration and feldspar porphyroclasts that deform by fracture and intracrystalline slip (Ludman, 1998; Ludman and Gibbons, 1999; Wang and Ludman, 2004). Deformation mechanisms and peak metamorphic grade suggests a starting deformation temperature of ~300-400°C. With continued dextral motion, viscous deformation was overprinted by frictional deformation. The eastern section was, therefore, at the uppermost part of the frictional-to-viscous transition during the onset of viscous deformation and transitioned during cooling/exhumation to an entirely brittle part of the crust. Differences between the brittle Waite strand (cataclasite and breccia) and the more “ductile” Kellyland strand (mylonites and ultramylonites, with cataclasite) suggest that the Waite section was the active strand during the latter part of faulting in this section of the Norumbega fault system (Wang and Ludman, 2002).

Dextral deformation has been divided by researchers into stages based on overprinting structures and timing constraints from sheared plutons (Ludman, 1998; Ludman and Gibbons, 1999; Ludman et al., 1999; Wang and Ludman, 2002; Wang and Ludman, 2004). Stage 1 involved the initiation of viscous shearing to form a zone that ranges in width from 5 km to 300m and includes phyllonites, schistose mylonites, protomylonites, and sheared granites (i.e. Deblois pluton). The timing of Stage 1 dikes and veins and the intrusion of the Bottle Lake plutonic

complex constrain this episode to the few million years between 383 and 380 Ma (Ludman, 1998). A strain-free period separates Stage 1 from the later stages (Ludman, 1998; Ludman and Gibbons, 1999). Stage 1 is quickly followed by Stage 2, also dated to around ~380Ma (bracketed by the Bottle Lake complex and the Passadumkeag River pluton; Ludman, 1998; Ludman et al., 1999). Focused Stage 2 high strain zones of mylonite, ultramylonite, cataclasite, and breccia overprint the regional viscous deformation. Dominantly frictional deformation continued through Stages 3 and 4. The lower limit of Stage 2 deformation (and the onset of Stage 3 and 4) is unconstrained at this time, but Stage 2 is interpreted by Ludman (1998) to correspond with the Late Devonian to Carboniferous strike-slip faulting elsewhere on the Norumbega fault system.

1.3.2.2. South-Central Maine. The south-central section is part of the high-grade, “deeper” segment of the Norumbega fault system. It is a ~30 km wide zone of distributed shear with <1 km-wide focused high-strain strands that include the Sandhill Corner and the Liberty-Orrington strands (Figs. 1.5, 1.6; West and Hubbard, 1997; West, 1999; Marsh et al., 2009). The Sandhill Corner shear zone is considered the main strand of the Norumbega fault system in the south-central section connecting the Casco Bay Restraining Bend in the southwest with the Kellyland and Waite strands of the eastern section (Osberg et al., 1985; Pankiwskyj, 1976).

Much of the thermochronologic data along the Norumbega fault system (apatite fission track and $^{40}\text{Ar}/^{39}\text{Ar}$ mineral cooling ages; Figs. 1.7, 1.8) cover rocks from the south-central section, and timing constraints on dextral deformation in this region are largely based on these ages (West and Lux, 1993; West and Hubbard, 1997; West, 1999; West and Roden-Tice, 2003; West et al., 2008). The oldest $^{40}\text{Ar}/^{39}\text{Ar}$ hornblende cooling ages suggest that distributed dextral shearing in this area started no later than ~380Ma (Fig. 1.7; West and Lux, 1993; West and Hubbard, 1997). Fracturing and fluid infiltration preceded viscous deformation in the Liberty-Orrington strand at the edge of the Lincoln Syenite, with a temperature estimate of 400-500°C (from thermodynamic modeling of the recrystallized assemblage; Marsh et al., 2009). The wider

zone of dextral deformation in south-central Maine cooled (or was exhumed) through the muscovite closure temperature ($320 \pm 20^\circ\text{C}$) by $\sim 320\text{Ma}$ (West and Lux, 1993; West and Hubbard, 1997). $^{40}\text{Ar}/^{39}\text{Ar}$ analysis of the 60-90 μm size fraction of muscovite from mylonite samples from the Sandhill Corner strand exhibit ages around $\sim 290\text{Ma}$ indicating that dextral strike-slip activity continued (or was reactivated) after 320Ma on this localized strand following regional shearing (West and Lux, 1993). Mutually-overprinting pseudotachylyte and mylonite indicative of deformation within frictional-to-viscous transition depths has been identified in the sheared rocks of the Sandhill Corner strand (see Chapter 2).

1.3.2.3. Casco Bay Restraining Bend and Coastal Brittle Zones. The southern, coastal section of the Norumbega fault system in Maine preserves a complex history of dextral transpression in an $\sim 30\text{km}$ wide zone of distributed dextral shear deformation overprinted by multiple high-strain strands in a restraining bend geometry (Figs. 1.5, 1.6; Swanson, 1992; Swanson, 1999a,b; Swanson and Bampton, 2009). The main strands in this section are the Flying Point and Nonsuch River faults, with the Mackworth, South Portland, Cape Elizabeth, Harpswell, Philippsburg, and Broad Cove faults as minor strands within the restraining bend. Swanson (1999b) indicates that shearing “localized along upright (initially oblique) F2 fold limbs that have rotated into the trend of the fault”. The dextral, non-coaxial component of strain was primarily accommodated along the focused fault strands, particularly those strands closest to the main fault trace, while a significant component of layer normal coaxial shortening caused upright folding, layer parallel elongation and southward extrusion of fault-bounded blocks (resulting from combined dextral and sinistral shear), and dextral overthrusting to the northwest (Swanson, 1999b; Swanson and Bampton, 2009).

Syntectonic pluton and pegmatite emplacement, including the intrusion of the Sebago Pluton, in the southern part of the Norumbega fault system continued into the late Carboniferous, much later than in other areas along the fault system (Tomascak et al., 1996). $^{40}\text{Ar}/^{39}\text{Ar}$

hornblende cooling ages of 266-295Ma and muscovite cooling ages of 246-249Ma from the west side of the Flying Point Fault indicate that this area may have remained at a higher temperature longer during the history of dextral deformation (Fig. 1.7; West et al., 1993). However, Mesozoic normal offset on the reactivated Flying Point fault created a discontinuity in mineral cooling ages across the main fault trace complicating the cooling history in this area (West et al., 1993, 2003, 2008; West and Roden-Tice, 2003). For these reasons, constraints on the onset of regional dextral shearing and transpressional deformation in this area are limited to geologic relationships and overprinting structures. U-Pb monazite geochronologic ages of undeformed pegmatites west of the Flying Point fault place a lower limit on regional dextral shearing within the vicinity of the main fault trace at 280 Ma (Tomascak et al., 1996).

Local crustal thickening during transpression in the coastal section of the fault system may have contributed to the exhumation of coastal high strain zones through frictional-to-viscous transition depths and into the frictional regime (Swanson, 2006a). Frictional structures extensively overprint the mylonites and ultramylonites of the high-strain fault strands in many coastal localities, including a number of pseudotachylite-bearing “fault-vein arrays”: the Two Lights array of the Broad Cove Strand, the Harbor Island array, and the related Fort Foster Brittle Zone of the Southern Mylonite Zone (Fig. 1.6; Swanson, 1988; 2004; 2005; 2006a). Swanson (2005b, 2006a,b) described fault zone rip-out structures from these well-developed vein arrays and traced the fault structures on the mesoscale from the R-shears of the initial vein array, through P-shear linkage, and ultimately to the formation of a through-going fault. Similar well-developed fault vein arrays are not present or have yet to be identified in the south-central portion of the Norumbega fault system. Swanson also noted that an association between pseudotachylite and mylonite/ultramylonite suggests that the subvertical mylonitic fabric may play a role in preferentially localizing later frictional slip (Swanson, 1988; 2004).

1.3.3. Geologic Setting of the Study Area: The Sandhill Corner Shear Zone

The Sandhill Corner shear zone in south-central Maine is a northeast-trending, subvertical, mylonitic shear zone that is largely contained within the Cape Elizabeth Formation of the Casco Bay Group (Fig. 1.9; Grover and Fernandes, 2003; Pankiwskyj, 1976; West and Peterman, 2004; West and Lux, 1993). The majority of the Cape Elizabeth Fm. in the study area is characterized by partially migmatized, upper amphibolite facies, metasedimentary rocks

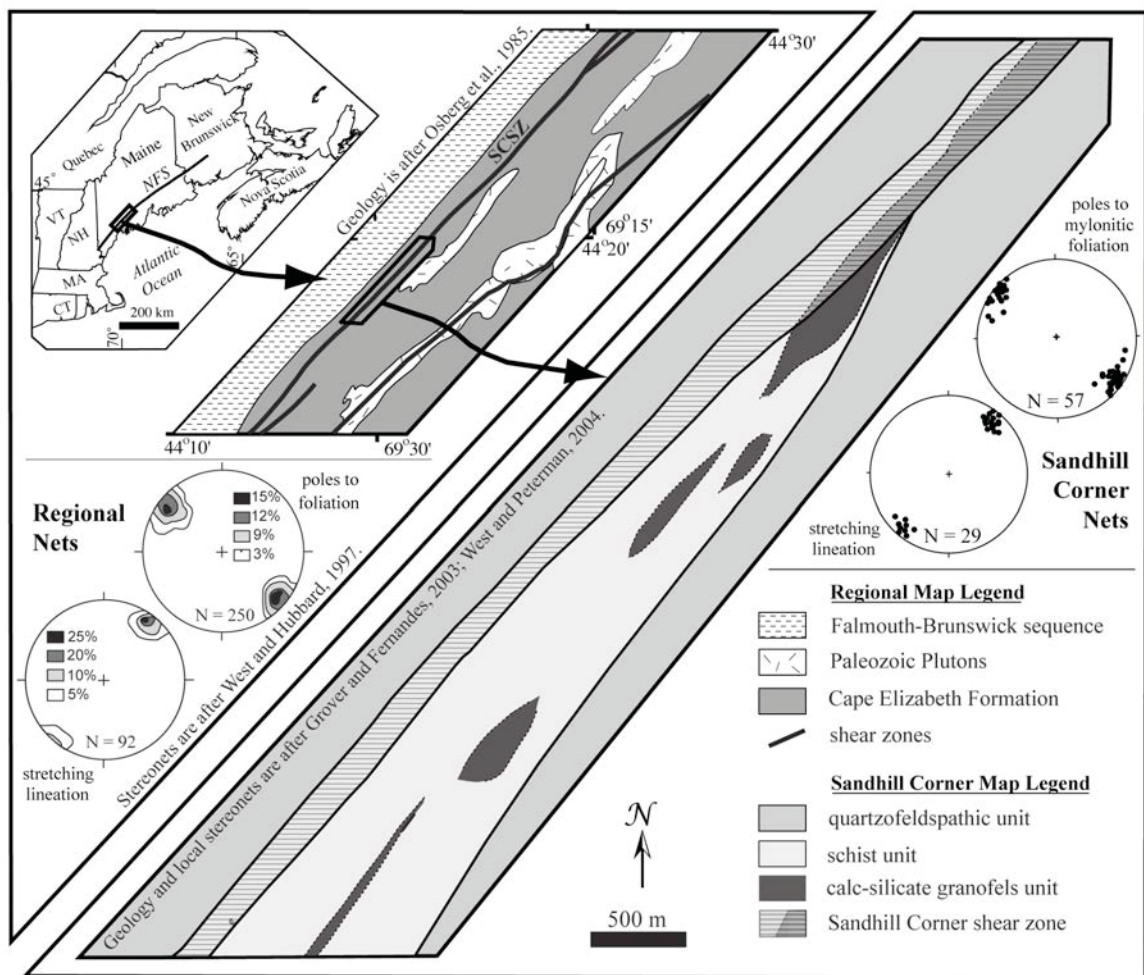


Figure 1.9. Geologic map of the study area within the Norumbega fault system. Regional nets include mylonitic and non-mylonitic rocks of the Norumbega fault system. Local nets of the Sandhill Corner shear zone (SCSZ) show that foliation and lineation orientations in the mylonite are consistent with regional orientations. Regional and local nets are both equal area, lower hemisphere projections. Norumbega fault system-NFS. Regional geology is after Osberg et al. (1985), regional nets are after West and Hubbard (1997), and local geology and nets are after Grover and Fernandes (2003) and West and Peterman (2004).

(biotite + quartz + plagioclase \pm muscovite \pm garnet \pm sillimanite \pm tourmaline) (Grover and Fernandes, 2003; West and Peterman, 2004). For the purposes of this document, we henceforth refer to these rocks simply as the quartzofeldspathic unit. In addition to these quartzofeldspathic rocks, a pelitic schist member (the Crummett Mountain member of West and Peterman [2004] or the Scarboro Fm. of Grover and Fernandes [2003]) and a calc-silicate granofels unit of the pelitic schist member have been recognized and mapped separately. The graphite-rich, pelitic schist (quartz + plagioclase + muscovite + biotite + garnet + andalusite \pm sillimanite with abundant andalusite-bearing quartz veins) is host to the many, complexly-folded and boudinaged lenses of layered calc-silicate granofels (quartz + plagioclase + amphibole \pm calcite \pm biotite). Within the study area, the Sandhill Corner shear zone is ~300-500m wide, follows the contact between the quartzofeldspathic unit and the schist unit, and includes mylonite and ultramylonite derived largely from the migmatitic, micaceous, quartzofeldspathic gneisses and the sheared margin of the pelitic schist (see Chapter 4). In the northern-most part of the study area where the schist unit thins, the western margin of a calc-silicate granofels lens is also highly sheared, and the core of the shear zone coincides with the lithologic contact between the quartzofeldspathic unit and calc-silicate granofels unit (see Chapter 4).

Mylonites within the Sandhill Corner shear zone are characterized by subhorizontal stretching lineations and kinematic indicators consistent with dextral transpressive deformation. They are medium to dark gray in color, fine-grained, and contain porphyroclasts of feldspar and coarse-grained muscovite (presumably derived from pegmatites within the quartzofeldspathic metasedimentary rocks) that are smeared out along mylonitic foliation planes creating a well-defined mineral lineation (West and Hubbard, 1997). Thin sections cut perpendicular to the mylonitic foliation and parallel to the mineral elongation lineation reveal shear bands, muscovite fish, sigma and delta feldspar clasts, and both grain shape and crystallographic preferred orientations (see West and Hubbard [1997] for a more detailed discussion of the kinematic indicators). All kinematic indicators unambiguously indicate dextral strike-slip shear. Quartz

ribbons within the mylonites of the Sandhill Corner shear zone are dominated by microstructures consistent with dislocation creep (see Chapter 3) whereas feldspar porphyroclasts deformed exclusively by fracture and intracrystalline slip (Hirth and Tullis, 1992; West and Hubbard, 1997). These microstructures are consistent with a temperature of mylonitization between ~300°C and 450-500°C (Passchier and Trouw, 2005; Stipp et al., 2002a,b). Dynamic recrystallization processes in quartz produced Type-II cross-girdle CPO patterns in c-axis pole figures with dominant maxima in the macroscopic foliation plane at right angles to the mineral lineation (see Chapter 3), with CPOs and a high kinematic vorticity number (0.97 ± 0.03) that suggest plane strain conditions and monoclinic strain symmetry (Iacopini et al., 2007; Johnson et al., 2009a,b). Cataclasite and pseudotachylyte veins cut the mylonitic foliation (West and Hubbard, 1997), and as presented in Chapter 2, pseudotachylyte and mylonite are mutually-overprinting, indicating coeval frictional and viscous deformation (Handy et al., 2007). There is little evidence via either the quartz microstructures, a change in the mineral assemblages (including a lack of pervasive chlorite retrogression), or thermobarometric discontinuities to indicate that the Sandhill Corner shear zone experienced later, low temperature reactivation or overprint in the study area (West and Hubbard, 1997).

Chapter 2

IDENTIFYING DEFORMED PSEUDOTACHYLYTE AND ITS INFLUENCE ON THE STRENGTH AND EVOLUTION OF A CRUSTAL SHEAR ZONE AT THE BASE OF THE SEISMOGENIC ZONE *

2.1. Chapter Abstract

On a strand of the Norumbega fault system, a Paleozoic, subvertical, seismogenic fault system in northeastern New England, USA, we document changes associated with the formation and deformation of pseudotachylyte to form ultramylonite/phyllonite layers. We consider how those textural and mineralogical changes affected the rheology of the layer and how significant volumes of pseudotachylyte over time may have weakened the shear zone.

The Norumbega fault system is characterized by a number of mylonitic shear zones exhumed from depths of ~10-15km, some of which preserve evidence for mutually-overprinting pseudotachylyte and mylonite. Along one of these, the Sandhill Corner shear zone, all stages of the pseudotachylyte to ultramylonite/phyllonite transformation are preserved, from (1) primary pseudotachylyte structures to (2) initial mineral crystallization, (3) grain coarsening and reactions, and (4) viscous deformation. Our observations show that ultramylonite layers exhibit identifying features that when present together are distinctive of a pseudotachylyte origin. Using these features, we estimate that ~5- 50% of the rock volume in the Sandhill Corner shear zone (mean ~30%, locally >50%) is deformed pseudotachylyte, suggesting that deformed pseudotachylyte may be more prevalent than previously thought in faults exhumed from the base of the seismogenic zone.

The Sandhill Corner shear zone localized along the contact between two rheologically-contrasting units. Mylonite fabric intensity and the occurrence of fresh and deformed

** The content of this chapter is published in: Price et al., 2012. Tectonophysics, v.518-521, p. 63-83. doi:10.1016/j.tecto.2011.11.011.*

pseudotachylyte increase with proximity to the contact and shear zone core, indicating that seismic rupture also localized there. A decrease in grain size promoting grain-size-sensitive creep and a progressively interconnected mica network associated with local basal slip within the deformed pseudotachylyte both worked to decrease the strength of those layers. The formation of multiple generations of weak, deformed pseudotachylyte layers at or near the lithologic contact may have played an important role in the spatiotemporal persistence of the shear zone core.

2.2. Introduction

The structure and rheology of large-displacement, plate-boundary parallel fault zones change with depth as pressure-dependent fracture and frictional sliding in the upper crust transitions to dominantly temperature- and strain-rate-dependent viscous creep in the mid-to-lower crust (Brace and Kohlstedt, 1980; Handy et al., 2007; Kohlstedt et al., 1995; Scholz, 1998; Sibson, 1986). This change in deformation behavior is transitional over a variable depth interval (~10-20km) that is referred to as the frictional-to-viscous transition (FVT; Schmid and Handy, 1991), a zone that is coincident with the base of the seismogenic zone in crustal-scale faults (e.g. Handy et al., 2007; Scholz, 1998; Sibson, 1986). The style of deformation across the FVT zone is dependent on the seismic cycle. Within a seismogenic fault zone, transient deformation associated with the coseismic and postseismic periods of the cycle is superimposed over the long-term (10^3 - 10^5 yr) interseismic deformational fabrics (e.g. Handy et al., 2007; Rolandone et al., 2004). During a rupture event, fractures propagate into the middle crust forming coseismic breccia, cataclasite, and/or pseudotachylyte in the lower parts of the FVT, and coseismic loading increases strain rates in the middle crust during the postseismic period (e.g. Ellis et al., 2006; Ellis and Stöckert, 2004a,b; Küster and Stöckert, 1999; Montési, 2004; Rolandone et al., 2004; Trepmann and Stöckert, 2003). A return to interseismic elastic loading in the upper crust reestablishes a trend toward steady-state strain rates in the middle crust, and interseismic viscous deformational fabrics dominate. Therefore, rocks from FVT depths within a long-lived

seismogenic fault zone should preserve evidence for a complex history of alternating deformation mechanisms, fluctuating strain rates, and overprinting brittle/frictional structures and viscous deformational fabrics. Yet, study of such rocks has been hampered not only by a lack of preservation due to overprint but also by the difficulty in positively identifying mutually-overprinting frictional structures and viscous deformational fabrics, such as coeval pseudotachylyte and mylonite (e.g. Handy et al., 2007; Lin, 2008b; Lin et al., 2005; Sibson, 1980; White, 1996). As a result, the extent of pseudotachylyte production at the FVT is not entirely clear, and it is not well understood to what degree such coseismic structures influence shear zone rheology and development.

Much of the difficulty with identifying coeval mylonite and pseudotachylyte stems from the difficulty in recognizing a pseudotachylyte vein once it has been viscously deformed. Through wear, comminution, and frictional melting, the formation of a pseudotachylyte vein causes a marked decrease in grain size, and once deformed, it is nearly identical in appearance to a milling-derived ultramylonite layer. The production of ultramylonite from the viscous deformation of pseudotachylyte has been documented in the literature where cross-cutting relationships are clear (e.g. Lin, 2008a,b; Lin et al., 2003; Passchier, 1982; Sibson, 1980; Takagi et al., 2000; White, 1996, 2004). However, typical pseudotachylyte-specific features (e.g. cross-cutting relationships, flow banding, and the presence of devitrification structures) can become obscured or obliterated during deformation making them difficult to identify (Passchier, 1982; Sibson, 1980). Pseudotachylyte recrystallizes under the same conditions at which the mylonite is deforming, so the vein mineral assemblage may be similar or even identical to the host rock assemblage, further obfuscating the layer's origin. As a result, the extent of pseudotachylyte production at the FVT is poorly known. Furthermore, deformed pseudotachylyte and other brittle structures may act as sites of strain localization, controlling the location of ductile structures (Guermani and Pennacchioni, 1998; Passchier, 1982; White, 1996) and perhaps influencing the rheology of developing shear zones. Therefore, identification of deformed pseudotachylyte is a

key step in investigating what proportion of ultramylonite layers in a shear zone originated as pseudotachylyte veins as well as what influence multiple generations of pseudotachylyte may have on the rheological evolution of an ultramylonite-rich shear zone.

On a strand of the Norumbega fault system in south-central Maine, USA, we investigate methods for the identification of deformed pseudotachylyte and consider its rheological effect. The Norumbega fault system of northeastern New England is a long-lived, orogen-parallel, subvertical, dextral transpressive, seismogenic, Paleozoic fault system characterized by focused mylonitic shear zones. It is an ancient analogue to the San Andreas fault system and is an ideal place to study the interaction between frictional and viscous deformation. One of the mylonitic shear zones of the Norumbega fault system, the Sandhill Corner shear zone, has been exhumed from FVT depths and preserves excellent evidence for mutually-overprinting pseudotachylyte and mylonite. In our study of this shear zone, we (1) document how the pseudotachylyte veins changed mineralogically and microstructurally as they were deformed and overprinted; (2) present criteria for the identification of deformed pseudotachylyte; (3) use those criteria to estimate the amount of deformed pseudotachylyte within the shear zone; and (4) in the context of geological observations, consider how the introduction and deformation of pseudotachylyte may have influenced the strength and evolution of a shear zone at the base of the seismogenic zone. Based on our observations and measurements, we estimate that a significant percentage of the rock volume in the Sandhill Corner shear zone is deformed pseudotachylyte, suggesting that deformed pseudotachylyte may be much more prevalent than previously thought in faults exhumed from the base of the seismogenic zone.

2.3. Pseudotachylyte-derived Ultramylonite Layers

Pseudotachylyte-derived ultramylonite layers have been described where mutually-overprinting pseudotachylyte and mylonite have been documented (Kirkpatrick et al., 2009; Koch and Masch, 1992; Lin, 2008a,b; Lin et al., 2003, 2005; McNulty, 1995; Moecher and Steltenpohl,

2009; Passchier, 1982, 1984; Pennacchioni and Cesare, 1997; Sibson, 1980; Takagi et al., 2000; Ueda et al., 2008; White, 1996, 2004). For the purposes of this chapter, (1) a mylonite is a foliated and strongly lineated rock with a fine-grained matrix (~50-90%) that contains porphyroclasts and quartz veins; (2) an ultramylonite is an ultra-fine-grained layer that contain less than 10% porphyroclasts within a coarser-grained mylonite; (3) a protomylonite is the foliated protolith of the mylonite with less than 50% matrix; and (4) a phyllonite is an ultra-fine-grained, foliated, mica-rich unit or layer within or adjacent to the schist (Passchier and Trouw, 2005). A pseudotachylyte is a vein of quenched and/or devitrified glass that is formed from frictional melting during seismic slip, from shear heating and melting associated with plastic instabilities at great depths and pressures (e.g. Hobbs et al., 1986; John et al., 2009; Keleman and Hirth, 2007), or from bolide impact (e.g. Spray, 1998). We restrict our discussion here to pseudotachylyte formed at the crustal FVT (~10-20 km depth) through brittle/frictional processes associated with the seismic cycle (Handy et al., 2007; Spray, 1995). Ultramylonite layers can result from a high degree of accumulated shear strain through extreme grain size reduction during viscous flow (Passchier and Trouw, 2005) but also can form from the viscous deformation of pseudotachylyte veins (Passchier, 1982; Sibson, 1980). An undeformed pseudotachylyte that is frictionally-derived has a matrix of glass that typically contains remnant single crystal xenocrystic clasts or host rock-derived fragments. It may have branching injection veins and fractures at a high angle to the foliation, flow bands and folds, and microlites that crystallized from the melt before it quenched (Lin, 2008a; Philpotts, 1964; Sibson, 1975). A deformed pseudotachylyte vein contains an ultra-fine-grained matrix that crystallized from the glass with a small proportion of remnant single crystal xenocrystic clasts that persist as “porphyroclasts”. It can be nearly identical in appearance to an ultramylonite layer formed by grain size reduction of a normal mylonite, thus requiring a method of identification in order to distinguish one type of ultramylonite from the other.

Characteristic features unique to frictional melt veins can be useful in identifying deformed pseudotachylyte. Passchier and Trouw (2005) listed these as cross-cutting relationships, the disruption of layering, the presence of microlites, and/or the loss/abundance of certain phases due to non-equilibrium melting. Cross-cutting relationships that form during fracturing and frictional slip, such as injection veins and sharp boundaries with the host rock, are the most-diagnostic identifiers. However, the cross-cutting relationships are commonly lost in strongly sheared pseudotachylyte veins as they are transposed into the mylonitic foliation. Existing layering is also disrupted during comminution; Passchier and Trouw (2005) pointed out that pseudotachylyte should not contain contemporaneous quartz or calcite veins. Microlites, phases that directly crystallize from the melt, are identified by their distinctive shapes (simple granules or needles to complex bowtie, dendritic, spherulitic, or skeletal shapes) and/or compositions (e.g. Fe- or S-rich phases) (Lin, 2008a,b). In a deformed pseudotachylyte vein, distinctive microlite morphologies are commonly destroyed and may only be preserved in pockets of undeformed matrix at the edges of the vein, in injection veins, or in the strain shadows of clasts. Finally, because the matrix is not formed by equilibrium melting during frictional slip, the minerals with the lowest melting temperature melt first as well as those minerals that fracture into the smallest size fraction, leaving them scarce as inclusions in the pseudotachylyte matrix (Philpotts, 1964; Sibson, 1975). Feldspar and quartz, on the other hand, preferentially remain as clasts resulting in a silica-depleted melt relative to the host rock composition (Lin, 2008a; Philpotts, 1964).

Detailed studies of deformed pseudotachylyte have documented differences between the host rock and pseudotachylyte-derived ultramylonite layers that may provide other methods for identification (Lin, 2008a,b; Lin et al., 2003; Moecher and Steltenpohl, 2009; Passchier, 1982; Sibson, 1980; Takagi et al., 2000; Ueda et al., 2008; White, 1996, 2004). These include changes in the mineral assemblage and/or modal mineralogy, differences in mineral chemistry, and differences in the character of strain. The mineral assemblage of the ultramylonite layer is a

function of the assemblage of the recrystallized melt matrix, the types of xenocrystic clasts, the recrystallization of clasts during deformation, and the presence and/or composition of a fluid during deformation (Passchier, 1982; Takagi et al., 2000; White, 1996). In some cases, the mineral assemblage of the ultramylonite band varies very little from the host rock assemblage, but in other cases, there is a marked difference. Differences between the host rock and vein assemblage have been attributed to the increased oxide or sulfide content in the ultramylonite as a result of microlite formation (Takagi et al., 2000; Ueda et al., 2008), an increase in the amount of hydrous phases (Sibson, 1980), the growth of new minerals in the presence of hydrothermal fluids (Takagi et al., 2000; Ueda et al., 2008), and the breakdown and/or metamorphic re-equilibration of metastable clast phases (Moecher and Steltenpohl, 2009; Passchier, 1982). In addition to assemblage differences, the composition of specific minerals (e.g. feldspar, biotite, or amphibole) may differ between the pseudotachylyte vein and the host rock. Through investigation of mineral compositional changes in plagioclase, amphibole, and K-feldspar, White (1996) documented a possible decrease in the anorthite component in plagioclase (although not a trend that is statistically distinguishable) and a slight increase of $(\text{Na}+\text{AlIV})/\text{Si}$ in the rims of amphibole. Compositional differences may reflect different temperature conditions during growth, perhaps due to locally elevated temperatures associated with vein formation (Lin, 2008a; Lin et al., 2003; Philpotts, 1964; White, 1996). Finally, mineral dislocation densities and crystallographic preferred orientations (CPOs) may differ between the host rock and deformed pseudotachylyte veins. Passchier (1982), Koch and Masch (1992), and White (1996, 2004) all showed that dislocation densities in pseudotachylyte matrix quartz grains are low and heterogeneously distributed relative to the host rock, indicating little to no intracrystalline deformation in quartz within the vein matrix. Ueda et al. (2008) presented a CPO for olivine within the matrix of a deformed ultramafic pseudotachylyte that has a different orientation maximum from the host rock CPO.

2.4. Field Observations

A number of sampling traverses reveal that the contact between the quartzofeldspathic unit and the schist unit (or the calc-silicate granofels unit in the north) represents the core of the shear zone, with fabric intensity and the incidence of cataclasite and pseudotachylyte increasing with proximity to the lithologic contact. Northwest to southeast traverses across the shear zone in the southern part of the field area revealed a transition zone from quartzofeldspathic protomylonite to mylonite of up to 100m wide; a ~100-300m wide mylonite banded with thin, dark layers of ultramylonite; a less than 5m wide ultramylonite; a thin phyllonite of variable width up to 1-2m; ~5-10m of intensely sheared schist; and up to ~250m of heterogeneously-sheared schist. Due to poor exposure across the transition zone on this traverse, the exact nature of the contact between the protomylonite and the mylonite is unclear, but observations suggest a gradational transition. Similar northwest to southeast transects in the northern part of the field area reveals a much sharper transition from protomylonite to mylonite, a ~100m wide mylonite, a thin (<1m)-to-absent sheared schist, and a ~100m wide zone of sheared calc-silicate granofels. Pseudotachylyte is found in all of the rock units (see Section 2.2.2) cut by the shear zone.

Pseudotachylyte primarily occurs as mm- to cm-thick, foliation-parallel veins within the quartzofeldspathic mylonites and the sheared calc-silicate granofels unit. They are commonly found at the contact between different compositional bands within an outcrop. Individual pseudotachylyte veins, particularly in the quartzofeldspathic mylonites, can be followed along strike for up to a few meters in places where exposure permits. Identification of pseudotachylyte in outcrop depends on the degree of devitrification and the presence of cross-cutting relationships. Well-preserved pseudotachylyte veins are rare. They appear black on both fresh and weathered surfaces, display conchoidal fracture, and have a dull to sub-vitreous luster (Figure 2.1a). They are typically stained a reddish-brown color on weathered surfaces, with the staining focused in cracks that cut normal to the vein walls. Within the quartzofeldspathic mylonites,

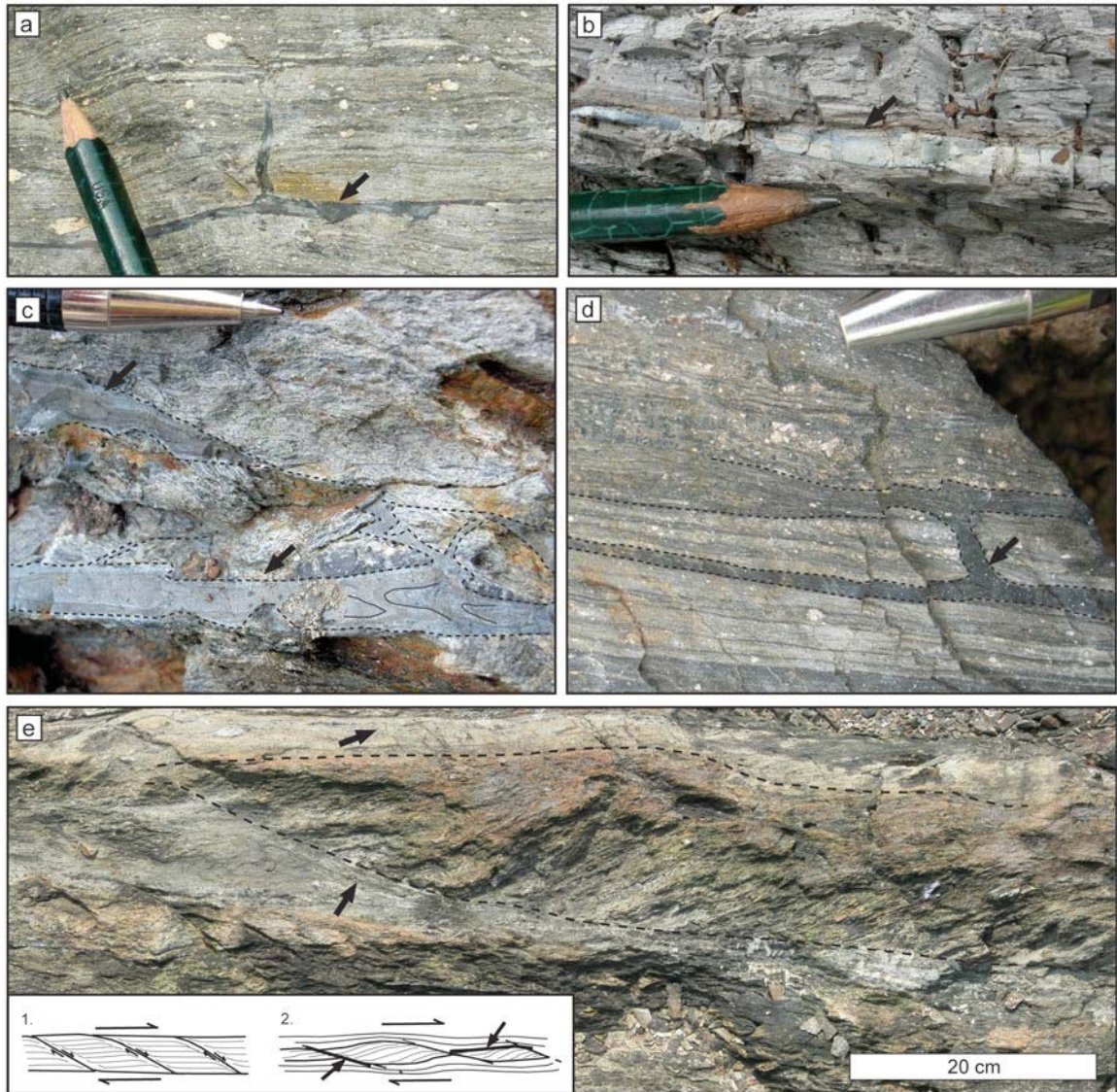


Figure 2.1. Field observations from rocks of the Sandhill Corner shear zone. Undeformed pseudotachylyte (arrows) in the (a) mylonite and (b) ultramylonite of the quartzofeldspathic unit and in the (c) sheared pelitic schists. (d) Deformed pseudotachylyte (arrow) in the quartzofeldspathic mylonite. (e) Pseudotachylyte also occurs in association with shear boudinage in the schist unit; arrows point to thin undeformed pseudotachylyte veins.

poorly-preserved (Figure 2.1b) and/or deformed pseudotachylyte veins (Figure 2.1c) appear as dark, fine-grained layers on freshly broken surfaces and range from dark to very light grey on the weathered surface. Their light weathered appearance makes them difficult to identify in outcrop without the presence of flow structures, injection veins, or other cross-cutting relationships. Within the sheared calc-silicate granofels, deformed pseudotachylyte is grey to brown in color

and is more easily identified in outcrop. Both the quartzofeldspathic mylonites and the sheared calc-silicate granofels unit have a light and dark banded appearance resulting from the presence of thin layers of ultramylonite.

Pseudotachylyte within the schist unit is present as either a thin vein in association with shear fractures (Figure 2.1e) or as a large fracture network (Figure 2.1d) within the immediate vicinity of the shear zone core. They appear dark to light brown-grey, with subtle variations in color defining flow structures in the larger vein networks, and may also be stained a reddish-brown color on weathered surfaces. It is unclear whether slip was great enough to form cataclasite or pseudotachylyte on every shear fracture in the schist, but thin pseudotachylyte has been identified in association with some boudin-bounding shear bands (e.g. Passchier, 1984) and foliation-parallel fractures within ~5m of the lithologic contact (Figure 2.1e). In places within ~1m of the contact in the schist, a pseudotachylyte network of veins and reservoir zones up to several centimeters in thickness occurs. These are among the thickest pseudotachylyte veins found. Exposure of a 1-2m wide layer of dark phyllonite occurs in places in the study area between the quartzofeldspathic unit and the sheared pelitic schists.

2.5. Analytical Methods

More than 100 oriented covered sections from three rock types (quartzofeldspathic, schist, and calc-silicate granofels units) and 25 polished sections were used in this study. Polished sections were mechanically polished to between 1 and 0.3mm grit and, if analyzed for mineral orientation data, chemically polished with a 0.02mm colloidal silica suspension. The Cameca SX100 electron microprobe (EPMA) at the University of Maine was used to make compositional x-ray maps (Figure 2.2; 15kV accelerating voltage, 20nA current, 0.02s count time, and a focused to 5µm beam) and to gather quantitative compositional data from multiple single point analyses (Table 1; 15kV accelerating voltage, 10nA current, 0.267s count time, and a focused to 5µm beam). The VEGA II XMU Scanning Electron Microscope (SEM) at the

University of Maine with TSL-OIM Data Collection and EDAX Genesis software was used to collect backscatter electron (BSE) images, electron dispersive spectroscopy (EDS) quantitative analyses, EDS element distribution and phase maps, and electron backscatter diffraction (EBSD) quartz orientation plots. Operating parameters during BSE and EDS data collection at high vacuum on carbon coated samples included an accelerating voltage of 20kV, a working distance of 10-15 mm, and a beam current of ~0.17nA (BSE) and ~0.8-10nA (EDS). Operating parameters during EBSD data collection on uncoated samples oriented at a 70° tilt at high vacuum included an accelerating voltage of 20kV, a working distance of 25mm, and a probe current of 10nA. Data acquisition parameters for the EBSD were set in the TSL-OIM software at 2x2 binning, high gain, a binned pattern size of 160, a theta step size of 0.5°, 8 bands, and 11 reflector families for quartz.

Quartz EBSD data were cleaned and plotted with the TSL-OIM post-processing software. EDS was coupled with EBSD (Nowell and Wright, 2004) to create mineral-specific orientation maps with a step size of 1-2mm. The data were filtered by both phase and confidence index (CI limit of 0.1) and then cleaned to remove spurious points and dauphine twins. The grain identification parameters were set at a 10° misorientation, a minimum diameter of triple the step size, and a minimum CI of 0.1. Quartz c-axis pole figures (Figure 2.8a,b) for the host rock and quartz clasts are equal area, lower hemisphere projections with linear contouring and were plotted from cleaned mineral orientation maps using one point per grain. The pole figure showing the clast CPO (Figure 2.8c) was created from a merged dataset of individual maps from several different quartz clasts. The pole figure for the host rock (Figure 2.8a) was plotted from a combined dataset from maps of two different quartz ribbons. The grain size in the recrystallized matrix of the deformed pseudotachylite was too small to resolve mineral type with automated coupled EDS-EBSD mapping, so the figure for the matrix grains (Figure 2.8c) plots points from a manually-collected dataset (minimum CI of 0.1).

BSE images of five mylonite samples of the quartzofeldspathic unit were used to calculate the average percent mica content (biotite + muscovite) in the matrix of a deformed pseudotachylyte (Figure 2.7). BSE image contrast was adjusted to highlight mica mineralogy within each image, and the threshold option in the NIH ImageJ software (<http://rsbweb.nih.gov/ij/>) was used to calculate the percent mica content by comparing the area of each mineral type relative to the total area of the image. The average percent mica content of a sample was calculated using several high-resolution BSE images collected from different areas on each thin section.

Eleven samples of pseudotachylyte vein matrix material were powdered, mounted on a quartz plate, and analyzed on the Scintag X2 x-ray diffractometer (XRD) at the University of Maine using DMSNT software (Figure 4). Care was taken to remove all wall material and any large, visible, entrained fragments before the samples were powdered. The diffractometer was set for Cu K α at 45kV and 40mA through 5° to 70° with a continuous scan rate of 2.5° per minute. The corrections for the resulting data were based on the analysis of a silicon standard.

The size-cumulative frequency plot of clasts in a deformed pseudotachylyte vein (Fig. 3.9) was created using stitched high-resolution BSE images (e.g. Tsutsumi, 1999). The contrast of the BSE images was optimized to distinguish clasts by mineralogy. The clasts (monomineralic clasts and rock fragments) were manually traced in a drafting program to create a black and white overlay. This overlay was imported as a high resolution image into the NIH ImageJ software where the area per clast was calculated. The diameter of the circle equivalent to the area of each clast was used to plot the data on a logarithmic size-cumulative frequency plot, with a clast diameter size interval of $10^{0.1}$. Only clasts greater than an equivalent diameter of ~10 μm were plotted because of difficulty in distinguishing smaller clasts from new matrix grains. A D value (two-dimensional) was calculated for the 20-150 μm size fraction (monomineralic clasts only) following the power-law form: $N = N' r^{-D}$, where r is the grain diameter, N is the cumulative

number of clasts with sizes greater than r , N' is a constant, and D is the power-law exponent (Shimamoto and Nagahama, 1992).

The percent area of deformed pseudotachylyte within standard-sized polished thin sections collected from across the shear zone (8 from the quartzofeldspathic mylonites, 3 from the calc-silicate granofels unit) was used as a proxy for the percent volume of deformed pseudotachylyte within the Sandhill Corner shear zone (see Section 2.7.3). Using the criteria outlined in Section 2.7.2, individual ultramylonite layers that likely originated as pseudotachylyte were manually traced in a drafting program to create a black and white overlay on full section BSE images. This overlay was imported into ImageJ where conservative estimates of the total area of deformed pseudotachylyte were calculated for each thin section. The calculated range in percent area reflects the total area values from multiple thin sections. Additional samples (2x3 inch sections) were also analyzed for percent area of deformed pseudotachylyte and yielded similar values as the standard-sized polished sections. These percent area values were not included in the percent range and mean cited in Section 2.7.3 because these larger slides were not systematically investigated with the SEM (only some of the criteria in Section 2.7.2 were used), although representative images of these large sections are shown in Figure 2.10.

2.6. Microscale Observations

2.6.1. Undeformed Pseudotachylyte

2.6.1.1. Quartzofeldspathic Unit. Pseudotachylyte within the quartzofeldspathic mylonites occurs as mm- to cm-thick single or paired, foliation-parallel veins with a melt-derived matrix that displays flow banding and folds, Fe-Ti oxide microlites, and rounded and embayed clasts. Paired concordant veins are linked by injection veins to form a ladder network, breccia, and/or quasi-conglomerate (Figure 2.2a; after Sibson, 1975). Multiple generations of pseudotachylyte overlap in space, and additional generations of pseudotachylyte are typically found where cataclasite or pseudotachylyte has already cut the foliation. A damage zone of

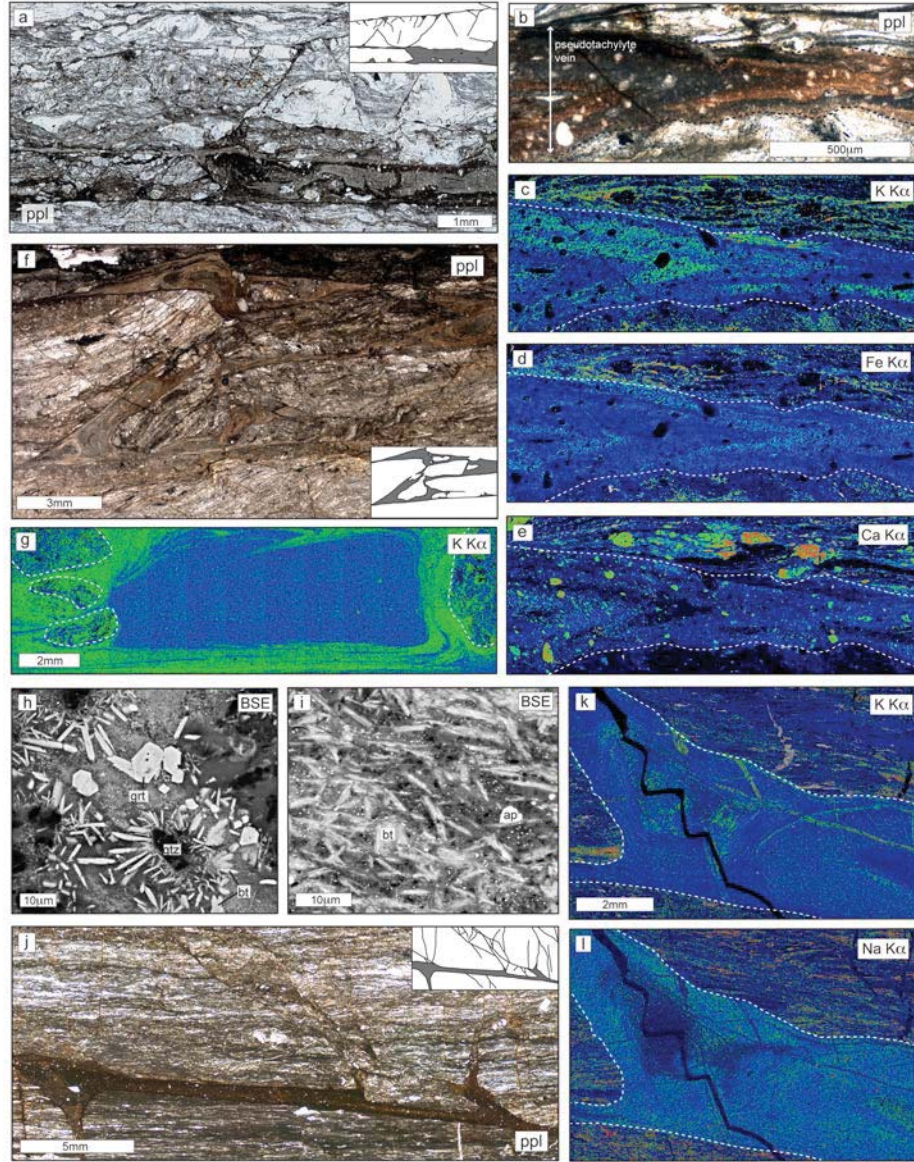


Figure 2.2. Photomicrographs, SEM-BSE images, and element distribution maps of primary pseudotachylyte features from the (a-e) quartzofeldspathic, (f-i) schist, and (j-l) calc-silicate granofels units. (a) Pseudotachylyte forms as mm- to cm-thick, single or paired, foliation-parallel veins in the quartzofeldspathic mylonites with (b-e) alternating Fe/Ca-rich and K-rich flow bands and fine, needle-shaped Fe-Ti oxide microlites. (f) Within the schist unit, pseudotachylyte occurs as mm-to-cm large reservoir zones connected by thin, melt-filled fractures and (g) contain flow structures best defined by variations in K content. (i) Biotite and unidentified ultra-fine-grained granules may have crystallized locally from the schist-derived melt, and (h) in one instance, at the edge of an entrained rock fragment, euhedral garnet grows on existing garnet fragments. (j) Thin, single, foliation-parallel pseudotachylyte veins in the highly fractured calc-silicate granofels unit connect slightly larger open reservoir zones that contain (k, l) flow structures defined by variations in K and other elements. Ppl-plane polarized; BSE-backscattered electron image; ap-apatite, bt-biotite, grt-garnet, and qtz-quartz; element maps c, d, and e were created using EMPA; g, k, and l are SEM-EDS element maps. Warmer colors represent higher elemental concentrations.

cataclasite and ultracataclasite surrounds many of the pseudotachylyte veins. The thickness of this damage zone ranges from a hundred microns up to a centimeter, in places wider than the thickness of the melt vein. The clasts contained within the pseudotachylyte are typically matrix-supported, rounded and embayed monomineralic clasts (quartz, plagioclase, less common K-feldspar, and rare tourmaline, zircon, and apatite) and polymineralic mylonite fragments resulting from the quasi-conglomerate vein structure. In some instances, feldspar clasts and mylonite fragments show evidence for in-situ melting at their margins (e.g. mantles and ghost rims). The only microlites present in the melt matrix are needle-shaped Fe-Ti oxides that are at most a few tens of microns in length (Lin, 2008a; Philpotts, 1964). Common in the melt matrix is a honeycomb-like, cellular texture (e.g. Macaudière et al., 1985; Sibson, 1975) that, in coarser samples, has a muscovite-like composition as determined by EDS analysis. The pseudotachylyte veins display melt flow structures in the form of bands and folds that reflect the viscous flow of areas of non-uniform chemical composition that formed when in a molten state (Lin, 2008a). Flow banding in pseudotachylyte veins from the quartzofeldspathic mylonites typically alternates between K-rich layers and Ca- and Fe-rich layers (Figure 2.2b-e).

2.6.1.2. Schist Unit. Pseudotachylyte within the schist unit occurs as a fracture network that comprises large reservoir zones (mm to cm) containing flow structures connected by thin (μm to mm), melt-filled fractures (Figure 2.2f). Due to the limited exposure of schist containing pseudotachylyte, the larger extent and structure of a single pseudotachylyte fracture network is currently unknown. Clasts within the matrix are typically small in both size and number and include schist fragments, quartz, plagioclase, garnet, variable amounts of andalusite, and rarely K-feldspar and apatite. Flow structures are common within the reservoir zones with banding and folds that follow zone margins (Figure 2.2f,g). Flow bands are predominantly defined as high- or low-K layers, with low-K layers associated with relatively higher amounts of Na, Mn, and/or Fe and high-K layers associated with relatively higher amounts of Mg (Figure 2.2g). Low K layers

also correspond with a higher proportion of mineral clasts, schist fragments, and elongate lenses of ultracataclasite, all of which locally show evidence for in-situ melting. Ultracataclasite lenses are distinctive zones within the melt that comprise greater than 90% clasts and are incompletely mixed with the surrounding melt matrix. K-rich layers are the only layers that contain the honeycomb-like, cellular texture. Microlites do not appear to be prevalent in the pseudotachylyte of the schist unit, although needle-shaped Fe-Ti oxide microlites occur in some high-K layers. Ultra-fine-grained granules and needle-shaped biotite crystals occur locally in the low-K layers and may also represent primary, crystallized phases (Figure 2.2i). The granular microlites are too small (<3mm) to confidently identify, but EDS analyses of the largest of these phases suggest a garnet composition. In one sample, at the edge of a fragment clast where there is evidence for in-situ melting, euhedral garnet crystals with angular-shaped fragment cores occur (Figure 2.2h). EPMA quantitative analyses of these garnets indicate a lower range in X_{Fe} and slightly higher ranges in X_{Mn} and X_{Mg} when compared to garnet from outside of the pseudotachylyte vein (X_{Fe} -0.47 to 0.57, X_{Mn} -0.26 to 0.32, and X_{Mg} - 0.14 to 0.22 inside; X_{Fe} -0.59 to 0.75, X_{Mn} -0.14 to 0.27, and X_{Mg} - 0.07 to 0.09 outside; Table 1).

2.6.1.3. Calc-silicate Granofels Unit. Pseudotachylyte within the calc-silicate granofels unit occurs as thin (mm), single, foliation-parallel veins with a melt matrix that is rich in clasts and that is mixed with layers and pods of ultracataclasite (Figure 2.2j). The calc-silicate granofels unit is highly fractured around the pseudotachylyte vein, with single fractures cutting into the rock away from the vein typically creating wide injection veins. Despite the many fractures, there is much less cataclasite around the pseudotachylyte vein in the calc-silicate granofels than seen around the pseudotachylytes of the quartzofeldspathic mylonites. In many places, multiple generations of pseudotachylyte overlap in space, with younger generations preferentially forming at sites of previous pseudotachylyte generation. Flow structures are best developed in the injection veins with banding that follows vein margins (Figure 2.2k,l). Flow

Table 2.1. EMPA mineral compositions from within the matrix of pseudotachylyte veins (inside) in comparison with the composition of minerals from the surrounding host rock (outside).

Quartzofeldspathic Unit					Schist Unit					Ca-Si Granofels Unit				
bt outside PT		bt inside PT			bt outside PT		bt inside PT			bt outside PT		bt inside PT		
129		129			225		211			211		112		
wt %					wt %					wt %				
SiO ₂	36.76	35.45	36.68	37.67	SiO ₂	35.40	37.19	40.14	38.57	SiO ₂	37.77	39.01	37.16	38.44
TiO ₂	0.88	3.33	1.44	2.89	TiO ₂	1.66	1.66	0.63	1.98	TiO ₂	0.12	0.98	0.64	0.90
Al ₂ O ₃	18.20	17.36	18.32	18.09	Al ₂ O ₃	19.32	19.74	22.88	23.14	Al ₂ O ₃	18.78	18.59	19.08	19.08
FeO	17.59	19.10	18.34	21.04	FeO	18.49	18.55	15.79	17.06	FeO	18.04	17.69	16.65	16.16
MnO	0.34	0.34	0.16	0.28	MnO	0.31	0.19	0.25	0.50	MnO	0.22	0.15	0.21	0.21
MgO	11.19	9.63	9.97	6.52	MgO	10.28	8.30	6.32	6.60	MgO	11.00	9.72	12.17	11.14
CaO	0.04	0.01	0.01	0.11	CaO	0.00	0.00	0.07	0.05	CaO	0.02	0.02	0.15	0.36
Na ₂ O	0.05	0.03	0.02	0.01	Na ₂ O	0.04	0.02	0.09	0.07	Na ₂ O	0.06	0.15	0.23	0.61
K ₂ O	9.55	9.62	9.59	8.58	K ₂ O	8.32	9.01	9.00	7.84	K ₂ O	8.69	9.09	8.11	8.16
BaO	0.02	0.14	0.13	0.12	BaO	0.18	0.00	0.10	0.05	BaO	0.03	0.00	0.06	0.06
F	0.34	0.21	0.13	0.08	F	1.05	0.45	0.24	0.25	F	0.41	0.36	0.46	0.26
Cl	0.04	0.03	0.06	0.06	Cl	0.00	0.01	0.00	0.01	Cl	0.03	0.26	0.01	0.00
H ₂ O	3.78	3.80	3.86	3.90	H ₂ O	3.42	3.76	3.99	3.99	H ₂ O	3.78	3.79	3.78	3.93
Total	98.78	99.06	98.70	99.33	Total	98.47	98.88	99.49	100.09	Total	98.95	99.82	98.70	99.30
APFU for 22 oxygens					APFU for 22 oxygens					APFU for 22 oxygens				
Si	5.58	5.44	5.59	5.72	Si	5.41	5.62	5.87	5.63	Si	5.68	5.81	5.57	5.70
Al	3.26	3.14	3.29	3.24	Al	3.48	3.51	3.94	3.98	Al	3.33	3.26	3.37	3.33
Ti	0.10	0.38	0.16	0.33	Ti	0.19	0.19	0.07	0.22	Ti	0.01	0.11	0.07	0.10
Fe	2.23	2.45	2.34	2.67	Fe	2.36	2.34	1.93	2.08	Fe	2.27	2.20	2.09	2.00
Mn	0.04	0.04	0.02	0.04	Mn	0.04	0.02	0.03	0.06	Mn	0.03	0.02	0.03	0.03
Mg	2.53	2.20	2.26	1.48	Mg	2.34	1.87	1.38	1.44	Mg	2.47	2.16	2.72	2.46
Ca	0.01	0.00	0.00	0.02	Ca	0.00	0.00	0.01	0.01	Ca	0.00	0.00	0.02	0.06
Na	0.02	0.01	0.00	0.00	Na	0.01	0.01	0.02	0.02	Na	0.02	0.04	0.07	0.18
K	1.85	1.88	1.86	1.66	K	1.62	1.74	1.68	1.46	K	1.67	1.73	1.55	1.54
Ba	0.00	0.01	0.01	0.01	Ba	0.01	0.00	0.01	0.00	Ba	0.00	0.00	0.00	0.00
F	0.16	0.10	0.06	0.04	F	0.51	0.21	0.11	0.12	F	0.20	0.17	0.22	0.12
Cl	0.01	0.01	0.02	0.01	Cl	0.00	0.00	0.00	0.00	Cl	0.01	0.07	0.00	-0.01
H ₂ O	3.83	3.89	3.92	3.95	H ₂ O	3.49	3.78	3.89	3.88	H ₂ O	3.80	3.76	3.78	3.88
XFe	0.47	0.53	0.51	0.64	XFe	0.50	0.56	0.58	0.59	XFe	0.48	0.51	0.43	0.45

Quartzofeldspathic Unit					Schist Unit					Ca-Si Granofels Unit				
pl outside PT		pl inside PT			grt outside PT		grt inside PT			pl outside PT		pl inside PT		
129		129			211		211			112		112		
wt %					wt %					wt %				
SiO ₂	63.31	62.56	63.63	64.51	SiO ₂	36.33	36.08	35.54	36.43	SiO ₂	59.05	56.78	60.60	59.49
Al ₂ O ₃	22.88	22.86	22.80	23.05	TiO ₂	0.08	0.04	1.46	0.19	Al ₂ O ₃	25.67	27.33	23.31	24.91
FeO	0.05	0.05	0.41	0.44	Al ₂ O ₃	20.54	20.23	20.50	20.68	FeO	0.15	0.13	1.35	0.43
MgO	0.00	0.00	0.08	0.11	FeO	28.06	33.79	21.71	25.26	MgO	0.01	0.01	0.85	0.12
CaO	4.81	4.98	4.61	4.31	MnO	11.86	6.11	13.79	11.37	CaO	7.92	9.73	5.63	7.67
Na ₂ O	8.66	8.32	8.57	6.12	MgO	2.01	2.19	4.30	3.63	Na ₂ O	6.80	5.80	7.15	5.56
K ₂ O	0.28	0.23	0.14	0.19	CaO	1.14	1.09	1.86	1.11	K ₂ O	0.10	0.10	1.01	0.16
Total	99.98	98.99	100.23	98.73	Y ₂ O ₃	0.04	0.18	0.31	0.11	Total	99.69	99.87	99.89	98.34
APFU for 8 oxygens					APFU for 12 oxygens					APFU for 8 oxygens				
Si	2.80	2.79	2.81	2.85	Si	2.97	2.97	2.88	2.97	Si	2.64	2.55	2.72	2.68
Al	1.19	1.20	1.19	1.20	Al	1.98	1.96	1.96	1.99	Al	1.35	1.45	1.23	1.33
Fe	0.00	0.00	0.02	0.02	Fe	1.92	2.32	1.47	1.72	Fe	0.01	0.00	0.05	0.02
Mg	0.00	0.00	0.00	0.01	Ti	0.00	0.00	0.09	0.01	Mg	0.00	0.00	0.06	0.01
Ca	0.23	0.24	0.22	0.20	Mg	0.24	0.27	0.52	0.44	Ca	0.38	0.47	0.27	0.37
Na	0.74	0.72	0.73	0.52	Mn	0.82	0.43	0.95	0.79	Na	0.59	0.50	0.62	0.49
K	0.02	0.01	0.01	0.01	Ca	0.10	0.10	0.16	0.10	K	0.01	0.01	0.06	0.01
An	0.23	0.25	0.23	0.28	Y	0.00	0.01	0.01	0.00	An	0.39	0.48	0.30	0.43
					XFe	0.62	0.75	0.47	0.57					
					XMn	0.08	0.09	0.17	0.14					
					XCa	0.03	0.03	0.05	0.03					
					XMg	0.27	0.14	0.31	0.26					

Notes: APFU= atoms per formula unit; PT=pseudotachylyte; XFe=Fe/(Fe+Mg) for biotite; An=Ca/(Ca+Na); XFe=Fe/(Fe+Mg+Mn+Ca) for garnet, XMg=Mg/(Fe+Mg+Mn+Ca), XMn=Mn/(Fe+Mg+Mn+Ca), XCa=Ca/(Fe+Mg+Mn+Ca); bt-biotite, grt-garnet, & pl-plagioclase.

bands are weakly developed and are primarily defined by the K and Na content. The higher-K, low-Na layers typically correspond with a slightly higher level of Ca, Mg, and Fe as well as a significantly higher proportion of mineral clasts and ultracataclasite layers and pods, all of which show evidence for in-situ melting. Clasts include rock fragments, amphibole, epidote, quartz, plagioclase, and rarely K-feldspar. A cellular texture is present in places but is uncommon. Fine, needle-shaped Fe-Ti oxide microlites occur locally.

2.6.2. Recrystallized and Deformed Pseudotachylyte

Observations of the petrologic and microstructural relationships in recrystallized and deformed pseudotachylyte were made on samples with unambiguous cross-cutting relationships. In Section 2.7.3, we use the characteristics of recrystallized and deformed pseudotachylyte derived from these unambiguous areas to determine pseudotachylyte abundance throughout the rock. For the purposes of this chapter, we classify recrystallized pseudotachylyte as veins that contain grains large enough (>3-5mm) to image and analyze and deformed pseudotachylyte as veins where micas and other elongate minerals show some degree of alignment resulting from dextral shear deformation. XRD analyses of matrix material from undeformed pseudotachylyte veins from all rock types indicate that the samples analyzed have no remaining glass content (Figure 2.3). The undeformed pseudotachylyte veins described in Section 2.6.1 are cryptocrystalline rather than glassy whereas the observations described in this section refer to those pseudotachylyte veins where the quenched glass matrix has recrystallized, or devitrified, to the point where the mineral grains are observable with the SEM as well as those veins that have also been deformed. The degree of pseudotachylyte deformation is measured by the degree of shear fabric development, such as mineral alignment and porphyroclast recrystallization, with the most deformed veins containing the best-developed matrix shear fabrics and microstructures. Photomicrographs of recrystallized and deformed pseudotachylyte are shown in Figures 2.4, 2.5 and 2.6.

The recrystallized and deformed pseudotachylyte veins within the three rock types share a number of features. The recrystallized pseudotachylyte veins have an ultra-fine-grained matrix that on the 10-20mm scale contains a relatively homogenous mixture of all phases present in the

Figure 2.3. Representative powder x-ray diffraction spectra of pseudotachylyte matrix material from the Sandhill Corner shear zone. The broad band at 2θ of $12\text{--}42^\circ$ (Lin, 2008a) observed in patterns of volcanic glass is absent in the analyzed samples. More than one pattern from pseudotachylyte of the schist unit is included to show the variation in mineral content between samples, including the presence of chlorite. CPS-counts per second; am-amphibole, bt-biotite, chl-chlorite, fd-feldspar, ms-muscovite, and qz-quartz.

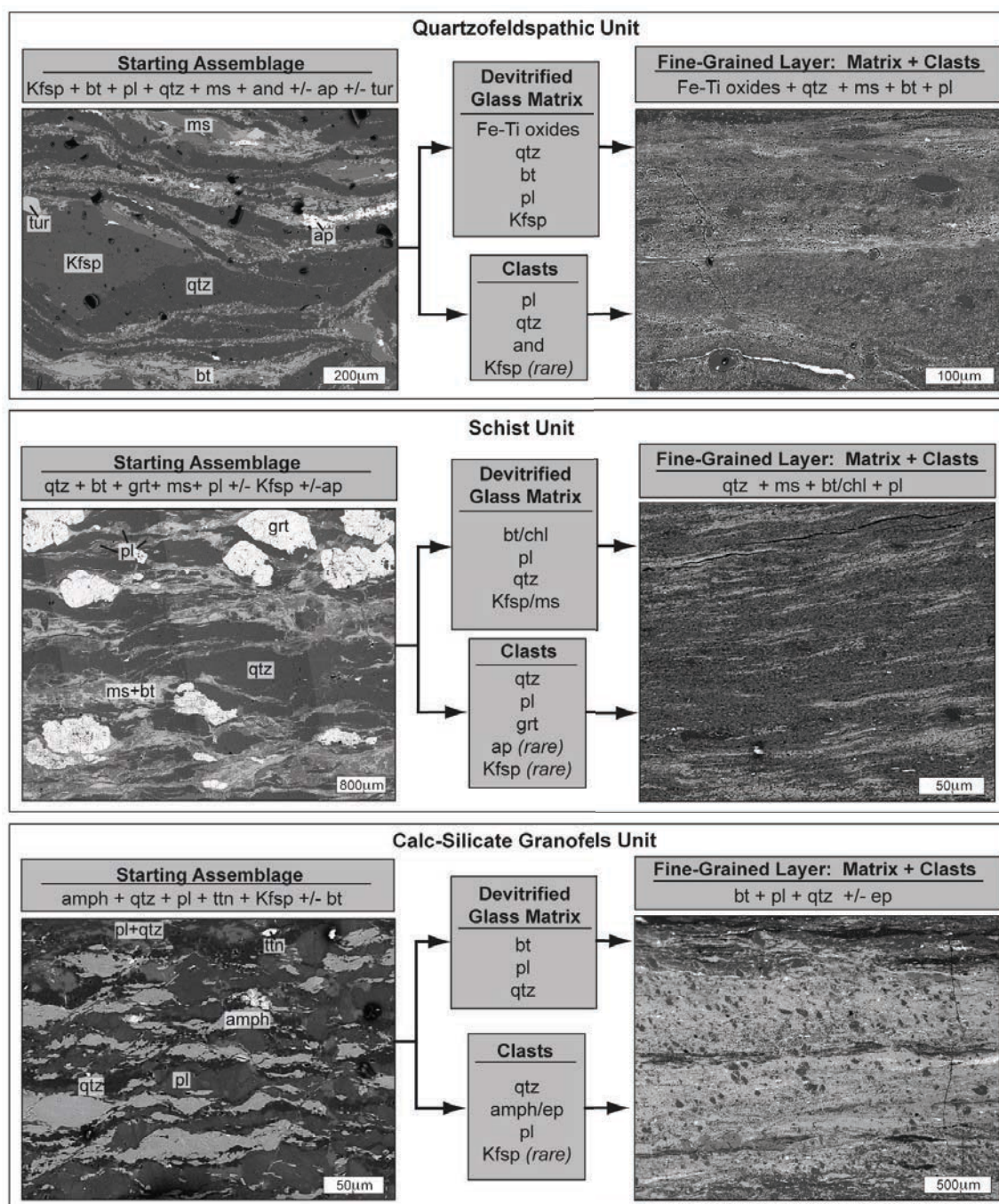


Figure 2.4. A change in the mineral assemblage and texture occurs during the formation, recrystallization, and deformation of pseudotachylyte in each rock type. Representative SEM-BSE images show the difference between the coarser-grained, layered texture of the host rock and the relatively homogenous, ultra-fine-grained texture of the resulting pseudotachylyte-derived ultramylonite layer. Amph-amphibole, and-andalusite, ap-apatite, bt-biotite, chl-chlorite, ep-epidote, grt-garnet, kfsp-K-feldspar, ms-muscovite, pl-plagioclase, qtz-quartz, ttn-titanite, and tur-tourmaline.

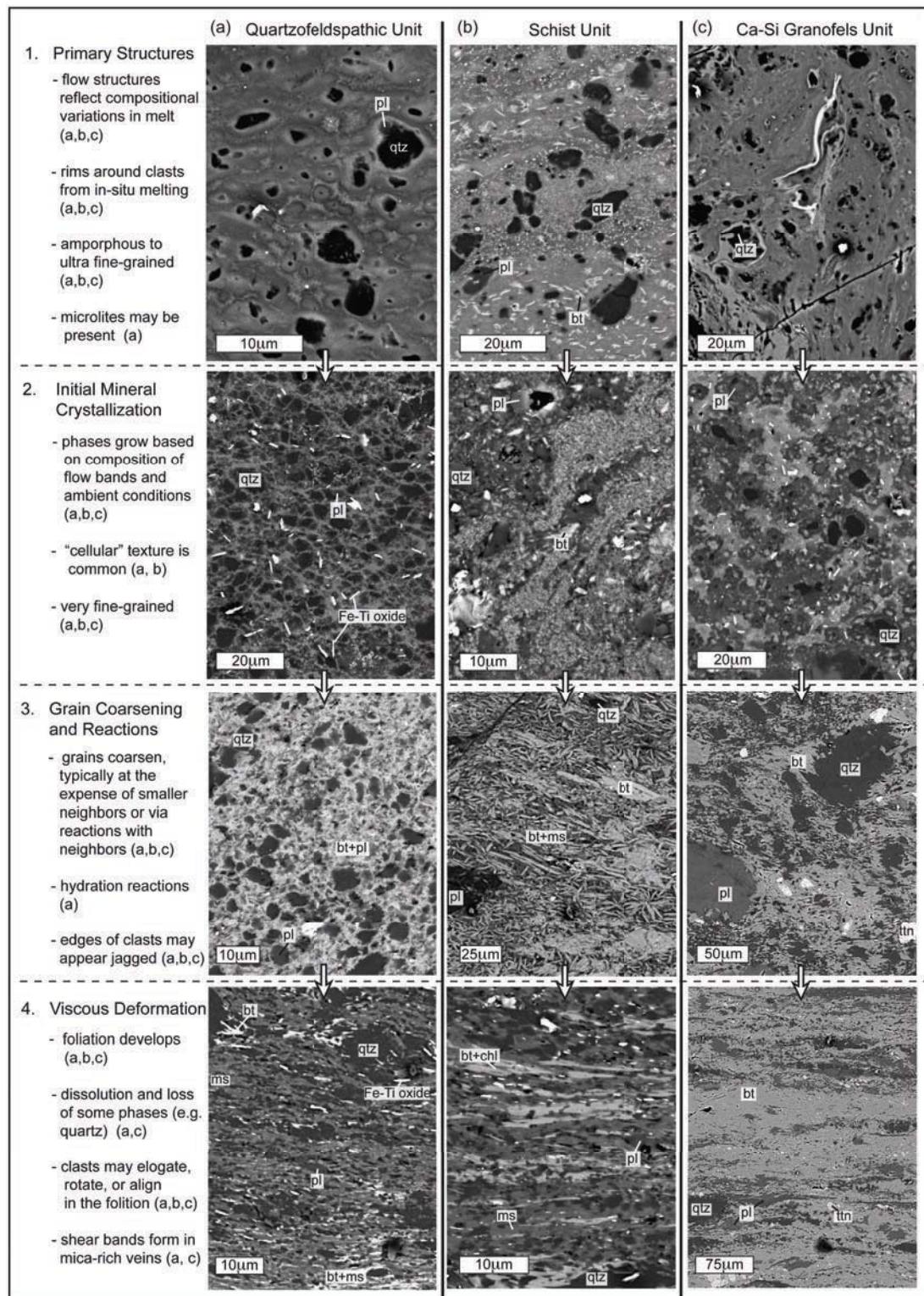


Figure 2.5. Examples of the stages of transformation of a pseudotachylyte vein to an ultramylonite/phyllonite layer within the three rock types of the Sandhill Corner shear zone. BSE-images are from samples representative of each stage. Bt-biotite, chl-chlorite, ms-muscovite, pl-plagioclase, qtz-quartz, and ttn-titanite.

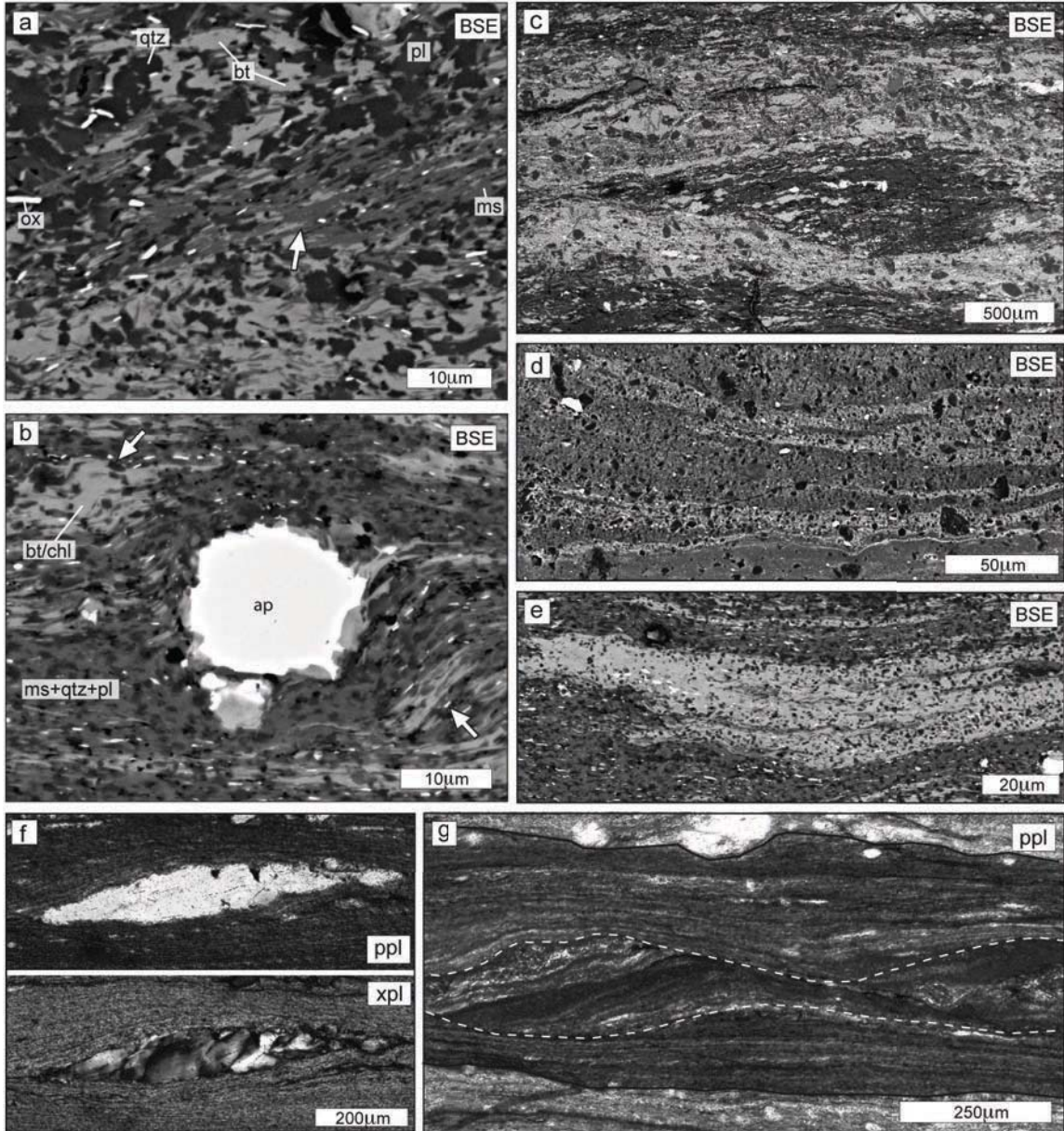


Figure 2.6. Examples of the features seen in deformed pseudotachylyte veins. (a) Mica grains that are aligned in the foliation and/or (b) at the edges of clasts locally show thinning and kinking (arrows) as well as bookshelf style cleavage steps that are consistent with basal slip along {001}. (c) Rock fragments appear as islands in the ultra-fine-grained matrix of deformed pseudotachylyte. (d,e) Flow structures may be preserved in the mineral distributions of deformed pseudotachylyte veins, particularly in the schist unit (d-flow bands/folds in undeformed pseudotachylyte, e-flow structure-like features in deformed pseudotachylyte). With deformation, (f) monomineralic quartz clasts become elongate and are recrystallized to form sigma clasts and thin ribbons, and (g) rock fragments may show internal deformation in the form of shear bands that do not extend into the finer-grained matrix. (a, f, g) Quartzofeldspathic unit, (b, d, e) schist unit, (c) calc-silicate granofels unit; BSE-backscattered electron image; ap-apatite, bt-biotite, chl-chlorite, ms-muscovite, ox-Fe-Ti oxide, pl-plagioclase, and qtz-quartz.

recrystallized matrix assemblage without segregation into monomineralic layers. Variations in elemental abundances between K-rich and K-poor layers of flow bands and folds coincides on the ~50-100mm scale with a larger spatial variation in the relative abundance of matrix phases. Muscovite is more common in the K-rich layers, and biotite and plagioclase are more common in the K-poor layers. Coarser recrystallized veins contain fewer mineral grains, and the edges of the monomineralic clasts have a jagged appearance (Figure 2.5). Entrained rock fragments in undeformed veins appear as “islands” in the fine-grained matrix (Figure 2.6c).

The deformed pseudotachylyte veins contain an internal foliation that is concordant with the external mylonitic foliation and that is best defined by the alignment of micas and Fe-Ti oxide needles, where present (Figure 2.6a). A second weaker fabric set oriented at an angle to the foliation (ranges between ~30-40° and ~60-70°) is typical, particularly in the quartzofeldspathic mylonites, and is similar to R and P shear orientations for layer-parallel simple shear in anisotropic rocks (e.g. Swanson, 1988). Variably-developed shear bands may also be present in the fine-grained matrix, particularly in the calc-silicate granofels unit (also documented by White, 2004). Mica dominates along these shear bands, and quartz and feldspar grains are less common relative to the rest of the matrix. Matrix mica grains that are aligned in the foliation or within shear bands locally show thinning, kinking, and bookshelf-style cleavage steps (Figure 2.6a), and matrix quartz grains present within these areas have the greatest degree of elongation. Quartz and feldspar grains are most equant where mica grains are not well-aligned in the foliation and in deformed pseudotachylyte veins that are relatively mica-poor. In those instances, mica grains are found to truncate at the edge of other grains and do not appear thinned perpendicular to the slip direction. Entrained rock fragments in deformed pseudotachylyte appear elongate and are typically cut by internal shear bands that do not continue into the fine-grained matrix (Figure 2.6g). Feldspar porphyroclasts, where present, are commonly rigid clasts, and quartz porphyroclasts may be recrystallized to form sigma clasts. In the most deformed

pseudotachylyte, plagioclase porphyroclasts appear elongate and quartz clasts appear as thin ribbons (Figure 2.6f).

2.6.2.1. Quartzofeldspathic Unit. The matrix of recrystallized pseudotachylyte veins within the quartzofeldspathic mylonites contains an assemblage of quartz + plagioclase + biotite \pm K-feldspar \pm muscovite (Figures 2.4, 2.5). The recrystallized assemblage is not strikingly different from the host rock assemblage, although there is a modal increase of mica (biotite and/or muscovite) in the recrystallized and deformed pseudotachylyte veins when compared to the host rock (Figure 2.7). Ca- and Fe-rich bands contain a greater amount of biotite and plagioclase, and

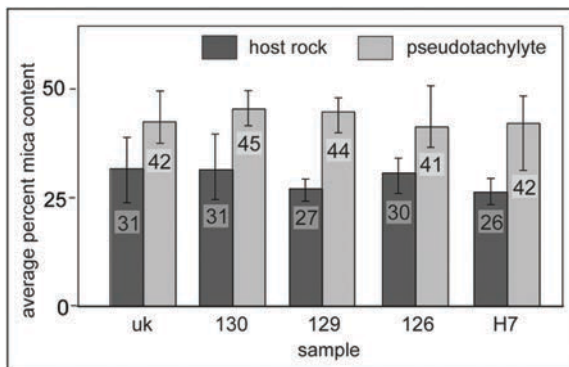


Figure 2.7. Average percent mica content of the recrystallized matrix of deformed pseudotachylyte in the mylonites of the quartzofeldspathic unit as compared to the host rock. Although the deformed pseudotachylyte veins contain the same mineral assemblage as the host rock, they have a higher average percent mica content. Bars represent the range in data, and the numbers on the graph are the mean.

K-rich bands contain a greater amount of K-feldspar and/or muscovite. Muscovite is not present in all K-rich layers, particularly those layers with the finest grain size. Conversely, K-feldspar does not persist in more coarse and deformed veins; muscovite dominates the K-rich layers in those veins. Biotite and plagioclase are present in all veins studied, independent of the grain size or degree of deformation. Muscovite is partially replaced by biotite in places within the matrix, and biotite occurs between clasts in the cataclasite surrounding the pseudotachylyte veins. EPMA quantitative analyses indicate a higher but overlapping range in the X_{Fe} component for the biotite inside the pseudotachylyte matrix when compared to the biotite from outside the pseudotachylyte

vein (X_{Fe} -0.49 to 0.74 inside; X_{Fe} -0.46 to 0.54 outside; Table 1) but no difference in the anorthite component of the plagioclase.

Within the deformed pseudotachylyte veins of the quartzofeldspathic mylonites, deformed quartz porphyroclasts exhibit a cross girdle c-axis pattern in EBSD-derived quartz pole figures (Figure 2.8b) similar to the c-axis pattern from quartz-rich ribbons in the host rock (Figure 2.8a). Quartz pole figures of the matrix quartz grains in the deformed pseudotachylyte (Figure 2.8c) exhibit a relatively random distribution of points without a clear c-axis pattern.

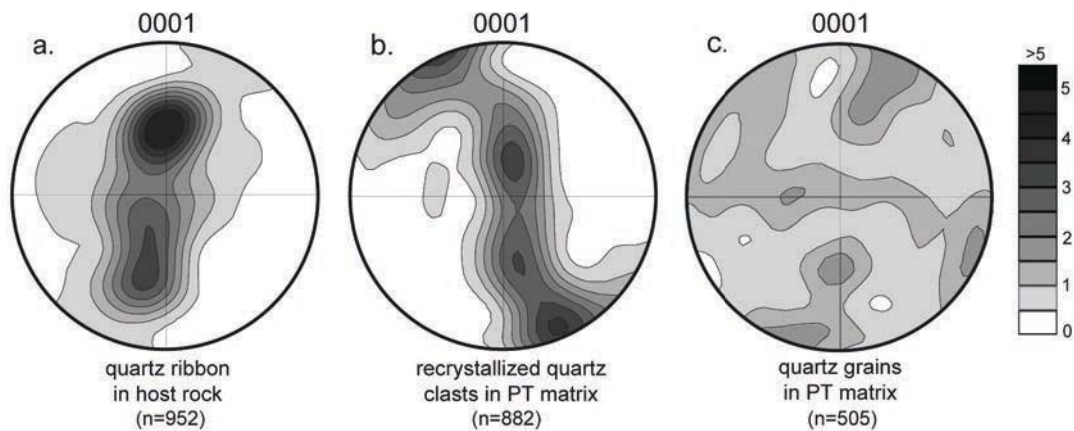


Figure 2.8. SEM-EBSD derived quartz c-axis pole figures from a sample of the quartzofeldspathic mylonites. (a) Host rock quartz ribbons and (b) recrystallized quartz clasts of the pseudotachylyte matrix show cross girdle patterns in the pole figures whereas (c) the quartz grains of the recrystallized pseudotachylyte matrix have a relatively random distribution of points. The pole figures are equal area lower hemisphere projections and display linear contouring (the scale with multiples of uniform density is shown). The host rock and recrystallized clast orientations are plotted as one point per grain derived from several merged EBSD mineral orientation map datasets; matrix grains are plotted from a manually collected dataset.

2.6.2.2. Schist Unit. The matrix of a recrystallized pseudotachylyte vein within the schist unit is dominated by mica minerals, with a mineral assemblage of biotite + muscovite + quartz \pm plagioclase (Figures 2.4, 2.5). Due to sample heterogeneity and the limited number of samples with unambiguous cross-cutting relationships, it is unclear whether there is a change in modal mica in the recrystallized vein when compared to the host rock. Biotite is found in the

low-K layers. A mixture of muscovite, plagioclase, and/or quartz occurs in the low-K layers between the blades of biotite and in areas where biotite is less common (Figure 2.5). XRD analyses indicate that in some samples chlorite is present in addition to biotite but is not prevalent (Figure 2.3b, c). K-rich layers primarily contain muscovite, and some particularly K-rich pseudotachylyte veins occur where muscovite is the only mineral present. Biotite mineral compositions from inside the pseudotachylyte vein have an overlapping but slightly higher, narrower range in X_{Fe} when compared to the composition of biotite from outside the vein (EMPA: X_{Fe} -0.58 to 0.59 inside; X_{Fe} -0.49 to 0.57 outside; Table 1).

Unambiguous examples of deformed pseudotachylyte in the schist unit are few. The deformed matrix contains a mass of aligned micas studded with fine-grained plagioclase and quartz (Figure 2.5). The mixture of biotite/chlorite and muscovite that is coincident with flow bands and folds appears as distinctive wispy intergrowths, lenses, and flattened folds (Figure 2.6d,e). Quartz ribbons are rare or absent.

2.6.2.3. Calc-silicate Granofels Unit. The matrix of a recrystallized pseudotachylyte vein in the calc-silicate granofels unit contains an assemblage distinct from the surrounding host rock mineral assemblage (Figures 2.4, 2.5). The host rock contains amphibole + plagioclase + quartz + titanite + epidote \pm chlorite with less common layers of K-feldspar + quartz \pm biotite of igneous/pegmatite origin, whereas the pseudotachylyte matrix contains prevalent biotite and plagioclase with an absence of chlorite. Flow banding seen in cryptocrystalline, undeformed pseudotachylyte veins does not spatially correlate with the distribution of minerals in the recrystallized vein matrix. EMPA quantitative analyses indicate an overlapping but higher range in the X_{Fe} component of biotite and an overlapping but slightly higher, wider range in the An component of plagioclase from outside the vein than from inside (X_{Fe} -0.43 to 0.47 and An-0.30 to 0.43 inside; X_{Fe} -0.47 to 0.52 and An-0.39 to 0.68 outside).

The grain size distribution pattern within the mildly deformed pseudotachylyte veins in the calc-silicate granulites unit displays a modified power-law relationship (as plotted in a log-log clast size versus frequency diagram; Figure 2.9; Ray, 1999, 2004; Sammis et al., 1986). The two-dimensional D-value (fractal dimension) for the plot shown in Figure 2.9 is ~ 2.3 , which is consistent with published D-values for pseudotachylyte (Lin, 2008a). In the most deformed veins, this fractal relationship is lost because clasts are recrystallized into fine, elongate ribbons, which alternate with the biotite + plagioclase matrix to create a banded appearance.

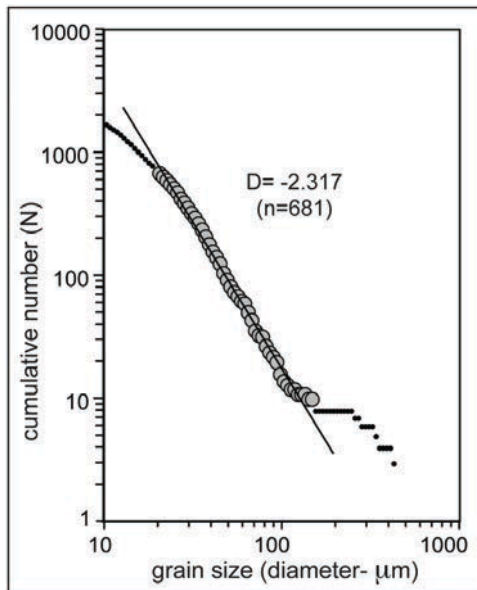


Figure 2.9. A clast size-frequency diagram of clasts within a deformed pseudotachylyte in the calc-silicate granulites unit displays a modified power-law relationship. The trend line for the 20-150 μm size range, as shown by the large grey points, is plotted with a D value of 2.317 (two-dimensional; $n=681$) and includes only monomineralic clasts (feldspar, quartz, and titanite). The total range of data (smaller black circles), includes both monomineralic clasts and rock fragments (10-880 μm ; $n=1707$). The step in the data at the higher size fraction reflects the inclusion of the larger rock fragments in the data set, and the “rounding” or “fall-off” of the data at the smaller size fraction may reflect the loss of some of the finer grains to in-situ melting (Ray, 2004).

2.7. Discussion

2.7.1. The Transformation From Pseudotachylyte Veins to Ultramylonite/Phyllonite Layers

The textural and mineralogical changes that occurred within the studied pseudotachylyte veins during formation, recrystallization, and deformation are presented in Figure 2.5. Our model of this process is divided into four steps: (1) formation of primary pseudotachylyte structures, (2) initial mineral crystallization, (3) grain coarsening and reactions, and (4) viscous deformation.

Pseudotachylyte veins in all rock types started with the primary structures that were created during vein formation. These include: (a) clasts and microlites of variable type and abundance and (b) flow bands and folds that reflect compositional variations in the matrix. Differential melting during frictional slip strongly influenced the types of clasts that remained (dominantly quartz and plagioclase). Fe-Ti oxide microlite crystallization added new phases to the matrix mineral assemblage. We also interpret the larger blades of biotite and the ultra-fine-grained, potentially metastable garnet granules in the schist unit as microlites. The growth of biotite microlites indicates that the activity of water in the melt must have been high enough to crystallize a phyllosilicate.

The types of ultra-fine-grained phases that grew from the quenched glass were influenced by the chemical composition of the glass (reflecting flow structures), reaction kinetics, and the ambient metamorphic conditions (pressure, temperature, water fugacity, etc). This matrix assemblage may be unchanged from the host rock assemblage, such as with the quartzofeldspathic mylonites, or it may differ greatly as in the calc-silicate granofels unit (see Figure 2.4). Even if the assemblage is unchanged from the host rock, the modal abundance of these minerals may be changed, such as an increase in mica content in the quartzofeldspathic mylonites (e.g. Figure 2.7). The composition of the matrix minerals (e.g. X_{Fe} in biotite, X_{Fe} in garnet, or the An component of plagioclase) commonly differ from that of the host rock. However, the overlap in the ranges suggests that the new matrix assemblage grew at relatively unchanged metamorphic conditions from the host rock and that the differences may reflect changes in the modal abundances of a mineral, small amounts of an undetected secondary phase (e.g. small amounts of chlorite in biotite of the schist unit), or small-scale heterogeneities in element distributions in the quenched glass. In some cases, the spatial variation in the composition of the glass, as reflected by flow bands and folds, was great enough to influence the distribution of phases (e.g. Figure 2.6d,e).

Grain coarsening reactions and secondary reactions influenced the evolution of the matrix assemblage beyond initial grain growth from the quenched glass. As the matrix minerals grew, coarsening occurred at the expense of smaller neighbors and caused the edges of clasts to become jagged. Also, fluid infiltration along grain boundaries, fractures, and/or microcracks influenced the growth of secondary hydrous phases. In the calc-silicate granofels unit, amphibole porphyroclasts were replaced by secondary epidote. In the quartzofeldspathic mylonite, biotite grew in fractures and cataclasite layers and from the alteration of muscovite with the addition of K and/or Fe, perhaps from a circulating fluid. Muscovite also formed as a secondary phase from the hydration of K-feldspar in some K-rich layers. The muscovite-like composition of the fine, honeycomb-like, cellular structure observed in some cryptocrystalline veins may represent fluid pathways and initial sites of hydration. This cellular texture may have facilitated the development of the observed shear band-like matrix fabrics ($\sim 30\text{-}40^\circ$ and $\sim 60\text{-}70^\circ$) in some recrystallized pseudotachylyte veins.

At some point following pseudotachylyte formation, the rocks of the shear zone once again flowed viscously, deforming the pseudotachylyte veins. The time interval between pseudotachylyte formation and the renewal of viscous deformation in the rocks of the Sandhill Corner shear zone is unknown. The most important unconstrained variables are the amount of time necessary for vein recrystallization, and the degree and timing of shearing following the coseismic slip event. It is likely that viscous deformation began shortly after the melt matrix quenched and that the initial crystallization of the glass and deformation were synchronous. However, areas of crystallized but undeformed matrix within deformed pseudotachylyte veins suggest that crystallization occurred prior to or very early during deformation (Takagi et al., 2000).

As deformation proceeded, mineral dissolution and/or recrystallization created an internal foliation that, at high shear strain, became sub-parallel to the mylonitic foliation. Platy micas grains became aligned in the foliation either through diffusion-mediated processes or locally by

basal slip. Granular minerals like quartz and feldspar within the matrix assemblage either became elongate in the foliation or were lost, presumably through dissolution; this effect is most obvious in the shear bands that formed in the vein matrix. Rock fragments in the matrix deformed internally and may have been elongated, cut by shear bands, and/or disaggregated. Depending on their size, monomineralic clasts either became elongate in the foliation, such as quartz clasts that recrystallized into ribbons, or persisted as rigid porphyroclasts that may have become aligned in the matrix at an angle to the foliation. Once the pseudotachylyte vein was strongly deformed, it resembled an ultra-fine-grained phyllonite or ultramylonite layer.

2.7.2. Criteria for the Identification of Deformed Pseudotachylyte

Passchier and Trouw (2005) list specific criteria for the identification of pseudotachylyte, including cross-cutting relationships, sharp layer boundaries, the disruption of layering, the presence of microlites, and the loss/abundance of certain phases due to non-equilibrium melting. Other researchers (Kirkpatrick et al., 2009; Koch and Masch, 1992; Lin, 2008a,b; Lin et al., 2003, 2005; McNulty, 1995; Moecher and Steltenpohl, 2009; Passchier, 1982, 1984; Pennacchioni and Cesare, 1997; Sibson, 1980; Takagi et al., 2000; Ueda et al., 2008; White, 1996, 2004) also cite characteristic features such as these to distinguish ultramylonite layers as deformed pseudotachylyte, with cross-cutting relationships being the most important. For this reason, in this study, we also relied on those pseudotachylyte veins that had clear cross-cutting relationships. Other studies described features within deformed pseudotachylyte that were also observed in the rocks of the Sandhill Corner shear zone but not specifically listed as identifying criteria, including changes in the mineral assemblage from the host rock (e.g. Moecher and Steltenpohl, 2009; Passchier, 1982; Sibson, 1980; Takagi et al., 2000; Ueda et al., 2008; White, 1996), variations in the spatial distribution of phases inherited from flow structures (White, 1996), and an ultra-fine-grained, polymineralic matrix (Passchier, 1982; Ueda et al., 2008; White, 1996, 2004). Here we expand on these features and those observed in this study (e.g. degree of

clast recrystallization, fractal size distribution of clasts) to develop a more comprehensive list of characteristic features that may be used to identify deformed pseudotachylyte. It is important to note that any single feature could have an origin not related to the formation, recrystallization, and/or deformation of pseudotachylyte, so identifying a combination of characteristic features will lead to a more reliable interpretation.

1. Cross-cutting relationships- Places where the foliated host rock fabric is truncated, or cross-cut, by the cryptocrystalline to fine-grained matrix of the pseudotachylyte are the clearest and best indicators of pseudotachylyte. These may occur at the vein edge (if the pseudotachylyte cuts the host rock at an angle to the foliation), where it cuts porphyroclasts, or where injection veins branch off of the main vein. Cross-cutting relationships can be obscured during deformation as the truncated host rock continues to recrystallize and as injection veins are transposed into the shear foliation by progressive shear strain.

2. Sharp layer boundaries- A sharp boundary with the host rock is commonly listed as a cross-cutting relationship. We make the distinction here for those layer boundaries without any clear cross-cutting relationships, such as at the edge of foliation-parallel veins or deformed veins where other cross-cutting relationships have been obscured. The edge of a pseudotachylyte vein is a sharp and distinct boundary. Even when observed at the highest magnification, the fine-grained texture of the recrystallized and deformed pseudotachylyte matrix typically directly abuts the coarser-grained, layered mylonite (or is surrounded by a cataclasite damage zone).

3. Presence of host rock fragments- Fragments of the host mylonite that are entrained within the pseudotachylyte matrix (via the breccia or quasi-conglomerate structures of Sibson [1975]) will appear as identifiable, isolated islands (e.g. Figure 2.6c). The foliation present in the clast may be either parallel or oblique to the surrounding mylonitic foliation. During deformation, the clasts typically become elongate in the foliation and/or are cut by shear bands that form within the clast, changing them from isolated islands into thin, coarse layers within the deformed pseudotachylyte.

Even with deformation, these fragments may still be identified if the edges maintain a truncated appearance or if the internal deformation appears unrelated to the surrounding melt matrix, such as shear bands that do not continue into the fine-grained matrix.

4. Ultra-fine-grained, polymineralic matrix- The matrix of the deformed pseudotachylyte from all three rock types in the Sandhill Corner shear zone is remarkably similar: relatively homogenous, polymineralic, and ultra-fine-grained (Figure 2.5, stage 4). This observation has been documented by other authors (e.g. Passchier, 1982; Ueda et al., 2008; White, 1996, 2004). At the micron-scale, the ultra-fine-grained matrix contains the same polymineralic assemblage throughout the vein, with variations only in the relative proportions of each mineral. This sharply contrasts with the surrounding mylonite (e.g. Figure 2.4), where the more heterogeneous phase distribution is largely inherited from and limited to the products of reacted or recrystallized porphyroclasts.

5. Inherited compositional variations from flow structures- Flow bands and folds within a pseudotachylyte vein are defined by compositional variations in the melt. These compositional variations may be inherited when the new mineral assemblage grows, with a layer preferentially growing more of one mineral than another, creating patterns such as layers and folds that are unrelated to deformational fabrics. Although compositional layering is a normal occurrence in mylonites, variations inherited from flow structures occur as patterns in the abundance of a given mineral in the otherwise ultra-fine-grained, polymineralic matrix as described above (e.g. White, 1996). These larger-scale patterns in mineral distribution may be preserved even with recrystallization and deformation. For example, the layers and folds preserved within the mica-rich matrix of the deformed pseudotachylyte of the schist unit are defined by the relative abundance of biotite versus muscovite (or chlorite). In some cases, even fold closures are preserved in the distribution pattern of certain phases (e.g. Figure 2.6 d,e).

6. Lack of quartz ribbons and the disruption of large-scale layering- In all rock types in this study, the host rock contains some degree of large-scale (>100mm) layering, resulting from

elongate quartz veins or from long layers containing mineral fragments from the reaction/recrystallization of porphyroclasts. In their paper documenting a mylonite/ultramylonite transition in a shear zone from northwest Argentina, Hippertt and Hongn (1998) showed that layering defined by progressively folded and attenuated quartz veins is maintained even through to the ultramylonite stages. Prominent quartz veins and other types of larger-scale layering are relatively absent in the pseudotachylyte matrix (Passchier and Trouw, 2005), even with inherited flow banding. As a pseudotachylyte vein deforms, however, elongated rock fragments or recrystallized monomineralic clasts can still give the appearance of large-scale layering.

7. Types of monomineralic clasts- During comminution and frictional melting, minerals with the lowest melting temperature melt first as well as those minerals that fracture into the smallest size fraction (e.g. micas, pyroxene, and amphiboles). This leaves rounded monomineralic clasts that are generally limited to only a few mineral types, particularly quartz and feldspar, so a pseudotachylyte vein should be dominated by those minerals (Passchier and Trouw, 2005; Sibson, 1975). The presence of other minerals should be rare, although they may still be preserved in a rock fragment or pod of cataclasite that is incorporated into the matrix during deformation. Therefore, it is important to consider both the abundance of rounded feldspar and quartz clasts, for example, and the relative absence of mica and hornblende.

8. Differences between the matrix and host rock mineral assemblages- The differences between the recrystallized mineral assemblage of the deformed pseudotachylyte matrix and the host rock assemblage can include a change in mineral types, a variation in the modal amounts of the minerals, or just a change in mineral chemistry (see Section 2.3.1). Although the matrix assemblage is commonly nearly identical to the host rock assemblage, in some cases, it may be different enough to be useful as an identifying feature. For example, in the calc-silicate granofels unit, the recrystallized pseudotachylyte has a distinctly different mineral assemblage from the host rock. The host rock contains an assemblage of amphibole + plagioclase + quartz + titanite with isolated pegmatitic layers of K-feldspar + quartz \pm rare biotite (Figure 2.4). Amphibole is

deformed and recrystallized to epidote \pm chlorite in the host rock. The mixing of the chemical constituents of K-feldspar, titanite, and amphibole during melting leads to a new matrix assemblage of biotite + plagioclase (amphibole, titanite, and K-feldspar occur only as remnant clasts). Because biotite is abundant only in the pseudotachylyte matrix assemblage of the calc-silicate granofels unit, the presence of biotite can be used to help identify deformed pseudotachylyte veins in those rocks. It is important to carefully document the differences individually for each rock type and to determine on a case-by-case basis if the difference between the vein matrix assemblage and the host rock assemblage is distinctive enough to be useful; a common change (e.g. an increase in modal mica) that occurs in one rock type may not occur in another.

9. Size-frequency distribution of clasts- The processes of comminution and frictional melting during pseudotachylyte formation leaves rounded clasts that may display a modified power-law relationship in a clast size-frequency diagram (Sibson, 1975; Lin, 2008a). In theory, the process of comminution creates a fractal grain size distribution that is then modified during melting (Ray, 1999, 2004; Sammis et al., 1986). During melting, dynamic and in-situ, the smallest size fraction is lost, and the volume of the remaining clasts is decreased by melting along the rims. Despite this, the fractal grain size distribution pattern should still be preserved above a certain size fraction for monomineralic clasts within a pseudotachylyte vein (Ray, 1999, 2004). Our observations suggest that this pattern may also persist within mildly deformed pseudotachylyte veins, even with additional modification during recrystallization and limited deformation (Figure 2.9). Conversely, porphyroclast size within viscously-produced mylonites and ultramylonites may stabilize at a minimum critical grain size (depending on the mineral type, orientation distribution, conditions of viscous flow, and grain size reduction mechanism) producing a population of clasts that are relatively similar to each other in size rather than display a fractal grain size distribution (Michibayashi, 1996; Olesen, 2008; Tsutsumi, 1999).

10. Degree of clast recrystallization- During comminution, quartz veins and ribbons are fractured and rounded to create monomineralic quartz clasts. Over time, with deformation, these veins will recrystallize to form sigma-clasts and ribbons. At intermediate stages, quartz may persist as moderate- to large-sized, isolated, relatively undeformed clasts. Under the conditions of deformation within the Sandhill Corner shear zone, all quartz should be thoroughly recrystallized, so the presence of undeformed or only mildly deformed rounded quartz clasts in an ultramylonite layer may indicate a deformed pseudotachylyte vein (e.g. Figure 2.6f).

Samples with clear cross-cutting relationships from the Sandhill Corner shear zone were used to select a diagnostic set of characteristic features to identify deformed pseudotachylyte in each rock type. Deformed pseudotachylyte in the quartzofeldspathic mylonites is best identified by sharp layer boundaries, an ultra-fine-grained polymineralic matrix, the presence of Fe-Ti oxides, undeformed or only mildly deformed quartz clasts, and, in some cases, a fractal grain size distribution and the presence of mylonitic fragments. Deformed pseudotachylyte in the schist unit is best identified by an ultra-fine-grained polymineralic matrix, a relative lack of garnet, a lack of thick quartz veins, and a pattern of mineral distribution inherited from flow structures. Deformed pseudotachylyte of the calc-silicate granofels unit is best identified by the presence of ubiquitous biotite, a fractal grain size distribution, the presence of rock fragments, and an ultra-fine-grained polymineralic matrix. Using these identifying characteristic features, a majority of the ultramylonite/phyllonite layers within rocks of the Sandhill Corner shear zone are suspected of having a pseudotachylyte origin (see Section 2.7.3). The 1-2m wide layer of dark phyllonite at the core of the shear zone contains multiple generations of thick veins of schist-hosted pseudotachylyte, and the mesoscopic banded appearance of the quartzofeldspathic mylonites (dark grey to black layers) and the sheared calc-silicate unit (dark brown layers) described in Section 2.4 are the result of multiple generations of deformed pseudotachylyte in the host rock.

2.7.3. Implications for the Global Abundance of Deformed Pseudotachylyte

The identification of a significant volume of ultramylonite layers as deformed pseudotachylyte in the Sandhill Corner shear zone indicates that deformed pseudotachylyte may be more prevalent than previously thought in faults at the base of the seismogenic zone. Using percent area calculated from polished thin sections as a proxy for percent volume (see Section 2.5), we estimate that between ~5% and 50% (mean ~30%) of the rock volume of the quartzofeldspathic mylonites and sheared calc-silicate granofels unit is deformed pseudotachylyte (Figure 2.10). The shear zone core is defined by a (~1-5m wide) zone of an ultra-fine-grained,

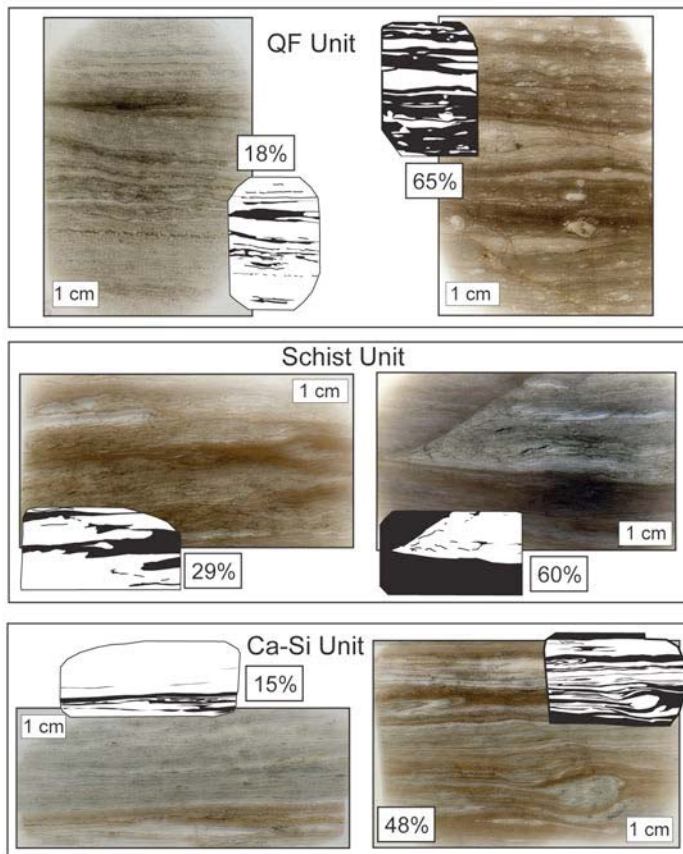


Figure 2.10. Examples of deformed pseudotachylyte distribution at the thin section scale in rocks from the Sandhill Corner shear zone. Deformed pseudotachylyte is black on the insets.

largely pseudotachylyte-derived ultramylonite/phyllonite rock where the volume of deformed pseudotachylyte is locally >50%. Given the evidence for overprinting generations of pseudotachylyte, the total volume of frictionally-generated melt formed over the lifetime of the

shear zone (including remelting of existing pseudotachylyte veins) was probably higher than even these estimates.

Sibson and Toy (2006) state that the frequency-magnitude relationship for earthquakes suggests that pseudotachylyte should be widespread in crust exhumed from seismogenic depths even though field studies indicate that fault-hosted pseudotachylyte is comparatively rare and only occurs in special circumstances. They state that over ten million years, a seismically active plate-bounding fault should experience 10^5 M8 earthquakes, 10^6 M7 earthquakes, and 10^7 M6 earthquakes, all of which have the potential to create pseudotachylyte. Using the Alpine fault in New Zealand as an example, Sibson and Toy (2006) calculate an expected pseudotachylyte thickness of 1km (assuming no reshear), but much less has actually been observed. As a result, they suggest (a) that slip was localized along the same surface with reshear and remelting of the same material or (b) that pseudotachylyte was not a common product of seismic slip in the Alpine fault zone. They propose that the apparent scarcity of pseudotachylyte either results from a lack of preservation or that dynamic mechanisms, such as thermal overpressuring, lowered frictional resistance during slip.

It is commonly accepted that pseudotachylyte occurs preferentially in intact crystalline rock lacking an intergranular pore fluid (Sibson and Toy, 2006). However, pseudotachylyte occurs in rocks that do not fit this description (e.g. Bjørnerud, 2010). In the Sandhill Corner shear zone, all of the rock types contain pseudotachylyte, with the largest veins found in the pelitic schist unit. In addition, there is evidence that some fluid was present during the seismic cycle, including mineralized fractures spatially associated with pseudotachylyte that likely formed during coseismic slip, and shattered and mineralized feldspar, tourmaline, and garnet porphyroclasts similar to the shattered garnet microstructure attributed to coseismic loading by Trepmann and Stöckert (2002). The quartz filling these fractures was viscously deformed and refractured multiple times in a style consistent with deformation in the seismic cycle. Furthermore, fluid-filled vesicles and amygdules have yet to be identified in the pseudotachylyte

from the Sandhill Corner shear zone, suggesting that an interconnected fluid phase and thus fluid overpressuring during slip was unlikely in these rocks (Bjørnerud, 2010; Rice, 2006; Segall and Rice, 1995).

Assuming that pseudotachylyte generation occurs and is common in many different rock types, then the apparent scarcity of pseudotachylyte may be a result of the lack of preservation and/or identification of pseudotachylyte (Sibson and Toy, 2006); our study supports this explanation. Evidence from the Sandhill Corner shear zone suggests that younger pseudotachylyte veins preferentially overprint older generations, lending credence to the possibility of significant overprint and reshear within a zone of limited thickness. In addition, only the freshest pseudotachylyte veins are identified in the field (DiToro et al., 2006, 2009; Kirkpatrick et al., 2009; Lin 2008a). Additional detailed microstructural studies may be required to identify the older, deformed pseudotachylyte. Without such an analysis and in the absence of clear cross-cutting relationships, much of the pseudotachylyte that has been deformed into ultramylonite may remain unrecognized as such.

2.7.4. Deformation Mechanisms and Rheology of a Deformed Pseudotachylyte Vein

Pseudotachylyte-derived ultramylonite layers are described in the literature as weak zones into which strain localizes (Guermani and Pennacchioni, 1998; Passchier, 1982; White, 1996). Passchier (1982) describes large strains in deformed pseudotachylyte relative to the host rock and the presence of undeformed pseudotachylyte matrix protected in embayments within the host rock. Such weakening can result from the changes that occurred to the rock as the pseudotachylyte formed and recrystallized, including: (1) a decrease in grain size through frictional slip and recrystallization of the quenched glass leading to grain-size sensitive diffusion creep and grain boundary sliding (e.g. De Bresser et al., 2001; White et al., 1980); (2) a change in the mineral assemblage to a greater modal abundance of weaker phases (e.g. Shea and Kronenburg, 1992, 1993; Wintsch et al., 1995); and (3) a change in the microstructure to an

increasingly interconnected network of weak phases that serves as a stress-supporting matrix (e.g. Handy, 1990, 1994; Handy et al., 1999; Holyoke and Tullis, 2006; Johnson et al., 2004, 2008; Marsh et al., 2009). In the deformed pseudotachylyte veins from the Sandhill Corner shear zone, the monomineralic clasts are markedly reduced in size (typically 200 μ m or less) relative to the host rock grains, and recrystallized matrix grains coarsen and stabilize at a size up to a few tens of microns, similar to the stable grain size reported by White (1996). An increase in modal mica results from the hydration of K-feldspar to muscovite and the growth of biotite directly from the quenched glass in the deformed pseudotachylyte of the quartzofeldspathic and calc-silicate granofels units (and perhaps the schist unit). Finally, the fine-grained layers, quartz ribbons, and porphyroclast-rich layers are heterogeneously layered within the host rock whereas the deformed pseudotachylyte consists of a homogeneous, polymineralic, stress-supporting matrix surrounding remnant clasts.

Microstructural observations can be used to interpret which deformation mechanisms were operating in a deformed pseudotachylyte vein and thus better understand the rheology of the weak, fine-grained, mica-rich, recrystallized matrix. The larger quartz porphyroclasts ($\geq 100\mu$ m) within deformed pseudotachylyte veins show evidence for dislocation creep in the form of undulose extinction (Figure 2.6f), the development of subgrains, and quartz c-axis pole figures with a cross girdle CPO (Figure 2.8a). Smaller quartz grains ($< 100\mu$ m) are typically polygonal and do not have a clear quartz c-axis CPO, suggesting that grain-size-sensitive processes are active in the recrystallized matrix (Figure 2.8c). Passchier (1982) and White (1996, 2004) also report observations from deformed pseudotachylyte of the Saint-Barthélemy Massif, French Pyrenees and the Outer Hebrides Thrust, Scotland that show that both dislocation creep (high dislocation densities and a dislocation creep recrystallization microstructure in the quartz clasts) and grain-size-sensitive processes (low, heterogeneously distributed dislocation densities in quartz matrix grains) were operating simultaneously in quartz within the deformed

pseudotachylyte veins, with grain-size-sensitive processes dominant in the stress-supporting recrystallized matrix (Passchier, 1982; White, 1996, 2004).

Micas in the recrystallized matrix also show evidence for both dislocation creep and grain-size-sensitive processes. In areas of the deformed pseudotachylyte matrix where quartz and feldspar are polygonal, aligned mica grains truncate at the edges of the other grains and do not thin perpendicular to the {001} slip plane. The polygonal shape of quartz and feldspar suggests that grain-size-sensitive processes were dominant in those minerals, and because the micas do not show evidence of basal slip or kinking, grain-size-sensitive creep may also have been dominant in mica (Hippertt, 1994; Kronenburg et al., 1990; Shea and Kronenburg, 1992, 1993). Locally, mica grains do show thinning, kinking, and bookshelf-style cleavage steps suggesting basal slip along {001} (Kronenburg et al., 1990). These micas connect around feldspar and quartz grains and smaller clasts causing them to thin and become elongate or to dissolve leaving just mica-dominated layers (Hippertt, 1994). Quartz grains present within the areas where mica has the highest degree of interconnectivity also exhibit the greatest degree of elongation, although it is not clear if these elongate quartz grains deformed via dislocation creep or dissolution-precipitation creep.

Given the modes of weakening listed above and the discussion of active deformation mechanisms, we propose that both grain-size-sensitive processes within the recrystallized pseudotachylyte matrix and, locally, intracrystalline slip in micas were operating to influence the interseismic bulk rheology of an individual deformed pseudotachylyte vein (Figure 2.11a). The larger clasts that deform by dislocation creep are matrix-supported and, owing to their relatively small modal abundance, would have a minor influence on the bulk rheology. The lack of CPO development in the matrix quartz grains and the polygonal quartz and feldspar matrix grain shapes suggest grain-size-sensitive creep operating throughout the vein matrix (Hippertt, 1994), which would weaken the rheology of the layer at steady-state, interseismic strain rates because it would flow at a comparatively lower differential stress than the coarser-grained host rock. In

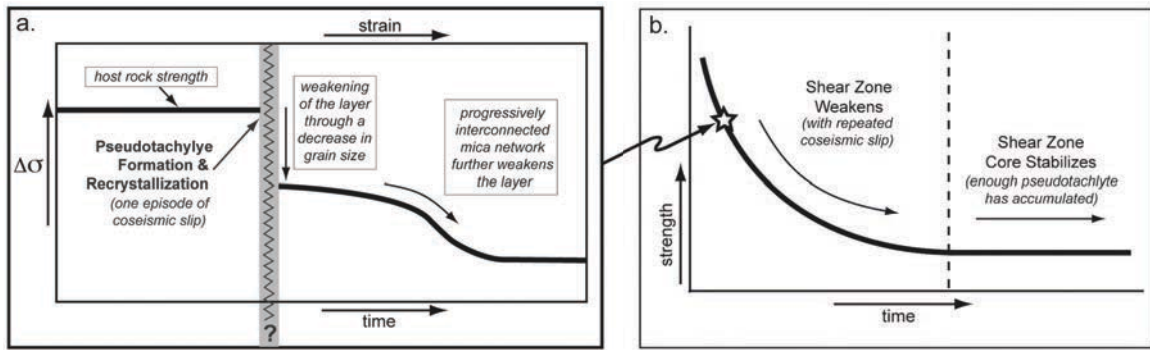


Figure 2.11. A conceptual model for weakening during (a) the formation and recrystallization of a single pseudotachylyte vein and (b) during the lifetime of the shear zone. (a) The formation and recrystallization of a pseudotachylyte vein causes a decrease in grain size from the host rock promoting grain-size-sensitive creep, and during deformation, micas may become interconnected to locally form a stress-supporting framework. (b) Over time, as multiple generations of pseudotachylyte preferentially form at or near the lithologic contact, the shear zone core progressively weakens. With enough deformed pseudotachylyte, the shear zone core remains continually weak stabilizing the shear zone core at the lithologic contact. The shaded region and question mark in (a) are meant to convey uncertainty in the amount of time required to crystallize a pseudotachylyte vein.

addition, the increase in modal mica would facilitate an interconnected mica network, provided that micas are optimally oriented for basal slip or become so through rotation and recrystallization (Handy, 1990, 1994; Handy et al., 1999). Locally, optimally-oriented mica grains do show evidence for localization via basal slip and interconnection, such as in particularly mica-rich layers and within shear bands. The change in the matrix texture to form a progressively interconnected mica network may further reduce the strength of the deformed pseudotachylyte layer with continued viscous shearing (e.g. Hippertt, 1994; Shea and Kronenburg 1992, 1993; Wintsch et al., 1995). Therefore, during the early stages of pseudotachylyte recrystallization and deformation, grain-size-sensitive creep in the stress-supporting vein matrix would control the rheology of the layer, but as the layer was sheared, micas optimally oriented for slip would create a progressively-developed mica network that would have markedly influenced the layer rheology only after interconnection had occurred (e.g. Bos and Spiers, 2002; Niemeijer and Spiers, 2005). The mechanisms of weakening during interseismic viscous shearing in deformed pseudotachylyte veins are most likely a composite of deformation mechanisms (both grain-size-sensitive creep and

slip in micas) that are dependent on time, strain, and the microstructure of the recrystallized matrix assemblage.

2.7.5. The Influence of Pseudotachylyte on the Strength and Evolution of the Sandhill Corner Shear Zone

The interaction between the frictional and viscous structures within the Sandhill Corner shear zone may have influenced the development and spatiotemporal persistence of the shear zone core. Fabric intensity increases in all rock types with proximity to the lithologic boundary suggesting that the contact between the two rheologically-contrasting units (i.e. schist and quartzofeldspathic units) was probably a guide for the initial localization of the high strain zone. The incidence of both fresh and deformed pseudotachylyte increases with proximity to the lithologic contact, and the thickest pseudotachylyte veins are located within <1m of the contact in the schist, suggesting that seismic rupture was also focused along the lithologic boundary. A deformed pseudotachylyte vein is weaker during viscous shear than the host rock as discussed in Section 2.7.4 (Figure 2.11a). Many generations of pseudotachylyte formation, recrystallization, and deformation at or near the lithologic contact over time would create a weak shear zone core. The presence of an ultra-fine-grained, largely pseudotachylyte-derived ultramylonite (<5m wide) and phyllonite layer (~1-2m wide) at the contact supports this conclusion.

The controls over whether a fault slips seismically or creeps aseismically on a weak fault core within the FVT are not well understood, especially given the complex and spatially variable dynamics at this depth level during the seismic cycle. Evidence for overprinting generations of pseudotachylyte within the shear zone core show that seismic slip continued to create pseudotachylyte even though a weak core had developed. Experiments on muscovite and halite gouge by Niemeijer and Spiers (2005, 2006) suggest that a fine-grained, mica-rich fault rock, like those containing large volumes of deformed pseudotachylyte, would have a velocity weakening

effect at high strain rates. A mechanism such as this may facilitate unstable slip and new pseudotachylyte formation at the shear zone core.

Over time, multiple generations of pseudotachylyte that preferentially formed at or near the lithologic contact (a large volume as this study suggests) may have helped to stabilize a perpetually weak shear zone core along the lithologic contact (Figure 2.11b; Takagi et al., 2000; Tanaka et al., 2004; White, 2004). Such a stabilizing relationship within the shear zone core may be common on major strands of seismogenic fault systems at FVT depths.

2.8. Summary and Conclusions

- The Sandhill Corner shear zone is a northeast-trending, mylonitic shear zone that has been exhumed from FVT depths (~10-15kms) and that preserves evidence for mutually-overprinting pseudotachylyte and mylonite. In the study area, it follows the contact between a quartzofeldspathic unit and a pelitic schist unit; the lithologic contact represents the core of the shear zone.
- All of the rock types within the Sandhill Corner shear zone (a quartzofeldspathic unit, a schist unit, and a calc-silicate granofels unit) contain both undeformed and deformed pseudotachylyte, and all stages of the transformation from pseudotachylyte to ultramylonite/phyllonite are preserved. These include: (1) primary pseudotachylyte structures, (2) initial mineral crystallization, (3) grain coarsening and reactions, and (4) viscous deformation.
- Pseudotachylyte-derived ultramylonite and phyllonite layers may be identified using a combination of the following features: (1) cross-cutting relationships; (2) sharp layer boundaries; (3) the presence of host rock fragments; (4) an ultra-fine-grained, polymineralic matrix; (5) inherited compositional variations from flow structures; (6) a lack of quartz ribbons and the disruption of large-scale layering; (7) the types of monomineralic clasts; (8) differences between the matrix and host rock mineral assemblages; (9) the size-frequency

distribution of clasts; and (10) the degree of clast recrystallization. Using a combination of these diagnostic features, we estimate that between ~5% and 50% of the rock volume in the Sandhill Corner shear zone (mean ~30%, locally >50% near the shear zone core) is deformed pseudotachylyte, suggesting that deformed pseudotachylyte may be more prevalent than previously thought in faults exhumed from the base of the seismogenic zone. In light of the evidence presented in this study, a detailed re-evaluation of ultramylonite and phyllonite layers in exhumed seismogenic faults zones may reveal evidence for a greater volume of pseudotachylyte at other localities around the world.

- Textural and mineralogical changes that occur during the formation, recrystallization, and deformation of large volumes of pseudotachylyte over time can weaken the rock by decreasing the grain size, changing the mineral assemblage, and changing the microstructure. Both grain-size-sensitive processes and intracrystalline slip within micas allow a deformed pseudotachylyte vein to be weaker than the host rock. The addition of multiple generations of weak layers of deformed pseudotachylyte preferentially forming over time at or near the lithologic contact may have played an important role in the persistence of the shear zone core.

Chapter 3

COMPLEX QUARTZ RECRYSTALLIZATION FABRICS FROM SHEARED QUARTZ RIBBONS WITH A STRONG PRE-EXISTING CRYSTALLOGRAPHIC PREFERRED ORIENTATION*

3.1. Chapter Abstract

Quartz microstructures and mineral orientation data are valuable tools for quantifying the conditions of deformation. As we better understand the dynamic and evolving nature of large crustal shear zones, it has become apparent that the development of quartz fabrics are strain path dependent. Furthermore, it is poorly understood how a pre-existing fabric affects this time dependent evolution. Using a large suite of quartz ribbon samples collected from across the Sandhill Corner shear zone (a strand of the Paleozoic, seismogenic, dextral strike-slip Norumbega fault system in south-central Maine, USA), we document complexities within the quartz microstructural record and crystallographic preferred orientation (CPO) data that reflect weakening associated with a strong, pre-existing CPO as well as the diverging recrystallization paths between samples from different parts of the shear zone.

Three grain types are observed in the quartz ribbons of the Sandhill Corner shear zone, (1) low aspect ratio, amoeboid grains inherited from the host rock; (2) high aspect ratio grains that represent stretched versions of the host rock grains and that formed at high strains via grain boundary migration recrystallization; and (3) smaller, more quant grains that replace the other two grain types via a combination of grain boundary migration and subgrain rotation recrystallization. Their spatial distribution indicates a general trend of localization at higher temperatures followed by continued dextral shearing, and perhaps further localization, at lower temperatures.

** The content of this chapter will be submitted for publication in August as: Price et al.*

The host rock of the Sandhill Corner shear zone contains asymmetrically folded quartz ribbons that display a strong pre-existing CPO that occurs as a c-axis maximum in one quadrant of the pole figure in the shear reference frame. Passive rotation of these ribbons places the c-axis maximum in an orientation coincident with rhomb $\langle a \rangle$ slip, a presumably “soft” orientation under the conditions of deformation. In samples closest to the shear zone core, this leads to a poorly-developed CPO, even under high strains, and a core-mantle or layered microstructure where the dominant deformation mechanism differs between grain orientation domains. In other samples closer to the edge of the shear zone, mechanical twinning may have been more prevalent, facilitating the formation of cross-girdle CPO patterns by promoting the activity of multiple slip systems. Therefore, although an inherited fabric does affect the development of the new fabric, creating a top-bottom asymmetry in the c-axis pole figure, the style and degree of the influence is dependent on the mechanisms operating within the evolving fabric and the conditions of deformation.

The quartz ribbons of the Sandhill Corner shear zone also preserve evidence that may reflect changing deformation conditions with the seismic cycle. Rare atypical microstructures that display patchy extinction patterns and heterogeneous distribution of subgrains represent the best evidence for rapidly decaying strain rates. The prevalent twinning as described above and large amoeboid-shaped grains with an overprint resulting from bulging with subgrain rotation recrystallization at the edge of the shear zone may be a result of transiently-elevated stresses/strain rates.

3.2. Introduction

Quartz deformation experiments and studies of naturally sheared rocks (e.g. Heilbronner and Tullis 2002, 2006a,b; Hirth and Tullis, 1992; Law et al., 1990; Lloyd and Freeman, 1994; Lloyd et al., 1992; Schmid and Casey, 1986; Stipp and Kunze, 2008; Stipp et al., 2002a,b; Toy et al., 2008; Tullis et al., 1973; van Daalen et al., 1999) have over the decades contributed

significantly to our understanding of non-coaxial quartz deformation. Grain boundary migration (fast and slow) and subgrain rotation recrystallization mechanisms combine to create three broad groups of recrystallization quartz microstructures that change dominance with temperature and/or strain rate: bulging, subgrain rotation, and grain boundary migration (Hirth and Tullis, 1992; Stipp et al., 2002a,b). These microstructures have been used to interpret the conditions of deformation within shear zones, including the temperature and coaxiality of strain. Furthermore, single crystal experiments (e.g. Hobbs, 1968) and careful microstructural analysis of naturally deformed samples (e.g. Law et al., 1990; Lister and Dornsiepen, 1982; Lloyd et al., 1992; Schmid and Casey, 1986) have shown a temperature-dependence on the dominant slip system active within a dynamically recrystallizing quartz crystal: basal $\langle a \rangle$, rhomb $\langle a \rangle$, prism $\langle a \rangle$, and prism $\langle c \rangle$. By connecting quartz microstructures with crystallographic preferred orientation (CPO) data, general trends have identified pole figure pattern types expected for a given microstructure (Law, 1990). For these reasons and others, quartz microstructures and mineral orientation data are valuable tools for quantifying the conditions of deformation.

As we better understand the dynamic and evolving nature of large crustal faults and shear zones, it has become increasingly apparent that the development of quartz microstructures and CPO patterns are strain path dependent. Quartz deformation experiments by Heilbronner and Tullis (2006b) show that the quartz microstructure, CPO, and rheology evolve with strain as the parent grains are completely recrystallized and as grains with “hard” orientations are replaced with grains of “soft” or “weak” orientations (Takeshita et al., 1999). Heilbronner and Tullis suggest that high strains and complete recrystallization are required for the achievement of microstructural and mechanical steady state. Interpretation of natural quartz data is complicated by this strain-dependent evolution, particularly given the difficulty in identifying whether or not a sample has been fully recrystallized.

Furthermore, it is poorly understood how other factors, such as a pre-existing fabric (i.e. a strong shape or crystallographic preferred orientation in the host rock), affects this time

dependent evolution. Many authors (e.g. Heilbronner and Tullis, 2006b; Halfpenny et al., 2006; Menegon et al., 2008; Stipp and Kunze, 2008; Stipp et al., 2002a) have documented the inheritance of the parent grain CPO in the recrystallized grains of a core-mantle microstructure, with the CPO of the daughter grains reflecting a more diffuse version of the parent CPO pattern. If a large proportion of parent grains are already in “soft” or “hard” orientations, will that facilitate or hinder the development of the new fabric and/or affect the mechanical evolution of the system? The study of Toy et al. (2008) on quartz fabrics from the Alpine Fault suggests that an inherited fabric does have an effect on the development of the new fabric. They propose that the development of a well-developed CPO at higher crustal levels, and thus strain localization with uplift, may have been dependent on the development of a weaker, pre-existing CPO at depth. The quartz microstructural record and CPO data from a strand of the Norumbega fault system in south-central Maine, USA presented in this study also indicates that a strong, pre-existing CPO can have a weakening effect but that the influence of the pre-existing fabric on the development of the new fabric may be strain path dependent.

The Norumbega fault system of northeastern New England was a long-lived, orogen-parallel, subvertical, seismogenic, Paleozoic, dextral strike-slip fault system characterized by focused mylonitic shear zones and is an ancient analogue to the San Andreas fault system. One of the fault strands, the Sandhill Corner shear zone, has been exhumed from frictional-to-viscous transition depths and preserves excellent evidence for mutually-overprinting pseudotachylite and mylonite (c.f. Handy et al., 2007). The host rock contains asymmetrically-folded quartz ribbons that display an axial planar shape preferred orientation (SPO) and a strong pre-existing CPO that occurs as a c-axis maximum in one quadrant of the pole figure in the shear reference frame. In many samples, passive rotation of these ribbons places the c-axis maximum in an orientation coincident with rhomb $\langle a \rangle$ slip, a presumably “soft” orientation for the conditions of deformation (~450°C). However, in only some samples does this seem have an effect, leading to a poorly-developed CPO and a core-mantle or layered microstructure where the dominant deformation

mechanism differs between grain orientation domains. In other samples, Dauphiné twinning may have been more prevalent, promoting the activity of other slip systems in addition to rhomb $\langle a \rangle$ slip and facilitating the formation of better-developed cross-girdle CPO patterns. Based on the data presented in this chapter, we propose that the recrystallization path controlled the weakening effect of the inherited CPO. Therefore, careful investigation of the microstructural evolution of quartz fabrics may be necessary before using cross-girdle CPO patterns to interpret the mechanical evolution of a shear zone.

3.3. Interpreting Non-Coaxial Quartz Deformation Fabrics

3.3.1. Optical Microstructures.

Early deformational and observational studies of quartz deformation mechanisms lead to the development of three regimes of distinctive dislocation creep recrystallization microstructures from experimental observations by Hirth and Tullis (1992). These regimes, as determined by the mechanical behavior of the samples, corresponded in the experimental setting to dominant slow grain boundary migration (Regime 1), subgrain rotation (Regime 2), and subgrain rotation with fast grain boundary migration (Regime 3). The change from one regime to next is associated with an increase in temperature and/or a decrease in strain rate (as controlled by the rates of grain boundary migration, dislocation climb, and dislocation production) and is influenced by the water content (Stipp et al., 2006).

The experiment-based regimes were compared to naturally-sheared samples collected from across a temperature gradient (Stipp et al., 2002a,b), providing a sequence of quartz microstructures that extended to higher temperatures than achievable in the laboratory. The natural microstructures are associated with the dominant recrystallization mechanisms in each temperature range: bulging (BLG), subgrain rotation (SGR), and grain boundary migration (GBM). These new groups do not directly correlate to the regimes of Hirth and Tullis (1992), with Regime 1 corresponding to the lower range of bulging (BLG1), Regime 2 to the upper part

of bulging into the subgrain rotation field (BLGII and SGR), and Regime 3 overlapping the boundary between the subgrain rotation and grain boundary migration fields (SGR and GBMI). The higher range of the GBM field observed in natural samples was not seen in the laboratory samples because of the onset of melting.

Initial identification of the dominant recrystallization mechanisms is commonly achieved through microstructural observation. BLG, which operates from ~280 up to 400°C for water present strain rates of 10^{-12} to 10^{-14} sec⁻¹ (based on Figure 3.7 of Stipp et al., 2002b), exhibits a core-mantle microstructure where parent grains (also referred to as porphyroclasts) with high dislocation densities and patchy, irregular undulatory extinction are surrounded by smaller, relatively dislocation-poor, new recrystallized grains (Hirth and Tullis, 1992; Stipp and Kunze, 2008; Stipp et al., 2002a,b). The parent grains may be stretched parallel to the shear foliation, and their edges have a serrated appearance. Experiments by Hirth and Tullis (1992) showed that the starting size of the parent grains may have an effect on the degree of recrystallization when BLG mechanisms operate. The orientation of new grains formed through BLG is controlled by the orientation of the lower energy neighboring grains. Triple junctions, twin boundaries, lamellae boundaries, pre-existing fractures, and parent grains with an orientation at a high angle to the foliation are preferred sites of BLG (Hobbs, 1968; Lloyd and Freeman, 1994; Stipp and Kunze, 2008; Stipp et al., 2002a,b; White 1976).

SGR, which operates from ~350 up to 500°C for water present strain rates of 10^{-12} to 10^{-14} sec⁻¹, is also associated with a core-mantle texture, but the parent grains will have the same dislocation density as the new grains and will exhibit a polygonal extinction pattern associated with the development of subgrains (e.g. Hobbs, 1968; Hirth and Tullis, 1992; Stipp et al., 2002a,b). The size of the new grains is the same as that of the subgrains. Like with BLG, subgrains and new grains form along fractures and lamellae boundaries, but in contrast, the orientation of the new grains is controlled by the orientation of the parent grain. Parent grains can also have a stretched appearance, commonly with very high aspect ratios, and are referred to as

ribbon grains. At higher strains, parent grains are completely replaced by subgrains and new grains. The polygonalized parent grains may result in layered orientation domains, which are clusters of new grains with related orientations (Pauli et al., 1996).

GBM operates above a temperature range of ~400-500°C for water present strain rates of 10^{-12} to 10^{-14} sec⁻¹ (Hirth and Tullis, 1992; Stipp et al., 2002a,b). As fast grain boundary migration begins at the upper range of SGR (Regime 3), new grains become irregular in shape with weakly lobate grain boundaries and are larger than the subgrain size. These irregular, elongate grains commonly form a shape-preferred orientation at an angle to the shear foliation. Within the range of GBM beyond the transition zone, recrystallized grains are large and are characterized by lobate grain boundaries, island grains, and very irregular grain shapes. The presence of a secondary phase, such as mica, can cause grain boundaries to be pinned, leading to a smaller recrystallized grain size and straightened grain boundaries. A checkerboard extinction pattern is present in quartz grains at the highest deformation temperatures.

3.3.2. CPO Patterns and Fabric Evolution.

Through the movement of dislocations along easy slip planes, the orientation of grains within deformed quartz ribbons and sheared quartzite line up to create a crystallographic preferred orientation (Hobbs, 1968; Law, 1990; Law et al., 1990; Lister and Hobbs, 1980; Lister et al., 1978). The c-axis pole figure plots display cross-girdle patterns characteristic of non-coaxial deformation (Schmid and Casey, 1986). Although multiple slip systems are active within a deforming quartz grain, certain slip planes and directions have the lowest activation energy (largest Schmid factor for a given crystal orientation) and are dominant (Lloyd et al., 1992; 1997). These include slip on the basal, rhomb, and prism faces with slip in the <a> direction, the dominance of which may change with increasing temperature. Basal <a> slip is active across a range of temperatures forming a c-axis peak at the edge of the figure near the pole to the foliation (Z-axis), while rhomb <a> and prism <a> slip operate at lower stress with higher temperatures

plotting between the Y- and Z-axes and at the Y-axis, respectively (Schmid and Casey, 1986; Toy et al., 2008). Prism $\langle c \rangle$ slip also occurs in conjunction with prism $\langle a \rangle$ slip at high temperatures ($>550/600^{\circ}\text{C}$), plots near the X-axis, and may be related to the checkerboard extinction pattern in higher temperature microstructures (Lister and Dornsiepen, 1982).

The connection between CPO patterns and quartz microstructures is complicated by the persistence of the host rock CPO (or orientation of the recrystallized parent grains) in the CPO of the recrystallized grains (e.g. Heilbronner and Tullis, 2006b; Halfpenny et al., 2006; Menegon et al., 2008; Stipp and Kunze, 2008; Stipp et al., 2002a). As described above, recrystallized grains through SGR recrystallization produce orientation domains that are influenced by the orientation of the parent grain. This is reflected in a recrystallized grain CPO pattern that is similar to the parent grains, only more “smeared out” and/or with a spread reflecting the sense of shear. Whether inherited from the host rock or developed as the parent grains are stretched before recrystallization, many authors (e.g. Halfpenny et al., 2006; Heilbronner and Tullis, 2006b; Pauli et al., 1996; Stipp et al., 2002a) report that the parent grains have c-axis maxima around the Z-axis normal to the foliation. Only with increased strain do the recrystallized grains form the characteristic cross girdle pattern (Heilbronner and Tullis, 2006b). CPO patterns are also maintained with static recrystallization, or annealing, where the grain orientations of the pre-existing fabric may persist (Heilbronner and Tullis, 2006a); the alignment of grain boundaries parallel to stable crystallographic boundaries may explain this persistence (e.g. Kruhl and Peternell, 2002).

Quartz c-axis pole figure patterns also evolve as slip systems change dominance with recrystallization, suggesting that the amount of strain and evolution of the microstructure may play an important role in CPO development. In their study of recrystallization fabrics in Regime 3, Heilbronner and Tullis (2006b) report that the c-axis pole figure pattern changes from maxima at the periphery (Z-axis) to paired maxima along the cross girdle between the Y- and Z-axes and ultimately to a single peak at the center of the pole figure (Y-axis) with increasing strain

indicating a transitional sequence of slip system dominance from basal $\langle a \rangle$ to rhomb $\langle a \rangle$ to prism $\langle a \rangle$ slip. They find that this transitional sequence is associated with rotation of the fabric skeleton such that parent grains and recrystallized grain domains are in orientations more favorable for slip.

The progression from basal $\langle a \rangle$ to rhomb $\langle a \rangle$ to prism $\langle a \rangle$ slip has been described as a change in a “single crystal orientation” fabric as it evolves from one dominant slip system to another and has been attributed to geometric constraints (Law et al, 1990; Lloyd et al., 1992; Lloyd and Freeman, 1994). Strain initially localized in grains with “weak” orientations, or orientations that favored slip in systems with the lowest critical resolved shear stress. Basal $\langle a \rangle$ slip has the greatest Schmid factor consistent with the initial development of maxima at the periphery of the pole figure, both in the parent and daughter grains. Although rhomb $\langle a \rangle$ and prism $\langle a \rangle$ are both dominant at higher temperatures within the experimental Regime 3, Heilbronner and Tullis (2006b) suggest that during the CPO evolution the dominance of rhomb $\langle a \rangle$ slip may be transitional and that those related orientation domains may be “geometrically incompatible for extended slip” in favor of domains associated with orientations that favor prism $\langle a \rangle$ slip. As the cross-girdle pattern distinctive of non-coaxial deformation develops with higher strains, these grains or grain domains in unfavorable orientations for slip are either rotated or replaced through recrystallization by those in favorable orientations in volume and number, leaving a greater proportion of grains with favorable orientations for slip (Heilbronner and Tullis, 2006b; Kruhl and Peternell, 2002; Takeshita et al., 1999).

It is not clear if the progressive change in dominant slip systems with strain is also associated with a change in the dominant deformation mechanism, particularly for conditions under which deformation regimes overlap. For example, Lloyd and Freeman (1994) and Trimby et al. (1998) both describe a change from SGR-dominant to GBM-dominant deformation with strain. However, the progression in either CPO development or mechanisms evolution seen

under one set of conditions may not be typical of all shear conditions or be applicable to all host rock types (Heilbronner and Tullis, 2006b).

3.3.3. Crystallographic Misorientation Analysis.

Dynamic recrystallization mechanisms lead to non-random patterns in the misorientation between grains that can be used as a tool to interpret microstructural evolution of a quartz-rich rock, or quartz ribbons and veins (Wheeler et al., 2001). The differences in orientation between two grains can at the simplest be described by the magnitude of rotation and the angle of rotation, which by convention is the smallest angle of rotation with a maximum of 104.5° (Neumann, 2000). The nearest-neighbor misorientation, as plotted on a histogram, describes the angle of rotation between two adjacent grains, providing the misorientation across grain and subgrain boundaries, whereas the random-pair misorientation describes the misorientation profile of the entire population of grains. The differences between histograms plotting these two misorientation types can reflect interactions between neighboring grains and/or reflect orientation inheritance from a parent grain (Neumann, 2000). Coupled with inverse pole figures (IPF) plotting the axes of rotation, the nearest-neighbor misorientation angle can be used to determine whether or not a grain or subgrain boundary may have resulted from a single crystallographically-controlled rotation (plotting within the allowed regions of the figure) as well as, in some cases, the active slip system (Lloyd et al., 1997; Wheeler et al., 2001).

Misorientation analyses are particularly useful in identifying subgrain rotation recrystallization and crystallographic Dauphiné twinning mechanisms in quartz (Wheeler et al., 2001; Lloyd, 2004; Lloyd and Freeman, 1994; Neumann, 2000). Because subgrains form through accumulation of dislocations at tilt boundaries, the misorientation angle between (sub)grains and the parent grain is small, forming a large peak at low angles ($<15\text{-}20^\circ$) in the nearest-neighbor misorientation histogram. IPF plots of the misorientation axes for these low angle grain boundaries should also show clustering around the crystallographic axes associated with the

dominant slip system: clustering around the c-axis for prism $\langle a \rangle$ slip, the rhomb axis for rhomb $\langle a \rangle$ slip, and the m-axis for basal $\langle a \rangle$ slip (Neumann, 2000). Similarly, Dauphiné twins form through 60° rotations about the c-axis (as shown by a cluster of rotation axes around the c-axis on the inverse pole figure) that corresponds to a peak around 60° on the nearest-neighbor misorientation histogram (Lloyd, 2004). Such a prominent peak is consistent with twinning as an important mechanism for grain size reduction and grain boundary formation (Lloyd, 2004). The low-angle peak and the peak at 60° that are present in the nearest-neighbor plots should be absent in the random-pair plots (Wheeler et al., 2001).

Progressive recrystallization may modify misorientation data. Continued subgrain rotation recrystallization would continue to rotate new grains away from the parent grains widening the low angle peak in the nearest-neighbor misorientation histogram (Trimby et al., 1998); this can be shown in grain orientation maps where the misorientation angle increases from the center to the edge of a recrystallized grain (Stipp and Kunze, 2008). The 60° peak would also widen in the nearest-neighbor histograms as the adjacent twins recrystallized forming subgrains ($\pm 15^\circ$ for a range of $45\text{--}75^\circ$; Stipp and Kunze, 2008), but if the rotation axes are parallel to the c-axis, the shape may be asymmetrically skewed towards lower angle boundaries due to symmetry constraints (Lloyd, 2004). In addition, twinning creates positive and negative crystallographic forms that are not equivalent, with the resistance to slip lower on negative than on positive forms; this can be seen as an asymmetry around the m positions in IPF plots of misorientation rotation axes (Neumann, 2000; van Daalen et al., 1999). Boundaries with misorientation angles greater than 60° may form through subgrain rotation if multiple slip systems were active, but the regions of “allowed” misorientation axis orientations on IPF maps decreases with increasing misorientation angle (Wheeler et al., 2001). High angle boundaries have also been attributed to GBM recrystallization, the inheritance from host grain boundaries (e.g. Jiang et al., 2000), and the growth of new grains in fractures and microcracks (Hippertt and Egydio-Silva, 1996; Vernooij et al., 2006a,b).

More detailed interpretation of misorientation data in the context of mechanisms other than SGR is not as clear. BLG recrystallization is difficult to interpret using misorientation analysis because the process that detaches bulges may form low angle boundaries (i.e. subgrain rotation) or high angle boundaries (e.g. fracturing) (Stipp and Kunze, 2008). Grain boundary migration occurs above a threshold misorientation (Lloyd and Freeman, 1994; Trimby et al., 1998) and either increases or decreases the boundary misorientation angle depending on the sign of the dislocations that the boundary accumulates as it sweeps through a grain (Trimby et al., 1998). In addition to the formation of high angle boundaries, GBM recrystallization may lead to the loss of boundaries within certain angle ranges. Neumann (2000) identified a transition gap at $5\text{-}15^\circ$ in nearest-neighbor misorientation histograms that he attributed to the preferential removal of low angle boundaries by the migration of existing grain boundaries. Lloyd (2004) described a “saddle” of fewer boundaries with intermediate misorientation angles ($\sim 30^\circ$) that he suggested may also be a result of other recrystallization mechanisms, such as GBM. GBM may also disrupt the cluster of rotation axes in IPF maps that are formed by SGR.

Grain boundary sliding may also disrupt or modify boundary misorientations, although the effect is poorly understood. Large steps in misorientation rotation angle occur at the boundary between the parent and daughter grains in quartz sample that display the core-mantle microstructure (Trimby et al., 1998; Halfpenny et al., 2004, 2006). The daughter grains between parents of two different orientations are mixed (Halfpenny et al., 2006) and the misorientation axes of $20\text{-}30^\circ$ boundaries have weakened alignment in IPF plots, suggesting that grain boundary sliding may be altering the misorientations of the boundaries within these zones following subgrain rotation (Halfpenny et al., 2004, 2006; Rutter and Brodie, 2004). Weakened CPOs, weakened or randomized alignment of rotation axes in IPF plots, and near random misorientation rotation angle histogram patterns have all been associated with grain boundary sliding and/or grain size sensitive flow (Fliervoet, et al., 1997, 1999; Jiang et al., 2000; Law, 1990).

3.4. Field Observations

Quartz ribbons within the schist and quartzofeldspathic host rock are asymmetrically-folded. Within the study area, the folds plunge to the north and verge to the west (Fig. 3.1a,b). Associated with the folds is an axial planar foliation that has a dip of $\sim 50\text{-}60^\circ$ to the east and a strike that is $\sim 30\text{-}40^\circ$ from that of the shear foliation. The transition from the heterogeneously sheared schist to the highly-sheared schist is well-exposed in and around a blueberry field in the southern part of the field area. Here the folds are either (a) rotated into concordance with the shear foliation, flattened, and thinned (Fig. 3.1e); or (b) attenuated and imbricated (Fig. 3.1c,d), where the bottom, or western-most, limbs are typically thinned and the top, or eastern-most, limbs are stacked. Within the most highly sheared samples, the relationship between upper and lower fold limbs is typically lost (Fig. 3.1e,f), and the thinned quartz ribbons are further disrupted by shear banding and shear boudinage. The mylonite transition zone is not as well-exposed, but the quartz ribbons within the mylonite are also thinned (mm-scale) and rotated into concordance with the shear foliation.

3.5. Analytical Methods

Oriented thin sections and polished sections of quartz ribbons from the Sandhill Corner shear zone and host rocks were cut perpendicular to the subvertical shear foliation and parallel to the subhorizontal lineation, with the exception of the host rock fold samples that were cut perpendicular to the axial planar foliation and fold hinge line. Quartz ribbons described in this chapter were largely collected within the southern part of the field area, where the shear zone comprises only the quartzofeldspathic and schist units. The observations and data from these samples are consistent with observations and data from quartz ribbons collected elsewhere within the Sandhill Corner shear zone.

Quartz CPO and misorientation plots are based on quartz mineral orientation maps created using electron backscatter diffraction (EBSD) on polished sections of quartz ribbons

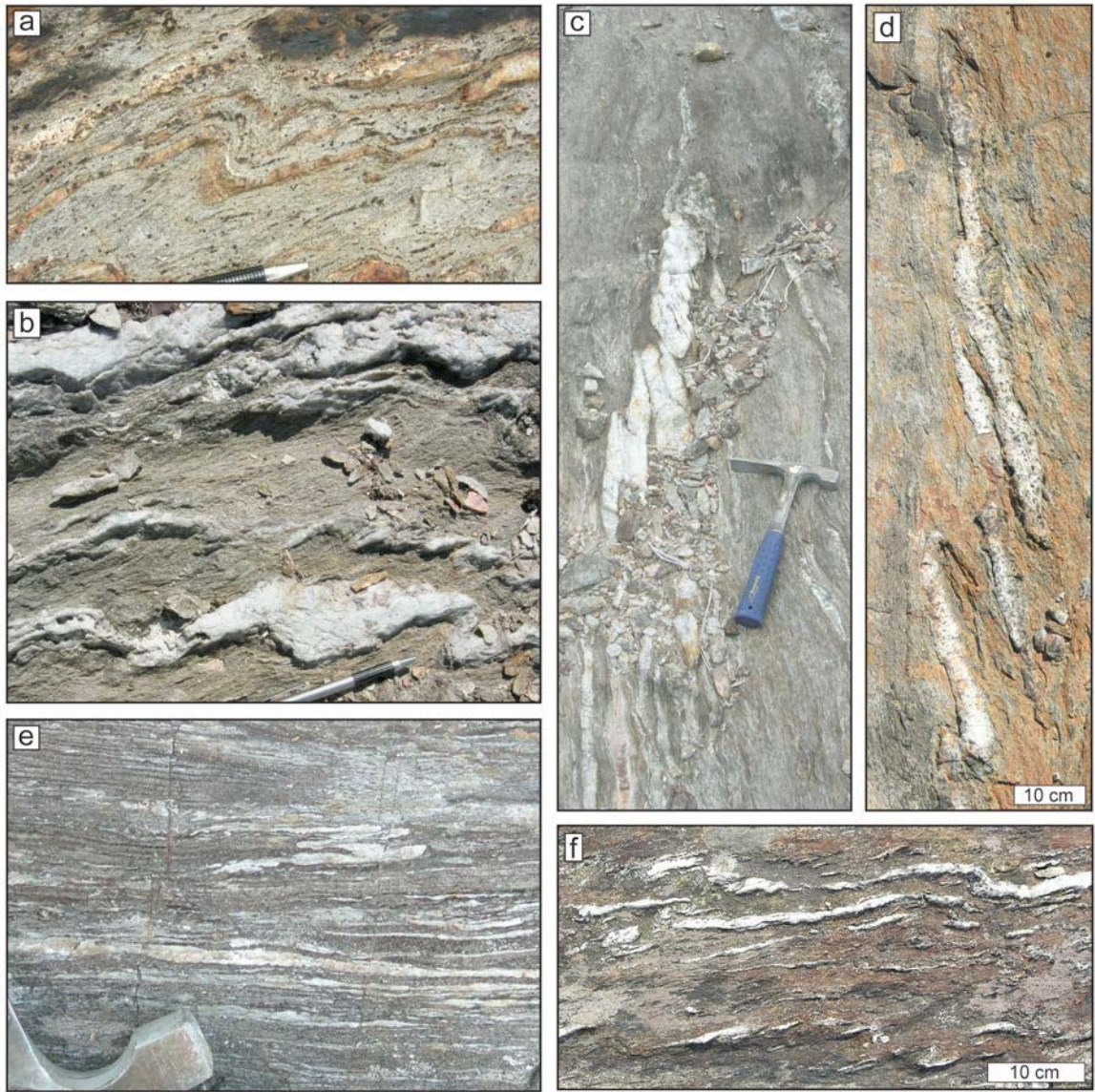


Figure 3.1. Field images of quartz ribbons within the schist host rock and sheared schist of the Sandhill Corner shear zone. (a, b) The host rock contains asymmetrically-folded quartz ribbons that are plunging to the north and verging to the west; an axial planar foliation is commonly associated with the folds. Within the shear zone, (c,d) fold limbs are attenuated and imbricated, and (e, f) quartz ribbons are rotated into the shear foliation and thinned. This deformation is achieved through both passive rotation and internal recrystallization. All images show near horizontal pavement outcrops; (a, b, e, f)-southeast at the top of the image; (c) northeast at the top; (d) southwest at the top.

(Nowell and Wright, 2004). Polished sections were mechanically polished to 0.3 μ m grit and chemically polished with a colloidal silica suspension. Electron dispersive spectroscopy (EDS) was coupled with EBSD to create mineral-specific orientation maps using the VEGA-XMU Scanning Electron Microscope at the University of Maine with TSL-OIM Data Collection and EDAX Genesis software. Operating parameters during EBSD data collection on uncoated samples oriented at a 70° tilt at high vacuum included an accelerating voltage of 20kV, a working distance of 25mm, and a probe current of 10nA. Data acquisition parameters for the EBSD were set in the TSL-OIM software at 2x2 binning, high gain, a binned pattern size of 160, a theta step size of 0.5°, 8 bands, and 11 reflector families for quartz. The step size for mineral orientation maps varied between 2 μ m and ~10 μ m depending on grain size of the sample.

Quartz EBSD data were cleaned and plotted with the TSL-OIM post-processing software. The data were filtered by both chemistry (i.e. quartz chemistry) and confidence index (CI limit of 0.1) and then cleaned to remove spurious points (neighbor CI correlation; minimum CI of 0.1). The confidence index is a parameter used by the processing software to determine pattern indexing accuracy based on a voting system in which each pattern solution is compared to the next best solution and then ranked. A higher CI should correspond to a better result, although in some cases the number of votes for the first two solutions can be exactly the same leading to a correctly indexed orientation but a CI of 0. To recover these points, the data were run through a cleanup routine that increases the CI of a point that has a low CI but the same orientation as a set number of points that surround it (neighbor orientation correlation; tolerance angle 5°, minimum CI of 0.1, clean up level 2). The grain identification parameters were set at a 10° misorientation, a minimum equivalent diameter of triple the step size, and a minimum CI of 0.1.

Quartz c-axis pole figures are equal area, lower hemisphere projections with linear contouring. They were plotted from cleaned mineral orientation maps using one average orientation per grain. For consistency given the subhorizontal lineation, all pole figures are

plotted with the northeast to the right side of the pole figure, unless stated otherwise. Mineral misorientation plots were limited to rotation angles between 5-104.5° following symmetry constraints and recommendations of Prior (1999). Where the quartz mineral orientation maps are used to show quartz grain types, the data were further cleaned to show one uniform orientation per grain and to remove Daulphiné twins.

3.6. Quartz Microstructures

Three quartz grain types dominate in the recrystallized quartz ribbons in rocks of the Sandhill Corner shear zone. These include (1) large, amoeboid, low aspect ratio grains; (2) large, elongate, high aspect ratio grains; and (3) small, commonly equant grains. These grain types are found independently within some ribbons as well as in combination within other ribbons. In this section and in Figures 3.2 and 3.3, we describe the observed quartz microstructures in terms of the grain types and where in the shear zone the microstructures are found. We also present atypical microstructures that do not fit one of the aforementioned types. An interpretation of the deformation mechanisms that may have formed these microstructures is presented in the discussion (Section 3.9.1).

3.6.1. Grain Type 1- Amoeboid, Low Aspect Ratio Grains

Asymmetrically folded quartz ribbons within the schist and quartzofeldspathic host rock display large (>100mm), irregularly-shaped grains with lobate grain boundaries, some local undulatory extinction, and smaller island grains (Figs. 3.2 and 3.3). Although the aspect ratio of the grains is relatively low, the grains form a shape preferred orientation that is axial planar to the asymmetric F3 folds and the local S3 crenulation cleavage fabrics.

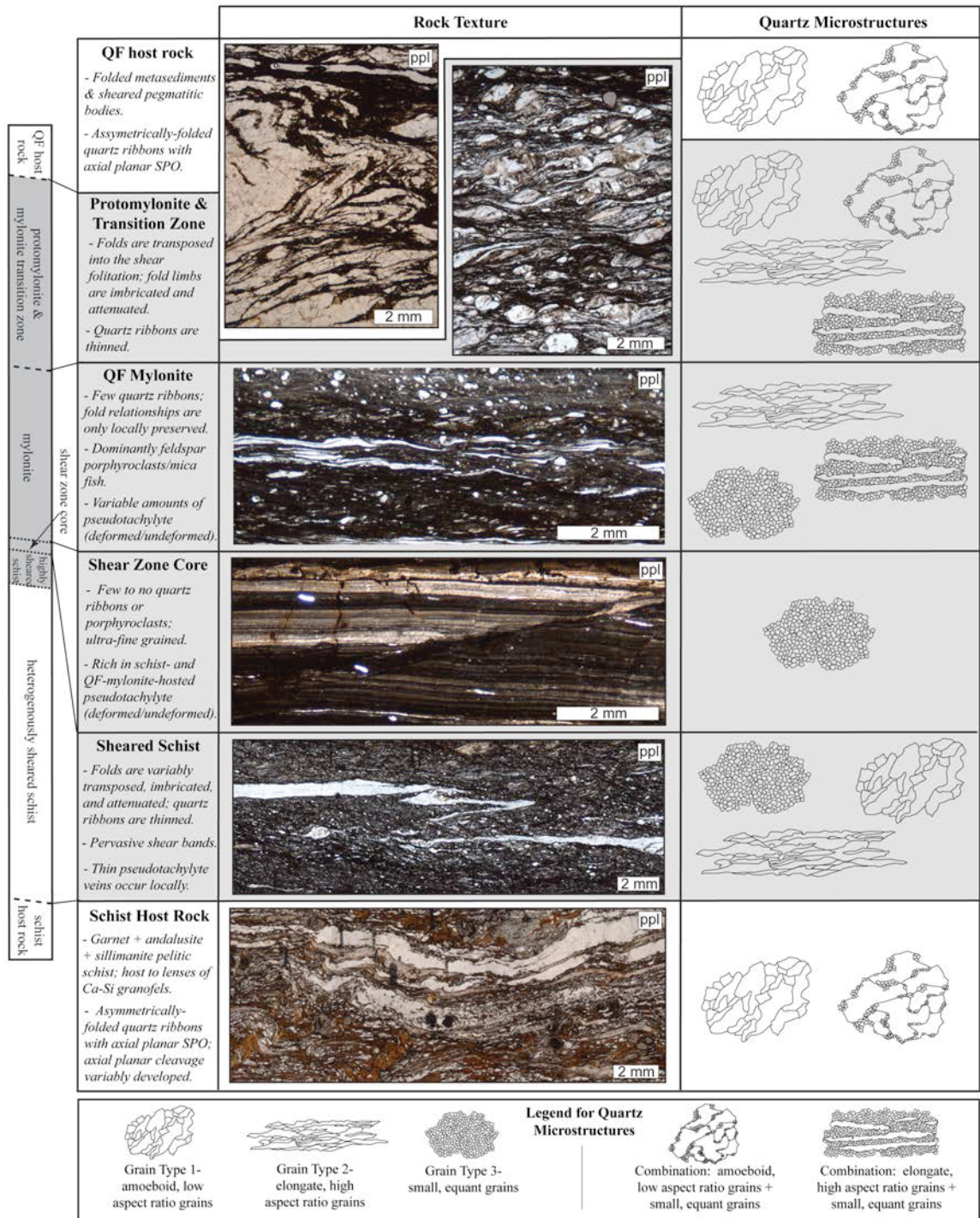


Figure 3.2. A chart showing the across strike variation in rock type and quartz microstructures from the Sandhill Corner shear zone within the southern part of the study area. The parts highlighted in grey represent the areas mapped as “shear zone” in Figure 1.9. All images are plane-polarized photomicrographs (ppl).

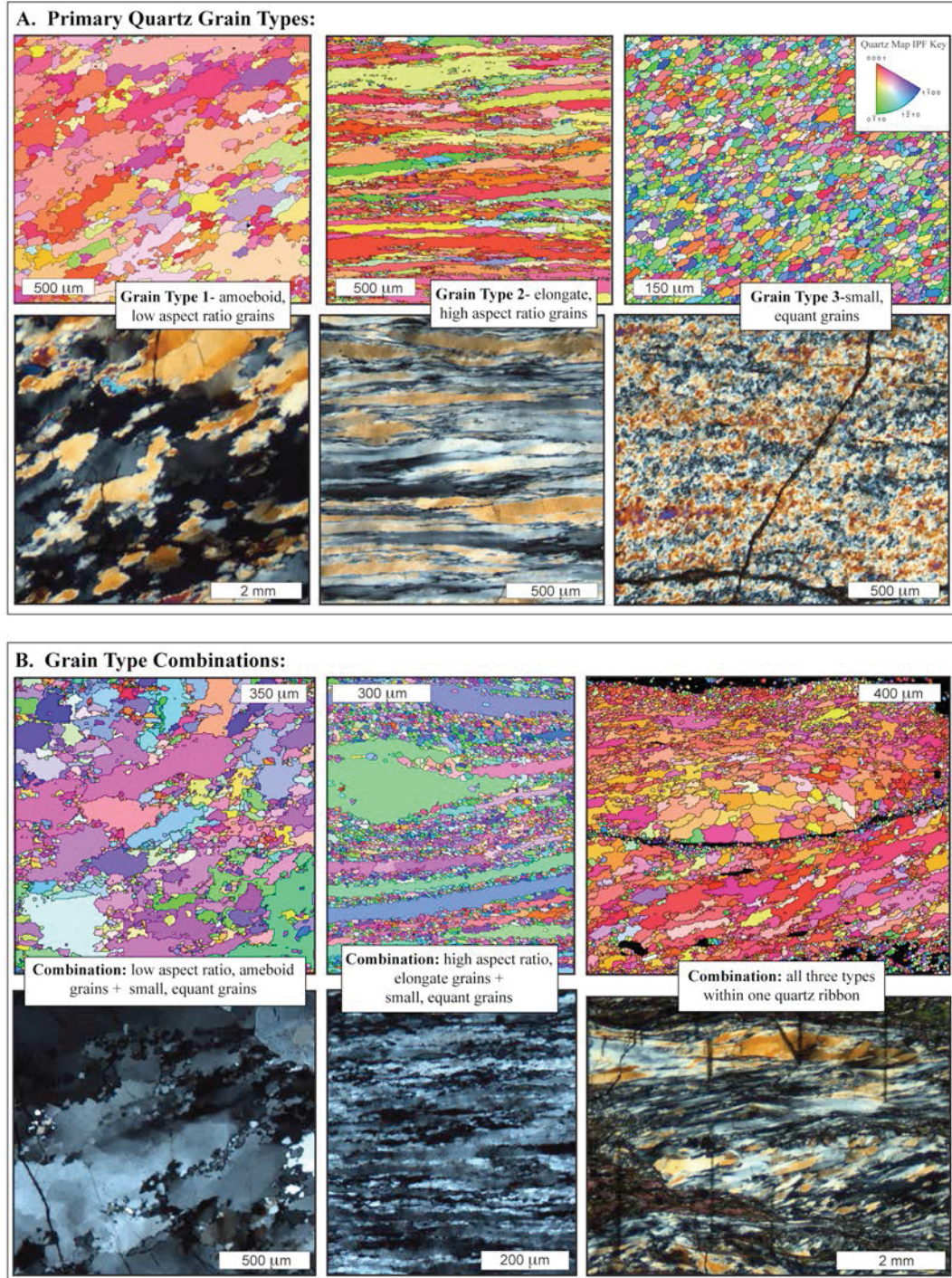


Figure 3.3. Quartz microstructures comprise one or a combination of three primary quartz grain types within deformed quartz ribbons of the Sandhill Corner shear zone. Each microstructure type is presented as a representative SEM-EBSD produced grain orientation map (upper) and a representative cross-polarized photomicrograph (lower). Colors in the orientation map corresponded to the IPF key provided. Orientation maps show one uniform orientation per grain with grain boundaries (a boundary misorientation of $\geq 10^\circ$) outlined in black. Dauphiné twins were removed from the orientation maps.

3.6.2. Grain Type 2- Elongate, High Aspect Ratio Grains

Straight quartz ribbons parallel to the shear foliation within the mylonite, sheared schist, and locally in the protomylonites contain long, thin grains with high aspect ratios that are aligned parallel to the shear foliation (Figs. 3.2 and 3.3). Where asymmetric folds have been rotated towards the foliation, these elongate grains may locally define a shape preferred orientation axial planar to the rotated fold, whether or not the fold has been rotated into complete alignment with the foliation. The grains display broad undulatory extinction, and smaller elongate island grains are present. The boundaries of these grains are lobate, particularly where they interfinger, but otherwise have a straight appearance along their length. The grain boundaries may locally have a high-frequency, serrated appearance in places where a few smaller, more equant grains are present along the boundary. Ribbons that contain only Type 2 grains do not show significant evidence for polygonal subgrains. Elongate grains that display the core-mantle microstructure and that do contain subgrains are described below as a combination microstructure. The size of the elongate, high aspect ratio grains is typically large (>100mm in equivalent diameter) but is not exclusively so, with some veins containing smaller, very highly elongate grains.

3.6.3. Grain Type 3- Small, Equant Grains

Quartz ribbons in the quartzofeldspathic mylonite, the shear zone core, and sheared schist closest to the shear zone core display grains that are smaller (<~80mm) and more equant than either of the other two grain types (Figs. 3.2 and 3.3). Type 3 grains are a mixture of irregularly shaped grains with weakly lobate grain boundaries and more polygonal grains with straighter grain boundaries; in only a few rare samples are the small grains all polygonal in shape. The more elongate of the small, irregularly-shaped grains define a shape-preferred orientation at an angle to the shear foliation that varies in strength between samples. Extinction patterns in many samples also show layering of elongate grain orientation domains (groupings of small grains with similar orientations) that are parallel to the shear foliation. The layering is more pronounced in

some ribbons than in others (more commonly in the quartzofeldspathic mylonite samples), and not all ribbons with only Type 3 grains display this layering.

3.6.4. Combinations of Grain Types

Grain type combinations are dominated by a mixture of large and small grains: (a) Types 1 and 2, or (b) Types 2 and 3 (Fig. 3.3). The first combination (a) of the large, low aspect ratio, amoeboid-shaped grains (Type 1) and smaller, more equant grains (Type 3) is only found in the schist host rock, the quartzofeldspathic host rock, and the protomylonite at the edges of the shear zone (Fig. 3.2). Type 3 grains, which are polygonal in shape, are typically found along the boundaries between the larger Type 1 grains giving them a serrated appearance. Type 1 grains display bulges in places, display patchy extinction patterns, and contain subgrains, particularly with increased proximity to grain boundaries. In places, smaller Type 3 grains have completely replaced the larger Type 1 grains. Shear fractures in the protomylonite, including rare pseudotachylite, are associated with this combination of grains (Fig. 3.4), and the replacement of Type 1 by Type 3 grains is more prevalent where these fractures occur.

The second combination (b) of large, elongate, high aspect ratio grains (Type 2) and smaller, more equant grains (Type 3) is present in the quartzofeldspathic protomylonite and common in the mylonite (Fig. 3.2). The Type 3 grains surround the larger Type 2 grains creating a core-mantle microstructure (Fig. 3.3). The Type 2 grains have patchy extinction and contain subgrains, most prominently at their boundaries. Smaller Type 3 grains are both polygonal and irregular in shape. The proportion of Type 2 to Type 3 grains is variable and is not directly associated with proximity to the shear zone core. In ribbons with a larger proportion of smaller Type 3 grains, the smaller grains commonly display layering grain orientation domains, particularly ribbons from the quartzofeldspathic mylonite samples.

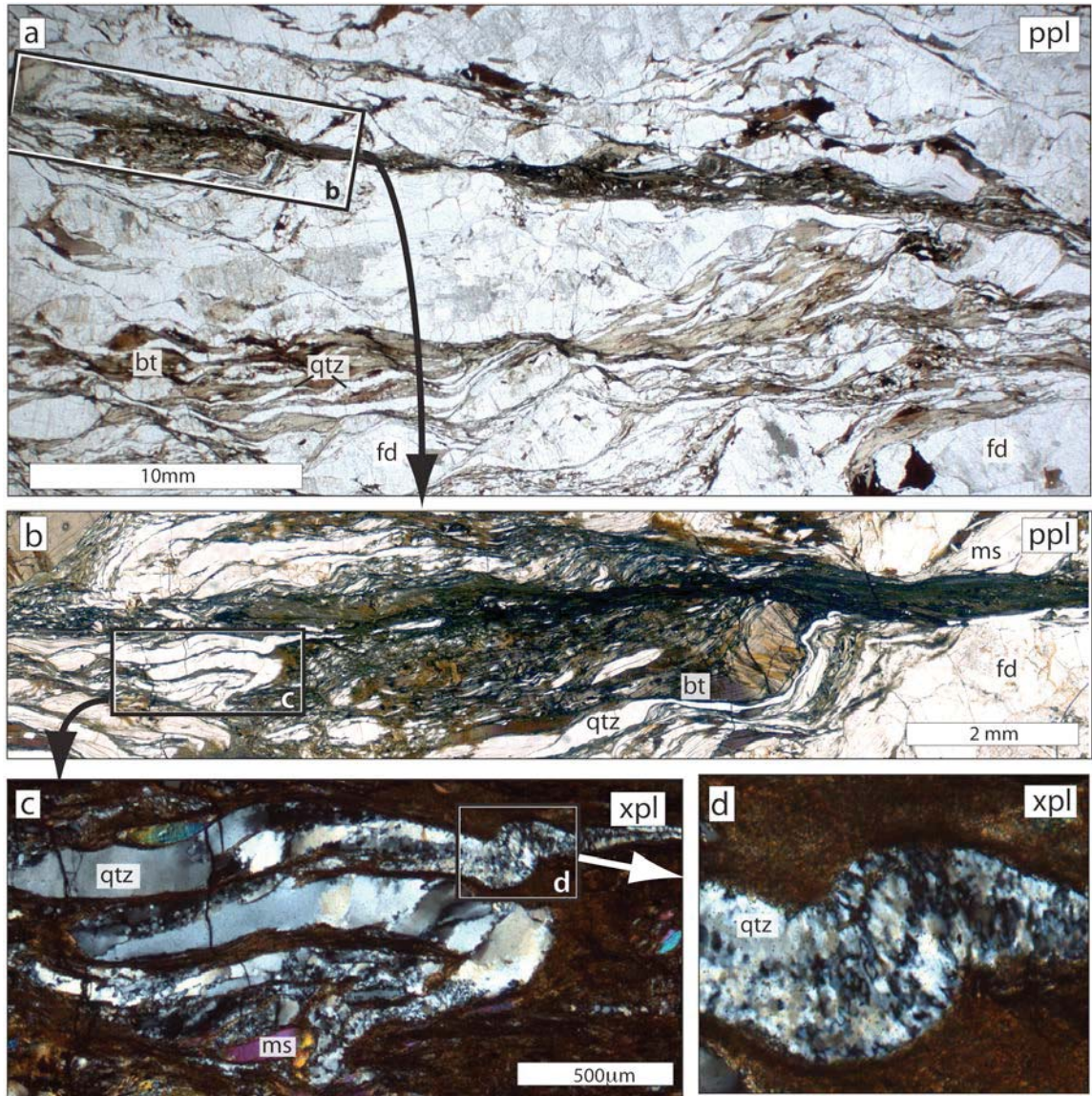


Figure 3.4. The replacement of large, amoeboid quartz grains (Type 1) by (c,d) smaller, more equant grains (Type 3) in quartz ribbons in the (a) protomylonite is more prevalent where (b) shear fractures and rare pseudotachylyte occur. (a, b) are plane-polarized and (c,d) are cross-polarized photomicrographs; bt-biotite, fd-feldspar, ms-muscovite, and qtz-quartz.

Quartz ribbons containing all three grain types (Fig. 3.3) are predominantly found in the sheared schist where the folded ribbons are variably transposed, imbricated, and attenuated. Limbs that have been thinned show elongate, high aspect ratio grains (Type 2) that are aligned parallel to the limb edge and the shear foliation, whereas the limbs that have been rotated and/or

imbricated but not thinned display amoeboid, low aspect ratio grains (Type 1) that maintain the fold-related SPO at an angle to the shear foliation. The large grains (Type 1 and 2) locally contain subgrains and smaller, more equant grains (Type 3) along grain boundaries, but do not show a well-developed core-mantle microstructure. Clusters of small Type 3 grains are found at the edges of quartz ribbons that have large grains at the center.

3.6.5. Atypical Quartz Microstructures

Some quartz ribbons display atypical extinction patterns and uncommon relationships between grains that do not fit into the microstructure groups listed above (Fig. 3.5). First, large single crystal quartz ribbons and grains of pegmatite origin within the quartzofeldspathic mylonite are cut by discontinuous strings of small polygonal grains (Fig. 3.5b). These strings are at most a few grains in width, are dominantly foliation parallel, and do not cut across the entire host grain. The host grain displays patchy extinction but is not pervasively subgrained. Where these host grains are surrounded by the core-mantle microstructure (Type 2 + 3 grains), the large, host grain and the Type 3 grains surrounding it have the same extinction point in crossed polarized light. Second, within quartz ribbons dominated by Type 3 grains, groups of grains with similar orientations (e.g. grain orientation domains) display fracture-like extinction patterns (Fig. 3.5a). These shapes range from single, fracture-like bands that cut the ribbon at an angle to the foliation, to patterns that resemble a fracture network. Finally, a few quartz ribbons display irregularly, blocky and patchy extinction patterns that are associated with heterogeneous subgrain distributions (Fig. 3.5c-f). These ribbons are spatially associated with pseudotachylyte and deformed pseudotachylyte veins, and have an anomalously low proportion of indexed points when mapped for crystal orientation with the SEM-EBSD.

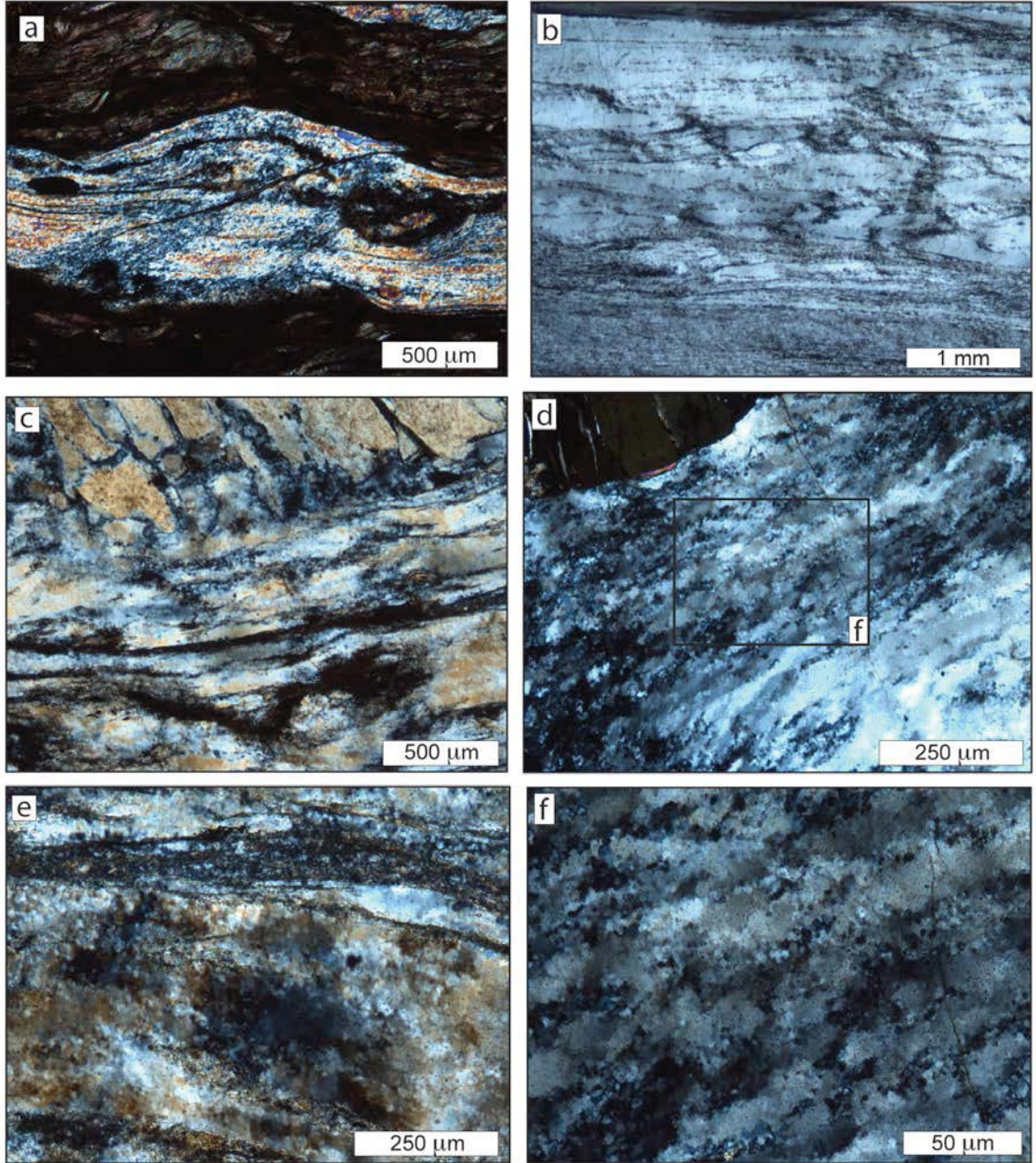


Figure 3.5. Atypical quartz microstructures observed within deformed quartz ribbons of the Sandhill Corner shear zone. (a) Extinction patterns preserve healed fractures in quartz ribbons. (b) Discontinuous fractures are decorated by strings of small polygonal grains that cut large single crystal grains leading to a core-mantle style microstructure in pegmatitic quartz. (c-f) A few quartz ribbons display irregular, blocky and patchy extinction patterns that are associated with heterogeneous subgrain distributions and that may be a result of variable or rapidly decaying strain rates associated with the coseismic slip and post-seismic creep. All images are cross-polarized photomicrographs.

3.7. Quartz CPO Patterns

3.7.1. Host Rock CPO

The quartz ribbons in the schist and quartzofeldspathic host rock are asymmetrically folded with an associated CPO (Fig. 3.6). Plotted within a reference frame relative to the fold (i.e. perpendicular to the axial plane and normal to the fold axis), the CPO appears as a broad c-axis maximum overlapping the right and left edges of the pole figure normal to the axial plane and an a-axis girdle within the axial plane. C-axis pole figures for individual fold limbs and c-axis figures from sections around the fold do not show significant, reproducible differences in CPO patterns (e.g. Hongn and Hippertt, 2001). Within the reference frame of the shear zone (i.e. perpendicular to the subvertical foliation, parallel to the subhorizontal lineation, and the right side of the pole figure corresponding to the northeast direction), the c-axis maximum of the host rock plots in the upper left quadrant of the pole figure and the a-axis plots as a girdle that extends from the upper right to the lower left quadrant $\sim 30^\circ$ from the edge of the pole figure. The strength of the host rock CPO varies from sample to sample. Within the quartzofeldspathic unit, pegmatitic bodies also contains quartz veins that are not folded and thus, do not display this CPO (e.g. 264, Fig. 3.7).

3.7.2. Shear Fabric CPO Patterns

Figure 3.7 shows representative CPO pole figures produced from sheared quartz ribbons of the schist unit, and the quartzofeldspathic mylonite and protomylonite. The c-axis patterns observed can be grouped into a number of types: (a) single maximum; (b) paired maxima in the top and bottom hemispheres of the pole figure; and (c) an elongate cross girdle from the top to the bottom of the pole figure. These c-axis pattern types are observed from samples collected from all the rock units deformed within the shear zone. However, the cross girdle patterns (c) are more likely to be found from quartz ribbons of the highly-sheared schist protomylonite, and mylonite

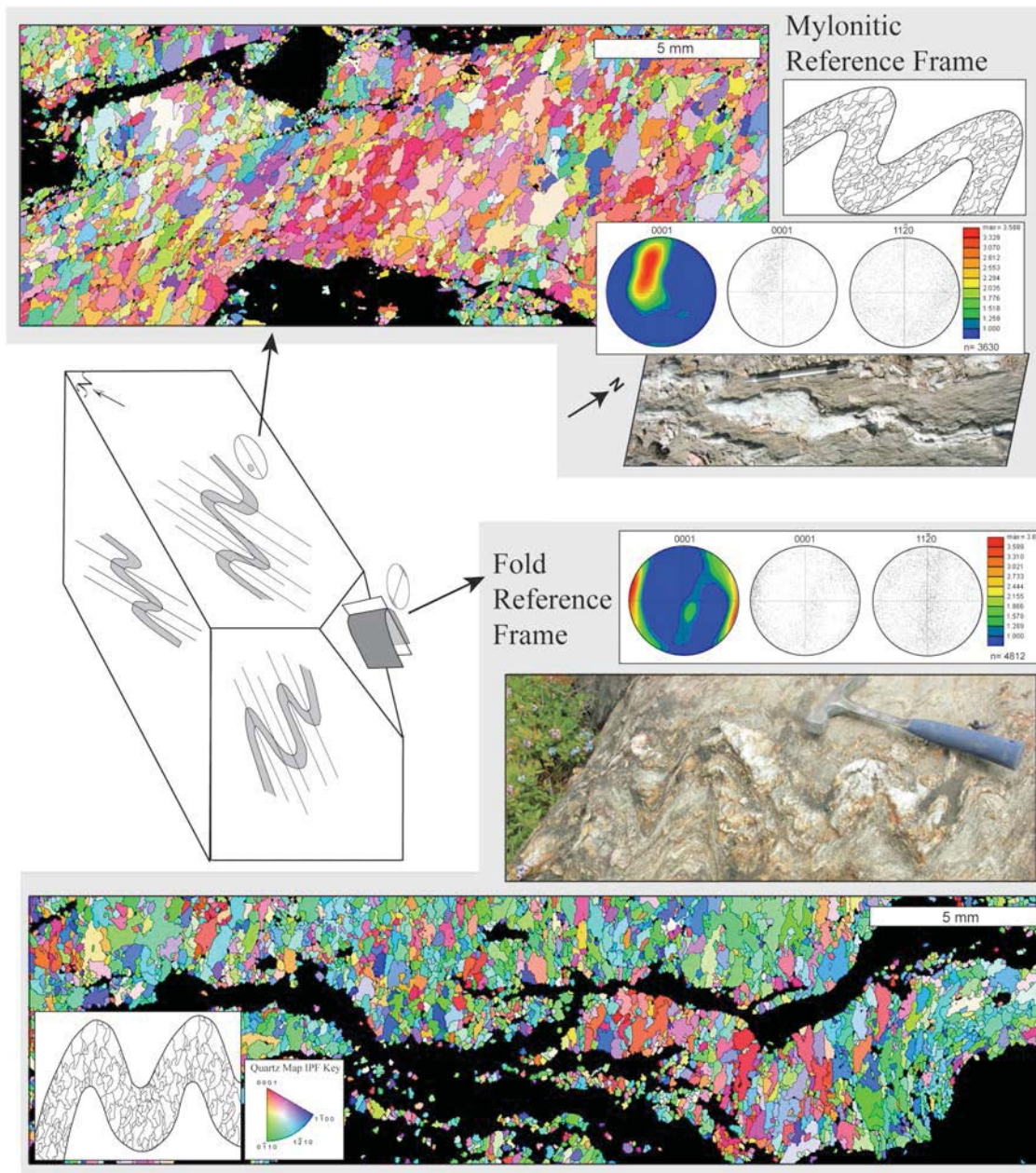


Figure 3.6. The pre-existing host rock quartz fabric. In the fold reference frame (bottom), the quartz grains define an SPO axial planar to the fold and a CPO of a single c-axis maximum at the periphery of the pole figure. This same fabric in the mylonitic reference frame (top) appears as an SPO at an angle to the shear foliation and a single c-axis maximum in one quadrant of the pole figure. The field photo of an inclined rock face in the fold reference frame was taken facing north-northwest; the northwest is at the top of the photo of the horizontal outcrop in the mylonitic reference frame. Quartz microstructure is presented as a SEM-EBSD produced grain orientation map; colors in the orientation map corresponded to the IPF key provided. Orientation maps show one uniform orientation per grain with grain boundaries (a boundary misorientation of $\geq 10^\circ$) outlined in black and Dauphiné twins removed. The c-axis (0001) and a-axis (11-21) pole figures are equal area lower hemisphere projections plotting one point per grain derived from the orientation maps. C-axis plots display linear contouring (the scale for each with multiples of uniform density is shown).

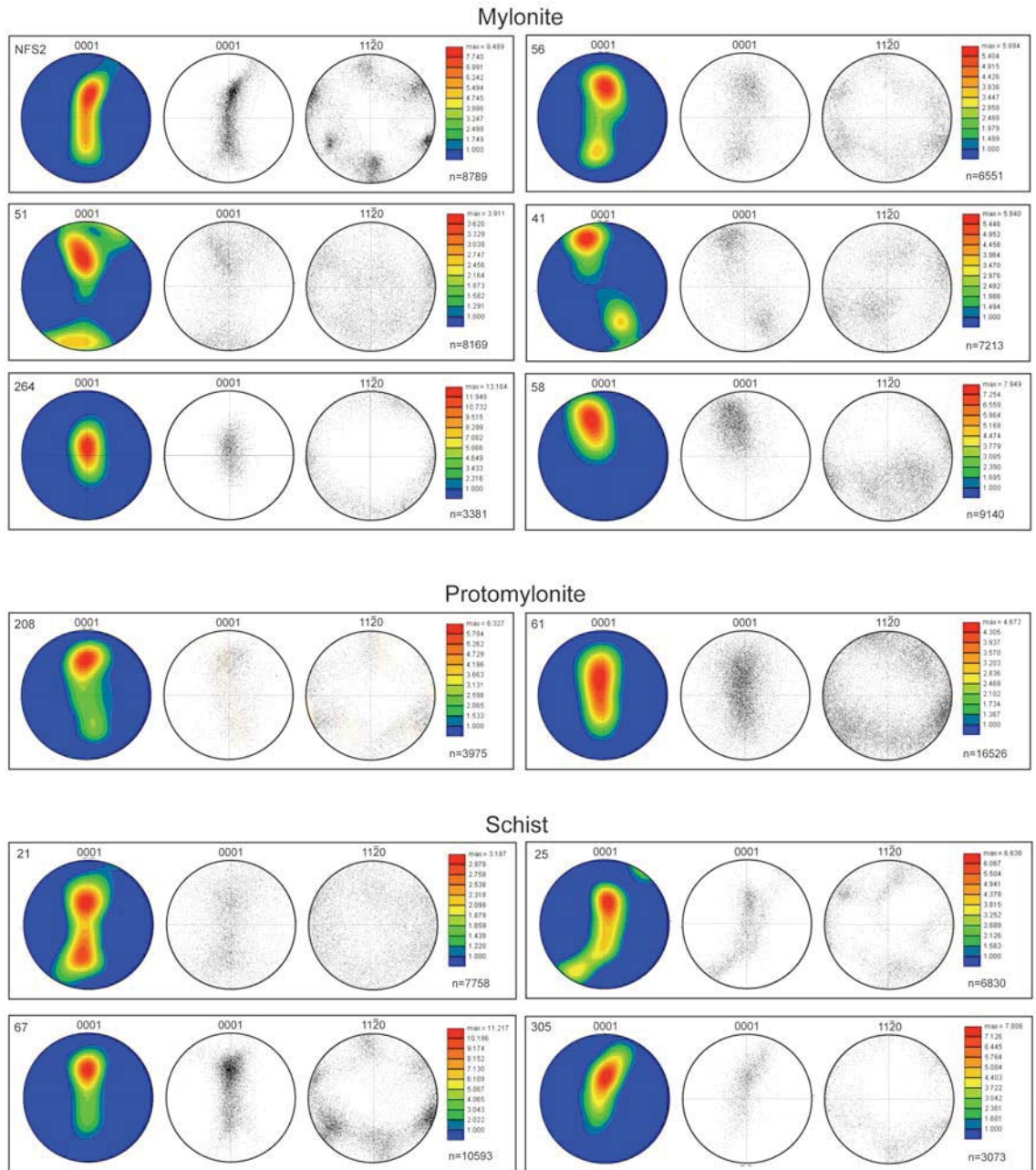


Figure 3.7. A suite of c-axis (0001) and a-axis (11-21) pole figures showing CPO patterns typical of quartz veins found within the quartzofeldspathic mylonite, protomylonite, and sheared schist of the Sandhill Corner shear zone. The pole figures are equal area lower hemisphere projections plotting one point per grain derived from SEM-EBSD mineral orientation maps. C-axis plots display linear contouring (the scale for each with multiples of uniform density is shown).

transition zone, whereas the single and paired maxima (a, b) are more likely to be found from ribbons in the quartzofeldspathic mylonite.

In samples that display a single c-axis maximum, the cluster of poles is typically located either in the upper left quadrant of the pole figure (58, Fig. 3.7) or in the center of the upper hemisphere (305, Fig. 3.7). Only one sample displays a c-axis maximum at the center of the pole figure (264, Fig. 3.7); this sample was collected from an unfolded pegmatitic quartz vein of the quartzofeldspathic mylonite. In samples that show paired maxima, one maximum is stronger (i.e. contains more poles), and the location of this maximum is comparable to the location of the c-axis maximum in the samples that only have one cluster of poles (41 vs. 58, Fig. 3.7). The second “weaker” maximum is located in the lower hemisphere in an orientation mirror to the maximum in the upper hemisphere (41, 51; Fig. 3.7). The spread of poles around these maxima may appear to form a very weak cross girdle pattern connecting the maxima across the center of the pole figure (56, Fig. 3.7) or to form a pattern at the periphery of the pole figure consistent with the “tails” commonly seen at the edges of the pole figure in better developed cross girdle patterns (51 and 305, Fig. 3.7).

Where the c-axis patterns display a cross girdle pattern, the cross girdles are nearly perpendicular to the left-right equator of the pole figure (i.e. the flow plane is nearly parallel or at a small angle to the foliation). In most samples, the cross girdle either does not show tails at the edge of the pole figure or the tails are only weakly developed. In the few samples where these tails are better developed and display a left-right asymmetry, the pattern asymmetry is weak but consistent with dextral deformation (67, Fig. 3.7). Most cross girdle patterns also display a top-bottom asymmetry, where the top of the girdle contains a stronger cluster of poles than the lower half of the girdle. The location of the stronger cluster of poles is comparable to the location of the upper hemisphere maximum where only a single cluster is present as described above (67, Fig. 3.7). Some cross girdle samples also display two clusters of points within the cross girdle, one at

the center of the upper hemisphere and one at the center of the lower hemisphere (56 and 21, Fig. 3.7). Typically, the cluster in the upper hemisphere is stronger, creating a top-bottom asymmetry.

3.7.3. CPO Patterns and Quartz Microstructures

A comparison between the CPO patterns of the large and small grains from samples of mixed grain types (e.g. core-mantle microstructure; combination of Types 2 and 3) shows little difference in the c-axis pole figure patterns (Fig. 3.8). In samples that show a cross girdle pattern, the large and small grains will both display the same pattern shape. The patterns between the large and small grains do differ in the clustering of the poles, with the small grains displaying a more diffuse pattern. The large grains are more likely to show a stronger clustering of points as a single maximum in the upper hemisphere of the c-axis pole figure or as a pair of maxima, one at the center of each hemisphere. The paired maxima are most commonly associated with the Type 2 grains. There is no clear correlation between the presence of tails in the c-axis pole figure and grain size; if a sample displays a cross girdle pattern with tails, the figure of the large and small grains will both display tails.

Ribbons containing only the small Type 3 grains commonly display single or paired maxima rather than well-developed cross girdles, particularly within the ribbons of quartzofeldspathic mylonite and samples from the shear zone core. In samples where these ribbons display alternating layering of elongate grain orientation domains, the paired c-axis maxima reflect the orientations of the grain domains. For example, Figure 3.9 shows that the top maxima is associated with one fabric domain and that the bottom maxima is associated with the other fabric domain.

3.8. Misorientation Analysis

Figure 3.9 and 3.10 shows a selection of representative misorientation rotation angle profiles based on the shapes of the nearest-neighbor profiles (red) relative to the random-pair

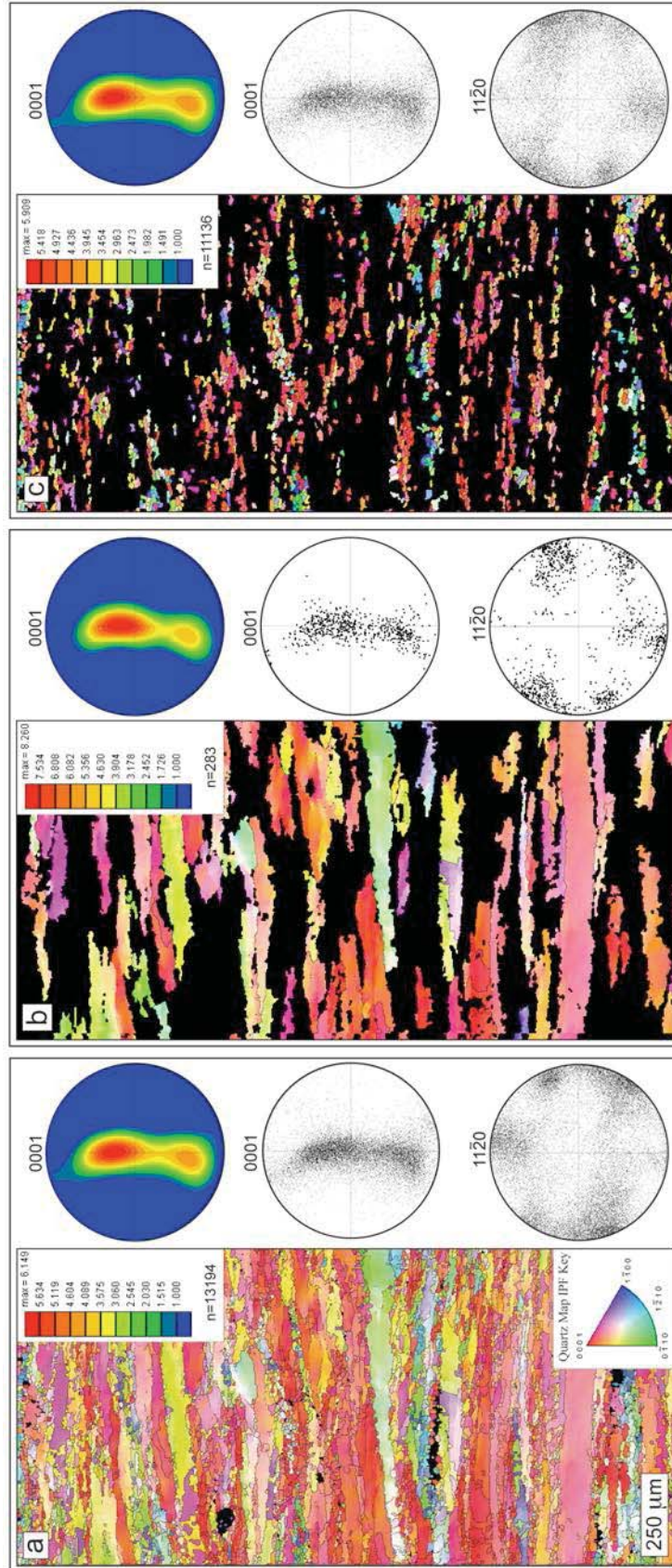


Figure 3.8. Quartz CPO patterns for different grain size fractions of a deformed quartz ribbon. Orientation maps and pole figures show (a) all sizes, (b) $>80\text{mm}$, and (c) $<30\text{mm}$ (equivalent diameter). C-axis plots display linear contouring (the scale for each with multiples of uniform density is shown). The c-axis (0001) and a-axis (11-21) pole figures are equal area lower hemisphere projections plotting one point per grain derived from SEM-EBSD mineral orientation maps. Colors in the orientation map corresponded to the IPF key provided, and grain boundaries (boundary misorientation of $\geq 10^\circ$) are outlined in black.

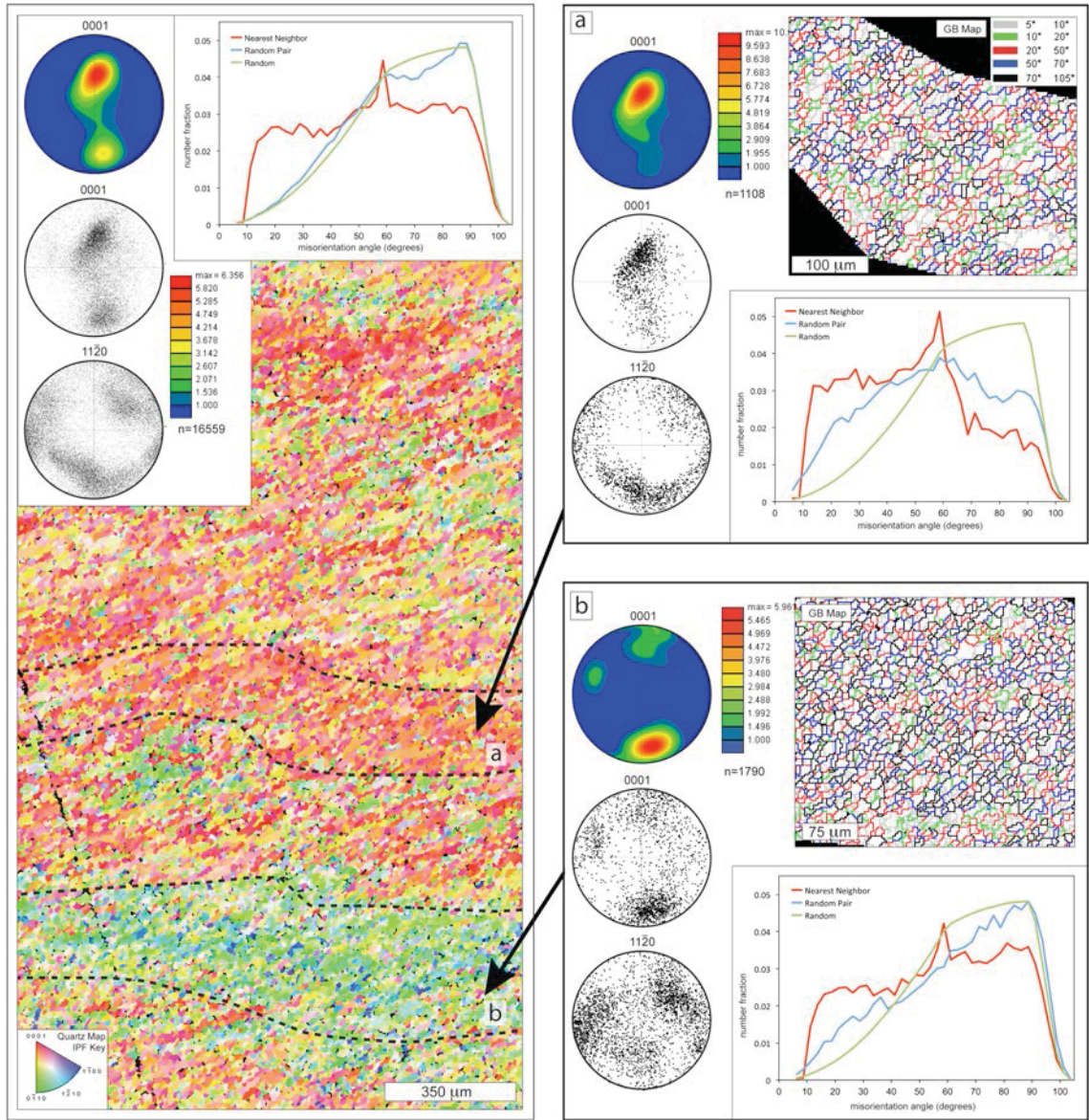


Figure 3.9. Fine-grained samples with layered grain orientation domains show different CPO patterns and misorientation rotation angle histogram profiles for each of the grain domains. Data for the entire sample are shown at left, and data for outlined grain domains a and b are shown at right. The histogram plots show the random (green), random-pair (blue), and nearest-neighbor (red) profiles. The c-axis (0001) and a-axis (11-21) pole figures are equal area lower hemisphere projections plotting one point per grain. CPO and misorientation data were derived from the SEM-EBSD mineral orientation maps. C-axis plots display linear contouring (the scale for each with multiples of uniform density is shown). Colors in the orientation and grain boundary maps correspond to the IPF map and misorientation angle ranges provided.

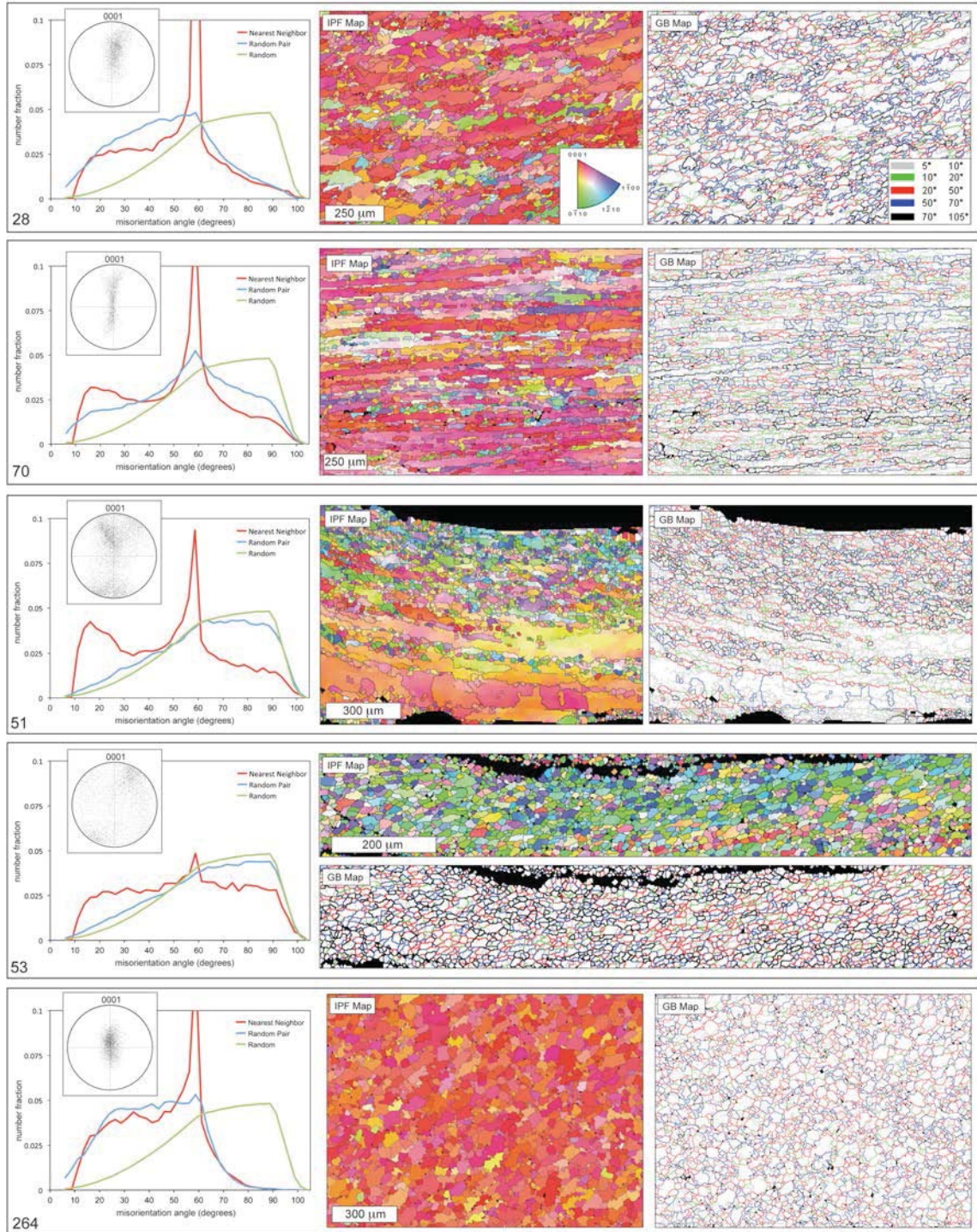


Figure 3.10. Misorientation rotation angle histogram plots, misorientation angle boundary maps (GB Map), mineral orientation maps (IPF Map), and c-axis (0001) pole figure of selected samples from the Sandhill Corner shear zone. The histogram plots show the random (green), random-pair (blue), and nearest-neighbor (red) profiles. The pole figures are equal area lower hemisphere projections plotting one point per grain. CPO and misorientation data were derived from the SEM-EBSD mineral orientation maps. Colors in the orientation map corresponded to the IPF key provided, and grain boundaries (boundary misorientation of $\geq 10^\circ$) are outlined in black. Colors in the grain boundary map correspond to the misorientation angle ranges shown in the key.

(blue) and random (green) profiles. All nearest-neighbor profiles are dominated by a peak at 60° that deviates from the random-pair profiles, consistent with Dauphiné twins. The nearest-neighbor profiles of many samples (28 and 264, Fig. 3.10) show an increase in the number fraction at 10° that stays constant through to 50° where the number fraction increases to the peak at 60° . After the 60° peak, the number fraction decreases making the peak appear asymmetric. In a few samples, the decrease in number fraction after 60° is abrupt (264, Fig. 3.10), and the nearest-neighbor profile follows the random-pair profile. In most samples, the transition is gradual, with the number fraction steadily decreasing with increasing misorientation up to $\sim 90^\circ$ (28, Fig. 3.10). The random-pair profile in these samples typically increases gradually from the low and high angle ends of the profile to a less pronounced peak around 60° . Commonly the number fraction of the nearest-neighbor profile between 10 - 30° is higher than the random-pair profile creating a second, smaller peak at low rotation angles. Quartz ribbons that display these types of misorientation profiles also commonly display a well-developed cross girdle c-axis CPO pattern.

In contrast, many quartz ribbons display a flat nearest-neighbor profile, where the number fraction is roughly the same from 10° to 95° (53, Fig. 3.10). The only significant variation in the flat nearest-neighbor profile is the peak at 60° . The random-pair profile approximates the random profile in these samples. Quartz ribbons with a CPO of a single or paired c-axis maxima display the flat misorientation profiles, particularly in those samples from the quartzofeldspathic mylonite and the shear zone core with Type 3 grains or a combination of Type 2 and 3 grains. Variations in samples that display near flat misorientation profile (51 and 70, Fig. 3.10) include a decrease in the number fraction at higher misorientation angles of both the nearest-neighbor and random-pair profiles, suggesting transitional states between the flat profile and the profile described in the paragraph above.

The grain boundary maps show the correlation between misorientation angle at grain boundaries and grain microstructure. Where there is a combination of large and small grain

types, the highest misorientation angles ($>70^\circ$) and angles associated with Dauphiné twins ($50-70^\circ$) are at the boundaries of the large grains. The large grains are cut by lower angle boundaries ($<20^\circ$) and Dauphiné twin boundaries (28 and 70, Fig. 3.10). Where the large grains are mantled by smaller grains, the misorientation angle between the large and small grains is typically greater than 30° . In ribbons that contain only small Type 3 grains and alternating layering of elongate grain orientation domains, the orientation domains display different misorientation profiles (Fig. 3.9). The grain domains that are associated with the c-axis maxima in the upper hemisphere of the pole figure have a stepped nearest-neighbor misorientation profile, with $10-50^\circ$ rotations displaying a higher number fraction than $70-100^\circ$ rotations. The random-pair profile for these domains is a rounded curve with the highest misorientations around 60° , and the nearest-neighbor profile deviates from this with more low angle boundaries ($<40^\circ$) and fewer high angle boundaries ($>60^\circ$). The grain domains that are associated with the weaker c-axis maxima in the lower hemisphere of the pole figure, have a stepped nearest-neighbor profile that has slightly more boundaries with high angles ($>60^\circ$). The random-pair profile for these domains is similar to the random profile, and the nearest-neighbor profile also deviates from this with more low angle boundaries ($<40^\circ$) and fewer high angle boundaries ($>60^\circ$). In total, with both domains included, the quartz ribbon shows a flat nearest-neighbor profile with a near random random-pair profile.

IPF plots of misorientation axes orientations show a clustering of rotation axes plotting near the c-axis for misorientations in or less than the $60-70$ degree rotation interval (Fig. 3.11). In all samples, the strongest clustering is found within the $50-60$ degree rotation interval and to a lesser degree the $40-50$ interval. The presence and/or strength of c-axis clustering in other rotation angle intervals is sample dependent, with some samples displaying strong clustering and other samples with diffuse or no clustering. For misorientation rotations greater than $\sim 70^\circ$, points cluster at the edge of the forbidden zone. Many samples also show clustering at the sides of the

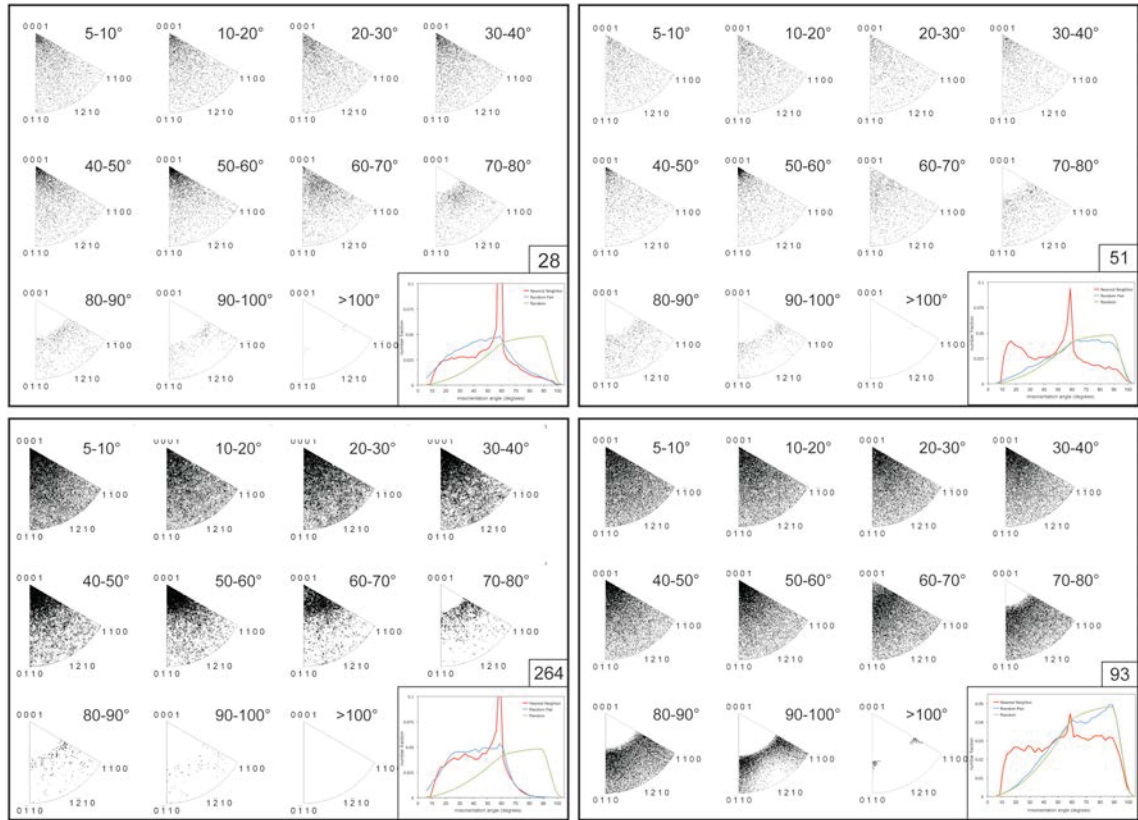


Figure 3.11. Misorientation data for four selected samples from the Sandhill Corner shear zone. Misorientation rotation axes are plotted on inverse pole figures for rotation angle ranges from 5-104.5°. Misorientation rotation angle histogram profiles show the random (green), random-pair (blue), and nearest-neighbor (red) profiles. Misorientation data were derived from the SEM-EBSD mineral orientation maps.

pole figure in the 70-80, 80-90, and/or 90-100 degree intervals, including clustering about the rhombohedral (r and z) orientations. Diffuse clustering around the prism (m) orientations or a-axis occurs in only a few rare samples. Overall, there does not appear to be a clear, unambiguous correlation between the clustering of rotation axes and quartz microstructure, CPO patterns, or misorientation angle profiles.

3.9. Discussion

3.9.1. Interpretation of Quartz Microstructures

The large, low aspect ratio, amoeboid Type 1 grains are characteristic of the host rock fabric. The island grains and lobate grain boundaries of Type 1 grains reflect deformation by GBM recrystallization mechanisms. At the edges of the shear zone (particularly within the sheared schist unit), the folded asymmetric quartz ribbons of the host rock were passively transposed without internal recrystallization (Figs. 3.1 and 3.12). Fold limbs that were passively

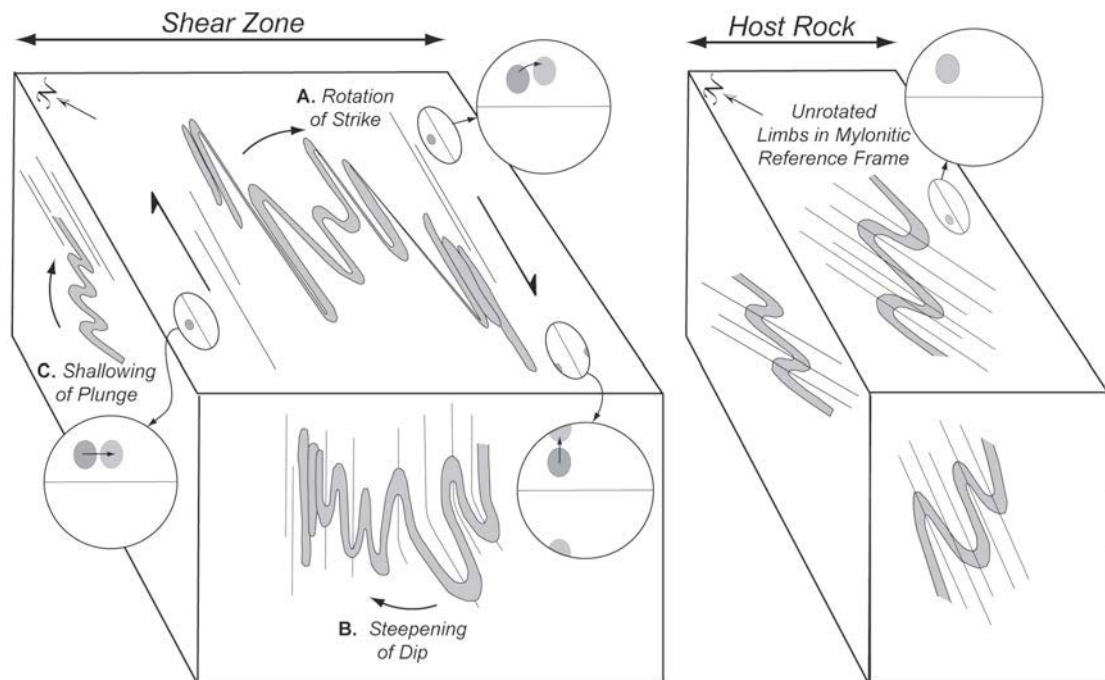


Figure 3.12. A schematic diagram showing how the passive rotation of folded quartz ribbons of the host rock would change the location of the inherited CPO in the rocks of the Sandhill Corner shear zone.

rotated into the mylonitic foliation display the SPO that was originally axial planar to the asymmetric folds of the host rock but that is now at an angle to the mylonitic foliation (Fig. 3.6). This passive rotation was most likely accommodated by deformation in the host matrix, such as through slip within layers rich in biotite.

At the edge of the shear zone in the schist unit and in the protomylonite (Fig. 3.2 and 3.3), the Type 1 grains are overprinted along the grain boundaries by Type 3 grains. The serrated Type 1 grain boundaries, the presence of subgrains near the grain boundaries, and the presence of bulges indicate that these Type 3 grains formed from a combination of SGR and BLG recrystallization mechanisms. These microstructures may indicate deformation at the lowest temperatures (assuming a constant strain rate), but they are localized only at the edge of the shear zone with no other evidence for BLG recrystallization operating elsewhere in the Sandhill Corner shear zone. Given that variable strain rates are expected during the seismic cycle within a seismogenic shear zone, it is possible that the overprint of Type 3 grains in these samples instead reflects deformation at a transiently elevated strain rates.

We interpret the large, high aspect ratio Type 2 grains to reflect high strains at comparatively higher temperature conditions. The island grains and lobate grain boundaries of these grains is also consistent with deformation by GBM recrystallization mechanisms. Type 2 grains are found in transposed and recrystallized folded quartz ribbons of the sheared schist where the fold limbs have been attenuated and where strain was accommodated by dynamic recrystallization in addition to passive rotation. Type 2 grains (aka ribbons grains) are typically associated in the literature with SGR recrystallization through the development of the core-mantle microstructure. However, Type 2 grains are commonly found in the Sandhill Corner shear zone without any evidence for subgrains or Type 3-style new grains, particularly within the quartzofeldspathic mylonites. For that reason, we interpret these grains to reflect recrystallization by GBM mechanisms at high strains (“stretched” versions of Type 1 grains) that may be overprinted via SGR recrystallization forming the core-mantle microstructure. What drives the transition to SGR and the overprint by Type 3 grains is unclear. It may reflect either temperature or strain rate changes and/or may be associated with the path-dependent evolution of the microstructure (e.g. ribbon grains form prior to subgrains during the accumulation of strain at SGR/GMB conditions; Lloyd and Freeman, 1994; Trimby et al., 1998).

Alternatively, Type 2 grains may originate from large quartz crystals of pegmatite origin that are sheared and cut by foliation-parallel fractures (Fig. 3.5b). These fractures are discontinuous, have a string of small new grains along them (Vernooij et al., 2006b), and produce elongate slivers that are ultimately surrounded by smaller grains forming a core-mantle microstructure. This is a secondary source of Type 2 grains, primarily in pegmatitic quartz, and does not reflect the modification of the host rock fabric. It is not clear whether the fractures in pegmatitic quartz resulted from transiently high coseismic/postseismic strain rates or form as a result of locally-elevated stresses during interseismic viscous flow (Ellis and Stockert, 2004a; Kohlstedt and Weathers, 1980; Rolandone et al., 2004).

The majority of the small Type 3 grains display microstructures that are consistent with both SGR and GBM recrystallization mechanisms. The polygonal shape of some grains and the core-mantle microstructure with subgrained parent grains indicates SGR recrystallization, whereas the irregular, weakly lobate shapes of the other daughter grains indicates that GBM is also active. It is unclear whether all the daughter grains are larger than the subgrain size in the parent grains, but that is the case with many daughter grains. We interpret these Type 3 grains as overprinting the parent Type 1 and 2 grains. Where only Type 3 grains are present, we interpret the grain orientation domains to reflect the orientations of the replaced Type 2 parent grains (Pauli et al., 1996; Halfpenny et al., 2004, 2006). The core-mantle microstructure is more prevalent near the center of the shear zone and ribbons that comprise only Type 3 grains are found within or closest to the shear zone core, indicating higher strains nearest the core (Fig. 3.2).

The other atypical microstructures (Fig. 3.5a, c-f) are uncommon in the Sandhill Corner shear zone and may reflect deformation associated with coseismic slip and postseismic creep. This connection is supported by the spatial association of the atypical microstructures with pseudotachylite and deformed pseudotachylite as well as the increased incidence of these microstructures with proximity to the shear zone core. Where intergranular fractures cut quartz ribbons and can be traced into the mylonite/schist matrix, a mass of fine-grained quartz grains

fills the fractures and extinction patterns display the original fracture pattern (e.g. Trepmann et al., 2007). One such sample that was mapped for quartz grain orientations via the SEM-EBSD showed similar orientations for the quartz inside and outside the fracture, suggesting that the orientation of the host ribbon grains may have influenced the nucleation and orientation of the new quartz filling the fracture. Those rare quartz ribbons that display irregularly, blocky and patchy extinction patterns (Fig. 3.5c-f) may represent the best evidence for quartz microstructures that formed during elevated and/or rapidly decaying strain rates (Ellis and Stöckert, 2004a; Kohlstedt and Weathers, 1980; Rolandone et al., 2004; Trepmann and Stöckert, 2003). As Kim et al. (2010) show, new quartz grains and a “mylonitic” microstructure can both be produced during coseismic slip. The anomalously low proportion of indexed points during SEM-EBSD mapping supports the possibility that quartz ribbons that display these abnormal extinction patterns have lattice-scale defects like microfractures or a particularly high dislocation density (Schwartz et al., 2009).

3.9.2. The Pre-existing CPO in Recrystallized Quartz CPO Patterns

Sheared quartz ribbons the Sandhill Corner shear zone typically display c-axis CPO patterns that are asymmetric across the foliation line (top-bottom asymmetry). Whether the c-axis pattern displays a single maximum in the upper hemisphere, paired maxima above and below the foliation line, or a full cross girdle, the upper hemisphere typically contains a higher number of clustered points. The host rock CPO plots as a single c-axis maximum in the upper left part of the quadrant when plotted in the mylonitic reference frame. The location of this maximum is coincident with or close to the location of the point cluster in the CPO patterns of the sheared samples. We interpret the top-bottom asymmetry of the c-axis pole figures of the sheared quartz ribbons to reflect the persistence of the pre-existing CPO in the shear fabric. This interpretation is further supported by the CPO of ribbons with a core-mantle microstructure. Although the c-axis patterns are similar between the two grain sizes (parent vs. daughter), the plot of the larger

grain size range commonly shows a stronger clustering of points as a single maximum in the upper hemisphere of the c-axis pole figure, reflecting the inherited orientation of the large grains from the host rock fabric. However, there are discrepancies between the location of the c-axis maximum of the host rock and the point cluster in top-bottom asymmetric c-axis patterns of the sheared samples. In some samples, the location of the host rock maximum and sheared sample maximum are the same (58, Fig. 3.7), but in many sheared samples, the cluster of points is in the center of the upper hemisphere rather than the upper left quadrant (67, Fig. 3.7). This difference can be accounted for by the passive rotation of the limbs of the folded quartz ribbon during shearing, as accommodated by deformation in the surrounding matrix and as is observed in outcrop (Section 3.4 and Fig. 3.1).

Figure 3.12 illustrates the possible types of passive rotation and the effect they would have on the location of the inherited c-axis maximum. A rotation of the quartz ribbon into the strike of the mylonitic foliation (Fig. 3.12A) would move the c-axis maximum to a location closer to the east-west line in the center of the upper quadrant. This type of rotation is commonly observed in the field and is the best explanation for the discrepancy between the location of the point cluster in the host rock and the sheared c-axis patterns. A rotation that would shallow the plunge of the fold (Fig. 3.12C) would produce an effect similar to a rotation into the strike of the foliation. Either of the above mentioned rotations (Fig. 3.12A or C) would place the inherited c-axis maximum in an orientation coincident with recrystallization dominated by rhomb $\langle a \rangle$ slip. On the other hand, if the dip of the fold limbs increased (Fig. 3.12B), the inherited c-axis maximum would move to the outer edge of the pole figure in an orientation coincident with recrystallization dominated by basal $\langle a \rangle$ slip. Quartz ribbons with c-axis maximum in such a position (41, Fig. 3.7) are present in the Sandhill Corner shear zone, particularly within the quartzofeldspathic mylonite. It should be noted that paired c-axis maxima at the edge of the pole figure have been documented as a pattern observed early in the fabric progression described by

Heilbronner and Tullis (2006b) and thus may also reflect dominant basal $\langle a \rangle$ slip during the early stages of quartz fabric evolution.

In addition to passive rotation, most quartz ribbons are also dynamically recrystallized. Dislocation creep primarily via SGR and GBM should spread out the c-axis pattern and form a cross girdle pattern characteristic of non-coaxial deformation. In some samples, this well-developed cross girdle is present, with a weak top-bottom asymmetry. In other samples, the cross girdle appears incomplete with a strong top-bottom asymmetry (305, Fig. 3.7) or with only the “tails” present at the edges of the pole figure (51, Fig. 3.7). Most common are the paired maxima, one within the center of each hemisphere, in an orientation coincident with recrystallization dominated by rhomb $\langle a \rangle$ slip. The upper hemisphere maximum in these patterns is better developed and is defined by a greater number of points, supporting the hypothesis that the upper maximum is inherited. Where alternating grain orientation domains are present (e.g. all Type 3 grains or core-mantle microstructure of Type 2 + Type 3), each peak in the CPO pattern is associated with one dominant grain orientation (Fig. 3.9; Halfpenny et al., 2004, 2006; Heilbronner and Tullis, 2006b; Pauli et al., 1996). Given that the inherited CPO would reflect only one c-axis maximum in the upper hemisphere of the CPO, the presence of paired maxima in these CPO patterns implies that the lower maximum, and thus the orientation of a large proportion of the quartz grains, may be formed during recrystallization. The development of these grains with alternating “rhomb” orientations is considered in more detail in Section 3.9.5.3.

3.9.3. Quartz CPO Data and IPF Plots of Misorientation Rotation Axes

Inverse pole figure plots of the orientation of grain boundary misorientation rotation axes are compatible with the active slip systems inferred by the c-axis CPO patterns. The cross girdle c-axis CPO pattern that is variably-developed within quartz ribbons of the Sandhill Corner shear zone suggests dislocation creep dominated by slip in the prism $\langle a \rangle$ and rhomb $\langle a \rangle$ directions.

Poorly-developed tails at the edges of some of the pole figures indicates only a moderate contribution of slip in the basal $\langle a \rangle$ direction. IPF plots of the misorientation rotation axes show diffuse clustering around the c-axis (Fig. 3.11). The strongest clustering around the 50-60 degree rotation interval is consistent with Dauphiné twinning, while c-axis clustering in other rotation angle intervals (e.g. 40-50 interval) probably reflects recrystallization via dominant prism $\langle a \rangle$ slip. However, the clustering is weak in many samples, indicating that other factors may be influencing the orientation of the rotation angles, such as the activity of multiple or paired slip systems, changes caused by GBM mechanisms, and/or a component of grain size sensitive flow, such as boundary sliding (Rutter and Brodie, 2004).

C-axis maxima in orientations coincident with rhomb $\langle a \rangle$ slip suggest that misorientation rotation axes should strongly cluster around the rhombohedral orientations in the IPF plots. Such clustering is present in many samples, but the clustering is weak and dominantly found in the higher rotation angle intervals (i.e. 70-100°). This suggests that either slip in the rhomb $\langle a \rangle$ direction is only dominant where rotation angles are high or that evidence for rhomb $\langle a \rangle$ slip is obscured by other processes (e.g. grain boundary sliding) at lower misorientation angles.

Rare samples that show c-axis cross girdle patterns with well-developed tails do have corresponding clusters in the basal $\langle a \rangle$ corners of the IPF plots. This indicates that the tails are formed through basal $\langle a \rangle$ slip as the CPO pattern suggests. C-axis patterns of just the large and just the small grains of these samples show cross girdles with tails in both plots. Therefore, the activity of basal $\langle a \rangle$ slip processes do not appear to be grain type-dependent. The formation of the c-axis pattern tails is not solely a result of the formation of new grains via SGR through dominant basal $\langle a \rangle$ slip, but rather the mechanisms and slip systems active in the deformation of the host grains also led to the formation of tails in the c-axis plots.

3.9.4. Misorientation Rotation Angles

Rotation angle histogram profile patterns of the nearest-neighbor misorientation angle between grains in sheared quartz ribbons typically lie between two “end member” types. The first type shows an increase in the number fraction of rotation angles at 10° that stays nearly constant through to 50° where the number fraction increases to the peak at 60° and then drops off at high angles (e.g. 28 and 264, Fig. 3.10). The peak at 60° reflects Dauphiné twins. An increase in the number fraction at low misorientation angles (10 - 20°), which in some cases creates a second prominent peak, indicates the formation of new grains via SGR recrystallization. The progressive rotation of these subgrains may lead to an increase in the number fraction of rotation angles between 20 and 50° (e.g. Trimby et al., 1998). The role of GBM mechanisms in increasing or decreasing rotation angles is not clear, but it is possible that the “flattening” of the misorientation profile between 10 - 50° is an effect of both SGR and GBM processes rather than just progressive rotation of new grains via SGR. The other rotation profile type is best described as a flat nearest-neighbor profile, where the number fraction increases at 10° misorientation and then stays roughly the same from 10° to 95° . A peak at 60° indicates Dauphiné twins, but this peak reflects a lower number fraction around 60° relative to the other misorientation angles and is not as prominent as the other profile type. This “flat” misorientation profile is most common in samples that also display c-axis maxima in orientations coincident with rhomb $\langle a \rangle$ slip.

Differences between the nearest-neighbor misorientation profile and the random-pair misorientation profile should reflect orientation inheritance from the parent grains. In the case of the misorientation profiles from the Sandhill Corner shear zone, the peak at 60° and the greater number fraction around 10 - 20° in the nearest-neighbor profile reflects relationships between Dauphiné twins and parent-daughter relationships resulting from SGR recrystallization, respectively. However, the random-pair misorientation profile may also provide additional information as to the recrystallization mechanisms of the quartz ribbon. First, in those samples that show a nearest-neighbor misorientation profile with number fractions dominantly in the 10 -

50° range, the random-pair misorientation angle profile increases to a peak around 60°, indicating a significant degree of twinning relationships throughout the sample. The samples that display these misorientation profiles are also those samples with the best developed c-axis cross girdle patterns, suggesting that twinning is an important component of quartz recrystallization and CPO development. Conversely, the samples that show a flat nearest-neighbor profile also display a random-pair profile that is the same as the random profile. The CPO for these samples are most likely to show a poorly-developed c-axis pattern, paired c-axis maxima in orientations coincident with rhomb <a> slip, or a single c-axis maximum in an orientation coincident with the inherited fabric. Although the small, Type 3 grains that compose these samples suggest significant amounts of recrystallization, the near random random-pair profile and the poorly developed CPO of these samples suggests that they are incompletely recrystallized.

A more detailed misorientation analysis of a sample containing Type 3 grains with layered grain orientation domains shows different misorientation profiles for each orientation domain (Fig. 3.9). The bulk sample displays a CPO with paired c-axis maxima in orientations coincident with rhomb <a> slip and a misorientation profile with a flat nearest-neighbor misorientation profile and a near random random-pair profile. The domain that plots as a single c-axis maximum in the upper hemisphere of the pole figure coincident with the location of the inherited CPO c-axis maximum shows a nearest-neighbor misorientation angle profile with a higher number fraction in the 10-50° range and a random-pair profile with a broad hump centered around 60°, similar to the first “end member” type described above. The other orientation domain that plots as a single c-axis maximum in the lower hemisphere of the pole figure shows a flatter nearest-neighbor misorientation angle profile with a greater number fraction in higher misorientation angles (>60°). These differences suggest that each orientation domain is deforming in different ways. Unfortunately, there is no clear connection between the misorientation angle profiles of the two domains and the clustering of the rotation axes in the IPF plots that would indicate that the differences are the result of the activity of different well-known

slip systems, although the activity of different paired slip systems may be a factor that would not be easily deduced from the IPF plots.

3.9.5. Factors Affecting Quartz Fabric Development

Combining observations of the quartz microstructure, CPO data, and misorientation data, two general categories of quartz fabrics are apparent: (1) ribbons with a mixture of grain types, cross-girdle c-axis patterns, low angle dominated nearest-neighbor misorientation angle profiles, and random-pair misorientation angle profiles that show a broad peak centered around 60°; and (2) ribbons with layered Type 2 grains, Type 2+3 grains in a core-mantle relationship, or Type 3 grain orientation domains that have poorly-developed CPO patterns; flat nearest-neighbor misorientation angle profiles; and near random random-pair misorientation angle profiles. As described in the sections above, these differences suggest that the dominance of different deformation mechanisms and/or active slip systems led to the different fabric types. Furthermore, the first fabric type is dominantly found in the sheared schist, the protomylonite, and the mylonite transition zone whereas the second fabric type is more commonly found within quartz ribbons from the shear zone core or the quartzofeldspathic mylonites. The association of quartz fabric type with location within the shear zone suggests that across-strike variations in deformation conditions may have affected the evolution of the quartz fabrics, whereas the association with host rock type suggests that differences in the rheology of the rock units may have also influenced the development of the fabrics.

3.9.5.1. Deformation Conditions. Increase in fabric intensity and decrease in grain size with proximity to the core of the Sandhill Corner shear zone indicate strain localization. As the shear zone localized, deformation conditions would have varied across the shear zone. Variations in flow stress, strain rates, and/or temperature would have influenced the dominant deformation mechanism, the grain size, and perhaps even the activity of different slip systems. In addition,

variations in the accumulated strain (via internal recrystallization) would also have influenced the progression of quartz fabric evolution from sample to sample. Although the deformation history indicated by the quartz microstructures is similar across the shear zone (i.e. large grains that deformed via dominant GBM overprinted by smaller grains formed via a combination of GBM and SGR), the shape of the larger grains (Type 1 vs. Type 2 grains) shows that the quartz ribbons closer to the core of the shear zone experienced a greater amount of accumulated strain (Fig. 3.2). This difference may have put the quartz fabrics on different “evolutionary paths”, affecting the mechanism by which they deform and ultimately the resulting fabric.

Differences in deformation conditions not clearly preserved in the microstructural record, particularly variations with the seismic cycle, may also have played a role in the quartz fabric evolution. For example, microfracturing may have driven a decrease in the grain size for many quartz ribbons near the shear zone core where pseudotachylyte and deformed pseudotachylyte are prevalent. These quartz ribbons would not show the misorientation profile and CPO patterns expected for a quartz veins that experienced extensive recrystallization via dislocation creep, and grain size sensitive processes (e.g. grain boundary sliding) may play a more prominent role at such finer grain sizes. Variable strain rates with the seismic cycle may have also affected the deformation mechanisms that were active, perhaps making them time-dependent. SGR and BLG mechanisms may be temporarily dominant over GBM during the elevated strain rates associated with post-seismic creep, affecting the path of fabric evolution. Microstructures suggest that BLG/SGR are active only at the edges of the shear zone (Type 1 + Type 3, Section 3.9.1), and given the association of these microstructures with shear fractures (Fig. 3.4), we propose that this is preserved evidence for transiently elevated strain rates in the rock record that had not been overprinted by subsequent viscous shear. An increased prevalence of Dauphiné twinning has also been associated with the elevated transient stresses associated with pseudotachylyte formation (Springer et al., 2009; Wenk et al., 2011).

3.9.5.2. The Inherited Fabric. The majority of the quartz ribbons of the Sandhill Corner shear zone started with a strong pre-existing fabric. Passive rotation of those ribbons would have controlled the location of the inherited c-axis maximum. If the inherited maximum was in an orientation coincident for easy slip under the conditions of deformation, then those grains would be in “soft” orientation, would slip more easily, and would persist as the sample was progressively recrystallized (Heilbronner and Tullis, 2006b; Takeshita et al., 1999). Given that few samples show evidence for dominant basal $\langle a \rangle$ slip either as tails at the periphery of the c-axis pole figure or as clusters of misorientation rotation axes in the associated regions of the IPF figures, the rotation of the inherited maximum to the edge of the pole figure (via passive rotation of the quartz ribbon) would place the quartz grains in a “harder” orientation. Because c-axis cross girdle patterns and clusters of misorientation axes in the IPF figures suggest that prism $\langle a \rangle$ and rhomb $\langle a \rangle$ slip were more dominant, the rotation of the inherited c-axis maximum to the center of the upper hemisphere or the center of the pole figure would place the quartz grains in “soft” orientations. The location of the inherited c-axis maximum is more commonly found in the rhomb $\langle a \rangle$ position in the schist unit and the more mica-rich protomylonites, while the inherited maximum is more likely to start in the basal $\langle a \rangle$ position in many mylonite samples. This difference in the style of passive rotation of the host quartz ribbons may reflect the accommodation of strain in the more mica-rich rock matrix around the ribbons prior to or during internal recrystallization. Given that the starting placement of the inherited c-axis maxima influences later deformation, differences in the style of rotation would be one explanation for the connection between the resulting quartz fabric and rock type.

Given differences in the starting CPO and the potential for grains to start in a “soft” orientation, how would this have affected the evolution of the quartz fabrics within the shear zone during recrystallization? Consider the second type of quartz fabric: ribbons with layered Type 2 grains, Type 2+3 grains in a core-mantle relationship, or Type 3 grain orientation domains that have poorly-developed CPO patterns; flat nearest-neighbor misorientation angle profiles; and

near random random-pair misorientation angle profiles. The inherited CPO is located in an orientation coincident with rhomb $\langle a \rangle$ slip, a “soft” orientation. This may have facilitated the elongation of the inherited Type 1 grains into Type 2 grains without an accompanying transformation of the c-axis CPO pattern (Neumann, 2000). This is further supported by the distinctly different c-axis pattern of the sheared quartz ribbon that originated as an unfolded pegmatitic vein in the quartzofeldspathic mylonite, where the well-developed c-axis maximum is located at the center of the pole figure rather than in one hemisphere (264, Fig. 3.7). The misorientation rotation axis IPF plots (Fig. 3.11) indicate that prism $\langle a \rangle$ slip is the dominant slip system in the rocks of the Sandhill Corner shear zone, but the most of the pole figures show c-axis maxima coincident with rhomb $\langle a \rangle$ slip. If the c-axis maximum coincident with rhomb $\langle a \rangle$ slip reflects the influence of the inherited CPO, then the c-axis maximum around the Y-axis of the figure of the pegmatitic quartz ribbon (as well as the misorientation rotation angle profile; 264, Fig. 3.10) may represent the CPO pattern that would have been produced if the inherited fabric was not present.

The location of the inherited c-axis maximum in an “easy” slip orientation alone does not prevent the development of a well-developed cross girdle pattern. Consider the first type of quartz fabric: cross-girdle c-axis patterns and low angle dominated nearest-neighbor misorientation angle profiles. The fabric may contain a variety of grain types (including Type 2 grains), and the inherited c-axis maximum is also commonly located in the middle of the upper hemisphere coincident with rhomb $\langle a \rangle$ slip. The persistence of the inherited CPO in these samples is evident in the top-bottom asymmetry of the cross-girdle pole figures and the clustering of points in the middle of the upper hemisphere when only the large “parent” grains are plotted. If slip in grains already in an “easy” orientation drives the persistence of the inherited c-axis pattern and prevents the development of a cross-girdle pattern, then these samples should also display a poorly-developed CPO pattern, but they do not. Therefore, the presence of the inherited fabric in a “soft” orientation does not prevent the development of the new CPO (and cross girdle

c-axis pattern), but under the right conditions can influence the type of fabric that ultimately develops. The difference between the two fabric types observed in the sheared quartz ribbons of the Sandhill Corner shear zone may be a result of differences in the active deformation mechanisms over time, perhaps reflecting differences in the condition of deformation as described above.

3.9.5.3. Twinning and Deformation Mechanisms. The contrasting misorientation data between the two fabric types of the Sandhill Corner shear zone may reflect differences in the active mechanisms operating to form each fabric (i.e. twinning, grain size sensitive processes, and dislocation creep). In the fabric type that shows the well-developed c-axis cross girdle patterns, the nearest-neighbor misorientation profiles show a comparatively greater number fraction for misorientation angles around 60° , and the random-pair profiles show a broad peak around 60° . These indicate a significant component of twin relations throughout those samples that may be related to an increased prevalence of Dauphiné twinning in this fabric type. This is consistent with the well-developed cross girdle c-axis patterns because twinning promotes slip via multiple slip systems in the $\langle a \rangle$ direction (Lloyd, 2004). On the other hand, the other fabric type displays a flat nearest-neighbor misorientation angle profile with a comparatively smaller peak at 60° and a near random random-pair misorientation profile. This suggests a difference in the development of Dauphiné twins or their subsequent modification. Specifically, (a) twinning may not have been as prevalent, (b) it was prevalent but evidence for it has since been lost (e.g. via grain boundary sliding), or (c) twinning operated in conjunction with other mechanisms and its contribution is un- or under-recognized.

Within the fabric that displays the flat nearest-neighbor misorientation profile and layered grain orientation domains, each grain domain displays a different misorientation angle profile. The grain domain that is coincident with the inherited fabric is similar to the fabric type that displays well-developed cross girdles as described above, suggesting that grains with those

orientations are replaced through twinning and SGR mechanisms. The grains in the other orientation display higher nearest-neighbor misorientation angles and a near random random-pair misorientation profile that may reflect active grain boundary sliding in these domains (Fliervoet, et al., 1997, 1999; Jiang et al., 2000). Therefore, if twinning was an important process in these samples, then either it was limited to certain orientations (e.g. only grains with the inherited orientations), or other mechanisms (e.g. grain boundary sliding) operating only in the “uninherited” orientation domains randomized the misorientation angles, obscuring evidence for twinning in those grains. Therefore, samples that show flat nearest-neighbor misorientation profiles may indicate the activity of additional mechanisms, perhaps influenced by the finer grain sizes, and have thus followed a diverging path of fabric evolution.

Twinning may also have played an important part in the development of the contrasting grain orientation domains that display paired maxima in each hemisphere of the c-axis pole figure. If the c-axis maximum in the upper hemisphere was inherited from pre-existing CPO, then there needs to be an explanation for the formation of the lower c-axis maximum. The development of a c-axis maximum in the lower hemisphere may have been associated with Dauphiné twinning through an interchange of the positive {r} and negative {z} rhomb directions (Menegon, et al., 2011; Tullis and Tullis, 1972) and the rotation of the c-axes into the lower hemisphere of the c-axis pole figure through rhomb $\langle a \rangle$ slip. In their study of twinned and recrystallized porphyroclasts, Menegon, et al. (2011) showed that when the r-rhomb twins (which have higher stored elastic strain energy; Tullis and Tullis, 1972) are compared to z-rhomb twins, the r- rhomb twins were more likely to be recrystallized, had twice as many low angle boundaries, and deformed via different slip systems. They suggest that these differences indicate different recrystallization paths for the two twin forms as well as different amounts of accumulated strain. It is possible that twinning had a similar influence in the samples that show a flat nearest-neighbor misorientation profiles and that differences between grain orientation domains or layered Type 2 grains may have started as differences between recrystallized twin forms. In

which case, twinning may have been an important process not only in the formation of the orientation domains but also in controlling the mechanisms of subsequent deformation.

3.9.6. Quartz Fabric Evolution in the Sandhill Corner Shear Zone

Based on the data presented in this chapter, we propose that the differences between quartz fabrics of the Sandhill Corner shear zone were influenced by the host rock CPO as well as the path of quartz fabric evolution. The top-bottom asymmetry observed in the c-axis pole figure of the sheared quartz ribbons reflect the inheritance of the host rock CPO. The location of that inherited CPO, a c-axis maximum in the upper hemisphere of the pole figure, is altered by the passive rotation of the asymmetrically-folded quartz ribbons. The style and degree of passive rotation may vary depending on rock type, indicating that part of the strain may be taken up by mica-rich domains in the rock. Typically, the quartz ribbons are rotated into the strike of the mylonitic foliation, placing the inherited c-axis maximum in the center of the upper hemisphere in an orientation coincident with rhomb $\langle a \rangle$ slip.

Within the mylonite and shear zone core, the host rock quartz grains are recrystallized via GBM to produce stretched ribbon grains. The formation of these grains may have been facilitated by the fact that they are already in “soft or easy” orientations (coincident with rhomb $\langle a \rangle$ slip), inherited from the pre-existing CPO. For this reason, the host CPO may persist even under high strain. Following a decrease in temperature (or an increase in strain rate), SGR mechanisms became more dominant causing an overprint of the ribbon grains via a core-mantle style microstructure and ultimately alternating grain orientation domains (Pauli et al., 1996). The alternating orientation domains correspond to a c-axis maximum in the center of the upper and lower hemispheres of the pole figure, one inherited from the host rock and the other that may have been produced by a combination of early mechanical twinning and rhomb $\langle a \rangle$ dominant slip. The difference in stored elastic energy of the Dauphiné twin forms (Tullis and Tullis, 1972) may have facilitated the formation of the core-mantle microstructure, where one twin more

readily recrystallized over the other (Menegon, et al., 2011). Differences in rotation recrystallization between the two twin forms may have caused the differences in the misorientation rotation angle profiles between the two grain orientation domains (Menegon, et al., 2011), but the randomized random-pair angle profile of one of the domains suggests that grain boundary sliding was also active. Grain boundary sliding may have played a role only in certain parts of the quartz microstructure, such as in the mantle between “parent” grains in the core-mantle microstructure. This would agree with the findings of Halfpenny et al. (2006) that suggest the “mantle” grains may have mixed through grain boundary sliding.

For quartz ribbons within the sheared schist, protomylonite, and mylonite transition zone, Dauphiné twinning was more prevalent, and the “soft” orientation of the inherited CPO may not have been enough to prevent the development of the new CPO. The deformation path of these grains was probably similar to those described in the preceding paragraph (i.e. the inherited CPO representing “soft” orientations and the recrystallized CPO initially dominated by the inherited CPO), but the history of these grains deviated at some point during overprint and recrystallization under GBM/SGR conditions. Conditions closer to the edge of the shear zone (e.g. a transiently higher flow stresses) may have been more conducive to the formation of Dauphiné twins, causing the quartz ribbons in the outer part of the shear zone to develop differently than those near the center of the shear zone. Because these fabrics are present in both the sheared schist and quartzofeldspathic protomylonite, it seems unlikely that these conditions were rock-type specific. Mechanical twinning may have lead to the activity of a greater variety of slip systems, promoting the development of a well-developed cross girdle pattern more characteristic of non-coaxial flow. Perhaps such cross girdle patterns do not readily form where inherited fabrics are in “soft” orientations unless Dauphiné twinning is prevalent.

3.10. Implications for the Deformation History of the Sandhill Corner Shear Zone

The grain types observed in the quartz ribbons of the Sandhill Corner shear zone (Fig. 3.3) and their spatial distribution indicate localization at relatively high temperatures through GBM that was followed by continued dextral shearing through SGR with GBM recrystallization. Although the transition to SGR/GBM could reflect either a decrease in temperature and/or an increased strain rate, we interpret the change to reflect a decrease in temperature, perhaps associated with exhumation as is consistent with the regional geology (West, 1999; West and Hubbard, 1997). The stretched ribbon grains (Type 2) reflect high strains at higher temperatures within the shear zone. They are found with lower aspect ratio Type 1 grains within the mylonite transition zone and the heterogeneously sheared schist but are the dominant higher temperature grain type in the mylonite and the schist closest to the shear zone core, indicating initial localization in the higher temperature part of the shear zone history (Fig. 3.2). Within the mylonite (and parts of the transition zone), the highly sheared schist, and the shear zone core, the higher temperature Type 2 grains (GBM) are overprinted by smaller equant Type 3 grains (SGR/GBM). An incomplete overprint forms core-mantle microstructures whereas a complete overprint leads to a fine grained ribbons with layered grain orientation domains (Pauli et al., 1996). Such overprint is found within the highly-sheared schist, the mylonite, and the shear zone core, and ribbons completely overprinted with only Type 3 grains are primarily found closest to the shear zone core. Although the quartz microstructures show progressive deformation and localization with decreasing temperatures, the data presented in this chapter suggest a divergence in the deformation path of the quartz ribbons to form two “end member” fabrics with contrasting CPO patterns and misorientation angle histogram profiles. One fabric type is more likely found within the mylonite and the shear zone core whereas the other is more common in the sheared schist, the protomylonite, and the mylonite transition zone. This suggests that the differences in the fabric types may be associated with the deformation conditions across the shear zone, which is consistent with the general trends in the microstructural data. Because of the differences in

deformation conditions, we propose that the quartz fabrics developed through different paths possibly by different mechanisms. The deformation associated with the transiently elevated stresses and variable strain rates in the seismic cycle may have also played a role in this divergence. Specifically, the development of more Dauphiné twins, which can be induced by coseismic pulses of transiently high stresses (Springer et al., 2009; Wenk et al., 2011), in the outer part of the shear zone may have been the driving factor in the formation of one fabric type over the other.

In the same way that much of the evidence for coseismic slip in the Sandhill Corner shear zone has been obscured by continued deformation (i.e. the deformation of pseudotachylyte to form abundant ultramylonite layers; Chapter 2), evidence for postseismic creep (and other evidence for coseismic slip) is probably also overprinted by interseismic viscous deformation. Rare atypical microstructures (Fig. 3.5) observed in the mylonites of the Sandhill Corner shear zone that display patchy extinction patterns and heterogeneous distribution of subgrains may represent quartz microstructures that formed during rapidly decaying strain rates associated with the seismic cycle (e.g. Rolandone et al., 2004; Trepmann and Stöckert, 2003). If commonly formed, these types of microstructures have largely been overprinted. Microstructures that show a BLG/SGR overprint (Type 1+ Type 3) at the edges of the shear zone in the protomylonite and heterogeneously-sheared schist may also reflect transiently elevated strain rates, but because interseismic shear deformation is contained within the mylonite and highly-sheared schist, these microstructures had not been overprinted by subsequent viscous shear. An increased prevalence of Dauphiné twinning in the outer shear zone may also be further evidence for elevated transient stresses (Springer et al., 2009; Wenk et al., 2011) that has gone unrecognized in seismogenic shear zones like the Sandhill Corner shear zone. It is interesting to note that mechanical twinning seems to be more prevalent in the fabric type outside of the shear zone core rather than inside where there is a greater proportion of deformed pseudotachylyte, which is opposite of what would be expected (Wenk et al., 2011). Although the evidence for twinning in the other fabric type may

be obscured by additional processes operating in the core of the shear zone, such as grain size sensitive creep or grain boundary sliding.

3.11. Conclusions

Data presented in this chapter show that a host rock CPO may persist in the sheared fabric even at high strains and that under the right circumstances can influence the development of the new fabric. The inherited CPO is reflected as a collection of points in the upper hemisphere of the c-axis pole figure plots, creating a top-bottom asymmetry. If the inherited CPO is in a “soft” orientation during shear deformation, such as in an orientation coincident with rhomb $\langle a \rangle$ slip, then it may hinder the development of the new CPO. This has implications for the interpretation of non-coaxial quartz fabrics because the absence of a well-developed CPO in sheared rock does not necessarily indicate that those rocks did not experience high strains. On the other hand, the placement of the inherited CPO in a “soft” orientation does not preclude the development of a well-developed cross-girdle c-axis pattern, especially if other factors such as twinning mitigate the weakening effect. Therefore, although an inherited fabric does affect the development of the new fabric, the style and degree of the influence is dependent on the mechanisms operating within the evolving fabric and the conditions of deformation over time.

Chapter 4

THE ALONG- AND ACROSS-STRIKE STRUCTURE OF A SHEAR ZONE AT THE BASE OF THE SEISMOGENIC ZONE, NORUMBEGA FAULT SYSTEM, MAINE*

4.1. Chapter Abstract

Determining the structure and rheology of a seismogenic fault at a variety of exposure depths is vital for understanding its strength and behavior. Most important is the structure of a fault within the frictional-to-viscous transition, a depth interval that is coincident with the base of the seismogenic zone and the crustal strength maximum. Using a strand of the Norumbega fault system (a dextral strike-slip, Paleozoic fault system in south-central Maine, USA) that has been exhumed from frictional-to-viscous transition depths (~10-15km), we have developed a detailed view of the structure of a subvertical seismogenic fault at the base of the seismogenic zone and consider the rheology of a fault at such depth levels.

Using several across strike-sample traverses along the Sandhill Corner shear zone, we developed maps of the spatial distribution of rock type, amount of pseudotachylyte and deformed pseudotachylyte, quartz microstructure, and quartz grain sizes. From these maps, we propose across-strike divisions of an outer shear zone, an inner shear zone, and a shear zone core. Overprinting quartz microstructures within monomineralic quartz ribbons indicate a transition from grain boundary migration dominated recrystallization to a combination of grain boundary migration and subgrain rotation recrystallization, consistent with deformation under decreasing temperatures through time (within a range of 400-500°C). In the outer shear zone, this overprint is variable with grain sizes within a range of 10-80µm. In the inner shear zone, the quartz grains are completely overprinted with grain sizes of 10-20µm. Contrasting quartz misorientation and

** The content of this chapter will be submitted for publication in August as: Price et al.*

CPO data also distinguish the inner shear zone from the outer shear zone. The shear zone core is a zone of ultramylonite/phyllonite within the inner shear zone that is rich in pseudotachylyte and deformed pseudotachylyte.

Grain sizes in monomineralic quartz ribbons are remarkably consistent along strike within the inner shear zone, indicating flow stresses of 60-100MPa. The fine-grained, micaceous matrix that surrounds these quartz ribbons would have promoted deformation via grain-size-sensitive, diffusion-mediated creep at a lower flow stress, suggesting that the quartz grains represent a maximum stress estimate for the Sandhill Corner shear zone. This maximum stress estimate is lower than those from other shear zones that were exposed from similar frictional-to-viscous transition depth levels, consistent with a weak inner shear zone and fault core. A weak fault core of deformed-pseudotachylyte-rich ultramylonite and phyllonite at depth correlates well with the weak fault core and principal slip zone of the slip-derived ultracataclasite in the near surface, suggesting mechanical coupling between depth levels.

4.2. Introduction

Determining the structure and rheology of a seismogenic fault at a variety of exposure depths is vital for understanding its strength and behavior. Much of what we know about the across-strike structure and rheology of a fault comes from detailed studies of faults in the near surface (0-5km) where the crust deforms via pressure-dependent fracture and frictional sliding (e.g. Chester et al., 1993; Faulkner et al., 2003; Jefferies et al., 2006a,b; Wibberley and Shimamoto, 2003). However, few studies describe the structure of a fault from within or across the frictional-to-viscous transition, a depth level of importance because it coincides with the base of the seismogenic zone as well as the strength maximum between the upper crust where deformation occurs on discrete surfaces and the mid-to-lower crust where strain is accommodated in broader zones of viscous flow. Among the documented examples of shear zones with coeval

frictional and viscous structures (e.g. Alpine Fault- Toy et al., 2008, 2011; Woodruffe Thrust, Lin et al., 2005; Outer Hebrides Thrust- Sibson, 1980; White, 1996), the Norumbega fault system of Maine is the only (or one of the few) known example(s) with an exhumed fossil frictional-to-viscous transition from a large-displacement, subvertical, strike-slip fault zone (c.f. Sibson and Toy, 2006). This study presents a view of the along- and across-strike structure of the Sandhill Corner strand of the Norumbega fault system and considers the rheology of such a fault at frictional-to-viscous transition depths.

Using several across strike-sample traverses along the Sandhill Corner shear zone, we developed maps of the spatial distribution of rock type, amount of pseudotachylyte and deformed pseudotachylyte, quartz microstructure, and quartz grain sizes. From these maps, we propose across-strike divisions of an outer shear zone, an inner shear zone, and a shear zone core. We discuss the development of this across-strike structure and implication of the microstructural data for the inferred strength and rheology of the shear zone.

4.3. Analytical Methods

Over 200 oriented thin sections and ~125 polished sections from the Sandhill Corner shear zone and host rocks were used in this study. The majority of the samples were collected within three areas of excellent exposure, labeled Sites A, B, and C on the map in Figure 4.1 (refer to the Appendix for detailed sample location information). Samples were cut perpendicular to the subvertical shear foliation and parallel to the subhorizontal lineation.

Quartz microstructural data are based on observations made with the polarized light microscope and orientation maps created using electron backscatter diffraction (EBSD) on polished sections of quartz ribbons (Nowell and Wright, 2004). Quartz grain size ranges were also calculated from mineral orientation maps. Polished sections were mechanically polished to 0.3 μ m grit and chemically polished with a colloidal silica suspension. Electron dispersive spectroscopy (EDS) was coupled with EBSD to create mineral-specific orientation maps using

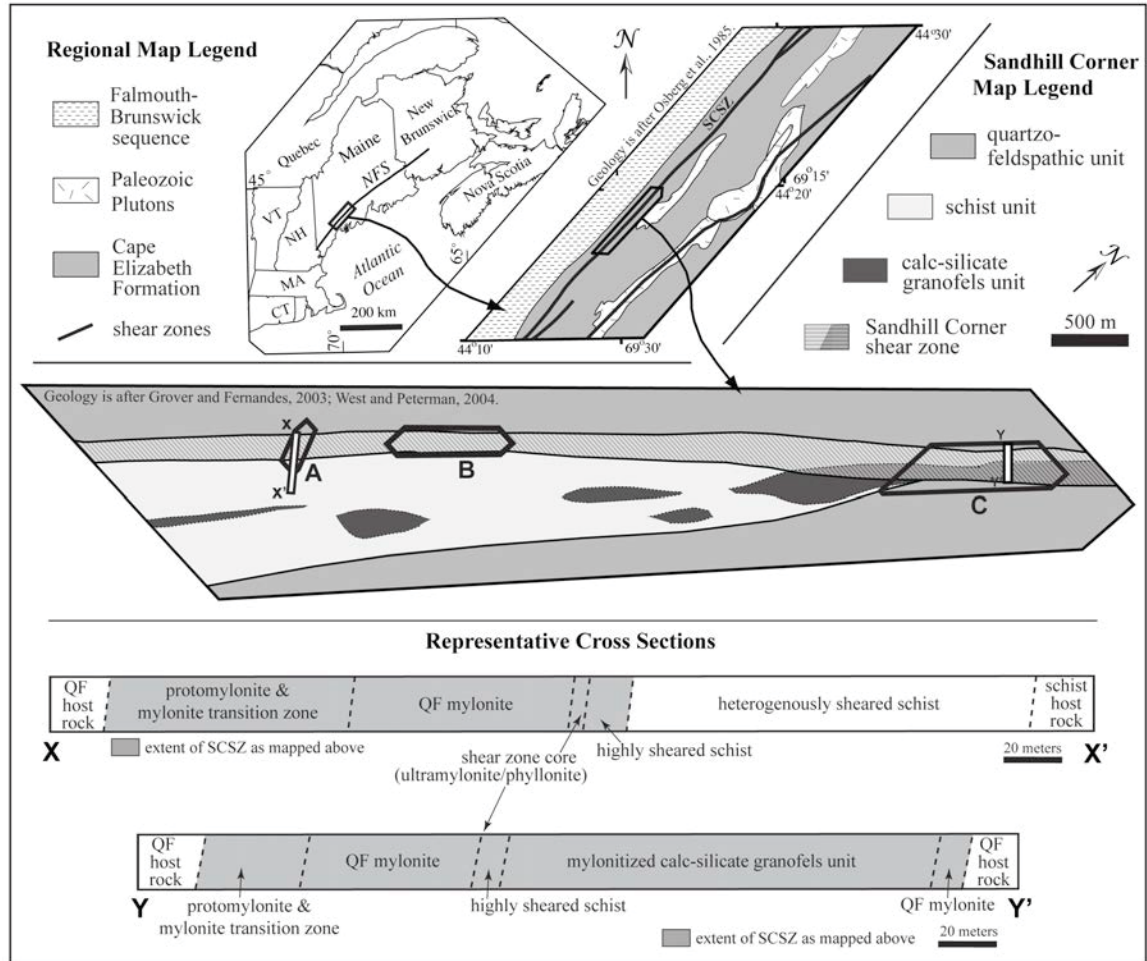


Figure 4.1. Geologic map of the study area within the Norumbega fault system showing the location of Sites A, B and C. X-X' and Y-Y' are representative cross sections of the southern and northern parts of the shear zone, respectively. Regional geology is after Osberg et al. (1985); local geology is after Grover and Fernandes (2003), West and Peterman (2004).

the VEGA-XMU Scanning Electron Microscope at the University of Maine with TSL-OIM Data Collection and EDAX Genesis software. Operating parameters during EBSD data collection on uncoated samples oriented at a 70° tilt at high vacuum included an accelerating voltage of 20kV, a working distance of 25mm, and a probe current of 10nA. Data acquisition parameters for the EBSD were set in the TSL-OIM software at 2x2 binning, high gain, a binned pattern size of 160, a theta step size of 0.5°, 8 bands, and 11 reflector families for quartz. The step size for mineral orientation maps varied between 2µm and ~10µm depending on grain size of the sample.

Quartz EBSD data were cleaned and plotted with the TSL-OIM post-processing software. The data were filtered by confidence index (CI limit of 0.1) and then cleaned to remove spurious points (neighbor CI correlation; minimum CI of 0.1). The confidence index is a parameter used by the processing software to determine pattern indexing accuracy based on a voting system in which each pattern solution is compared to the next best solution and then ranked. A higher CI should correspond to a better result, although in some cases the number of votes for the first two solutions can be exactly the same leading to a correctly indexed orientation but a CI of 0. To recover these points, the data were run through a cleanup routine that increases the CI of a point that has a low CI but the same orientation as a set number of points that surround it (neighbor orientation correlation; tolerance angle 5° , minimum CI of 0.1, clean up level 2). The grain identification parameters were set at a 10° misorientation, a minimum equivalent diameter of triple the step size, and a minimum CI of 0.1. Maps were also cleaned to show one uniform orientation per grain and to remove Dauphiné twins. Quartz grain size ranges reflect peaks on the area fraction-equivalent diameter histograms for each mapped sample. The equivalent diameter is the diameter of a circle with an area equal to the area of the mapped grain. The histograms were divided into 60 bins. Where reported as a single value, we use the diameter equivalent of the highest peak. Quartz c-axis pole figures are equal area, lower hemisphere projections with linear contouring. They were plotted from cleaned mineral orientation maps using one average orientation per grain with the northeast to the right side of the pole figure.

The percent of pseudotachylyte and deformed pseudotachylyte is a qualitative estimate determined from 2x3 inch thin sections. The percent reflects a conservative estimate of the area of the thin section that represents pseudotachylyte veins and pseudotachylyte-derived ultramylonite layers. Because the 200+ samples from the Sandhill Corner described in this study were not investigated with the same degree of scrutiny as the polished samples described in Chapter 3, the percentage estimates are grouped into one of three categories: little to no

pseudotachylyte (0%), some pseudotachylyte up to the average amount calculated in Chapter 2 (0-30%), and an above average amount of pseudotachylyte (>30%).

4.4. Spatial Distribution of Data Within the Sandhill Corner Shear Zone

Observations from samples collected from the Sandhill Corner shear zone within Sites A, B, and C were used to create maps showing the spatial distribution of rock type, the relative amounts of pseudotachylyte and deformed pseudotachylyte, quartz microstructures, and quartz grain sizes (Figures 4.2, 4.3, 4.4). Quartz crystallographic preferred orientation (CPO), grain size, and microstructural data for a representative selection of six samples per site are shown in Figures 4.5, 4.6, and 4.7 (see Figures A.1, A.2, and A.3 for maps showing the locations of all samples used in this study). The spatial distribution of data in each map type is discussed in detail below.

4.4.1. Rock Types

We divided the sheared rocks of the Sandhill Corner shear zone into four “rock types” with an additional rock type in the northern part of the study area (Figures 4.2, 4.3, 4.4). Within Sites A and B, these include from northwest to southeast: the quartzofeldspathic unit (QF) host rock, the QF protomylonite and mylonite transition zone, the QF mylonite, the highly-sheared schist, and the schist host rock (also see Fig. 3.2). Excellent pavement outcrop exposure within Site A shows localized zones of higher strain within the schist host rock outside of the shear zone as it has been traditionally mapped (highlighted in gray in the cross sections of Fig. 4.1). This zone of heterogeneously sheared schist is shown in the cross section in Figure 4.1 (section X-X’), but is not included within the map in Figure 4.2; it continues for an additional ~200-250m to the southeast. The edge of this zone is coincident along strike with the southeastern edge of the wider part of the shear zone shown in Site C (Fig. 4.4). Because of lower quality exposure, it is

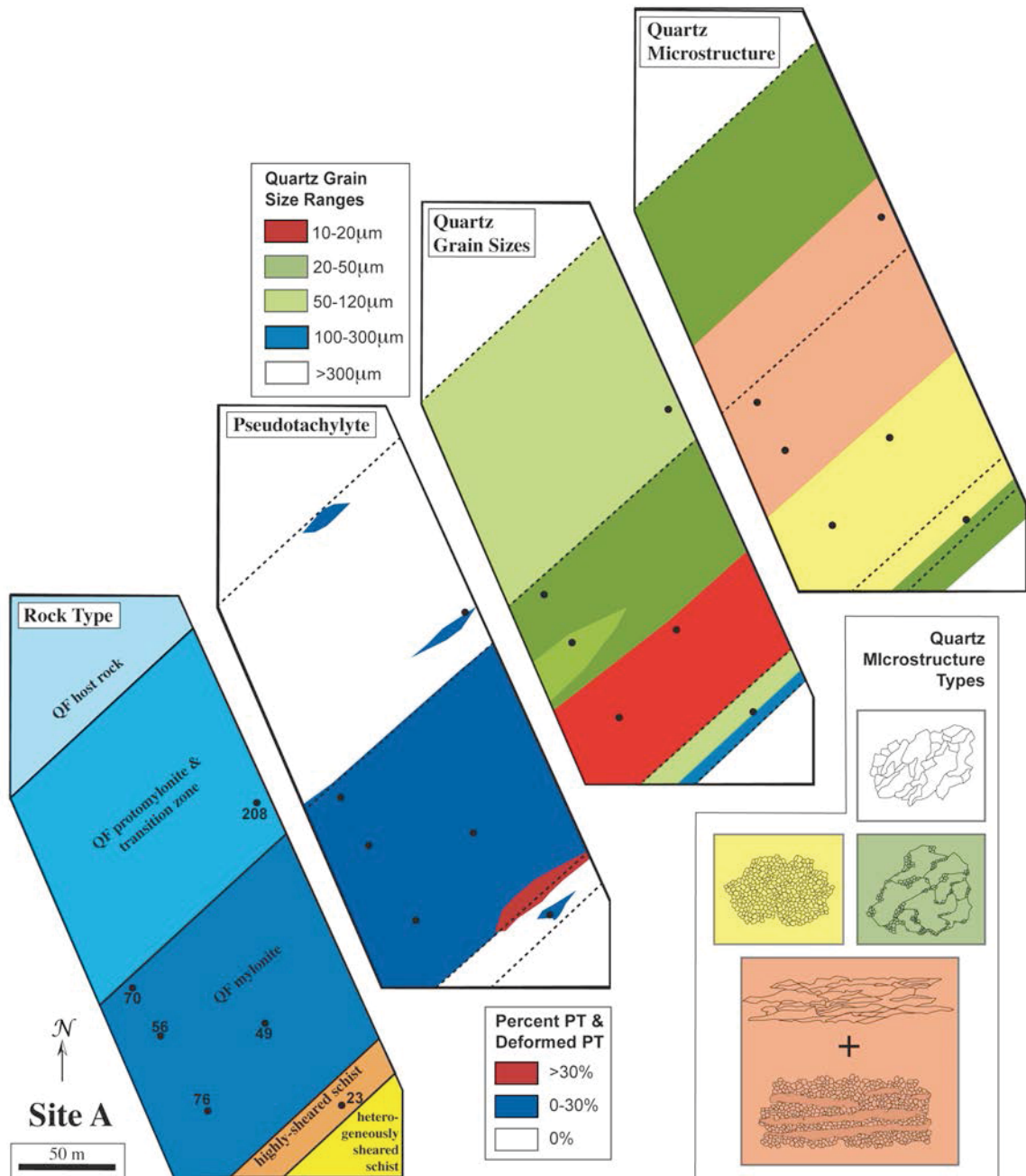


Figure 4.2. Maps of Site A showing the spatial distribution of rock type, the relative amounts of pseudotachylite and deformed pseudotachylite, quartz microstructures, and quartz grain sizes.

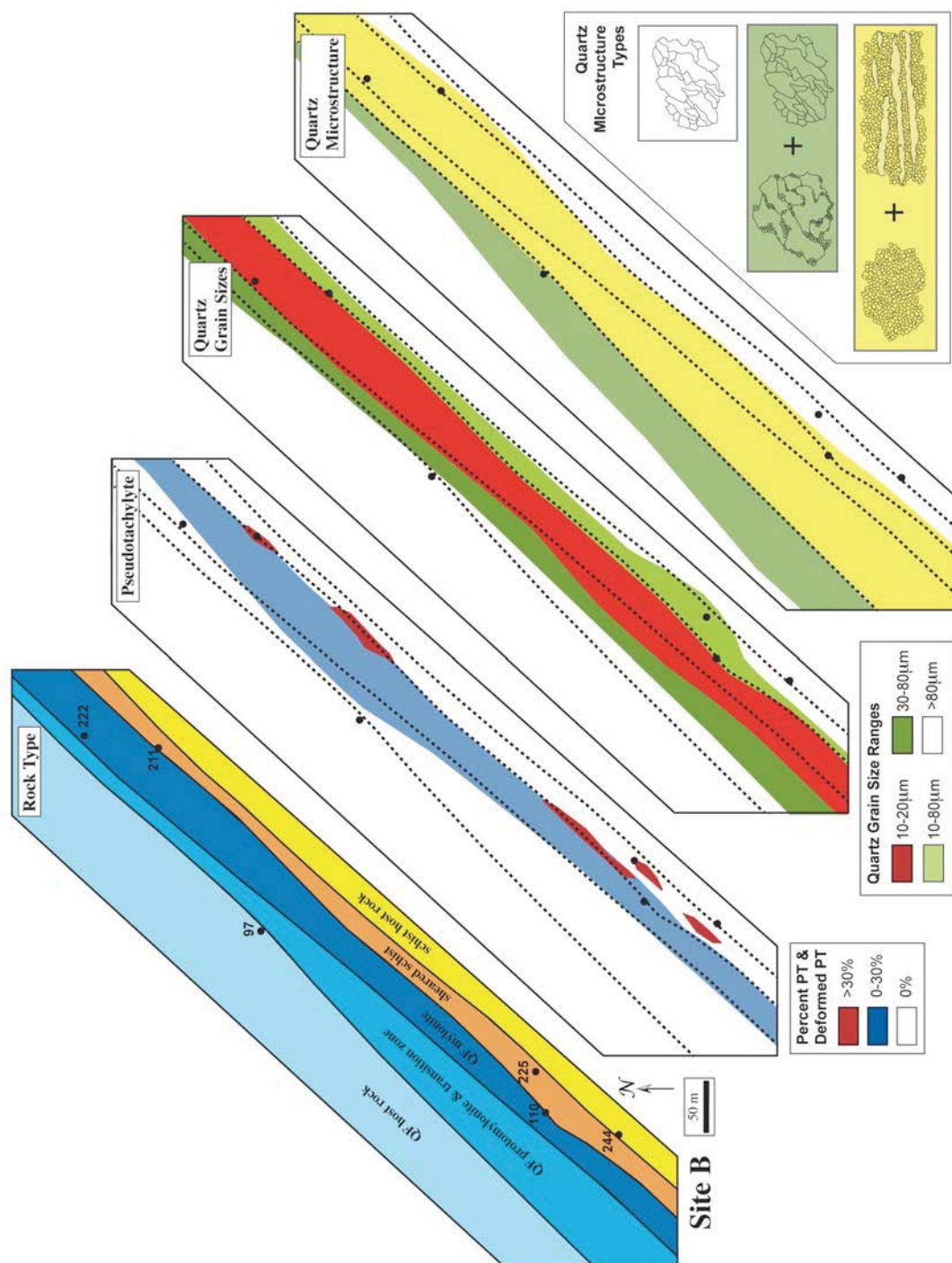


Figure 4.3. Maps of Site B showing the spatial distribution of rock type, the relative amounts of pseudotachylyte and deformed pseudotachylyte, quartz microstructures, and quartz grain sizes.

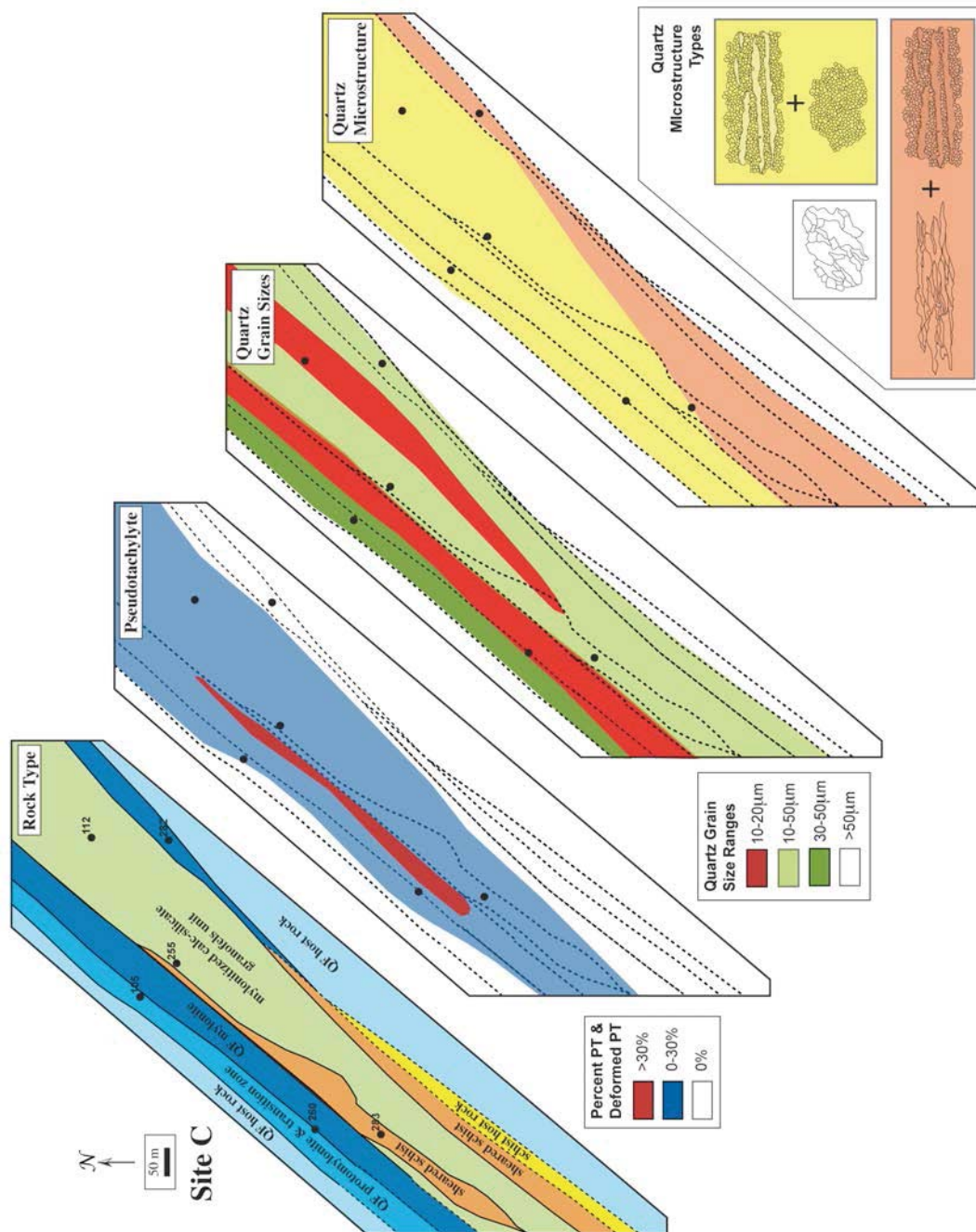


Figure 4.4. Maps of Site C showing the spatial distribution of rock type, the relative amounts of pseudotachylyte and deformed pseudotachylyte, quartz microstructures, and quartz grain sizes.

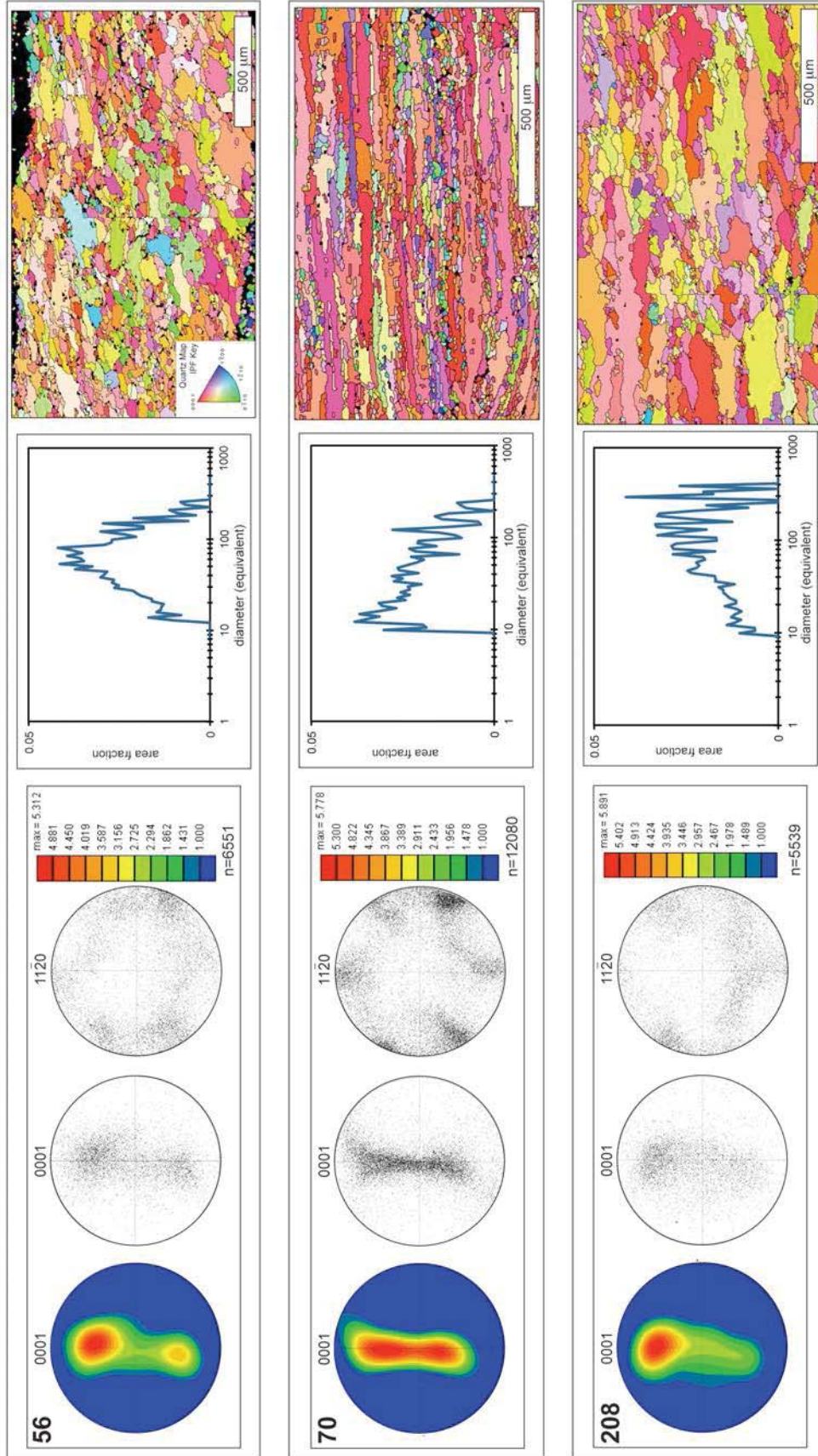


Figure 4.5. Quartz crystallographic preferred orientation (CPO), grain size, and microstructural data for a representative selection of six samples from Site A. The pole figures are equal area lower hemisphere projections plotting one point per grain. C-axis pole figures and grain size data were derived from the SEM-EBSD mineral orientation maps. Colors in the orientation map corresponded to the IPF key provided, and grain boundaries (boundary misorientation of $\geq 10^\circ$) are outlined in black.

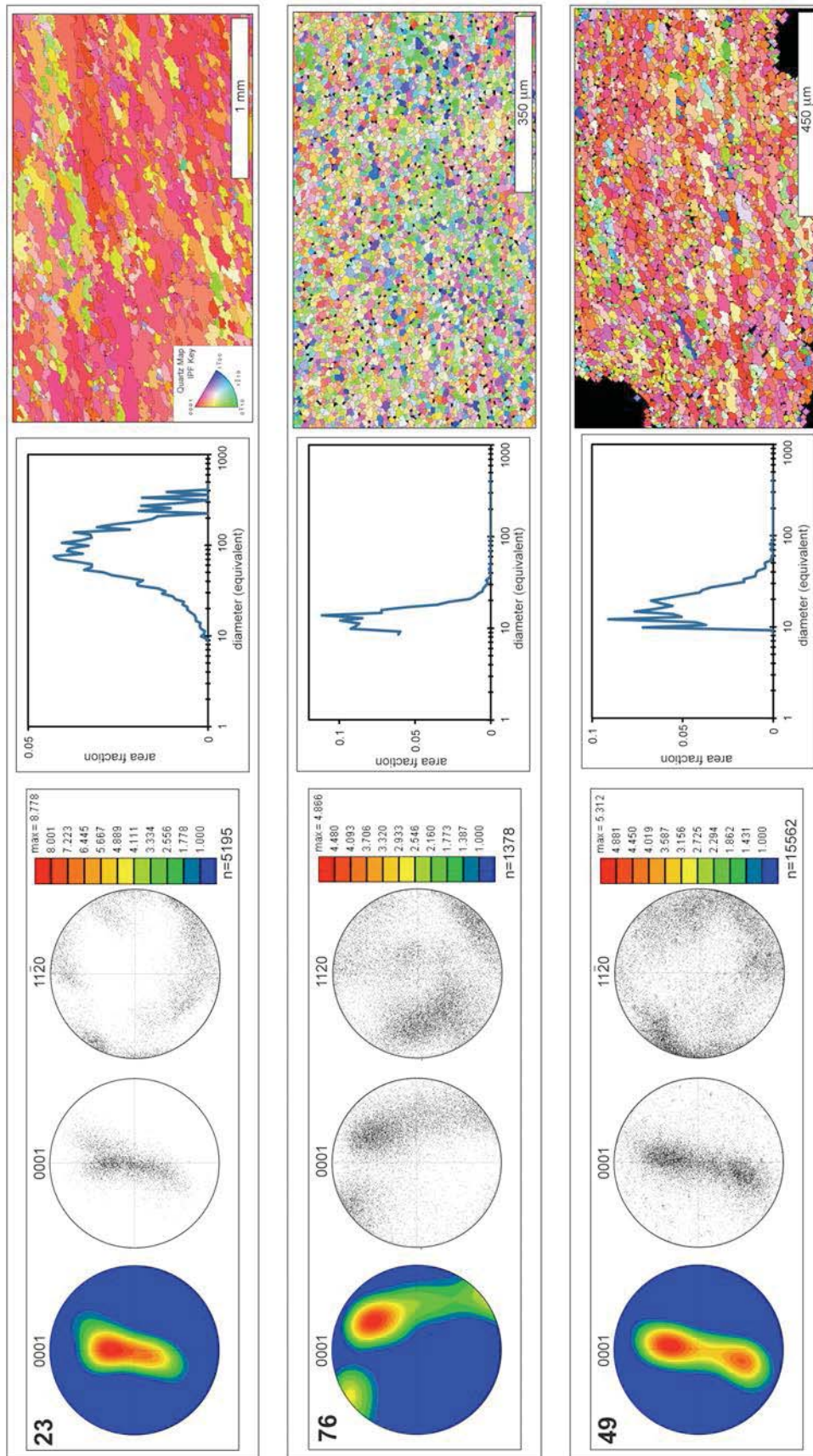


Figure 4.5 (continued). Quartz crystallographic preferred orientation (CPO), grain size, and microstructural data for a representative selection of six samples from Site A. The pole figures are equal area lower hemisphere projections plotting one point per grain. C-axis pole figures and grain size data were derived from the SEM-EBSD mineral orientation maps. Colors in the orientation map corresponded to the IPF key provided, and grain boundaries (boundary misorientation of $\geq 10^\circ$) are outlined in black.

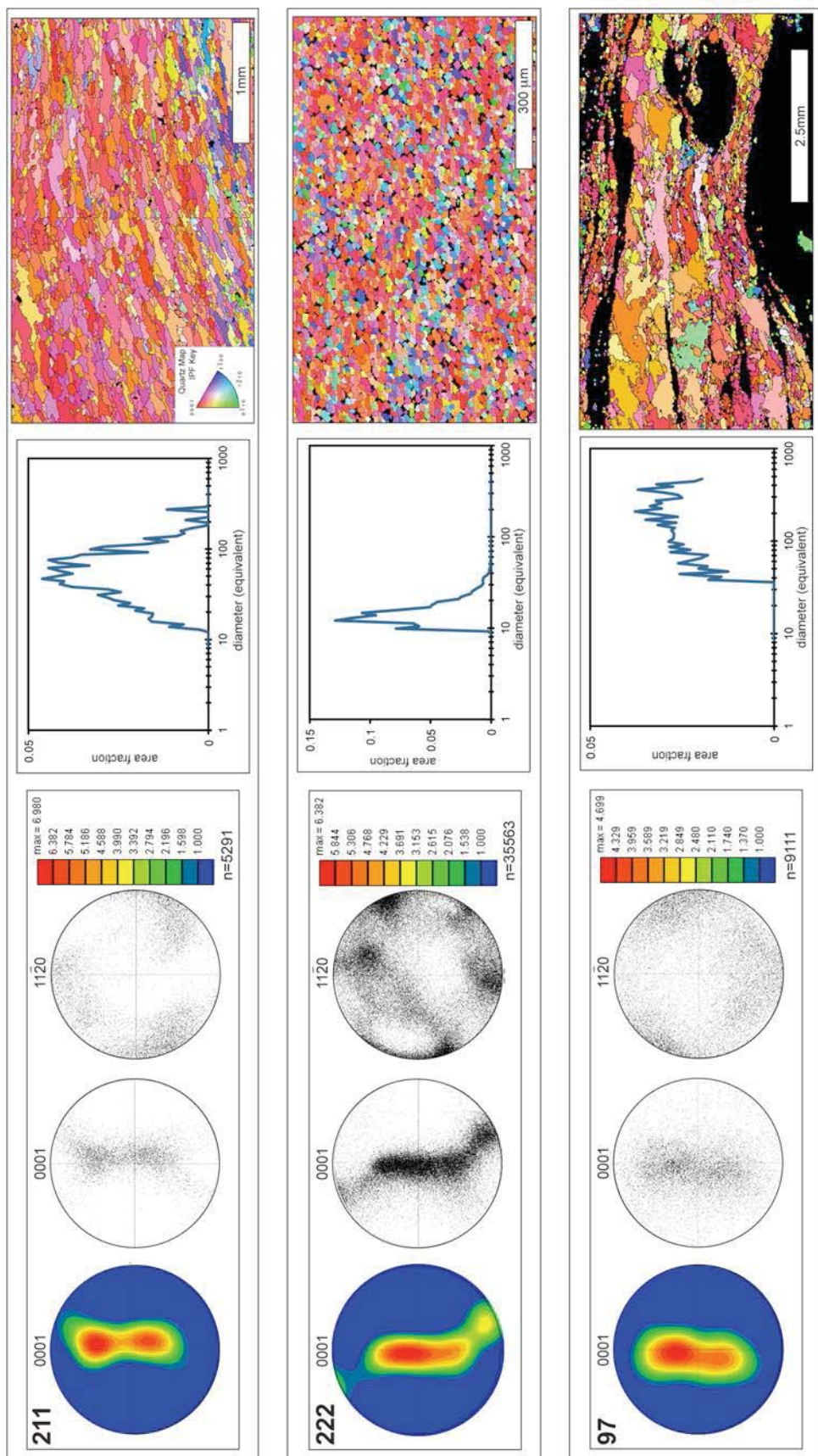


Figure 4.6. Quartz crystallographic preferred orientation (CPO), grain size, and microstructural data for a representative selection of six samples from Site B. The pole figures are equal area lower hemisphere projections plotting one point per grain. C-axis pole figures and grain size data were derived from the SEM-EBSD mineral orientation maps. Colors in the orientation map corresponded to the IPF key provided, and grain boundaries (boundary misorientation of $\geq 10^\circ$) are outlined in black.

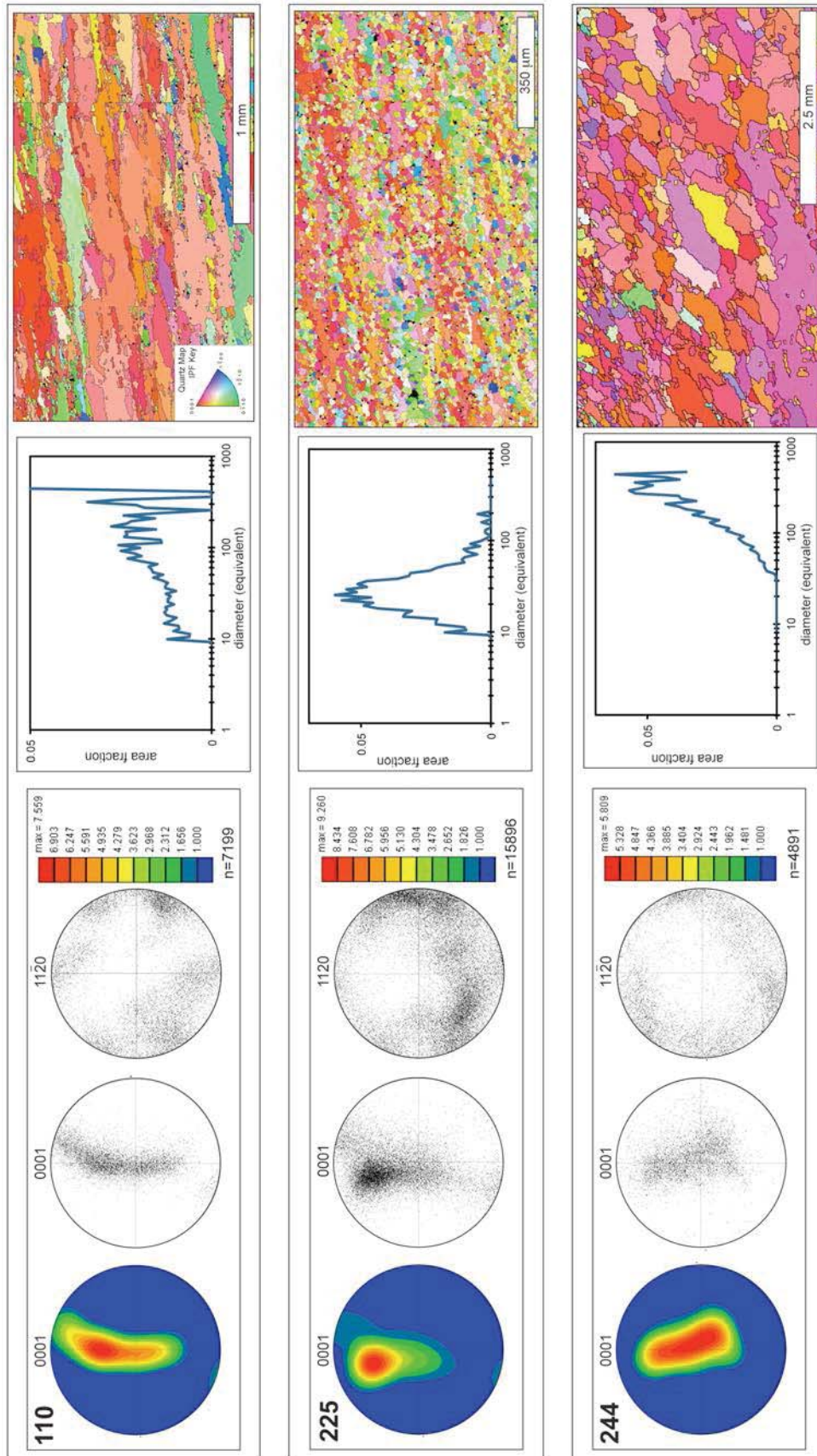


Figure 4.6 (continued). Quartz crystallographic preferred orientation (CPO), grain size, and microstructural data for a representative selection of six samples from Site B. The pole figures are equal area lower hemisphere projections plotting one point per grain. C-axis pole figures and grain size data were derived from the SEM-EBSD mineral orientation maps. Colors in the orientation map corresponded to the IPF key provided, and grain boundaries (boundary misorientation of $\geq 10^\circ$) are outlined in black.

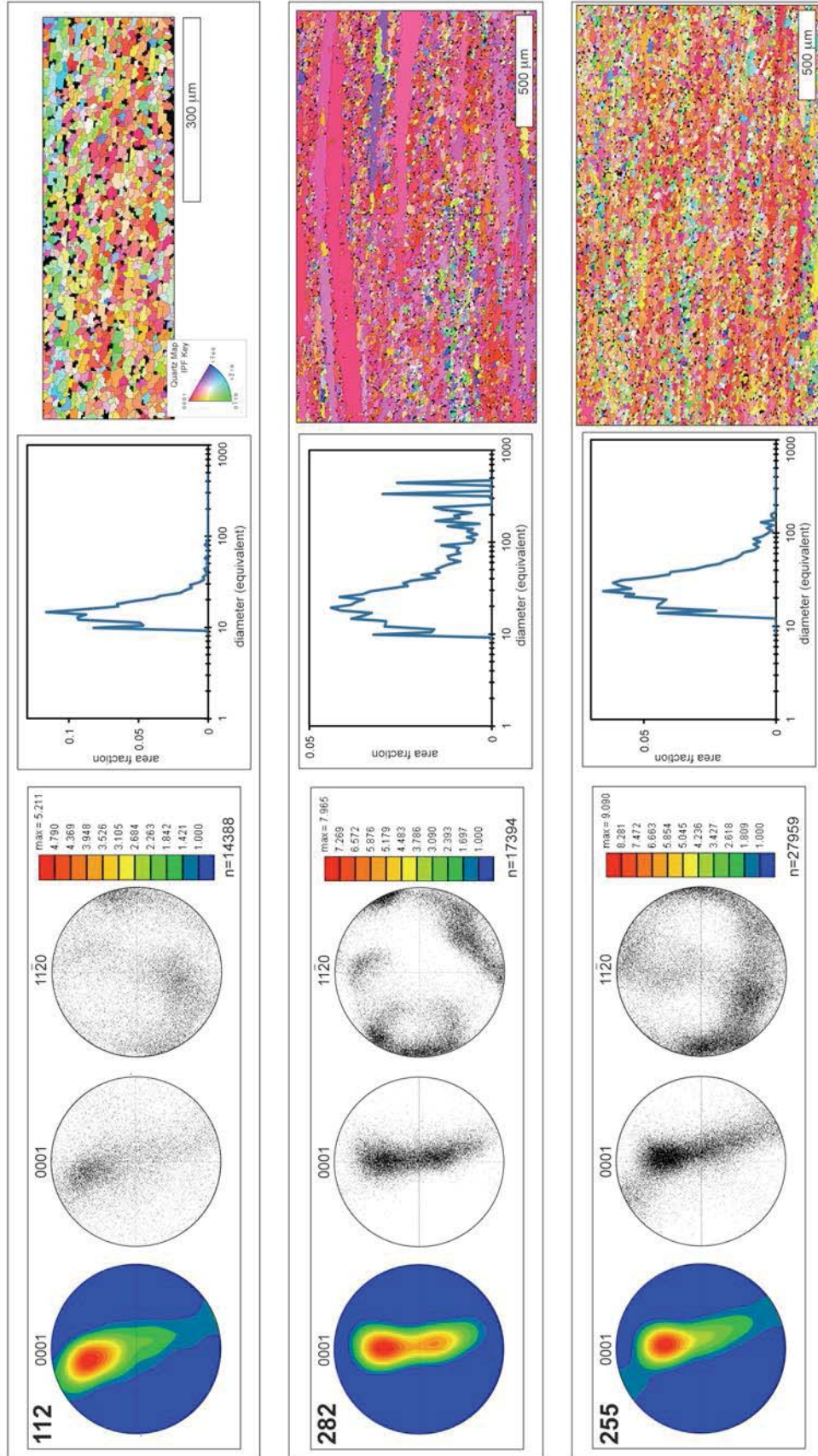


Figure 4.7. Quartz crystallographic preferred orientation (CPO), grain size, and microstructural data for a representative selection of six samples from Site C. The pole figures are equal area lower hemisphere projections plotting one point per grain. C-axis pole figures and grain size data were derived from the SEM-EBSD mineral orientation maps. Colors in the orientation map corresponded to the IPF key provided, and grain boundaries (boundary misorientation of $\geq 10^\circ$) are outlined in black.

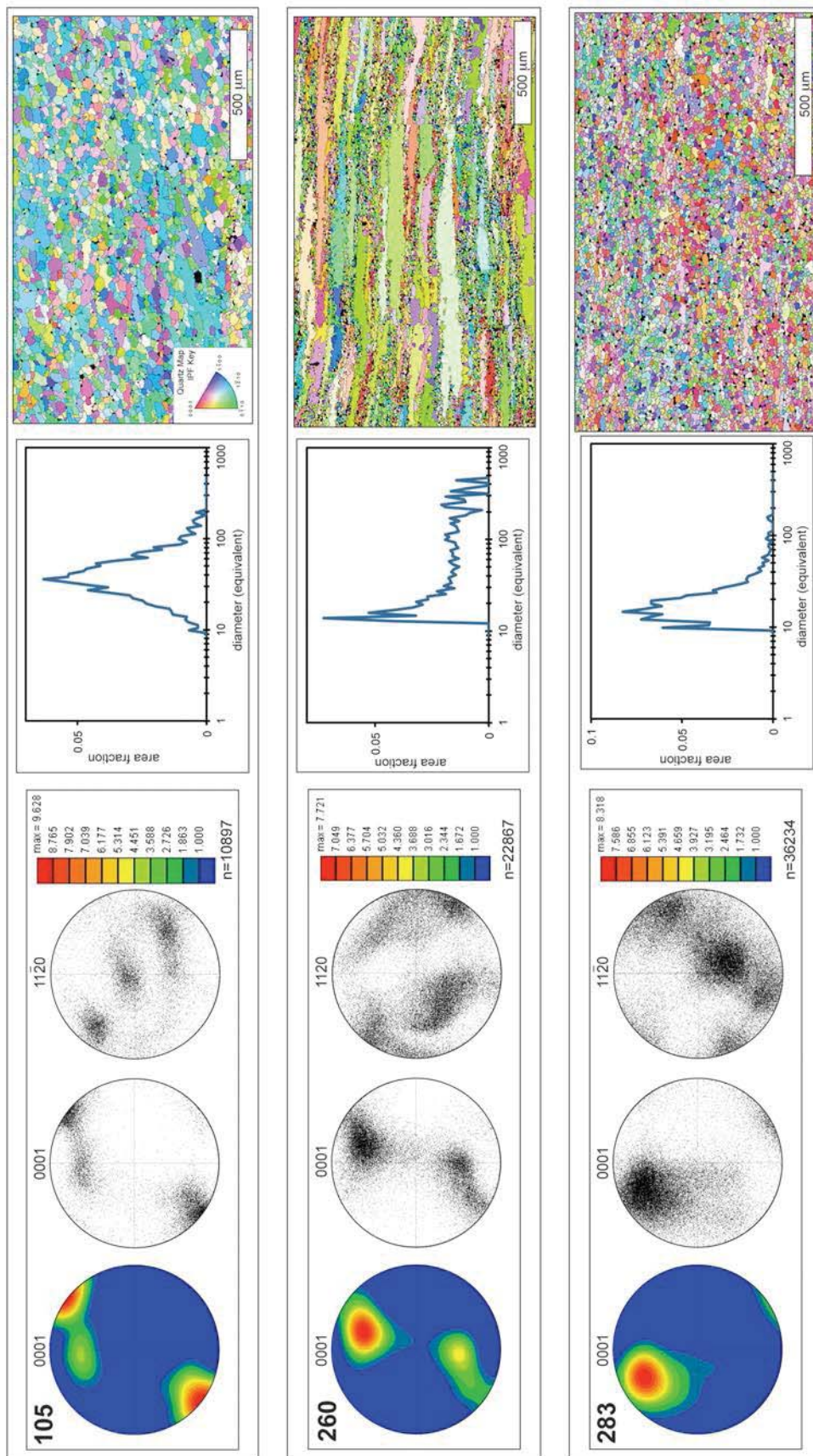


Figure 4.7 (continued). Quartz crystallographic preferred orientation (CPO), grain size, and microstructural data for a representative selection of six samples from Site C. The pole figures are equal area lower hemisphere projections plotting one point per grain. C-axis pole figures and grain size data were derived from the SEM-EBSD mineral orientation maps. Colors in the orientation map corresponded to the IPF key provided, and grain boundaries (boundary misorientation of $\geq 10^\circ$) are outlined in black.

not clear if a similar zone of heterogeneously-sheared schist is present beyond the southeastern edge of the shear zone in Site B (Fig. 4.3). Within Site C, the rock units from northwest to southeast include: the QF host rock, the QF protomylonite and mylonite transition zone, the QF mylonite, the highly-sheared schist, the sheared calc-silicate granofels unit, a second zone of QF mylonite, and the QF host rock (Figure 4.1, section Y-Y'). The second QF mylonite thins to the south in Site C where the southeastern edge is marked by sheared schist and a thin zone of the schist host rock (Fig. 4.4).

The divisions between the above-listed “rock types” are based on differences in composition and/or fabric intensity. For the purposes of this chapter, the host rock is considered unsheared, with asymmetric F3 folds and associated axial planar fabric that do not show pervasive thinning or recrystallization associated with the development of the mylonitic foliation. The host rock at the edge of the shear zone may show some localized fracturing or the quartz ribbons may show a local low temperature overprint (BLG/SGR, see Chapter 3), but these structures do not disrupt the character of the existing fabric in the host rock. The start of the protomylonite is delineated where the F3 folds are flattened and the host rock fabric is overprinted by the new shear fabric. Because the mylonitic rocks are layered within the protomylonite at the transition zone, the protomylonite and transitional mylonite are grouped together into one unit. The start of the mapped QF mylonite is defined where all samples uniformly display a strong shear foliation with a subhorizontal lineation and a fine-grained matrix (~50-90%) that contains porphyroclasts and quartz veins. The sheared calc-silicate granofels unit also follows this definition. The sheared schist (or highly sheared schist in Site A) is distinguished from the schist host rock by pervasive shear banding and asymmetrically-folded (F3) quartz ribbons that are flattened in the shear foliation and noticeably thinned (see Fig. 3.1).

The width of the shear zone and the rock units deformed by the shear zone differ between the northwest and southeast sections. Not including the heterogeneously-sheared schist of Site A, the shear zone is widest in Site C where the calc-silicate granofels unit is incorporated into the

shear zone. The width of the combined QF protomylonite, transition zone, and mylonite is widest in Site A. The protomylonite and transition zone at the northwestern edge of the shear zone in Site C is much thinner, and the change in fabric intensity is more abrupt than in Site A. The sheared schist also thins significantly at Site C.

4.4.2. Pseudotachylyte and Deformed Pseudotachylyte

Both pseudotachylyte and deformed pseudotachylyte are present in all three rock types within the Sandhill Corner shear zone (see Chapter 2). For the purposes of this paper, a pseudotachylyte is a vein of quenched and/or devitrified glass that is formed from frictional melting during seismic slip. A pseudotachylyte vein is recrystallized and viscously deformed to form an ultramylonite layer (i.e. an ultra-fine-grained layer that contain less than 10% porphyroclasts within a coarser-grained mylonite). The estimated average percent of pseudotachylyte and deformed pseudotachylyte is ~30% (see Chapter 2). The pseudotachylyte maps in Figures 4.2, 4.3, and 4.4 show the spatial distribution in of pseudotachylyte and deformed pseudotachylyte based on whether or not a given sample is above or below the average percent. In all three sites (Figures 4.2, 4.3, 4.4), pseudotachylyte is most prevalent in the QF mylonite and the sheared calc-silicate unit where pseudotachylyte-derived ultramylonite layers (dark grey to black layers in the QF mylonite and dark brown layers in the calc-silicate unit) give the rock a mesoscopic banded appearance. The only exception is the QF mylonite at the southeastern edge of the shear zone at Site C, which contains no evidence for pseudotachylyte or deformed pseudotachylyte. Some pseudotachylyte is also present in the protomylonite and transition zone and the sheared schist, but its distribution is highly variable and affected by sampling density.

Overall, the incidence of pseudotachylyte and deformed pseudotachylyte increases with proximity to the lithologic contact. The lithologic contact coincides with a zone of ultra-fine-grained, largely pseudotachylyte-derived ultramylonite/phyllonite rock where the volume of deformed pseudotachylyte is above average, and locally greater than 50%. This

ultramylonite/phyllonite is as wide as ~5m in places, enough to be considered a separate ultramylonite/phyllonite layer as is distinguished as the shear zone core in section X-X' in Figure 4.1. However, the perceived width of this zone is susceptible to effects of sampling density and outcrop availability, and thus is not treated as a distinct unit in the maps of Figures 4.2, 4.3, and 4.4.

4.4.3. Quartz Microstructural and Orientation Data

The presence and/or combination of three quartz grain types within sheared quartz ribbons in rock of the Sandhill Corner shear zone reflect a history of localization and changing deformation conditions (see Chapter 3). Low aspect ratio amoeboid grains formed via grain boundary migration (GBM) recrystallization are inherited from the host rock and, for the purposes of this chapter, reflect the unsheared state of the quartz ribbons (white areas of the microstructure maps in Figures 4.2, 4.3, and 4.4). High aspect ratio grains are stretched versions of the host rock grains that formed at high strains via GBM. These grains are associated with the initial localization of the high strain shear zone and are found within parts of the protomylonite and transition zone, the sheared schist, the calc-silicate unit, and the QF mylonite.

Smaller, more equant grains replace the other two grains via a combination of GBM and subgrain rotation (SGR) recrystallization and reflect a relatively lower temperature overprint. Incomplete overprint forms a core-mantle microstructure that is more common in the protomylonite and mylonite transition zone, parts of the sheared schist, and the outer edge of the QF mylonite. A complete overprint forms a fine-grained microstructure that is primarily found in the calc-silicate unit as well as the sheared schist and QF mylonite closest to the shear zone core (yellow areas of the microstructure maps in Figures 4.2, 4.3, and 4.4); the rocks that display these microstructures also contain higher percentages of pseudotachylyte and deformed pseudotachylyte.

C-axis CPO patterns and grain boundary misorientation rotation angle profiles from quartz ribbons of the inner part of the shear zone that have been completely overprinted are different from those of the incompletely overprinted samples towards the outer edge of the shear zone (see Chapter 3). Quartz ribbons from near the lithologic contact display poorly-developed CPO patterns in c-axis pole figures and misorientation angle histogram plots with flat nearest-neighbor misorientation angle profiles and near random random-pair misorientation angle profiles. Quartz ribbons collected further from the contact display better developed cross-girdle c-axis patterns and misorientation angle histogram plots with low angle dominated nearest-neighbor misorientation angle profiles and random-pair misorientation angle profiles with a broad peak centered around 60° . These differences indicate that the quartz ribbons within the center of the shear zone followed a different strain path via different mechanisms (e.g. twinning or grain boundary sliding) than the quartz ribbons from the edges of the shear zone (see Sections 3.9.5 and 3.9.6), differences that may be related to deformation with the seismic cycle.

At the edge of the shear zone within the host rock, sheared schist, and the protomylonite and mylonite transition zone, the unsheared low aspect ratio grains are also overprinted at their edges by smaller grains. These smaller grains are consistent with a combination of subgrain rotation and bulging recrystallization (green areas of the microstructure maps in Figures 4.2, 4.3, and 4.4), a microstructure that reflects shearing at a lower temperature or a higher strain rate than the deformation associated with the overprint in the center of the shear zone. This may represent evidence for transiently elevated strain rates, perhaps associated with post-seismic creep, preserved at the edges of the shear zone (see Chapter 3).

Although, the across-strike distribution of quartz microstructures as described above is similar among the three sites (Figs. 4.2, 4.3, 4.4), variations in the location and degree of the lower temperatures overprint distinguishes Site A from Sites B and C. Within Site A, there is a progression of microstructures from the QF host rock inward to the core of the shear zone. This includes a zone of the high temperature, high aspect ratio grains at the edge followed by ribbons

with the core-mantle-style overprint microstructure, and finally samples with a complete lower temperature overprint closer to the lithologic contact. The microstructures in Sites B and C are more spatially variable and not as “stratified”.

4.4.4. Quartz Grain Size Data

Peak quartz grain sizes range from 10 μ m to >300 μ m. Grain sizes larger than ~120-150 μ m correspond with the low aspect ratio, amoeboid grains of the host rock, and they reflect the grain sizes inherited from the host rock. The spatial distribution of quartz grain size data within the shear zone suggests two general groups: samples from near the lithologic contact with a tight grain size range of 10-20 μ m and samples further from the contact with a wider range in grain sizes between 10 and 80 μ m.

Samples collected at and near the lithologic contact within the QF mylonite display a peak on the histogram between 10-20 μ m (e.g. 49, Fig. 4.5; 222, Fig. 4.6). These samples display microstructures where the larger grains are completely overprinted by the smaller grains as described in the previous section (Section 4.4.3). Within Site C, there is a second zone in the calc-silicate unit where the quartz grain sizes are also within the 10-20 μ m range and is similarly at the edge of the area where the microstructures show a more complete lower temperature overprint (yellow area of the microstructure map in Fig. 4.4). Using the piezometer of Stipp and Tullis (2003), a grain size range of 10-20 μ m corresponds to a flow stress of ~60-100MPa.

The quartz grain sizes of samples further from the contact within the outer part of the shear zone are more variable between 10 and 80 μ m (e.g. 105, Fig.4.7), with a range of 10-30 μ m at the low end and a range of 50-80 μ m at the high end. The 50-80 μ m sizes at the high end reflect a minimum flow stress of ~20-30MPa, and the 10-30 μ m sizes at the low end indicate flow stresses of ~45-100MPa (Stipp and Tullis, 2003). These samples are commonly located within the sheared schist, the protomylonite and mylonite transition zone, parts of the QF mylonite at the

northwestern edge of the shear zone, and the QF mylonite at the southeastern edge of the shear zone in Site C (green areas of the microstructure map in Figs. 4.2, 4.3, 4.4). They are also typically associated with quartz microstructures that are incompletely overprinted. In Site A where the quartz grains are coarser within a small region of the QF mylonite (20-50 μm vs. 50-120 μm , Fig. 4.2), the size and types of porphyroclasts in the mylonite suggest that these samples came from what was originally a coarse-grained pegmatite body, indicating that some variations in grain size may also reflect differences in the host rock type.

4.5. Discussion

4.5.1. The Structure of the Sandhill Corner Shear Zone

Figure 4.8 shows the proposed across-strike divisions of the Sandhill Corner shear zone: an outer shear zone, an inner shear zone, and the shear zone core. The edge of the outer shear zone is defined by the extent of evidence for deformation associated with the new shear foliation (as discussed in Section 4.4.1). The outer shear zone contains quartz ribbons that display (a) a microstructure of larger grains formed by GBM recrystallization incompletely overprinted by smaller grains formed via a combination of GBM and SGR recrystallization; (b) better-developed cross-girdle c-axis pole figures; (c) misorientation angle histogram plots with low angle dominated nearest-neighbor misorientation angle profiles and random-pair misorientation angle profiles with a broad peak centered around 60°; and (d) variable peak grain sizes within a range of 10-80 μm . The outer shear zone contains a range of rock units, including the protomylonite and mylonite transition zone, most of the sheared schist, and parts of the QF mylonite and sheared calc-silicate unit.

The inner shear zone in contrast contains quartz ribbons that display (a) a microstructure completely overprinted by smaller grains formed via a combination of GBM and SGR

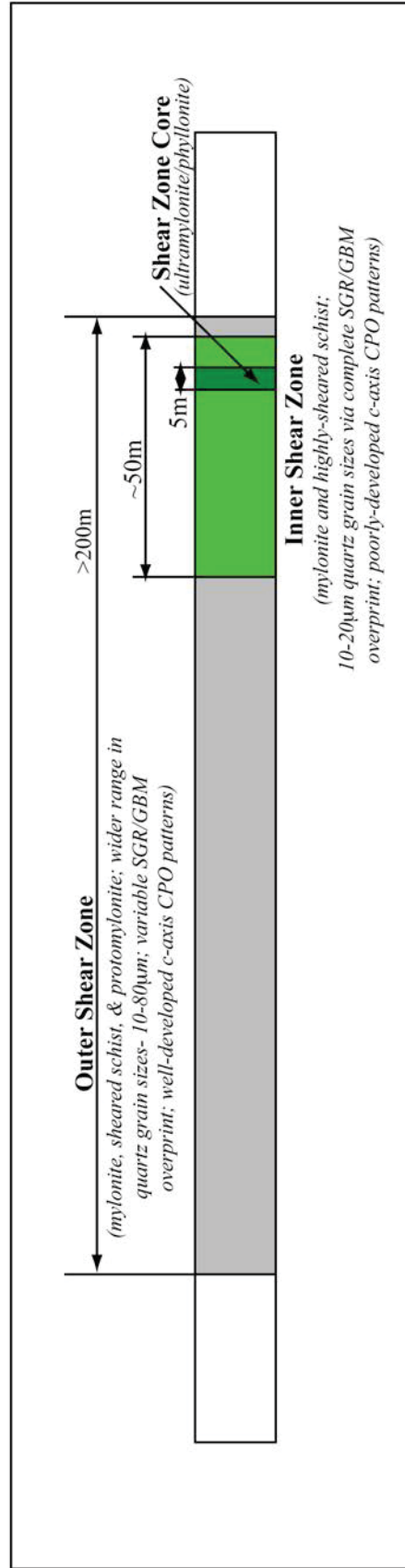


Figure 4.8. Schematic diagram showing the across-strike structure of the Sandhill Corner shear zone.

recrystallization; (b) poorly-developed cross-girdle c-axis pole figures; (c) misorientation angle histogram plots with flat nearest-neighbor and near random random-pair misorientation angle profiles; and (d) grain sizes consistently within a range of 10-20 μm . The quartz microstructural and orientation data is gradational between the inner and outer “end members”. For the purposes of this chapter, the division between the inner and outer shear zone is set at the boundary between the red and green zones in the grain size maps of Figures 4.2, 4.3, and 4.4, or at the edge of the zone with grain sizes consistently within 10-20 μm . Using this division, the inner shear zone contains the parts of the QF mylonite, sheared calc-silicate unit, and sheared schist closest to the lithologic contact where rocks have a relatively higher percentage of deformed pseudotachylyte and display the greatest fabric intensity.

The shear zone core is coincident with the contact between the quartzofeldspathic and schist units. It is defined as the zone of ultra-fine-grained, largely pseudotachylyte-derived ultramylonite/phyllonite rock at the lithologic contact within the inner shear zone where the volume of deformed pseudotachylyte is above average, and locally greater than 50%. Although the ultramylonite/phyllonite core appears discontinuous and its width variable (due to exposure and sampling density), the core is distinct enough to be considered an important component of the across-strike structure.

In the northern part of the study area, a calc-silicate granofels unit is incorporated into the shear zone and influences the thickness and across-strike structure of the shear zone. Despite the lithologic complexity, the grain size data within the outer shear zone is comparable along strike, with only minor differences in the maximum grain size of the range, and the grain sizes in the inner shear zone are consistently within 10-20 μm . In addition, the shear zone core, as distinguished by the increased percentage of deformed pseudotachylyte, remains along the contact between the quartzofeldspathic and schist units. The spatial distribution of quartz grain sizes within Site C suggests a second zone where quartz grain sizes are consistently within 10-

20 μ m that by the definition established above should be considered another “inner shear zone”. However, there is not an accompanying increase in the percentage of deformed pseudotachylyte within this zone to suggest a secondary core. For this reason, although the across-strike structure proposed in this chapter is based on the structure of Sites A and B, it is also applicable to Site C.

4.5.2. Interpreting the Deformation History of the Sandhill Corner Shear Zone

The Sandhill Corner shear zone initially localized along the contact between units two rheologically-contrasting units (the quartzofeldspathic and schist units). Quartz microstructures indicate host rock fabrics formed within the GBM field and that the shear zone, as represented by the width of the outer shear zone, also localized while GBM recrystallization was dominant. SGR is active from ~350 up to 500°C, GBM becomes active above 400-500°C, and GBM dominates above 500°C (Stipp et al., 2002a,b). Therefore, regional distributed dextral deformation formed the host rock fabrics when the temperature was above 500°C, and the initial localization of the Sandhill Corner shear zone probably occurred above or near 500°C as well. Fracture and frictional sliding was dominant in feldspar in the Sandhill Corner shear zone. Dislocation creep in feldspar becomes active between 450-600°C (Passchier and Trouw, 2005), so it is unlikely that initial localization occurred at temperatures much greater than 500°C.

The progression of quartz deformation mechanisms from GBM-dominant to a combination of GBM and SGR recrystallization mechanisms is reflected in the outer shear zone. This transition represents a decrease in temperature and/or an increase in strain rate over time (see Section 3.3.1). For water present strain rates of 10^{-12} to 10^{-14} sec⁻¹, SGR is active from ~350 up to 500°C, and GBM becomes active above 400-500°C (Stipp et al., 2002a,b). The later overprint of GBM with SGR places the continued shearing in the Sandhill Corner shear zone within a temperature range of 350-500°C. Only a few, rare quartz ribbons display microstructures consistent with SGR with little to no contribution of GBM, suggesting deformation conditions were above 400°C for much of the deformation history. The lack of evidence for pervasive BLG

recrystallization, which operates from ~280 up to 400°C, and the presence of biotite (and possibly metastable garnet- see Chapter 2) within deformed pseudotachylyte also support a range in deformation temperatures of 400-500°C.

The quartz CPO and misorientation data strongly suggest that at some point during shear deformation under conditions associated with SGR/GBM recrystallization, the deformation history of the quartz in the outer shear zone deviated from that of the inner shear zone. The complete SGR/GBM microstructural overprint indicates higher strains within the inner shear zone, and the quartz grain size data indicates that the inner shear zone was flowing at comparatively higher stresses, and probably higher strain rates, than the outer shear zone. However, variations in strain rate (interseismic) across the shear zone were not great enough to affect the across-strike distribution of quartz microstructures (e.g. microstructures indicate consistent SGR/GBM recrystallization across strike rather than an increased prevalence of SGR or BLG recrystallization within the inner shear zone or shear zone core).

The association between the inner shear zone and a higher percentage of pseudotachylyte and deformed pseudotachylyte suggests that the formation of the inner shear zone was associated with the seismogenic history of the fault. During the coseismic and post-seismic periods, elevated stresses and strain rates that were associated with the formation of pseudotachylyte in the inner shear zone would have loaded the outer shear zone. A higher degree of mechanical twinning in quartz ribbons of the outer shear zone, perhaps induced by transiently high stresses, is consistent with this view. In addition, the microstructures formed by a combination of bulging and subgrain rotation at the edges of the shear zone may be associated with elevated strain rates (or lower temperatures; see Chapter 3), suggestive of post-seismic creep. Recrystallization mechanisms in quartz operating during the interseismic periods would act on the transient microstructures differently (as is suggested by the more completely-developed CPO patterns in the outer shear zone; see Chapter 3) leading to the difference in the microstructural data. It is not well understood what caused the misorientation profiles common in the inner shear zone

(Fig. 3.10), but microfracturing or grain boundary sliding, perhaps affecting only quartz ribbons near the core of the shear zone, may have played a role.

Absolute timing of deformation within the Sandhill Corner shear zone is unclear. Apatite fission track and $^{40}\text{Ar}/^{39}\text{Ar}$ mineral cooling ages in south-central Maine (see Chapter 1) provide only limited timing constraints. $^{40}\text{Ar}/^{39}\text{Ar}$ cooling ages indicate regional cooling in the vicinity of the study area through $480\pm 20^\circ\text{C}$ (hornblende) between 380-365Ma and through $320\pm 20^\circ\text{C}$ (muscovite) between 320-340Ma (see Chapter 1; West and Lux, 1993; West and Hubbard, 1997). This suggests that the shear zone probably started to localize before or around 365Ma and that deformation ended by 320-340Ma, a span of ~40-60my, and possibly as short as 20my. However, the muscovite $^{40}\text{Ar}/^{39}\text{Ar}$ age of a mylonite sample from the Sandhill Corner shear zone (within Site A of this study), is 290Ma reflecting a range of ~80-90my of either continued or punctuated deformation (West and Lux, 1993). The younger muscovite age suggests that either (a) the shear zone remained at an elevated temperatures longer than the surrounding rock or (b) deformation/recrystallization of muscovite continued under temperature condition below $320\pm 20^\circ\text{C}$. Given a $\sim 5^\circ\text{C}$ per million cooling rate (determined from the regional mineral cooling ages), spatial temperature constraints from older cooling ages from samples collected nearby the shear zone, a lack of pervasive chloritization within the shear zone, and higher temperature conditions implied by quartz microstructures, the 290Ma age cannot currently be explained by either elevated temperatures conditions or low-temperature deformation. Because of the overprinting nature of the deformation and the ambiguity in the absolute timing constraints, it is unclear how much time deformation on the Sandhill Corner shear zone represents, and whether that deformation was continuous or episodic between periods of relatively little displacement.

4.5.3. Shear Zone Rheology and Fault Strength

Multiple generations of pseudotachylite that preferentially formed at or near the lithologic contact may have helped to stabilize a shear zone core and inner shear zone along the

lithologic contact that was weak in flow (see Chapter 2). The recrystallization and deformation of pseudotachylyte creates a rock in which the matrix would have been flowing during interseismic periods at a lower flow stress than the porphyroclasts and quartz ribbons through grain size sensitive creep and slip in progressively interconnected mica networks.

Quartz grain sizes indicate that quartz ribbons were experiencing flow stresses between 60-100MPa. Because the fine-grained matrix surrounding these ribbons would be deforming at lower flow stresses, 60-100MPa represents a maximum flow stress for the Sandhill Corner shear zone. This maximum stress estimate is lower than those from other shear zones that were exposed from similar frictional-to-viscous transition depth levels (>100MPa from sheared granitoids from the Whipple Metamorphic Core Complex; e.g. Behr and Platt, 2011), consistent with a weak fault core at the frictional-to-viscous transition (e.g. Holdsworth, 2004). Although the fault core may be relatively weak in interseismic flow, the abundance of pseudotachylyte at the fault core indicates that the strength of a fault zone across the frictional-viscous-transition was still strong enough for frictional slip rather than aseismic creep.

Use of the quartz grain size data hinges on the assumption that the stress estimates from the recorded quartz grain sizes of monomineralic ribbons are representative of the interseismic deformation conditions within the Sandhill Corner shear zone. It is important to consider whether quartz grain sizes truly reflect recrystallization via dislocation creep during interseismic steady state flow. Grain size reduction may have been facilitated by pervasive microfracturing or the grain sizes may have recorded transiently high stresses rather than interseismic conditions, both of which could lead to an overestimation of the flow stresses. Atypical quartz microstructures, for example, (see Chapter 3) may reflect such evidence for postseismic creep. Yet, these microstructures are rare and are found primarily near pseudotachylyte veins, suggesting that transient microstructures were largely overprinted during the interseismic periods and may not have affected the quartz grain sizes. Quartz orientation data from the inner shear zone may also indicate the operation of other deformation mechanisms, such as microfracturing or grain

boundary sliding. The flat nearest-neighbor misorientation angle profiles, the near random random-pair misorientation angle profiles, and the poorly-developed CPO pattern in the c-axis pole figures from quartz ribbons from the inner shear zone are inconsistent with high strains via dislocation creep recrystallization. However, quartz grain sizes are remarkably consistent along strike. Whatever mechanism is driving grain size reduction, it is operating within all parts of the inner shear zone maintaining a 10-20 μ m grain size.

4.5.4. Correlation With Other Crustal Levels

A weak fault core of ultramylonite and phyllonite at depth correlates well with the weak core of ultracataclasite in the near surface, and the inner shear zone of the Sandhill Corner shear zone may reflect the lower crustal equivalent of the fault core in the near surface. The increased fabric intensity, and higher percentage of pseudotachylyte and deformed pseudotachylyte in the inner shear zone suggest that much of the interseismic and coseismic deformation is focused within the inner shear zone and shear zone core in the same way that much of the displacement in the upper crust is localized within the fault core and principal slip zone forming cataclasite and ultracataclasite. Seismic rupture propagates down into the frictional-to-viscous transition from higher crustal levels forming pseudotachylyte that when recrystallized and deformed creates fine-grained layers that are weaker than the host rock, establishing the shear zone core. A localized, weak shear zone core and inner shear zone deforming at higher strain rates would concentrate and more effectively transfer stresses from bottom-driven flow up to higher crustal levels. A focused core and inner shear zone deforming at a higher strain rates may also drive strain localization in shear zones below the frictional-to-viscous transition. In this way, mechanical communication between crustal levels may have helped to develop a similarly weak core at other depths within a fault.

4.6. Summary and Conclusions

The spatial distribution of rock type, amount of pseudotachylyte and deformed pseudotachylyte, quartz microstructure, and quartz grain sizes within the Sandhill Corner shear zone of the dextral strike-slip Norumbega fault system of Maine provides a detailed view of the across-strike structure of a shear zone at the base of the seismogenic zone exhumed from frictional-to-viscous transition depths.

The Sandhill Corner shear zone contains an outer shear zone, an inner shear zone, and a shear zone core. The shear zone core is a zone of ultra-fine-grained, largely pseudotachylyte-derived ultramylonite/phyllonite rock at the lithologic contact. The surrounding shear zone is divided into outer and inner parts based on quartz microstructural and orientation data from monomineralic quartz ribbons. The outer shear zone contains quartz ribbons that display (a) a microstructure of larger grains formed by GBM recrystallization incompletely overprinted by smaller grains formed via a combination of GBM and SGR recrystallization; (b) better-developed cross-girdle c-axis pole figures; (c) misorientation angle histogram plots with low angle dominated nearest-neighbor misorientation angle profiles and random-pair misorientation angle profiles with a broad peak centered around 60° ; and (d) variable peak grain sizes within a range of 10-80 μm . The inner shear contains quartz ribbons that display (a) a microstructure completely overprinted by smaller grains formed via a combination of GBM and SGR recrystallization; (b) poorly-developed cross-girdle c-axis pole figures; (c) misorientation angle histogram plots with flat nearest-neighbor and near random random-pair misorientation angle profiles; and (d) grain sizes consistently within a range of 10-20 μm .

Quartz grain sizes indicate that quartz ribbons within the inner shear zone were deforming at flow stresses (interseismic) between 60-100MPa. The matrix surrounding the quartz ribbons are rich in deformed pseudotachylyte. This fine-grained, mica-rich matrix would deform at a lower flow stress than the quartz ribbons through grain size sensitive creep and slip in

progressively interconnected mica networks. Because of this, 60-100MPa represents a maximum flow stress for the Sandhill Corner shear zone. A weak fault core of deformed-pseudotachylyte rich ultramylonite and phyllonite at depth correlates well with the weak fault core and principal slip zone of the slip-derived ultracataclasite in the near surface, suggesting mechanical coupling between depth levels.

REFERENCES

- Behr, W.M., Platt, J.P., 2011. A naturally constrained stress profile through the middle crust in an extensional terrane. *Earth and Planetary Science Letters* 303, 181-192.
- Bjørnerud, M., 2010. Rethinking conditions necessary for pseudotachylyte formation: Observations from the Otago schists, South Island, New Zealand. *Tectonophysics* 490, 69-80.
- Bos, B., Spiers, C.J., 2002. Frictional-viscous flow of phyllosilicate-bearing fault rock: Microphysical model and implications for crustal strength profiles. *Journal of Geophysical Research* 107, B22028, doi:10.1029/2001JB000301.
- Brace, W.F., Kohlstedt, D.L., 1980. Limits on lithospheric stress imposed by laboratory experiments. *Journal of Geophysical Research* 85, 6248–6252.
- Caine, J.S., Evans, J.P., Forster, C.B., 1996. Fault zone architecture and permeability structure. *Geology* 24, 1025-1028.
- Chester, F.M., Evans, J.P., Biegel, R.L., 1993. Internal Structure and Weakening Mechanisms of the San Andreas Fault. *Journal of Geophysical Research* 98, 771-786.
- Childs, C., Manzocchi, T., Walsh, J.J., Bonson, C.G., Nicol, A., Schopfer, M.P.J., 2009. A geometric model of fault zone and fault rock thickness variations. *Journal of Structural Geology* 31, 117-127.
- De Bresser, J.H.P., Ter Heege, J.H., Spiers, C.J., 2001. Grain size reduction by dynamics recrystallization: can it result in major rheological weakening? *International Journal of Earth Sciences* 90, 28-45.
- DiToro, G., Hirose, T., Nielsen, S., Shimamoto, T., 2006. Relating high-velocity rock-friction experiments to coseismic slip in the presence of melts. In: Abercrombie, R.A., McGarr, A., DiToro, G., Kanamori, H. (Eds.), *Earthquakes: Radiated energy and the physics of faulting*. *Geophysical Monograph Series* 170, 121-134.
- DiToro, G., Pennacchioni, G., Nielsen, S., 2009. Pseudotachylytes and earthquake source mechanisms. *International Geophysics*, 94, 87-133.9
- Doll, W. G., Costain, J. K., Domoracki, W. J., Coruh, C., Ludman, A., Hopeck, J., 1996. Seismic reflection evidence for the evolution of a transcurrent fault system: the Norumbega fault zone, Maine. *Geology* 24, 251-254.
- Ellis, S., Beavan, J., Eberheart-Phillips, D., Stöckert, B., 2006. Simplified models of the Alpine Fault seismic cycle: stress transfer in the mid-crust. *Geophysical Journal International* 166, 386-402.
- Ellis, S., Stöckert, B., 2004a. Elevated stresses and creep rates beneath the brittle-ductile transition caused by seismic faulting in the upper crust. *Journal of Geophysical Research* 109, B05407, doi:10.1029/2003JB002744.

- Ellis, S., Stöckert, B., 2004b. Imposed strain localization in the lower crust on seismic timescales. *Earth Planets Space* 56, 1103-1109.
- Faulkner, D.R., Lewis, A.C., Rutter, E.H., 2003. On the internal structure and mechanics of large strike-slip fault zones: field observations of the Carboneras fault in southeastern Spain. *Tectonophysics* 367, 235-251.
- Faulkner, D.R., Mitchell, T.M., Rutter, E.H., Cembrano, J., 2008. On the structure and mechanical properties of large strike-slip faults. In: Wibberley, C.A.J., Kurz, W., Imber, J., Holdsworth, R.E., Collettini, C. (Eds.), *Structure of Fault Zones: Implications for Mechanical and Fluid-flow Properties*. Geological Society of London Special Publication 299, 139-150.
- Fliervoet, T.F., Drury, M., Chopra, P.N., 1999. Crystallographic preferred orientations and misorientations in some olivine rocks deformed by diffusion or dislocation creep. *Tectonophysics* 303, 1-27.
- Fliervoet, T.F., White, S.H., Drury, M., 1997. Evidence for dominant grain boundary sliding deformation in greenschist- and amphibolite-grade polymineralic ultramylonites from the Redbank Deformed Zone, Central Australia. *Journal of Structural Geology* 19, 1495-1520.
- Gerbi, C., West, D.P., Jr., 2007. Use of U-Pb geochronology to identify successive, spatially overlapping tectonic episodes during Silurian-Devonian orogenesis in south-central Maine, USA. *Geological Society of America Bulletin* 119, 1218-1231.
- Grover, T.W., Fernandes, L.C., 2003. Bedrock geology of the Weeks Mills 7.5' quadrangle, Maine. Maine Geological Survey Open-File Map 03-49, Scale = 1:24,000.
- Guermani, A., Pennacchioni, G., 1998. Brittle precursors of plastic deformation in a granite: an example from the Mont Blanc massif (Helvetic, western Alps). *Journal of Structural Geology* 20, 135-148.
- Guidotti, C.V., 1989. Metamorphism in Maine: an overview. In: Tucker, R.D., Marvinney, R.G. (Eds.), *Studies in Maine Geology: Igneous and Metamorphic Geology*. Maine Geological Survey 3, 1-17.
- Halfpenny, A., Prior, D.J., Wheeler, J., 2004. Using electron backscatter diffraction (EBSD) to measure misorientation between 'parent' and 'daughter' grains. Implications for recrystallization and nucleation. *Materials Science Forum* 467-470, 573-578.
- Halfpenny, A., Prior, D.J., Wheeler, J., 2006. Analysis of dynamic recrystallization and nucleation in a quartzite mylonite. *Tectonophysics* 427, 3-14.
- Handy, M.R., 1990. The solid-state flow of polymineralic rocks. *Journal of Geophysical Research* 95, 8647-8661.
- Handy, M.R., 1994. Flow laws for rocks containing two non-linear viscous phases: A phenomenological approach. *Journal of Structural Geology* 16, 287-301.

- Handy, M.R., Hirth, G., Burgmann, R., 2007. Continental Fault Structure and Rheology from the Frictional-to-Viscous Transition Downward. In: Handy, M.R., Hirth, G., Hovius, N. (Eds.), *Tectonic Faults: Agents of Change on a Dynamic Earth*. The MIT Press, Cambridge, Mass., USA, 139-181.
- Handy, M.R., Wissing, S.B., Streit, L.E., 1999. Frictional-viscous flow in mylonite with varied biminerale composition and its effect on lithosphere strength. *Tectonophysics* 303, 175-191.
- Hatheway, R.B., 1971. Evidence for Major Faulting in South-Central Maine. *Geological Society of America Bulletin* 82, 253-258.
- Heilbronner, R., Tullis, J., 2006a. The effect of static annealing on microstructures and crystallographic preferred orientations of quartzites experimentally deformed in axial compression and shear. In: de Meer, S., Drury, M.R., de Bresser, J.H.P., Pennock, G.M. (eds.), *Deformation Mechanisms, Rheology and Tectonics: Current Status and Future Perspectives*. Geological Society Special Publications 200, 191-218.
- Heilbronner, R., Tullis, J., 2006b. Evolution of c axis pole figures and grain size during dynamics recrystallization: Results from experimentally sheared quartzite. *Journal of Geophysical Research* 111, B10202, doi:10.1029/2005JB004194.
- Hibbard, J., 1994. Kinematics of Acadian deformation in the northern and Newfoundland Appalachians. *The Journal of Geology* 102, 215–228.
- Hippertt, J.F., 1994. Microstructures and c-axis fabrics indicative of quartz dissolution in sheared quartzites and phyllonites. *Tectonophysics* 229, 141-163.
- Hippertt, J., Egydio-Silva, M., 1996. New polygonal grains formed by dissolution-redeposition in quartz mylonite. *Journal of Structural Geology* 18, 1345-1352.
- Hippertt, J.F., Hongn, F.D., 1998. Deformation mechanisms in the mylonite/ultramylonite transition. *Journal of Structural Geology* 20, 1435-1448.
- Hirth, G., Tullis, J., 1992. Dislocation creep regimes in quartz aggregates. *Journal of Structural Geology* 14, 145–159.
- Hobbs, B.E., 1968. Recrystallization of single crystals of quartz. *Tectonophysics* 6, 353–401.
- Hobbs, B.E., Ord, A., Teyssier, C., 1986. Earthquakes in the ductile regime. *Pure and Applied Geophysics* 124, 309-336.
- Holdsworth, R.E., 2004. Weak faults - rotten cores. *Science* 303, 181-182.
- Holyoke III, C.W., Tullis, J., 2006. Formation and maintenance of shear zones. *Geology* 34, 105-108.
- Hongn, F.D., Hippertt, J.F., 2001. Quartz crystallographic and morphologic fabrics during folding/transposition in mylonites. *Journal of Structural Geology* 23, 81-92.

- Hubbard, M.S., 1999. Norumbega fault zone: Part of an orogen-parallel, strike-slip system, Northern Appalachians. In: Ludman, A., West, D.P., Jr., (Eds.), Norumbega Fault System of the Northern Appalachians. Geological Society of American Special Paper 331, 155-165.
- Hubbard, M.S. and Wang, H., 1999. Temperature variability during shear deformation: An interpretation of microstructures along the central Norumbega Fault zone, Maine. In: Ludman, A., West, D.P., Jr., (Eds.), Norumbega Fault System of the Northern Appalachians. Geological Society of American Special Paper 331, 25-40.
- Hubbard, M.S., West, D.P., Jr., Ludman, A., Guidotti, C.V., Lux, D.R., 1995. The Norumbega Fault Zone, Maine: a mid- to shallow-level crustal section within a transcurrent shear zone. *Atlantic Geology* 31, 109-116.
- Hussey, A.M., 1988, Lithotectonic stratigraphy, deformation, plutonism, and metamorphism, Greater Casco Bay Region, Southwestern Maine. In: Tucker, R.D., Marvinney, R.G. (Eds.), *Studies in Maine Geology: Igneous and Metamorphic Geology*. Maine Geological Survey, 17-34.
- Iacopini, D., Passchier, C.W., Koehn, D., Carosi, R., 2007. Fabric attractors in general triclinic flow systems and their application to high strain shear zones: a dynamical system approach. *Journal of Structural Geology* 29, 298–317.
- Imber, J., Holdsworth, R.E., Butler, C.A., Strachan, R.A., 2001. A reappraisal of the Sibson-Scholz fault zone model: The nature of the frictional to viscous (brittle-ductile) transition along a long-lived, crustal-scale fault, Outer Hebrides, Scotland. *Tectonics* 20, 601-624.
- Jefferies, S.P., Holdsworth, R.E., Shimamoto, T., Takagi, H., Lloyd, G.E., Spiers, C.J., 2006a. Origin and mechanical significance of foliated cataclastic rocks in the cores of crustal-scale faults: examples from the Median Tectonic Line, Japan. *Journal of Geophysical Research Solid Earth* 111, B12.
- Jefferies, S.P., Holdsworth, R.E., Wibberley, C.A.J., Shimamoto, T., Spiers, C.J., Niemeijer, A.R., Lloyd, G.E., 2006b. The nature and importance of phyllonite development in crustal-scale fault cores: an example from the Median Tectonic Line, Japan. *Journal of Structural Geology* 28, 220-235.
- John, T., Medvedev, S., Rüpke, L.H., Andersen, T.B., Podladchikov, Y.Y., Austrheim, H.A., 2009. Generation of intermediate-depth earthquakes by self-localizing thermal runaway. *Nature Geoscience* 2, 137-139.
- Johnson, S.E., Lenferink, H.J., Marsh, J.H., Price, N.A., Koons, P.O., West, D.P., Jr., 2009a. Kinematic vorticity analysis and evolving strength of mylonitic shear zones: new data and numerical results. *Geology* 37, 1075-1078.
- Johnson, S.E., Lenferink, H.J., Price, N.A., Marsh, J.H., Koons, P.O., West, D.P., Beane, R., 2009b. Clast-based kinematic vorticity gauges: the effects of slip at matrix/clast interfaces. *Journal of Structural Geology* 31, 1322-1339.

- Johnson, S.E., Marsh, J.H., Vernon, R.H., 2008. From tonalite to mylonite: coupled mechanical and chemical processes in foliation development and strain localization. In: Declan De Paor (Ed.), *Making Sense of Shear* (In honour of Carol Simpson). *Journal of the Virtual Explorer*, 30, 5, doi:10.3809/jvirtex.2009.00208.
- Johnson, S.E., Vernon, R.H., Upton, P.U., 2004. Foliation development and progressive strain-rate partitioning in the crystallizing carapace of a tonalite pluton: microstructural evidence and numerical modeling. *Journal of Structural Geology* 26, 1845-1865.
- Keleman, P.B., Hirth, G., 2007. A periodic shear-heating mechanism for intermediate-depth earthquakes in the mantle. *Nature* 446, 787-790.
- Kim, J., Ree, J., Han, R., Shimamoto, T., 2010. Experimental evidence for the simultaneous formation of pseudotachylyte and mylonite in the brittle regime. *Geology* 38, 1143-1146.
- Kirkpatrick, J.D., Shipton, Z.K., Persano, C., 2009. Pseudotachylytes: rarely generated, rarely preserved, or rarely reported. *Bulletin of the Seismological Society of America* 99, 382-388.
- Koch, N., Masch, L., 1992. Formation of Alpine mylonites and pseudotachylytes at the base of the Silvretta nappe, Eastern Alps. *Tectonophysics* 204, 289-306.
- Kohlstedt, D.L., Evans, B., Mackwell, S.J., 1995. Strength of the lithosphere: constraints imposed by laboratory experiments. *Journal of Geophysical Research* 100, 17587-17602.
- Kohlstedt, D.L., Weathers, M.S., 1980. Deformation-Induced Microstructures, Paleopiezometers, and Differential Stresses in Deeply Eroded Fault Zones. *Journal of Geophysical Research* 85, 6269-6285.
- Kronenberg, A.K., Kirby, S.H., Pinkston, J., 1990. Basal Slip and Mechanical Anisotropy of Biotite. *Journal of Geophysical Research* 95, 19257-19278.
- Kruhl, J.H., Peternell, M., 2002. The equilibration of high-angle grain boundaries in dynamically recrystallized quartz: the effect of crystallography and temperature. *Journal of Structural Geology* 24, 1125-1137.
- Küster, M., Stöckert, B., 1999. High differential stress and sublithospheric pore fluid pressure in the ductile regime- microstructural evidence for short-term post seismic creep in the Sesia Zone, Western Alps. *Tectonophysics* 303, 263-277.
- Law, R.D., 1990. Crystallographic fabrics: a selective review of their applications to research in structural geology. In: Knipe, R.J., Rutter, E.H. (eds.), *Deformation Mechanisms, Rheology and Tectonics*. Geological Society Special Publications 54, 335-352.
- Law, R.D., Schmid, S.M., Wheeler, J., 1990. Simple shear deformation and quartz crystallographic fabrics: a possible natural example from the Torridon area of NW Scotland. *Journal of Structural Geology* 12, 29-45.
- Lin, A., 2008a. *Fossil Earthquakes: The Formation and Preservation of Pseudotachylytes*. Springer, New York.

- Lin, A., 2008b. Seismic slipping in the lower crust inferred from granulite-related pseudotachylyte in the Woodroffe Thrust, Central Australia. *Pure and Applied Geophysics* 165, 215-233.
- Lin, A., Maruyama, T., Aaron, S., Michibayashi, K., Camacho, A., Kano, K., 2005. Propagation of seismic slip from brittle to ductile crust: Evidence from pseudotachylyte of the Woodroffe thrust, central Australia. *Tectonophysics* 402, 21-35.
- Lin, A., Sun, Z., Yang, Z., 2003. Multiple generations of pseudotachylyte in the brittle to ductile regimes, Qinling-Dabie Shan ultrahigh-pressure metamorphic complex, central China. *Island Arc* 12, 423-435.
- Lister, G.S., Dornsiepen, U.F., 1982. Fabric transitions in the Saxony granulite terrain. *Journal of Structural Geology* 4, 81-92.
- Lister, G.S., Hobbs, B.E., 1980. The simulation of fabric development during plastic deformation and its application to quartzite: the influence of deformation history. *Journal of Structural Geology* 2, 355-370.
- Lister, G.S., Paterson, M.S., Hobbs, B.E., 1978. The simulation of fabric development in plastic deformation and its application to quartzite: The model. *Tectonophysics* 45, 107-158.
- Lloyd, G.E., 2004. Microstructural evolution in a mylonitic quartz simple shear zone: the significant roles of dauphine twinning and misorientation. In: Alsop, G.I., Holdsworth, R.E., McCaffrey, K.J.W., Hand, M. (eds.), *Flow Processes in Faults and Shear Zones*. Geological Society Special Publications 224, 39-61.
- Lloyd, G.E., Farmer, A.B., Mainprice, D., 1997. Misorientation analysis and the formation and orientation of subgrain and grain boundaries. *Tectonophysics* 279, 55-78.
- Lloyd, G.E., Freeman, B., 1994. Dynamic recrystallization of quartz under greenschist conditions. *Journal of Structural Geology* 16, 867-881.
- Lloyd, G.E., Law, R.D., Mainprice, D., Wheeler, J., 1992. Microstructural and crystal fabric evolution during shear zone formation. *Journal of Structural Geology* 14, 1079-1100.
- Ludman, A., 1998. Evolution of a transcurrent fault system in shallow crustal metasedimentary rocks: the Norumbega fault zone, eastern Maine. *Journal of Structural Geology* 20, 92-107.
- Ludman, A., Gibbons, S., 1999. Multistage shearing of the Deblois granite in the Kellyland fault zone, eastern Maine. In: Ludman, A., West, D.P., Jr., (Eds.), *Norumbega Fault System of the Northern Appalachians*. Geological Society of American Special Paper 331, 41-57.
- Ludman, A., Lanzirotti, A., Lux, D., Wang, C., 1999. Constraints on timing and displacement of multistage shearing in the Norumbega Fault System eastern Maine. In: Ludman, A., West, D.P., Jr., (Eds.), *Norumbega Fault System of the Northern Appalachians*. Geological Society of American Special Paper 331, 179-194.
- McNulty, B.A., 1995. Pseudotachylyte generated in the semi-brittle and brittle regimes, Bench Canyon shear zone, central Sierra Nevada. *Journal of Structural Geology* 17, 1507-1521.

- Macaudière, J., Brown, W.L., Ohnenstetter, D., 1985. Microcrystalline textures resulting from rapid crystallization in a pseudotachylyte melt in a meta-anorthosite. *Contributions to Mineralogy and Petrology* 89, 39-51.
- Marsh, J.H., Johnson, S.E., Yates, M.G., West, D.P., Jr., 2009. Coupling of deformation and reactions during mid-crustal shear zone development: an in situ frictional–viscous transition. *Journal of Metamorphic Geology* 27, 531-553.
- Menegon, L., Piazzolo, S., Pennacchioni, G., 2011. The effect of Dauphiné twinning on plastic strain in quartz. *Contributions to Mineralogy and Petrology* 161, 635-652.
- Menegon, L., Pennacchioni, G., Heilbronner, R., Pittarello, L., 2008. Evolution of quartz microstructure and c-axis crystallographic preferred orientation within ductilely deformed granitoids (Arolla unit, Western Alps). *Journal of Structural Geology* 30, 1332-1347.
- Michibayashi, K., 1996. The role of intragranular fracturing on grain size reduction in feldspar during mylonitization. *Journal of Structural Geology* 18, 17-25.
- Moecher, D.P., Steltenpohl, M.G., 2009. Direct calculation of rupture depth for an exhumed paleoseismogenic fault from mylonitic pseudotachylyte. *Geology* 37, 999-1002.
- Montési, L.G.J., 2004. Postseismic deformation and the strength of ductile shear zones. *Earth Planets Space* 56, 1135-1142.
- Neumann, B., 2000. Texture development of recrystallized quartz polycrystals unraveled by orientation and misorientation characteristics. *Journal of Structural Geology* 22, 1695-1711.
- Niemeijer, A.R., Spiers, C.J., 2005. Influence of phyllosilicates on fault strength in the brittle-ductile transition: insights from rock analogue experiments. In: Bruhn, D., Burlini, L., (Eds.), *High Strain Zones: Structures and Physical Properties*. Geological Society, London, Special Publication 245, 303–327,
- Niemeijer, A.R., Spiers, C.J., 2006. Velocity dependence of strength and healing behavior in simulated phyllosilicate-breaking fault gouge. *Tectonophysics* 427, 231-253.
- Nowell, M.M., Wright, S.I., 2004. Phase differentiation via combined EBSD and XEDS. *Journal of Microscopy* 213, 296-305.
- Olesen, N.O., 2008. The microfabrics of a porphyroclast-rich quartzitic mylonite, Mjølfjell, Jotun Nappe Complex, Norway. *Norwegian Journal of Geology* 88, 89-101.
- Osberg, P.H., Hussey, A.M., II, Boone, G.M., 1985. *Bedrock Geologic Map of Maine*. Maine Geological Survey, Scale = 1:500,000.
- Pankiwskyj, K.A., 1976. Preliminary report on the geology of the Liberty 15' quadrangle and adjoining parts of the Burnham, Brooks, Belfast, and Vassalboro quadrangles in south-central Maine. *Maine Geological Survey Open-File Report* 76-79.
- Passchier, C.W., 1982. Pseudotachylyte and the development of ultramylonite bands in the Saint-Barthelemy Massif, French Pyrenees. *Journal of Structural Geology* 4, 69-79.

- Passchier, C.W., 1984. The generation of ductile and brittle shear bands in a low-angle mylonite zone. *Journal of Structural Geology* 6, 273-281.
- Passchier, C.W., Trouw, R.A.J., 2005. *Microtectonics*. Springer-Verlag, Berlin.
- Pauli, C., Schmid, S.M., Heilbronner, R.P., 1996. Fabric domains in quartz mylonites: localized three dimensional analysis of microstructure and texture. *Journal of Structural Geology* 18, 1183-1203.
- Pennacchioni, G., Cesare, B., 1997. Ductile-brittle transition in pre-Alpine amphibolite facies mylonites during evolution from water-present to water-deficient conditions (Mont Mary nappe, Italian Western Alps). *Journal of Metamorphic Geology* 15, 777-791.
- Philpotts, A., 1964. Origin of Pseudotachylytes. *American Journal of Science* 262, 1008-1035.
- Prior, D.J., 1999. Problems in determining the misorientation axes, for small angular misorientations, using electron backscatter diffraction in the SEM. *Journal of Microscopy* 195, 217-225.
- Ray, S.K., 1999. Transformation of cataclastically deformed rocks to pseudotachylyte by pervasion of friction melt: inferences from clast size analysis. *Tectonophysics* 301, 283-304.
- Ray, S.K., 2004. Melt-clast interaction and power-law size distribution of clasts in pseudotachylytes. *Journal of Structural Geology* 26, 1831-1843.
- Rice, J.R., 2006. Heating and weakening of faults during earthquake slip. *Journal of Geophysical Research* 111, B05311, doi: 10.1029/2005JB004006.
- Rolandone, F., Bürgmann, R., Nadeau, R.M., 2004. The evolution of the seismic-aseismic transition during the earthquake cycle: Constraints from the time-dependent depth distribution of aftershocks. *Geophysical Research Letters* 31, L23610, doi:10.1029/2004GL021379.
- Rutter, E.H., Brodie, K.H., 2004. Experimental grain-size sensitive flow of hot-pressed Brazilian quartz aggregates. *Journal of Structural Geology* 26, 2011-2023.
- Sammis, C.G., Osborne, R.H., Anderson, L.J., Banerdt, M., White, P., 1986. Self-similar cataclasis in the formation of fault gauge. *Pure and Applied Geophysics* 124, 53-78.
- Schwartz, A.J., Kumar, M., Adams, B.L., Field, D.P., 2009. *Electron Backscatter Diffraction in Materials Science*. Springer, New York.
- Schmid, S.M., Casey, M., 1986. Complete fabric analysis of some commonly observed quartz c-axis patterns. In: Hobbs, B.C., Heard, H.C. (eds.), *Mineral and Rock Deformation: Laboratory Studies*. American Geophysical Union, *Geophysical Monograph* 36, 263-286.
- Schmid, S.M., Handy, M.R., 1991. Towards a genetic classification of fault rocks: Geological usage and tectonophysical implications. In: Hsu, K.J., Mackenzie, J., Muller, D. (Eds.), *Controversies in Modern Geology*. Academic Press, London, 339-361.

- Scholz, C. H., 1998. Earthquakes and friction laws. *Nature* 391, 37-42.
- Scholz, C.H., 2002. *The Mechanics of Earthquakes and Faulting*. Cambridge University Press. Cambridge.
- Segall, P., Rice, J.R., 1995. Dilatancy, compaction, and slip instability of a fluid-infiltrated fault. *Journal of Geophysical Research* 100, 22,155-22,171.
- Shea, W.T., Kronenberg, A.K., 1992. Rheology and deformation mechanism of an isotropic mica schist. *Journal of Geophysical Research* 97, 15201–15237.
- Shea, W.T., Kronenberg, A.K., 1993. Strength and anisotropy of foliated rocks with varied mica contents. *Journal of Structural Geology* 15, 1097-1121.
- Shimamoto, T., Nagahamam, H., 1992. An argument against a crush origin for pseudotachylytes based on the analysis of clast-size distribution. *Journal of Structural Geology* 14, 999-1006.
- Shipton, Z.K., Soden, A.M., Kirkpatrick, J.D., Bright, A.M., Lunn, R.J., 2006. How thick is a fault? Fault displacement-thickness scaling revisited. *Earthquakes: Radiated Energy and the Physics of Faulting* 170, 193-198.
- Short, H.A., Johnson, S.E., 2006. Estimating vorticity from fibrous calcite veins, central Maine, USA. *Journal of Structural Geology* 28, 1167-1182.
- Sibson, R.H., 1975. Generation of pseudotachylyte by ancient seismic faulting. *Geophysical Journal of the Royal Astronomical Society* 43, 775-794.
- Sibson, R.H., 1980. Transient discontinuities in ductile shear zones. *Journal of Structural Geology* 2, 165-171.
- Sibson, R.H., 1986. Earthquakes and rock deformation in crustal fault zone. *Annual Reviews of Earth and Planetary Sciences* 14, 149-175.
- Sibson, R.H., Toy, V.G., 2006. The habit of fault-generated pseudotachylyte: presence vs. absence of friction-melt. In: Abercrombie, R.A., McGarr, A., DiToro, G., Kanamori, H. (Eds.), *Earthquakes: Radiated energy and the physics of faulting*. Geophysical Monograph Series 170, 153-166.
- Spray, J.G., 1995. Pseudotachylyte controversy: Fact for friction? *Geology* 23, 1119-1122.
- Spray, J.G., 1998. Localized shock- and friction-induced melting in response to hypervelocity impact. In: Grady, M.M., Hutchison, R., McCall, G.J.H., Rotherby, D. (Eds.), *Meteorites: Flux with time and impact effects*. London Geological Society, Special Publication 140, 195-204.
- Springer, D.S., Evans, J.P., Garver, J.L., Kirschner, D., Janecke, S., 2009. Arkosic rocks from the San Andreas Fault observatory at depth (SAFOD) borehole, central California: implications for structure and tectonics of the San Andreas Fault zone. *Lithosphere* 1, 206–226. doi:10.1130/L 13.1.

- Stewart, D. B., 1989, Crustal processes in Maine. *American Mineralogist* 74, 698–714.
- Stipp, M., Kunze, K., 2008. Dynamic recrystallization near the brittle-plastic transition in naturally and experimentally deformed quartz aggregates. *Tectonophysics* 448, 77-97.
- Stipp, M., Stünitz, H., Heilbronner, R., Schmid, S.M., 2002a. The eastern Tonale fault zone: a 'natural laboratory' for crystal plastic deformation of quartz over a temperature range from 250 and 700°C. *Journal of Structural Geology* 24, 1861-1884.
- Stipp, M., Stünitz, H., Heilbronner, R., Schmid, S.M., 2002b. Dynamic recrystallization of quartz: correlation between natural and experimental conditions. In: de Meer, S., Drury, M.R., de Bresser, J.H.P., Pennock, G.M. (eds.), *Deformation Mechanisms, Rheology and Tectonics: Current Status and Future Perspectives*. Geological Society Special Publications 200, 171-190.
- Stipp, M., Tullis, J., 2003. The recrystallized grain size piezometer for quartz. *Geophysical Research Letters* 30, doi: 10.1029/2003GL018444.
- Swanson, M.T., 1988. Pseudotachylyte-bearing strike-slip duplex structures in the Fort Foster Brittle Zone, S. Maine. *Journal of Structural Geology* 10, 813-828.
- Swanson, M.T., 1992. Late Acadian-Alleghenian transpressional deformation: Evidence from asymmetric boudinage in the Casco Bay area, coastal Maine. *Journal of Structural Geology* 14, 323-341.
- Swanson, M., 1999a. Kinematic indicators for regional dextral shear along the Norumbega fault system in the Casco Bay area, coastal Maine. In: Ludman, A., West, D.P., Jr. (Eds.), *Norumbega Fault System of the Northern Appalachians*. Geological Society of American Special Paper 331, 1-23.
- Swanson, M., 1999b. Dextral transpression at the Casco Bay restraining bend, Norumbega fault zone, coastal Maine. In: Ludman, A., West, D.P., Jr., (Eds.), *Norumbega Fault System of the Northern Appalachians*. Geological Society of American Special Paper 331, 85-104.
- Swanson, M.T., 2005a. Digital Mapping in a new pseudotachylyte locality from the Harbor Island fault zone, Muscongus Bay, Maine. *Geological Society of America Abstracts with Programs* 37, 59
- Swanson, M.T., 2005b. Fort Foster Brittle Zone: Dextral Pseudotachylyte-bearing Strike-Slip Fault Surfaces in Mylonitic Host Rocks, Kittery, Maine. AGU Chapman Conference, Portland, Maine, June 16, 2005.
- Swanson, M., 2006a. Late Paleozoic strike-slip faults and related vein arrays of Cape Elizabeth, Maine. *Journal of Structural Geology* 28, 456-473.
- Swanson, M., 2006b. Pseudotachylyte-bearing strike-slip faults in mylonitic host rocks, Fort Foster Brittle Zone, Kittery, Maine. In: Abercrombie, R.A., McGarr, A., DiToro, G., Kanamori, H. (Eds.), *Earthquakes: Radiated energy and the physics of faulting*. Geophysical Monograph Series 170, 167-179.

- Swanson, M.T., Bampton, M., 2009. Integrated digital mapping in geologic field research: An adventure-based approach to teaching new geospatial technologies in an REU Site Program. In: Whitmeyer, S.J., Mogk, D.W., Pyle, E.J. (Eds.), *Field Geology Education: Historical Perspectives and Modern Approaches*. Geological Society of American Special Paper 461, 117-133.
- Takagi, H., Kiyohiko, G., Shigematsu, N., 2000. Ultramylonite bands derived from cataclasite and pseudotachylyte in granites, northeast Japan. *Journal of Structural Geology* 22, 1325-1339.
- Takeshita, T., Wenk, H.R., Lebensohn, R., 1999. Development of preferred orientation and microstructure in sheared quartzite: comparison of natural data and simulated results. *Tectonophysics* 312, 133-155.
- Tanaka, H., Shimada, K., Toyoshima, T., Obara, T., Niizato, T., 2004. Heterogeneous material distribution, an important reason for generation of strain-localized mylonite and frictional slip zones in Hidaka metamorphic belt, Hokkaido, Japan. *Earth Planets Space* 56, 1225-1232.
- Tomascak, P.B., Krogstad, E.J., Walker, R.J., 1996. U-Pb monazite geochronology of granitic rocks from Maine: implications for late Paleozoic tectonics in the Northern Appalachians. *Journal of Geology* 104, 185-195.
- Toy, V.G., Prior, D.J., Norris, R.J., 2008. Quartz fabrics in the Alpine Fault Mylonites: Influence of pre-existing preferred orientations on fabric development during progressive uplift. *Journal of Structural Geology* 30, 602-621.
- Toy, V.G., Ritchie, S., Sibson, R.H., 2011. Diverse habitats of pseudotachylytes in the Alpine Fault Zone and relationships to current seismicity. In: Fagereng, A., Toy, V.G., Rowland, J.V. (Eds.), *Geology of the Earthquake Source: A Volume in Honour of Rick Sibson*. Geological Society, London, Special Publications 359, 97-113.
- Trepmann, C.A., Stöckert, B., 2002. Cataclastic deformation of garnet: a record of synseismic loading and postseismic creep. *Journal of Structural Geology* 24, 1845-1856.
- Trepmann, C.A., Stöckert, B., 2003. Quartz microstructures developed during non-steady state plastic flow at rapidly decaying stress and strain rate. *Journal of Structural Geology* 25, 2035-2051.
- Trepmann, C.A., Stöckert, B., Dorner, D., Moghadam, R.H., Küster, M., Röller, K., 2007. Simulating coseismic deformation of quartz in the middle crust and fabrics evolution during postseismic stress relaxation- An experimental study. *Tectonophysics* 442, 83-104.
- Trimby, P.W., Prior, D.J., Wheeler, J., 1998. Grain boundary hierarchy development in a quartz mylonite. *Journal of Structural Geology* 20, 917-935.
- Tsutsumi, A., 1999. Size distribution of clasts in experimentally produced pseudotachylytes. *Journal of Structural Geology* 21, 305-312.

- Tucker, R.D., Osberg, P.H., Berry, H.N., IV, 2001. The geology of a part of Acadia and the nature of the Acadian Orogeny across central and eastern Maine. *American Journal of Science* 301, 205-260.
- Tullis, J., Tullis, T.E., 1972. Preferred orientation produced by mechanical Dauphiné twinning. Thermodynamics and axial experiments. *Am. Geophys. U. Monogr.* 16, 67–82.
- Tullis, J., Christie, J.M., Griggs, D.T., 1973. Microstructures and Preferred Orientations of Experimentally Deformed Quartzites. *Geological Society of America Bulletin* 84, 297-314.
- Ueda, T., Obata, M., DiToro, G., Kanagawa, K., Ozawa, K., 2008. Mantle earthquakes frozen in mylonitized ultramafic pseudotachylytes of spinel-lherzolite facies. *Geology* 36, 607-610.
- van Daalen, M., Heilbronner, R., Kunze, K., 1999. Orientation analysis of localized shear deformation in quartz fibres at the brittle-ductile transition. *Tectonophysics* 303, 83-107.
- van Staal, C.R., 2007. Pre-Carboniferous metallogeny of the Canadian Appalachians. In: Goodfellow, W.D., (Ed.), *Mineral resources of Canada: A synthesis of major deposit-types, district metallogeny, the evolution of geological provinces, and exploration method: Jointly by the Mineral Deposit Division of the Geological Association of Canada and the Geological Survey of Canada.*
- Vernooij, M.G.C., den Brok, B., Kunze, K., 2006a. Development of crystallographic preferred orientation by nucleation and growth of new grains in experimentally deformed quartz single crystals. *Tectonophysics* 427, 35-53.
- Vernooij, M.G.C., Kunze, K., den Brok, B., 2006b. 'Brittle' shear zones in experimentally deformed quartz single crystals. *Journal of Structural Geology* 28, 1292-1306.
- Wang, C., Ludman, A., 2002. Evidence for post-Acadian through Alleghanian deformation in eastern Maine: multiple brittle reactivation of the Norumbega Fault system. *Atlantic Geology* 38, 37-52.
- Wang, C., Ludman, A., 2004. Deformation conditions, kinematics, and displacement history of shallow ductile shearing in the Norumbega fault system in the northern Appalachians, eastern Maine. *Tectonophysics* 384, 129-148.
- Wenk, H.R., Janssen, C., Kenkmann, T., Dresen, G., 2011. Mechanical twinning in quartz: Shock experiments, impact, pseudotachylites and fault breccias. *Tectonophysics* 510, 69–79. doi:10.1016/j.tecto.2011.06.016.
- West, D.P., Jr., 1999. Timing of displacements along the Norumbega Fault System, south-central and south-coastal Maine. In: Ludman, A., West, D.P., Jr., (Eds.), *Norumbega Fault System of the Northern Appalachians*. Geological Society of American Special Paper 331, 167-178.
- West, D.P., Jr., Guidotti, C.V., Lux, D.R., 1995. Silurian orogenesis in the western Penobscot Bay region, Maine. *Canadian Journal of Earth Science* 32, 1845-1858.

- West, D.P., Jr., Hubbard, M.S., 1997. Progressive localization of deformation during exhumation of a major strike-slip shear zone: Norumbega fault zone, south-central Maine, USA. *Tectonophysics* 273, 185-202.
- West, D.P., Jr., Lux, D.R., 1993. Direct dating of mylonitization by the $^{40}\text{Ar}/^{39}\text{Ar}$ method: An example from the Norumbega fault zone, Maine. *Earth and Planetary Science Letters* 120, 221-237.
- West, D.P., Jr., Lux, D.R., Hussey, A.M., 1993. Contrasting thermal histories across the Flying Point fault, southwestern, Maine: Evidence for Mesozoic displacement. *Geological Society of America Bulletin* 105, 1478-1490.
- West, D.P., Jr., Peterman, E.M., 2004. Bedrock Geology of the Razorville 7.5' quadrangle, Maine. Maine Geological Survey Open-File Map 04-29: Scale = 1:24,000.
- West, D.P., Jr., Roden-Tice, M.K., 2003. Late Cretaceous reactivation of the Norumbega fault zone, Maine: Evidence from apatite fission-track ages. *Geology* 31, 649-652.
- West, D.P., Jr., Roden-Tice, M.K., Potter, J.K., Barnard, N.Q., 2008. Assessing the role of orogen-parallel faulting in post orogenic exhumation: low temperature thermochronology across the Norumbega Fault System, Maine. *Canadian Journal of Earth Science* 45, 287-301.
- West, D.P., Jr., Sanford, J.C., 2009. Mylonite, cataclasite, and pseudotachylyte in the Jones Corner fault zone, south-central Maine: A polyphase history of shearing, faulting and seismicity. *Geological Society of America Abstracts with Programs* 41, 460.
- Wheeler, J., Prior, D.J., Jiang, Z., Spiess, R., Trimby, P.W., 2001. The petrological significance of misorientations between grains. *Contributions to Mineralogy and Petrology* 141, 109-124.
- White, J.C., 1996. Transient discontinuities revisited: pseudotachylyte, plastic instability and the influence of low pore fluid pressure on deformation processes in the mid-crust. *Journal of Structural Geology* 18, 1471-1486.
- White, J. C., 2004. Instability and localization of deformation in lower crustal granulites, Minas fault zone, Nova Scotia, Canada. In: Alsop, G.I., Holdsworth, R.E., McCaffrey, K.J.W., Hand, M. (Eds.), *Flow processes in faults and shear zones*. Geological Society, London, Special Publications 224, 25-37.
- White, S.H., Burrows, S.E., Carreras, J., Shaw, N.D., Humphreys, F.J., 1980. On mylonites in ductile shear zones. *Journal of Structural Geology* 2, 175-187.
- Wibberley, C.A.J., Shimamoto, T., 2003. Internal structure and permeability of major strike-slip fault zones: the Median Tectonic Line in Mie Prefecture, Southwest Japan. *Journal of Structural Geology* 25, 59-78.
- Wintsch, R.P., Christoffersen, R., Kronenberg, A.K., 1995. Fluid-rock reaction weakening of fault zones. *Journal of Geophysical Research* 100, 13021-13032.

APPENDIX

SAMPLE LOCATIONS WITHIN THE SANDHILL CORNER SHEAR ZONE

Table A.1. Location data for samples from the Sandhill Corner shear zone used within this study.

Date Collected	Sample	Rock Type	Field Area	Location (UTM)	
6/11/08	NAP08-1	CE	Quarry	463141	4905780
6/11/08	NAP08-2	CE	Quarry	463141	4905780
6/11/08	NAP08-3	CE	Crummet Mt.	460554	4903990
6/11/08	NAP08-4	CE	Crummet Mt.	460505	4902901
6/11/08	NAP08-5	CE	N of termination	Float	
7/2/08	NAP08-10	CM	BB-Field	459729	4902142
7/2/08	NAP08-11	CM	BB-Field	459727	4902139
7/2/08	NAP08-12	CM	BB-Field	459728	4902145
7/2/08	NAP08-13	CM	BB-Field	459728	4902146
7/2/08	NAP08-14	CM	BB-Field	459730	4902148
7/2/08	NAP08-15	CM	BB-Field	459729	4902148
7/2/08	NAP08-16	CM	BB-Field	459729	4902149
7/2/08	NAP08-17	CM	BB-Field	459731	4902153
7/8/08	NAP08-18	CM	BB-Field	459733	4902158
7/8/08	NAP08-19	CM	BB-Field	459734	4902159
7/8/08	NAP08-20	CM	BB-Field	459735	4902160
7/8/08	NAP08-21	CM	BB-Field	459734	4902161
7/8/08	NAP08-22	CM	BB-Field	459735	4902160
7/8/08	NAP08-23	CM	BB-Field	459740	4902169
7/8/08	NAP08-24	CM	BB-Field	459739	4902171
7/8/08	NAP08-25	CM	BB-Field	459746	4902170
7/8/08	NAP08-26	CM	BB-Field	459741	4902173
7/8/08	NAP08-27	CM	BB-Field	459737	4902172
7/8/08	NAP08-28	CM	BB-Field	459733	4902171
7/10/08	NAP08-29	CM	BB-Field	459754	4902165
7/10/08	NAP08-30	CM	BB-Field	459750	4902160
7/10/08	NAP08-31	CM	BB-Field	459745	4902145
7/10/08	NAP08-32	CM	BB-Field	459750	4902145
7/10/08	NAP08-33	CM	BB-Field	459748	4902136
7/10/08	NAP08-34	CM	BB-Field	459736	4902131
7/10/08	NAP08-35	CM	BB-Field	459750	4902103
7/10/08	NAP08-36	CM	BB-Field	459758	4902121
7/10/08	NAP08-37	CM	BB-Field	459800	4902143
7/10/08	NAP08-38	CM	BB-Field	459800	4902135

Table A.1. Continued.

Date Collected	Sample	Rock Type	Field Area	Location (UTM)	
7/11/08	NAP08-39	CM	BB-Field	459781	4901709
7/11/08	NAP08-40	CM	BB-Field	459727	4901751
7/11/08	NAP08-41	CE	BB-Field	459730	4902181
7/11/08	NAP08-42	CE	BB-Field	459727	4902180
7/15/08	NAP08-43	CE	BB-Field	459722	4902191
7/15/08	NAP08-44	CE	BB-Field	459721	4902192
7/15/08	NAP08-45	CE	BB-Field	float-sample missing	
7/15/08	NAP08-46	CE	BB-Field	459716	4902208
7/15/08	NAP08-47	CE	BB-Field	459717	4902208
7/15/08	NAP08-48	CE	BB-Field	459708	4902204
7/15/08	NAP08-49	CE	BB-Field	459710	4902215
7/15/08	NAP08-50	CE	BB-Field	459706	4902213
7/15/08	NAP08-51	CE	BB-Field	459707	4902213
7/15/08	NAP08-52	CE	BB-Field	459700	4902199
7/15/08	NAP08-53	CE	BB-Field	459712	4902205
7/15/08	NAP08-54	CE	BB-Field	459708	4902198
7/16/08	NAP08-55	CE	BB-Field	459602	4902233
7/16/08	NAP08-56	CE	BB-Field	459670	4902209
7/17/08	NAP08-57	CE	BB-Field Powerline	459042	4901469
7/17/08	NAP08-58	CE	BB-Field Powerline	459007	4901475
7/17/08	NAP08-59	CE	BB-Field Powerline	458731	4901410
7/17/08	NAP08-60	CE	BB-Field Powerline	458730	4901410
7/17/08	NAP08-61	CE	BB-Field Powerline	458750	4901393
7/17/08	NAP08-62	CE	BB-Field Powerline	458827	4901368
7/17/08	NAP08-63	CE	BB-Field Powerline	458859	4901366
7/17/08	NAP08-64	CE	BB-Field Powerline	458890	4901367
7/17/08	NAP08-65	CE	BB-Field Powerline	458933	4901353
7/17/08	NAP08-66	CE	BB-Field Powerline	458938	4901346
7/17/08	NAP08-67	CM	BB-Field Powerline	459078	4901419
7/17/08	NAP08-68	CE	BB-Field	459578	4902211
7/17/08	NAP08-69	CE	BB-Field	459660	4902226
7/17/08	NAP08-70	CE	BB-Field	459659	4902236
7/17/08	NAP08-71	CE	BB-Field	459663	4902250
7/17/08	NAP08-72	CE	BB-Field	459670	4902274

Table A.1. Continued.

Date Collected	Sample	Rock Type	Field Area	Location (UTM)	
7/17/08	NAP08-73	CE	BB-Field	459670	4902274
7/17/08	NAP08-74	CE	BB-Field	459697	4902193
7/17/08	NAP08-75	CE	BB-Field	459690	4902159
7/18/08	NAP08-76	CE	BB-Field	459688	4902168
7/18/08	NAP08-77	CE	BB-Field	459691	4902169
7/18/08	NAP08-78	CE	BB-Field	459693	4902168
7/18/08	NAP08-79	CE	BB-Field	459693	4902169
7/18/08	NAP08-80	CE	BB-Field	459693	4902168
7/18/08	NAP08-81	CE	BB-Field	459694	4902169
7/18/08	NAP08-82	CE	BB-Field	459674	4902285
7/18/08	NAP08-83	CE	BB-Field	459625	4902377
7/18/08	NAP08-84	CE	BB-Field	459642	4902395
7/22/08	NAP08-85	CM	Crummet Mt.	460393	4902913
7/22/08	NAP08-86	CM	Crummet Mt.	460413	4902886
7/22/08	NAP08-87	CM	Crummet Mt.	460427	4902921
7/23/08	NAP08-88	CE	Crummet Mt.	460487	4903008
7/23/08	NAP08-89	CE	Crummet Mt.	460479	4902999
7/23/08	NAP08-90	CE	Crummet Mt.	460485	4903001
7/23/08	NAP08-91	CE	Crummet Mt.	460484	4903008
7/23/08	NAP08-92	CE	Crummet Mt.	460487	4903006
7/23/08	NAP08-93	CE	Crummet Mt.	460453	4902990
7/23/08	NAP08-94	CE	Crummet Mt.	460457	4902987
7/23/08	NAP08-95	CE	Crummet Mt.	460451	4902993
7/23/08	NAP08-96	CE	Crummet Mt.	460416	4902997
7/23/08	NAP08-97	CE	Crummet Mt.	460382	4902987
7/23/08	NAP08-98	CE	Crummet Mt.	460388	4902992
7/23/08	NAP08-99	CE	Crummet Mt.	460376	4903009
7/24/08	NAP08-100	CE	Quarry	463159	4905961
7/24/08	NAP08-101	CE	Quarry	463168	4905962
7/24/08	NAP08-102	CE	Quarry	463161	4905953
7/29/08	NAP08-103	CE	Quarry	463170	4905956
7/29/08	NAP08-104	CE	Quarry	463165	4905954
7/29/08	NAP08-105	CE	Quarry	463161	4905946
7/29/08	NAP08-106	CE	Quarry	463168	4905920

Table A.1. Continued.

Date Collected	Sample	Rock Type	Field Area	Location (UTM)	
7/30/08	NAP08-107	CM	Crummett Mt.	460264	4902770
7/30/08	NAP08-108	CM	Crummett Mt.	460269	4902764
7/30/08	NAP08-109	CM	Crummett Mt.	460267	4902783
7/30/08	NAP08-110	CM	Crummett Mt.	460200	4902712
8/1/08	NAP08-111	CM?	Quarry	463206	4905905
8/1/08	NAP08-112	CaSi	Quarry	463430	4906031
8/1/08	NAP08-113	CaSi	Quarry	463428	4905993
8/1/08	NAP08-114	CaSi	Quarry	463424	4905999
8/1/08	NAP08-115	CE	Quarry	463390	4905908
8/1/08	NAP08-116	CE	Quarry	463427	4905875
2008	NAP08-121	CE	BB-Field	Float	
2008	NAP08-122	CE	BB-Field	Float	
2008	NAP08-123	CE	BB-Field	Float	
2008	NAP08-124	CE	Quarry	Float	
2008	NAP08-125	CE	Quarry	Float	
2008	NAP08-126	CE	Quarry	Float	
2008	NAP08-127	CE	Quarry	Float	
2008	NAP08-128	CE	Quarry	Float	
2008	NAP08-129	CE	Quarry	Float	
2008	NAP08-130	CE	Quarry	Float	
2008	NAP08-131	CE	Quarry	Float	
2008	NAP08-132	CE	Quarry	Float	
2008	NAP08-133	CE	Quarry	Float	
5/22/09	NAP09-200	CE	BB-Field-woods	459650	4902219
5/22/09	NAP09-201	CE	BB-Field-woods	459670	4902209
5/22/09	NAP09-202	CE	BB-Field-woods	459689	4902379
5/22/09	NAP09-203	CE	BB-Field-woods	459683	4902389
5/22/09	NAP09-204	CE	BB-Field-woods	459686	4902391
5/22/09	NAP09-205	CE	BB-Field-woods	459671	4902414
5/22/09	NAP09-206	CE	BB-Field-woods	459640	4902439
5/22/09	NAP09-207	CE	BB-Field-woods	459653	4902442
5/22/09	NAP09-208	CE	BB-Field-woods	459708	4902334
5/22/09	NAP09-209	CE	BB-Field-woods	459705	4902330
5/22/09	NAP09-210	CE	BB-Field-woods	459821	4902348

Table A.1. Continued.

Date Collected	Sample	Rock Type	Field Area	Location (UTM)	
5/27/09	NAP09-211	CM	Crummet Mt.	460563	4903083
5/27/09	NAP09-212	CM	Crummet Mt.	460568	4903082
5/27/09	NAP09-213	CM	Crummet Mt.	460580	4903096
5/27/09	NAP09-214	CM	Crummet Mt.	460582	4903084
5/27/09	NAP09-215	CM	Crummet Mt.	460587	4903047
5/27/09	NAP09-216	CM	Crummet Mt.	460585	4903039
5/27/09	NAP09-217	CM	Crummet Mt.	460595	4903021
5/27/09	NAP09-218	CE	Crummet Mt.	460554	4903099
5/27/09	NAP09-219	CE	Crummet Mt.	460556	4903123
5/27/09	NAP09-220	CE	Crummet Mt.	460550	4903118
5/27/09	NAP09-221	CE	Crummet Mt.	460572	4903177
5/27/09	NAP09-222	CE	Crummet Mt.	460574	4903158
5/27/09	NAP09-223	CE	Crummet Mt.	460575	4903193
5/27/09	NAP09-224	CM	Crummet Mt.	460237	4902730
5/27/09	NAP09-225	CM	Crummet Mt.	460240	4902721
5/27/09	NAP09-226	CM	Crummet Mt.	460207	4902688
5/2009	NAP09-227		various	Float	
5/2009	NAP09-228		various	Float	
5/2009	NAP09-229		various	Float	
5/2009	NAP09-230		various	Float	
5/2009	NAP09-231		various	Float	
5/2009	NAP09-232		various	Float	
5/2009	NAP09-233		various	Float	
5/29/09	NAP09-240	CM	Crummet Mt.	460182	4902669
5/29/09	NAP09-241	CM	Crummet Mt.	460186	4902667
5/29/09	NAP09-242	CM	Crummet Mt.	460185	4902667
5/29/09	NAP09-243	CM	Crummet Mt.	460196	4902669
5/29/09	NAP09-244	CM	Crummet Mt.	460177	4902643
5/29/09	NAP09-245	CM	Crummet Mt.	460172	4902642
5/29/09	NAP09-246	CM	Crummet Mt.	460164	4902620
5/29/09	NAP09-247	CE	Crummet Mt.	460150	4902647
5/29/09	NAP09-248	CE	Crummet Mt.	460167	4902684
5/29/09	NAP09-249	CE	Crummet Mt.	460156	4902688
5/29/09	NAP09-250	CE	Crummet Mt.	460153	4902704

Table A.1. Continued.

Date Collected	Sample	Rock Type	Field Area	Location (UTM)	
5/29/09	NAP09-251	CE	Crummett Mt.	460109	4902702
5/29/09	NAP09-252	CE	Crummett Mt.	460087	4902782
5/29/09	NAP09-253	CE	Crummett Mt.	460105	4902878
5/30/09	NAP09-254	CE	Quarry	463115	4906090
5/30/09	NAP09-255	CaSi	Quarry	463202	4905904
5/30/09	NAP09-256	CaSi	Quarry	463319	4905863
5/30/09	NAP09-257	CaSi	Quarry	463328	4905874
5/30/09	NAP09-258	CaSi	Quarry	463334	4905892
5/30/09	NAP09-259	CM	Quarry	463010	4905616
5/30/09	NAP09-260	CE	Quarry	462931	4905658
5/30/09	NAP09-261	CE	Quarry	462949	4905662
5/30/09	NAP09-262	CE	Quarry	462968	4905668
5/30/09	NAP09-263	CE	Quarry	462931	4905669
5/30/09	NAP09-264	CE	Quarry	462921	4905696
10/12/09	NAP09-270	CE	Quarry	463042	4905841
10/12/09	NAP09-271	CE	Quarry	463052	4906804
10/12/09	NAP09-272	CE	Quarry	463067	4905789
10/12/09	NAP09-273	CE	Quarry	463071	4905786
10/12/09	NAP09-274	CaSi	Quarry	462970	4905590
10/12/09	NAP09-275	CaSi	Quarry	462990	4905559
10/12/09	NAP09-276	CM	Quarry	463034	4905537
10/20/09	NAP09-277	CE	Quarry	463106	4905879
10/20/09	NAP09-278	CE	Quarry	463158	4905864
10/20/09	NAP09-279	CE	Quarry	463165	4905897
10/20/09	NAP09-280	CE	Quarry	463169	4905892
10/21/09	NAP09-281	CE?	Quarry	463397	4905881
10/21/09	NAP09-282	CE?	Quarry	463424	4905904
10/30/09	NAP09-283	CM	Quarry	462923	4905541
10/30/09	NAP09-284	CE	Quarry	462920	4905594
10/30/09	NAP09-285	CE	Quarry	463003	4905390
10/30/09	NAP09-286	CaSi	Quarry	462902	4905481
10/30/09	NAP09-287	CM	Quarry	462813	4905393

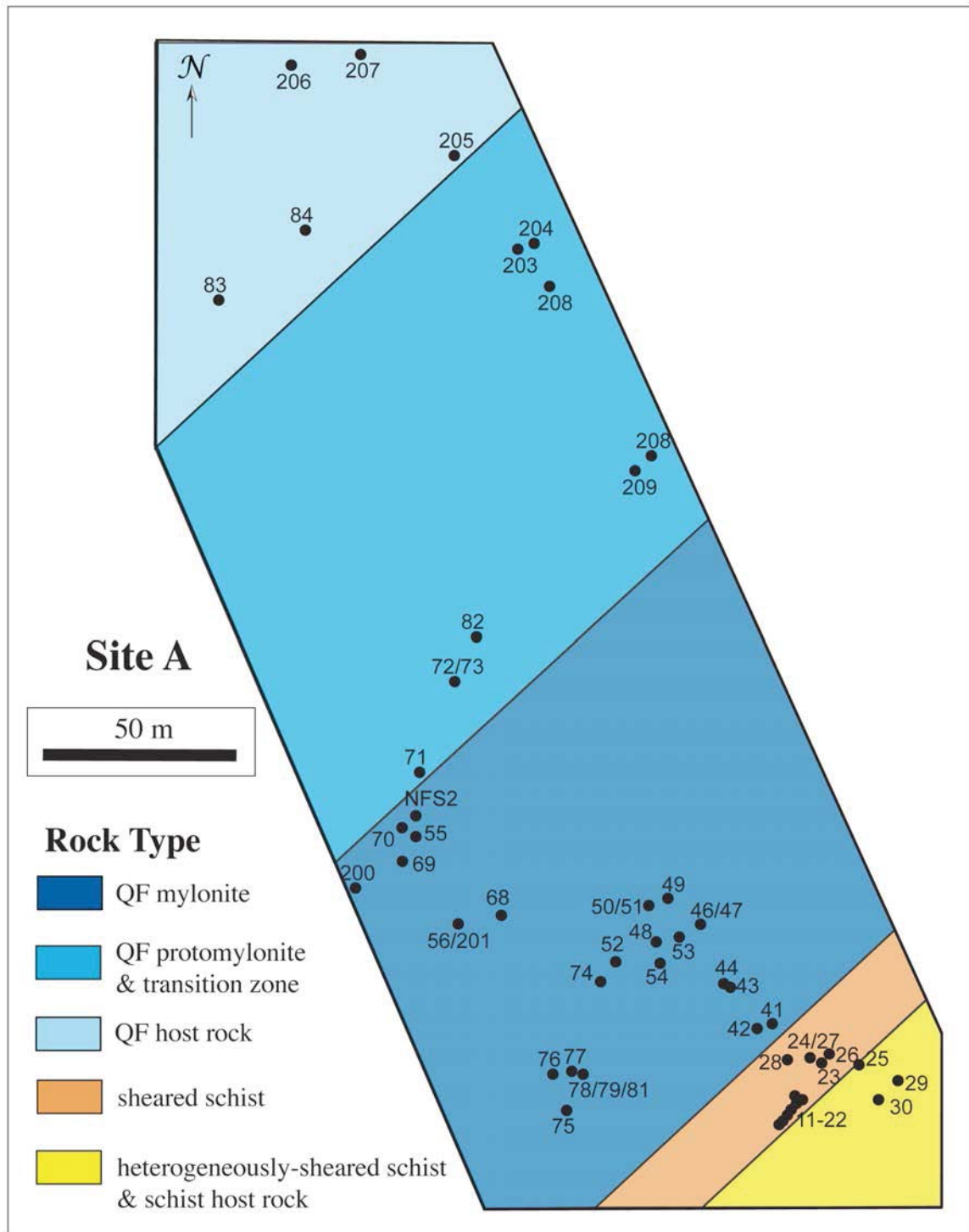


Figure A.1. A map of the blueberry field area (Site A) showing the location of numbered samples. Refer to Figure 4.1 for the site location on the regional map.

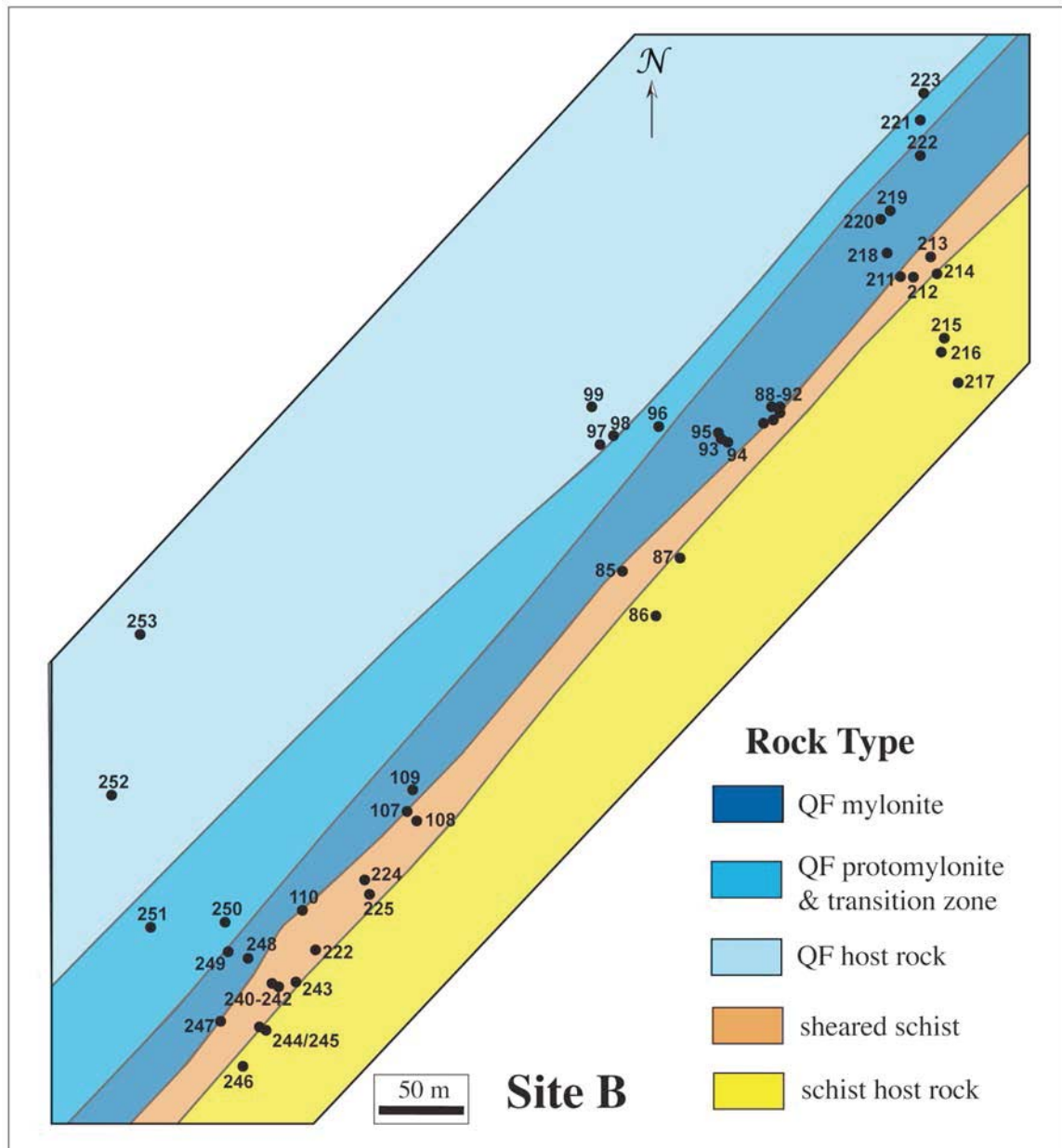


Figure A.2. A map of the Crummett Mountain area (Site B) showing the location of numbered samples. Refer to Figure 4.1 for the site location on the regional map.

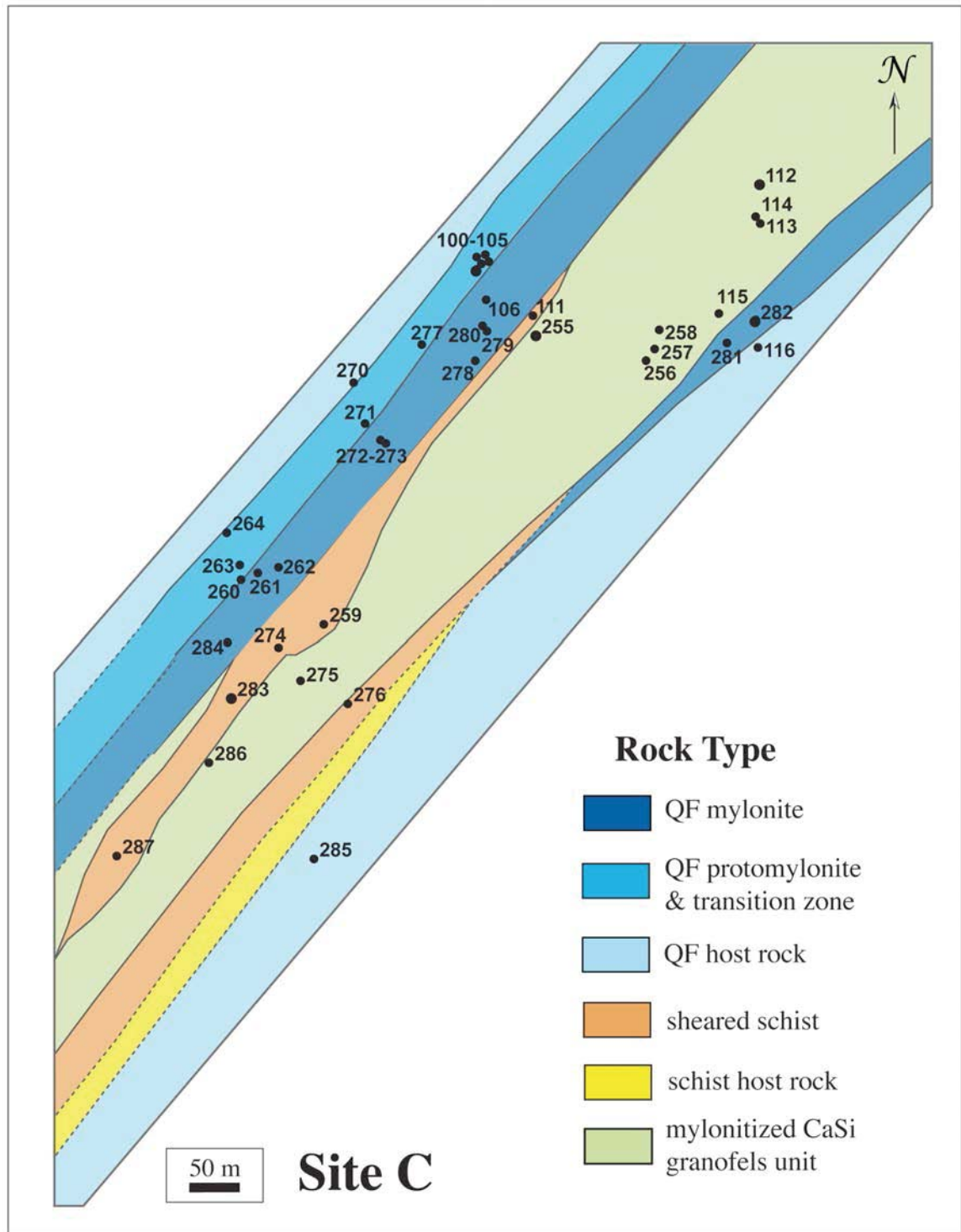


Figure A.3. A map of the Quarry area (Site C) showing the location of numbered samples. Refer to Figure 4.1 for the site location on the regional map.

BIOGRAPHY OF THE AUTHOR

Nancy Ann Price was born in Philadelphia, Pennsylvania in the summer of 1982. She grew up in Sicklerville, New Jersey and graduated as valedictorian in 2000 from Overbrook Regional Senior High School in Pine Hill, New Jersey. In May 2005, she graduated summa cum laude with distinction from the Richard Stockton College of New Jersey of Pomona, New Jersey with a Bachelor of Science degree in Biology and Geology. In September 2007, she received her Masters of Science degree in Geosciences from the University of Massachusetts-Amherst. She is a candidate for the Doctor in Philosophy degree in Earth Sciences from The University of Maine in May, 2012.